The New AC/DC Hybrid Microgrid Paradigm: Analysis and Operational Control

by

Abdelsalam Eajal

A thesis
presented to the University of Waterloo
in fulfillment of the
thesis requirement for the degree of
Doctor of Philosophy
in
Electrical and Computer Engineering

Waterloo, Ontario, Canada, 2018

Examining Committee Membership

The following served on the Examining Committee for this thesis. The decision of the Examining Committee is by majority vote.

External Examiner:	Rajiv Varma Professor, Department of Electrical & Computer Engineering, Western University
Supervisor(s):	Ehab El-Saadany Professor, Department of Electrical & Computer Engineering, Kumaraswamy Ponnambalam Professor, Department of Systems Design Engineering. University of Waterloo
Internal Member:	Kankar Bhattacharya Professor, Department of Electrical & Computer Engineering, University of Waterloo
Internal Member:	Ramadan El-Shatshat Lecturer, Department of Electrical & Computer Engineering, University of Waterloo
Internal-External Member:	Hector Budman Professor, Department of Chemical Engineering, University of Waterloo

I hereby declare that I am the sole author of this thesis. This is a true copy of the thesis, including any required final revisions, as accepted by my examiners.

I understand that my thesis may be made electronically available to the public.

Abstract

AC/DC hybrid microgrids (HMGs) represent a promising architecture that allows the hosting of innovative dc energy resources, such as renewables, and modern dc loads, such as electric vehicles, thereby reducing the number of conversion stages and offering other technical and cost benefits. Such advantages have prompted power distribution planners to begin investigating the possibility of hybridizing existing ac grids and designing new ac/dc hybrid clusters, referred to as microgrids, as a step toward an envisioned smart grid that incorporates multiple ac/dc microgrids characterized by "plug-and-play" features. Despite their potential, when either islanded or interfaced with the main grid, HMGs create challenges with respect to system operation and control, such as difficulties related to precise power sharing, voltage stability during a contingency, the control and management of power transfer through the interlinking converters (ICs), and the coordination of local distributed energy resources (DERs) with the hosting main grid.

An understanding of HMGs and their operational philosophy during islanding will assuredly pave the way toward the realization of a future smart grid that includes a plug-and-play feature and will alleviate any operational challenges. However, the planning and operation of such islanded and hybrid systems are reliant on a powerful and efficient power flow analysis tool. To this end, this thesis introduces a novel unified, generic, flexible power flow algorithm for islanded/isolated HMGs. The developed algorithm is generic in the sense that it includes consideration of the unique characteristics of islanded HMGs: a variety of possible topologies, droop controllability of the DERs and bidirectionality of the power flow in the ICs. The new power flow formulation is flexible and permits the easy incorporation of any changes in the DER operating modes and the IC control schemes. The developed algorithm was validated against a detailed time-domain model and applied for the analysis of a variety of operational and control aspects in islanded HMGs, including the problem of imprecise power sharing and droop control of the ICs. The proposed load flow program can form the basis of and provide direction for further studies of islanded HMGs.

This thesis also presents a deeper look at the problem of inaccurate active and reactive power sharing in islanded droop-based HMGs and proposes a unified and universal power sharing scheme that can simultaneously ensure precise power sharing in both ac and dc subgrids. Test results demonstrate the capability of the developed scheme with respect to achieving exact power sharing not only among DERs in proportion to their ratings but also among ICs that interface adjacent ac and dc microgrids. The developed unified power sharing scheme would assist system planners with the effective design of droop

characteristics for DERs and ICs, which would result in enhancements such as the avoidance of converter overloading and the achievement of precise load sharing.

Another operational aspect that was thoroughly investigated for this thesis is the possibility of voltage instability/collapse in islanded HMGs during contingencies. This research unveiled the possibility of voltage instability in HMGs that include constant power loads and a mix of synchronous-based and converter-based generating units. As indicated by the voltage stability analysis presented here, despite the fact that healthy microgrids have far-reaching loadability boundaries, the voltage at some ac/dc load buses can unexpectedly collapse during abnormal conditions. The analysis also revealed that fine tuning the droop characteristics of DERs and ICs can enlarge the voltage stability margin and safeguard the entire microgrid against collapse during contingencies, all without the sacrifice of a single load.

A final component of this thesis is the proposal of a two-stage stochastic centralized dispatch scheme for ac/dc hybrid distribution systems. The developed dispatch scheme coordinates the operation of a variety of DERs, such as distributed generators and energy storage systems. It also ensures the coordinated charging of electric vehicles and models the degradation of their batteries that occurs due to the vehicle-to-grid action. The energy coordination problem has been formulated as a two-stage day-ahead resource scheduling problem: the intermittent supply; the variable demand, which includes electric vehicles; and the fluctuating real-time energy price are all modelled as random variables. The first stage produces day-ahead dispatch decisions for the dispatchable DG units. For a set of possible scenarios over the next 24 h, the second stage determines appropriate corrective decisions with respect to the import/export schedule, storage charging/discharging cycles, and electric vehicle charging/discharging patterns. The simulation results demonstrate the effectiveness of the developed scheme for optimally coordinating the various components of future ac/dc hybrid smart grids.

Despite its substantial merits and value as a host for ac and dc technologies, a smart grid with HMGs creates previously unexperienced operational challenges for system planners and operators. The work completed for this thesis could help pave the way for the realization of ac/dc hybrid smart grids in years to come.

Acknowledgements

First and foremost, all thanks and praise be to Allah Almighty who has given me the strength and knowledge to come this far in my studies and to complete my Ph.D. thesis successfully.

I would like to express my gratitude to the Ministry of Higher Education of Libya for the generous sponsorship that afforded me the peace of mind to settle in Canada with my family and concentrate on my research.

Several people have contributed to this thesis in a number of ways. I am most grateful to my academic supervisors: Prof. Ehab El-Saadany and Prof. Kumaraswamy Ponnambalam. I especially appreciate Prof. Ehab's patience and helpful technical criticism and Prof. Ponnu's kindness and financial support. Constructive comments were also generously provided by my examining committee: Prof. Rajiv Varma, Prof. Hector Budman, Prof. Kankar Bhattacharya, and Dr. Ramadan El-Shatshat.

I would like to convey my respect and appreciation to the members of my research group for their fruitful discussions and to Dr. Yousef El-Rayani and Dr. Fadi Elghitani for their honest technical advice. The collaboration of my colleagues, Dr. Mostafa Shaaban, Dr. Aboelsood Zidan, Dr. Mohamed Abdelwahed, Dr. Maher Abdelkhalek, and Ameen Yazdavar, proved enormously valuable. A special note of thanks goes to my dear friend Ameen Yazdavar for his friendship and for sharing his thoughts during our technical discussions.

My sincere thanks also go to my wonderful family by marriage: my father-in-law, Ahmed Makhlof Arghawi, my mother-in-law, Soad Al-Sadek, and my sisters-in-law, Atiga and Fawzia. Your blessings and caring have always helped me embark on my next life adventure.

I am deeply grateful to my life partner, my wife Eman Makhlof, for her unfailing understanding. She tolerated the stressful times and shared both the ups and downs of my Ph.D. studies. This thesis was possible only through her love, care, and wisdom. Thank you, Om Abdelrahman!

I would also like to voice my appreciation and love for my children, whose sweet words, "Daddy never gives up; daddy finds a way," provided a source of inspiration and determination throughout my Ph.D. journey. Your daddy has found his way, and he hopes you'll find yours!

My parents, Aarif Eajal and Ermalh Omar, will always have my most heartfelt gratitude for their endless love and blessed prayers. This Ph.D. thesis is the fruit of their

struggle to ensure my well-being and higher education. May Allah reward them and have mercy upon them. Ameen!

Abdelsalam Eajal

Dedication

To my beloved parents, brothers, and sisters
and to my lovely family (my wife and my children, Abdelrahman, Ahmed, and Abdullah)
who bring colour to my life.

Table of Contents

List of Tables xv

List of Figures xvii

Nomenclature xx

1 Introduction 1

1.1 Preface . . . 1
1.2 Research Motivations and Challenges . . . 3
1.3 Thesis Statement and Objectives . . . 4
1.4 Thesis Organization . . . 5

2 Background and Literature Review 7

2.1 Introduction . . . 7
2.2 AC/DC Hybrid Microgrids . . . 7
2.3 Distributed Energy Resource Droop Control . . . 10
2.4 Interlinking Converter Droop Control . . . 13
2.5 Power Flow Analysis of AC/DC Hybrid Microgrids . . . 15
2.6 Power Sharing Control in Microgrids . . . 17
2.6.1 Communication-Based Power Sharing Schemes . . . 17
2.6.2 Distributed Power Sharing Schemes . . . 18
2.6.3 Communication-less Decentralized Power Sharing Schemes . . . 19
2.7 Voltage Instability/Collapse in Microgrids . . . 24
2.8 Energy Management in Microgrids . . . 26
2.9 Discussion . . . 30

3 A Unified Approach to the Power Flow Analysis **31**

3.1 Introduction . . . 31

3.2 System Model and Control . . . 32

3.2.1 Overhead Line and Underground Cable Models . . . 32

3.2.2 Load Model . . . 33

3.2.3 Distributed Energy Resource Model . . . 33

3.2.4 Interlinking Converter Model . . . 34

3.2.4.1 Control Strategy I . . . 35

3.2.4.2 Control Strategy II . . . 35

3.2.4.3 Control Strategy III . . . 37

3.3 Formulation of the Power Flow Problem . . . 38

3.3.1 AC Subgrids . . . 39

3.3.1.1 PQ Buses . . . 39

3.3.1.2 PV Buses . . . 40

3.3.1.3 AC Droop-Controlled Buses . . . 40

3.3.2 DC Subgrids . . . 41

3.3.2.1 Constant P Buses . . . 42

3.3.2.2 Constant V Buses . . . 42

3.3.2.3 DC Droop-Controlled Buses . . . 42

3.4 Trust-Region Method . . . 43

3.5 Design of the AC/DC Hybrid Test Systems . . . 47

3.5.1 AC and DC Load Data Collection . . . 47

3.5.2 AC and DC Voltage Level Selection . . . 47

3.5.3 AC and DC Subgrid Ratings . . . 47

3.5.3.1 AC and DC DER Ratings . . . 47

3.5.3.2 AC and DC DER Droop Gain Settings . . . 48

3.5.4 AC and DC Cable Selection . . . 48

3.5.4.1 Cable Impedance Calculation . . . 48
3.5.4.2 Voltage Drop Calculation . . . 49
3.5.5 Interlinking Converter Rating and Control . . . 49
3.6 Test Results and Discussions . . . 49
3.6.1 Algorithm Validation . . . 50
3.6.2 Algorithm Application . . . 51
3.6.2.1 6-Bus AC/DC Hybrid Microgrid . . . 52
3.6.2.2 12-Bus AC/DC Hybrid Microgrid . . . 53
3.6.3 Algorithm Robustness . . . 55
3.6.4 Algorithm Scalability . . . 56
3.7 Discussion . . . 60

4 A Precise and Unified Power Sharing Scheme 61
4.1 Introduction . . . 61
4.2 Power Sharing Problem in AC/DC Hybrid Microgrids . . . 63
4.2.1 Power Sharing in an AC Subgrid . . . 64
4.2.2 Power Sharing in a DC Subgrid . . . 66
4.2.3 Power Sharing Among Multiple Interlinking Converters . . . 67
4.3 Proposed Unified Power Sharing Scheme . . . 69
4.3.1 Power Sharing Performance Measure . . . 69
4.3.2 Power Sharing Problem Constraints . . . 71
4.3.2.1 AC/DC Power Flow Equations . . . 71
4.3.2.2 Droop-Controlled AC/DC DG Unit Constraints . . . 71
4.3.2.3 Interlinking Converter Constraints . . . 73
4.3.2.4 Bus Voltage, AC System Frequency, and Branch Current Limits . . . 74
4.4 Implementation Requirements of the Developed UPS Scheme . . . 76
4.5 Simulation Results and Discussions . . . 77

4.5.1 Power Sharing Versus Loading Level . . . 78
4.5.2 Power Sharing Versus Overloading Conditions . . . 79
4.5.3 Static Versus Optimal Droop Parameters . . . 79
4.5.4 Power Sharing versus AC/DC Topologies . . . 82
4.6 Discussion . . . 84

5 On the Loadability and Voltage Stability Analysis 85
5.1 Introduction . . . 85
5.2 Problem Description . . . 87
5.3 Case Studies . . . 92
5.3.1 Impact of a Contingency on the Loadability of the AC Microgrid . . . 93
5.3.2 Impact of Reactive Power Droop Gains on AC Microgrid Loadability 94
5.3.3 Impact of DER Location and Control Mode on AC Microgrid Loadability . . . 96
5.3.4 Impact of Shunt Capacitors on AC Microgrid Loadability . . . 97
5.3.5 Impact of a Contingency on the Loadability of the DC Microgrid . 98
5.3.6 Impact of Active Power Droop Gains on DC Microgrid Loadability 99
5.3.7 Impact of Network Reconfiguration on DC Microgrid Loadability . 100
5.3.8 Impact of AC and DC Microgrid Interfacing on the Loadability of the AC Side under a Contingency . . . 101
5.3.9 Impact of AC and DC Microgrid Interfacing on the Loadability of the DC Side under a Contingency . . . 102
5.4 Discussion . . . 102

6 Stochastic Centralized Dispatch Scheme 105
6.1 Introduction . . . 105
6.2 System Model and Control . . . 107
6.2.1 Electric Vehicle Demand Model . . . 107
6.2.2 Why this Electric Vehicle Demand Model? . . . 109

6.2.3 Renewable Energy Resource Model . . . 110
6.2.4 Energy Storage System Model . . . 110
6.2.5 Interlinking Converter Control . . . 110
6.3 Two-Stage Stochastic Optimization . . . 111
6.4 Scenario Reduction Technique . . . 112
6.5 Developed Stochastic Centralized Dispatch Scheme . . . 113
6.6 Implementation Requirements of the Developed Dispatch Scheme . . . 115
6.7 Problem Formulation . . . 115
6.7.1 Objective Function . . . 116
6.7.2 Constraints . . . 116
6.7.2.1 Multi-Period AC Power Flow Equations . . . 116
6.7.2.2 Multi-Period DC Power Flow Equations . . . 117
6.7.2.3 Interlinking Converter Constraints . . . 119
6.7.2.4 Electric Vehicle Constraints . . . 119
6.7.2.5 Energy Storage System Constraints . . . 121
6.7.2.6 Dispatchable Unit and Network Constraints . . . 122
6.8 Test System and Simulation Results . . . 123
6.8.1 System Description . . . 123
6.8.2 Simulation Results . . . 126
6.8.2.1 First-Stage Decision . . . 126
6.8.2.2 Second-Stage Decision . . . 127
6.8.2.3 Including Representation of EV Battery Degradation . . . 129
6.8.2.4 Renewable Power Correlation vs. Expected Energy Cost . . . 131
6.8.2.5 Importance of the Stochastic Dispatch Model . . . 131
6.8.3 Computational Aspects . . . 133
6.9 Discussion . . . 135

7 Conclusion, Contributions, and Future Work **137**

7.1 Conclusions 137

7.2 Contributions 139

7.3 Directions for Future Work 140

References **141**

APPENDICES **152**

A Test Systems Data **153**

A.1 6-Bus AC/DC Hybrid Microgrid Data 153

A.2 Medium Voltage-12-Bus AC/DC Hybrid Microgrid Data 154

A.3 33-Bus AC/DC Hybrid Microgrid Data 156

A.4 Low-Voltage 12-Bus AC/DC Hybrid Microgrid Data 160

A.5 38-Bus AC/DC Hybrid Microgrid Data 162

B List of Publications **165**

B.1 Peer-Reviewed Journal Articles 165

B.2 Journal Articles under Reveiw 165

B.3 Journal Articles in Preparation 165

B.4 Articles in Conference Proceedings 166

B.5 Posters 166

List of Tables

3.1 Summary of the HMG Power Flow Problem 44
3.2 Algorithm Validation against Time Domain Simulation 51
3.3 The Power Flow Solution for the Islanded 6-Bus AC/DC Hybrid Microgrid: (S_{base} = 18 kVA, ω = 0.9923 p.u.) 52
3.4 The Power Flow Solution for the Islanded 12-Bus AC/DC Hybrid Microgrid (S_{base} = 3 MVA) 54
3.5 The UPF Algorithm Performance with Respect to R/X Ratio 56
3.6 Power Flow Results for the 33-Bus AC/DC Hybrid Microgrid: AC Side . . 58
3.7 Power Flow Results for the 33-Bus AC/DC Hybrid Microgrid: DC Side . . 59
3.8 Power Flow Results for the 33-Bus AC/DC Hybrid Microgrid: ICs 59

4.1 Stand-alone AC and DC Microgrids with Static Droop 80
4.2 Interfaced AC/DC Hybrid Microgrid with Static Droop 80
4.3 Power Sharing Ratios for the Three Case Studies 81
4.4 Power sharing for different AC/DC topologies 84

5.1 Droop Parameters of Distributed Energy Resources and Interlinking Converters 93

6.1 Parameter Settings for the Interlinking Converters 124
6.2 Dispatchable Unit Data 125
6.3 Generation Schedule for the Dispatchable DG Units, in kW 128
6.4 Effects of Including EV Battery Degradation 131
6.5 Expected Costs, VSS, and EVPI 133
6.6 Solver Settings and Model Statistics 135

A.1 Bus Data for the 6-Bus Islanded AC/DC Hybrid Microgrid (S_{base} = 18 kVA, 208/600 V) 153

A.2 Bus Data for the 12-Bus Islanded AC/DC Hybrid Microgrid (S_{base} = 3 MVA, 2.4/7 kV) 154
A.3 Line Data for the 12-Bus Islanded AC/DC Hybrid Microgrid 155
A.4 33-Bus AC/DC Hybrid Distribution System Data: AC Bus Data 156
A.5 33-Bus AC/DC Hybrid Distribution System Data: AC Line Data 157
A.6 33-Bus AC/DC Hybrid Distribution System Data: DC Bus Data 158
A.7 33-Bus AC/DC Hybrid Distribution System Data: DC Line Data 159
A.8 Bus Data for the 12-Bus Islanded AC/DC Hybrid Microgrid (S_{base} = 10 kVA, 208/600 V) 160
A.9 Line Data for the 12-Bus Islanded AC/DC Hybrid Microgrid 161
A.10 38-Bus AC/DC Hybrid Distribution System Data: AC Bus Data 162
A.11 38-Bus AC/DC Hybrid Distribution System Data: AC Line Data 163
A.12 38-Bus AC/DC Hybrid Distribution System Data: DC Bus Data 164
A.13 38-Bus AC/DC Hybrid Distribution System Data: DC Line Data 164

List of Figures

1.1 New global investment in renewable energy in 2015 by technology. 2
1.2 Research objectives. 6

2.1 Sample architecture of an ac/dc hybrid microgrid. 8
2.2 The droop characteristics of ac and dc droop-controlled DGs. 10
2.3 DS inverse droop control: (a) ac-type units (b) dc-type units. 12
2.4 Formation of interlinking converter droop characteristics. 14
2.5 Equivalent circuit of the interlinking converter and its active power droop characteristics. 14
2.6 A single-line diagram of a generic ac/dc hybrid microgrid. 16
2.7 Control architecture of master-slave control. 18
2.8 Control architecture of distributed control. 19
2.9 Block diagram of a droop-controlled VSC-based DER. 20
2.10 PV curve at an ac load bus. 25
2.11 The hierarchical control structure of a multi-DG microgrid [70]. 27
2.12 A schematic diagram of a centralized energy management system. 28

3.1 Different distributed energy resource models. 34
3.2 AC/DC droop for the interlinking converter. 35
3.3 Resultant ac/dc droop with a no-power-transfer zone. 36
3.4 Flow chart of the HMG power flow algorithm. 46
3.5 6-bus ac/dc hybrid microgrid. 50
3.6 12-bus ac/dc hybrid microgrid. 54
3.7 33-bus ac/dc hybrid microgrid. 57

4.1 Simple six-bus ac/dc hybrid microgrid. 63

4.2 Power sharing in an ac subgrid: (a) active power sharing (b) reactive power sharing. . . . 65
4.3 Power sharing in a dc subgrid. . . . 67
4.4 Active power sharing between two interlinking converters. . . . 68
4.5 Reactive power sharing between two interlinking converters. . . . 69
4.6 Developed UPS scheme for islanded ac/dc hybrid microgrids. . . . 75
4.7 Proposed centralized control and communication architecture. . . . 76
4.8 12-bus ac/dc hybrid microgrid. . . . 77
4.9 Power sharing error versus loading level. . . . 78
4.10 AC/DC bus voltages with static and optimal droop. . . . 82
4.11 Power sharing error versus system topology: (a) power sharing in the ac subgrid (b) power sharing in the dc subgrid. . . . 83

5.1 A four-bus droop-controlled ac/dc hybrid microgrid: (a) one-line diagram (b) equivalent circuit with the droop characteristics. . . . 88
5.2 PV curves for a stand-alone two-bus ac/dc microgrid: (a) ac subgrid (b) dc subgrid. . . . 90
5.3 12-bus ac/dc hybrid microgrid. . . . 92
5.4 AC subgrid loadability before and after contingencies. . . . 94
5.5 AC subgrid loadability versus reactive power droop coefficients. . . . 95
5.6 AC subgrid loadability versus DER location and control. . . . 96
5.7 AC subgrid loadability versus shunt capacitor placement. . . . 97
5.8 DC subgrid loadability before and after contingencies. . . . 98
5.9 DC subgrid loadability versus active power droop coefficients. . . . 99
5.10 DC subgrid loadability versus network topology. . . . 100
5.11 AC subgrid loadability during a contingency before and after interfacing with the dc subgrid. . . . 101
5.12 DC subgrid loadability during a contingency before and after interfacing with the ac subgrid. . . . 103

6.1 AC/DC hybrid smart distribution system. 106
6.2 Parking durations: a) Lot_1; b) Lot_2. 108
6.3 Energy storage system model. 111
6.4 Developed architecture for the dispatch scheme. 113
6.5 Functional block diagram of the two-stage stochastic dispatch scheme. . . . 114
6.6 38-bus ac/dc hybrid smart distribution system. 123
6.7 Real-time energy price forecasting error. 125
6.8 Real-time energy price profile. 126
6.9 10 scenarios for: (a) regular demand; (b) solar power; (c) (−) correlated wind power; (d) (+) correlated wind power. 127
6.10 Day-ahead generation schedule. 128
6.11 Generation and demand profiles for one scenario. 129

Nomenclature

AC	Alternating Current.
AGs	EV Parking Lot Aggregators.
AMI	Advanced Metering Infrastructure.
D	Droop-Controlled.
DC	Direct Current.
DERs	Distributed Energy Resources.
DG	Distributed Generation.
DS	Distributed Storage.
ED	Economic Dispatch.
EMS	Energy Management System.
ESS	Energy Storage System.
EV	Electric Vehicle.
EVPI	Expected Value of Perfect Information.
FC	Fuel Cell.
HMG	Hybrid Microgrid.
IC	Interlinking Converter.
IDD	Island Interconnection Device.
kV	Kilo Volt.
kvar,Mvar	Kilo and Mega Volt-Ampere Reactive.
kW, MW	Kilo and Mega Watt.
LC	Local Controller of the Distributed Energy Resource.
LIB	Limit Induced Bifurcation.
LV, MV	Low Voltage and Medium Voltage.
MAS	Multi-Agent System.
MG	Microgrid.
MGCC	Microgrid Central Controller.
MILP	Mixed Integer Linear Programming.
MINLP	Mixed Integer Nonlinear Linear Programming.
MPC	Model Predictive Control.
MPPT	Maximum Power Point Tracking.
NLP	Nonlinear Programming.
OPF	Optimal Power Flow.
P	Constant Power.

PCC	Point of Common Coupling.
PQ	Active and Reactive Power.
PQ	Constant Active and Reactive Power.
PSI	Power Sharing Index.
PV	Constant Active Power and Voltage.
PV	Photovoltaic or Active Power/Voltage Depending on the Context.
R	Constant Resistance.
RESs	Renewable Energy Sources.
RTP	Real Time Price.
SGCC	Smart Grid Central Controller.
SNB	Saddle Node Bifurcation.
SOC	State of Charge.
T	Terminal Bus.
TDS	Time Domain Simulation.
TR	Trust Region.
UC	Unit Commitment.
UPF	Unified Power Flow.
UPS	Unified Power Sharing.
V	Constant Voltage.
V2G, G2V	Vehicle to Grid and Grid to Vehicle Capability, respectively.
VSC	Voltage Source Converter.
VSS	Value of Stochastic Solution.
WT	Wind Turbine.
Z	Constant Impedance.

Constants

$\eta_{ch_{i,k}}$	Charging efficiency of charger k in parking lot i.
η_{ch}, η_{dis}	Charging and discharging efficiency of the ESS, respectively.
π_s	Probability of scenario s.
n_D^{ac}, n_D^{dc}	Number of ac and dc droop-based buses, respectively.
n_G^{ac}, n_G^{dc}	Number of dispatchable units of ac and dc type, respectively.
n_R^{ac}, n_R^{dc}	Number of renewable units of ac and dc type, respectively.
n_B, n_L	Number of buses and lines, respectively.
n_P	Number of constant power dc buses.
n_V	Number of voltage-controlled dc buses.
n_{ac}, n_{dc}	Number of ac and dc buses, respectively.
n_{ch_i}	Number of chargers in parking lot i

n_{DG}	Number of all DG units (dispatchable and nondispatchable).
n_{ESS}	Number of energy storage systems.
n_{EV_b}	Number of EVs being charged at bus b.
n_{ic}	Number of interfacing converters.
n_{Lot}	Number of parking lots with G2V capability.
n_{PQ}	Number of constant power ac buses.
n_{PV}	Number of constant voltage-controlled ac buses.
$P^{rate}_{ch_{i,k}}$	Maximum charging rate of charger k in parking lot i.
P^{rate}_{ESS}	Charging/Discharging rate of the ESS.
y_{ik}, g_{ik}, b_{ik}	Admittance, conductance, and susceptance of ac line ik, respectively.

Operators

$(\hat{\bullet})$	Normalization operator.
$\mathbb{E}\{\bullet\}$	Expectation operator.
$\wedge, \vee$	*and* and *or* operators, respectively.

Parameters

ω_0	No-load frequency.
$\omega_{min}, \omega_{max}$	Minimum and maximum frequency, respectively.
ρ_{ac}, ρ_{ac}	Desired loading of ac and dc subgrids with respect to their ratings.
θ_{ik}	Phase angle of the entry ik^{th} in the bus admittance matrix.
θ_r	Weighting risk factor.
G_{ik}	Entry ik^{th} in the bus conductance matrix.
$P^{max}_{G,dc}$	Rated active power of a dc distributed energy resource.
$P_{ch_{b,k}}$	Charging power of the vehicle k connected at bus b (kW).
$P_{D,b}, Q_{D,b}$	Active and reactive power demands at bus b , respectively.
$P_{ic,max}, Q_{ic,max}$	Maximum active and reactive power of an interlinking converter.
$P_{R,b}$	Renewable power production at bus b.
R_d	Droop resistance of dc droop-controlled distributed energy resource.
R_{ac}, R_{dc}	AC and DC line resistance, respectively.
S^{max}_G	Rated apparent power of an ac distributed energy resource.
S_{base}	Base apparent power in MVA.
$V_{ac,0}, V_{dc,0}$	No-load ac and dc voltage, respectively.
$V_{ac,base}, V_{dc,base}$	Base ac and dc voltage, respectively.
$V_{ac,min}, V_{ac,max}$	Minimum and maximum ac voltage, respectively.
$V_{dc,min}, V_{dc,max}$	Minimum and maximum dc voltage, respectively.

X_{ac}	AC line reactance.
Y_{ik}	Entry ik^{th} in the bus admittance matrix.

Sets

$\mathcal{B}, \mathcal{L}$	Set of all buses and lines, respectively.
$\mathcal{B}_G^{ac}, \mathcal{B}_G^{dc}$	Set of buses with dispatchable units of ac and dc types, respectively.
$\mathcal{B}_D^{ac}, \mathcal{B}_D^{dc}$	Set of ac and dc droop-controlled buses, respectively.
$\mathcal{B}_R^{ac}, \mathcal{B}_R^{dc}$	Set of ac and dc buses with renewables, respectively.
$\mathcal{B}_{ic}^{ac}, \mathcal{B}_{ic}^{dc}$	Set of ac and dc terminal buses, respectively.
$\mathcal{B}_{ac}, \mathcal{B}_{dc}$	Set of ac and dc buses, respectively.
$\mathcal{B}_{DG}$	Set of all DG units (dispatchable and nondispatchable).
$\mathcal{B}_{EV}$	Set of all buses with EVs.
$\mathcal{B}_{PQ}$	Set of ac constant power buses.
$\mathcal{B}_{PV}$	Set of ac voltage-controlled buses.
$\mathcal{B}_P$	Set of dc constant power buses.
$\mathcal{B}_V$	Set of dc voltage-controlled buses.
$\mathcal{H}$	Set of unit commitment scheduling horizon.
$\mathcal{IC}$	Set of interfacing converters.
$\mathcal{N}_{ESS}$	Set of energy storage systems.
$\mathcal{N}_{Lot}$	Set of parking lots with G2V capability.
$\mathcal{S}$	Set of scenarios.

Variables

α_c	Firing angle of converter c.
$\Delta e_{\omega V}$	Power sharing error.
δ_b	Phase angle of the voltage at ac bus b.
γ_p, γ_q	Active and reactive power droop gains of a droop-controlled interlinking converter, respectively.
$\lambda_{ac,LIB}$	Limit-induced bifurcation in ac microgrids.
$\lambda_{ac,SNB}, \lambda_{dc,SNB}$	Saddle node bifurcations in ac and dc microgrids, respectively.
$\lambda_{ac}, \lambda_{ac}$	AC and DC loadabilities, respectively.
ω	Frequency of an ac microgrid.
a_c	Transformer tap ratio of the converter at bus b.
C_{imp}, C_{exp}	Costs of import and export, respectively, ($).
C_{unit_i}	Operating cost of the dispatchable unit i ($).
$cos\phi_b$	Power factor at the ac side of the converter at bus b.

$I_{ic,dc,b}, V_{ic,dc,b}$	DC current and voltage of the converter at bus b.
$m_{p,ac}, m_{p,dc}$	Active power droop gains of ac and dc-type droop-controlled distributed energy resources, respectively.
n_q	Reactive power droop gain of ac-type droop-controlled distributed energy resource.
$P_{ESS}^{ch}, P_{ESS}^{dis}$	Charging and discharging powers of the ESS, respectively.
P_{DR}, Q_{DR}	Distributed energy resource active and reactive powers, respectively.
P_{ESS}	Power output of the ESS.
P_{EV_i}	EV active power demand at parking lot i.
$P_{G,ac,b}, Q_{G,ac,b}$	Active and reactive power generations at ac bus b, respectively.
$P_{ic,ac}, P_{ic,dc}$	Active and reactive power requested by ac and dc side, respectively.
P_{ic}, Q_{ic}	Interlinking converter active and reactive power transfers, respectively.
P_{imp}, P_{exp}	Power import and export with the utility grid, respectively.
SOC_{EV}, SOC_{ESS}	State of charge of the EV and ESS, respectively.
u, u_{EV}, u_{ESS}	Commitment decision of dispatchable unit, charging Decision of EV , charging decision of ESS, $u, u_{EV}, u_{ESS} \in \{1, 0\}$, respectively.
V_{ac}, V_{dc}	AC and DC bus voltages, respectively.

Chapter 1

Introduction

1.1 Preface

The use of an ac grid has been the dominant practice since 1891, which marked the end of the war of currents between Thomas Edison, who was in favour of dc, and Nikola Tesla, who supported ac [1]. However, recent advances in dc distributed energy resources (DERs), such as photovoltaic systems (PVs), fuel cells (FCs), and energy storage systems (ESSs), as well as the rapid increase in the adoption of modern dc loads, such as electric vehicles (EVs) and electric drives, have caused power engineers to reconsider the value of dc as a distribution architecture. However, the necessity for ac loads and ac energy sources to be connected through ac/dc converters entails additional conversion requirements. The most suitable topology that can accommodate both ac and dc technologies with less need for such conversion is a hybrid one [2]. A hybrid structure is envisioned as hosting a variety of types of distributed resources, with solar- and wind-based DERs probably dominating.

Solar and wind-based renewable energy is the fastest-growing renewable energy source worldwide. As indicated in Figure 1.1, in 2015, 94.3 % of the total global investment in renewable energy was in solar and wind energy [3]. At 56 %, solar energy was the leading technology, accounting for $161 billion, with wind energy in second place, at 38.3 % with $109.6 billion. The remaining 5.7 % was composed of biomass, small hydro, biofuels, geothermal, and ocean energy.

The main driving force behind the rapid growth of renewable energy has been the increase in fossil fuel prices, which has also triggered government initiatives. In the Canadian province of Ontario, for example, to promote the use of clean and renewable energy sources (RESs), the government has initiated the Feed-In Tariff program (FIT), for renewable energy projects over 10 kW, and the microFIT Program, for renewable energy projects of 10 kW or less. Ontario's long-term energy plan calls for about 20,000 MW of renewable energy to be brought into service by 2025, representing about half of the provincial installed capacity [4]. RESs with small-scale fuel-fired energy sources are known as distributed generation (DG) or distributed generators (DGs). The adoption of DG has allowed energy investors and consumers to install different types of DG and to participate in system operations

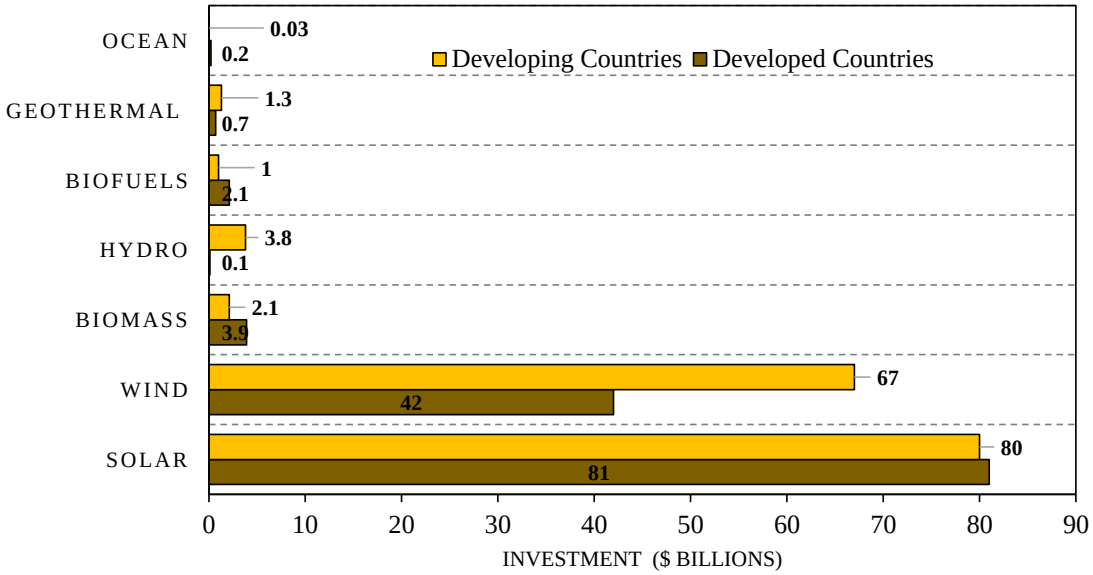

Figure 1.1. New global investment in renewable energy in 2015 by technology.

during on-demand periods. In addition to DG, another advanced technology attracting growing interest is ESSs, which can store energy and inject it back into the grid when it is needed. Innovative technologies are not limited to energy resources. Modern loads such as plug-in EVs are widely accepted as a promising means of transportation. Because of the lower environmental impact of EVs, governments offer incentives for electrifying transportation systems. For example, Ontario offers rebates of up to $14,000 for EV buyers under the Electric Vehicle Incentive Program [5]. According to 2017 global EV outlook forecasts, by 2040, 54 % of new vehicle sales and 33 % of the global vehicle fleet will be electric [5].

Within distribution networks, the growing application of DERs, both DGs and ESSs, and the transition to EVs have led to the introduction of innovative structures known as a microgrids [6] and a smart grid [7]. A microgrid, which constitutes the building block of the future smart grid, can be defined as a cluster of energy resources and loads with static or dynamic electric boundaries that acts as a self-controlled entity, operating autonomously and coordinating its own resources [6,8,9]. A smart and active distribution system that includes DERs can thus have multi-coupled microgrids [10], with each microgrid able to operate in two modes: grid-connected and islanded (autonomous). In grid-connected mode, the microgrid can trade energy with its hosting main grid and other neighbouring microgrids

in order to maximize its profit. In autonomous mode, on the other hand, the microgrid strives to meet its demand or at least the critical portion of the demand, through local generation with minimal load shedding. The microgrid operation objective can therefore change from economical to technical as the operation mode changes from grid-connected to islanded. Regardless of their mode of operation, such emerging systems introduce an operational control philosophy that necessitates steady-state and dynamic analysis tools tailored to their special features. This background motivated the development of the new analysis and operational control strategies for ac/dc hybrid microgrids (HMGs) presented in this thesis.

1.2 Research Motivations and Challenges

The widespread use of dc energy resources such as PV panels, the recent installations of dc loads such as elevator drives and light-emitting diode (LED) illumination, and the transition to plug-in EVs have created a demand for more extensive ac/dc and dc/dc conversions. The number of these conversion systems can be expected to escalate rapidly as additional dc technologies are being widely adopted. The use of dc microgrids for hosting dc technologies has already been proposed [11], but ac energy resources and ac loads would require ac/dc converters before they can be connected to dc microgrids. Because it would reduce the conversion requirements associated with the use of both ac and dc microgrids, an ac/dc hybrid infrastructure would be advantageous [1], [12].

HMGs are coupled dynamical ac and dc systems that feature power exchange capability. Each HMG has its own steady-state and dynamic characteristics, including 1) inherent and direct coupling between the ac frequency and the dc voltage, 2) interlinking converters (ICs) that adopt a droop-based control strategy in order to determine the amount and direction of the power transfer, 3) the possibility of both the ac and dc subgrids to be relatively comparable in terms of size or available generation so that no single subgrid can provide unlimited support to the other subgrid. The implementation of HMGs necessitates the development of a generalized power flow analysis approach that incorporates the distinguishing characteristics and special operational philosophy of autonomous HMGs, such as operational control based on droop characteristics.

Droop control allows local DERs to participate autonomously in frequency/voltage control and to share the microgrid load. However, in spite of its technical merits that include system security and reliability, such a decentralized control strategy creates the inherent limitation of imprecise power sharing in the ac and dc microgrids, which is attributable to mismatching line impedances and unequal voltage drops across the feeders.

Imprecise power sharing could eventually lead to the overstressing of some components and the consequent activation of overcurrent protection relays. This inexact power sharing problem arises not only among droop-controlled DERs but also among multiple ICs that are equipped with droop characteristics.

Another operational difficulty that might appear in HMGs during islanding is the voltage instability/collapse phenomenon. Despite the proximity of energy resources to load centers and the insignificant length of feeders, voltage instability can occur unexpectedly in microgrids during extreme events. The constant power characteristics of some loads, a poor loading power factor, and limited DG reactive power capability also contribute to voltage instability in ac microgrids. The problem of voltage instability can also be observed in highly resistive dc microgrids that are subject to constant power loads during contingencies.

Further, due to recent advances in small-scale renewable and low-carbon energy resources, and to governmental initiatives, the installation of a variety of energy resources before and after the customer's meter will continue to grow. A large portion of the energy resources in a future smart grid will likely be renewables, which are characterized by their intermittent nature. In addition to the stochastic quality of renewable energy, the uncertain arrival times, parking durations, and states of charge of EVs also increase the level of uncertainty. Both the intermittent nature of renewable energy and the random behaviour of EV owners complicate smart grid energy management and necessitate stochastic modelling of the energy management problem.

Motivated by these challenges, this research resulted in the development of a steady-state analysis tool and operational control schemes that can address the operational philosophy and challenges associated with HMGs: 1) a mix of DERs: dispatchable, non-dispatchable, synchronous-based, and converter-based; 2) the lack of sufficient physical inertia during islanding; 3) limited frequency and voltage support during autonomous operation mode; 4) the intermittent nature of RESs; and 5) the mobility and variability of EV power demand.

1.3 Thesis Statement and Objectives

Operational control of HMGs during both modes of operation was selected as the central theme of the research, which was aimed at achieving four main objectives, summarized as follows:

1) Develop a generalized and unified power flow (UPF) algorithm for islanded HMGs. The developed power flow algorithm is novel in the sense that it considers the key characteristics of an islanded/isolated ac/dc system, e.g., the lack of a slack bus in either the ac or the dc subgrids and the droop controllability of the DGs and ICs. The developed power flow algorithm for smart distribution systems with an ac/dc hybrid topology, plug-and-play feature, and varied modes of operation will serve as a valuable analysis tool that will enable system planners and operators to investigate planning and operational aspects of islanded HMGs.

2) Develop an optimal universal power sharing scheme that is able to minimize the sharing error among 1) droop-based DGs in the ac subgrid, 2) droop-based DGs in the dc subgrid, and 3) droop-based ICs in the case of multiple interfacing points between the ac and dc subgrids.

3) Investigate the presence of voltage instability/collapse during islanding and contingencies by means of a steady-state voltage stability analysis aimed at identifying the control parameters and operational practices that can enhance microgrid loadability during severe events.

4) Develop a centralized stochastic dispatch scheme for ac/dc hybrid smart distribution systems based on the building of a developed dispatch model, beginning with the stochastic modelling of the randomness introduced by RESs, EVs, conventional loads, and the energy price. The design of the developed dispatch scheme is based on two-stage stochastic optimization. The first stage involves determining the daily generation schedule of the dispatchable DG units, while the second stage entails ascertaining appropriate corrective decisions for mitigating the uncertainties, such as ESS charging/discharging.

These objectives are classified and illustrated schematically in Figure 1.2.

1.4 Thesis Organization

The remainder of this thesis is organized in six additional chapters:

Chapter 2: supplies the necessary background about HMGs with respect to their operational control philosophies. This chapter also includes a review of the state of the art with respect to power sharing, voltage stability, and energy management in the context of microgrids, identifying gaps in the published literature.

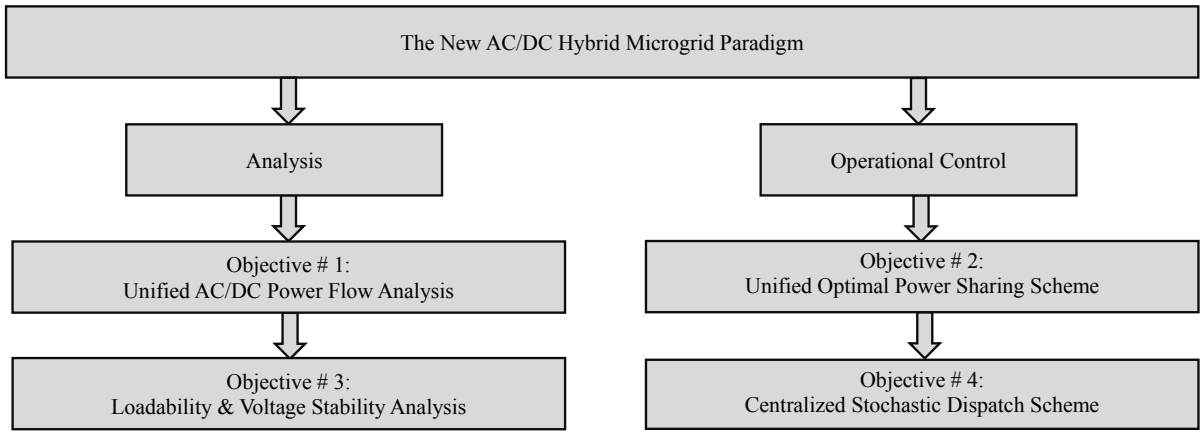

Figure 1.2. Research objectives.

Chapter 3: introduces the unified phasor formulation of the developed ac/dc power flow routine and details the steady-state modelling of the system components.

Chapter 4 explains the development of a precise and universal power sharing scheme for droop-controlled HMGs.

Chapter 5: examines the existence of voltage collapse in islanded HMGs during contingencies.

Chapter 6: presents the developed stochastic centralized dispatch scheme for ac/dc hybrid smart distribution systems. The stochastic modelling of system components that are random in nature is also described.

Chapter 7: provides concluding remarks, highlights the salient contributions of this thesis, and provides insight into the possible directions for future research on HMGs.

Chapter 2

Background and Literature Review

2.1 Introduction

The advent of today's advanced metering infrastructure (AMI) and advanced control strategies has enabled ac and dc microgrids to be interfaced, coordinated, and controlled efficiently. The ac/dc microgrid concept allows system operators to partition their distribution systems into ac, dc, and ac/dc clusters of distributed resources and loads. The stable, secure, reliable, and economical operation of the entire distribution system is dependent on the way each cluster is operated and controlled. Successful operation and control of ac/dc microgrids will seamlessly facilitate the implementation of future ac/dc smart grids [13]. With its unique ac/dc topological structure, the future smart grid requires a comprehensive review of existing management and control schemes so that new operational control strategies can be designed to enable hassle-free ac/dc hybrid microgrid (HMG) implementation. This chapter furnishes the background necessary for an understanding of the HMG concept. Also provided is a review of the state of the art with respect to existing analysis tools and operational control schemes, along with an analysis and critical synthesis. The literature review process was based on the problem description, system modelling, formulation, and methodologies applied. The analysis and assessment of the literature led to the identification of existing research gaps in the context of HMGs, which were then set as objectives for the work presented in this thesis.

2.2 AC/DC Hybrid Microgrids

An HMG can be defined as an architecture that integrates two or more independent ac and dc microgrids via bidirectional interlinking converters (ICs). The ICs facilitate power management between adjacent ac/dc microgrids. A sample HMG architecture is illustrated in Figure 2.1, which indicates that both ac and dc subgrids are connected to the utility grid through an island interconnection device (IID) [14], which can be either a static switch or an ac/dc converter. The dc subgrid is interfaced with the main grid and with its adjacent ac subgrids through bidirectional ICs, which can be either voltage source converters

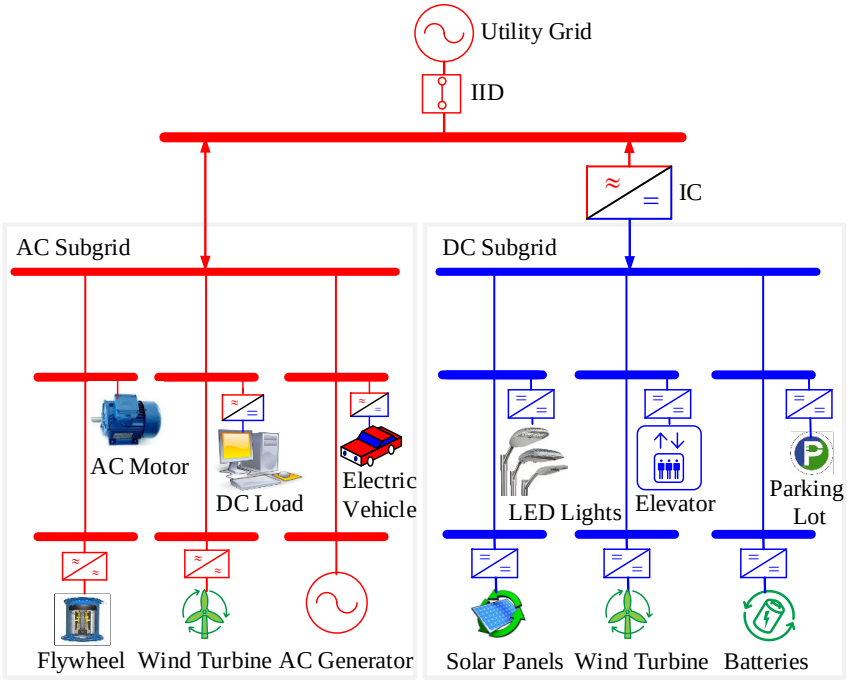

Figure 2.1. Sample architecture of an ac/dc hybrid microgrid.

(VSCs) [15] or back- to-back converters [16]. The IC represents the cornerstone of HMG management and control. The primary IC control objective is the effective management of the power transfer between the ac and dc subgrids. In islanded operation, the IC controller can also be designed to ensure 1) equal loading of the ac and dc subgrids based on their ratings, 2) minimal load shedding and renewable power curtailment in the entire hybrid system, and 3) an adequate reserve and loadability margin for an overloaded subgrid.

The ac subgrid in the hybrid structure shown in Figure 2.1 involves mainly ac distributed energy resources (DERs) and ac loads, while the dc subgrid consists predominantly of dc DERs and dc loads [15]. Any excess energy produced in the dc subsystem can be stored in dc energy storage systems (ESSs) such as batteries. At the same time, surplus energy produced in the ac subsystem can be stored in ac ESSs such as flywheels.

Like its ac and dc building blocks, an HMG can operate in two modes: grid-connected and islanded (autonomous). In grid-connected mode, the dispatchable DERs operate in current control mode, as the voltage provision is ensured by the main grid. The renewable energy resources (RESs) operate in maximum power point tracking (MPPT) mode in order to harvest their maximum available power. Any power mismatch between the local supply

and demand is compensated for by the hosting ac utility grid. In this mode of operation, the ICs ensure seamless power transfer between the ac and dc subsystems and also control the dc voltage. In contrast, in autonomous mode, the dispatchable DERs adopt droop characteristics in order to share the load and provide voltage support. The RESs may operate in MPPT or off-MPPT mode according to the frequency and ac/dc voltage. Any power deficit is supplied by ESSs, which can operate in discharging mode as long as their states of charge permit. If the amount of energy released by the ESSs is inadequate, a load curtailment scheme is then activated [1]. Likewise, during periods of excess renewable power generation when the ESSs are fully occupied, a renewable power curtailment scheme is then initiated.

The ac/dc hybrid architecture offers some economical and technical advantages over purely ac and dc layouts, which can be summarized as follows [1, 17–19]:

1) The number of conversion stages that are used for connecting dc loads and dc DERs to the host ac network is reduced.

2) Conversion costs and losses are decreased because ac/dc loads and DERs of the same type are interfaced with the rest of the network through one or two interfacing converters.

3) As dc technologies become more mature, the capital cost associated with building a purely dc infrastructure and installing multiple ICs will be outweighed by the return on investment in ac/dc structures.

4) No synchronization is required in a dc subgrid, which simplifies control of dc-type DERs.

5) Control of harmonics is enhanced since all dc loads are connected to the dc side of the hybrid system.

6) The zero and negative sequence currents caused by unbalanced ac loading and fault conditions can be solved.

7) In abnormal conditions, each subgrid can disconnect from its neighbouring subgrid and operate in stand-alone mode to supply its own load.

To derive the benefits of hybridizing ac and dc, a practical roadmap must be established for transforming existing ac distribution grids from traditional to smart grids that incorporate multiple ac/dc microgrids. Such a roadmap requires planning and operational studies that include the following [1]:

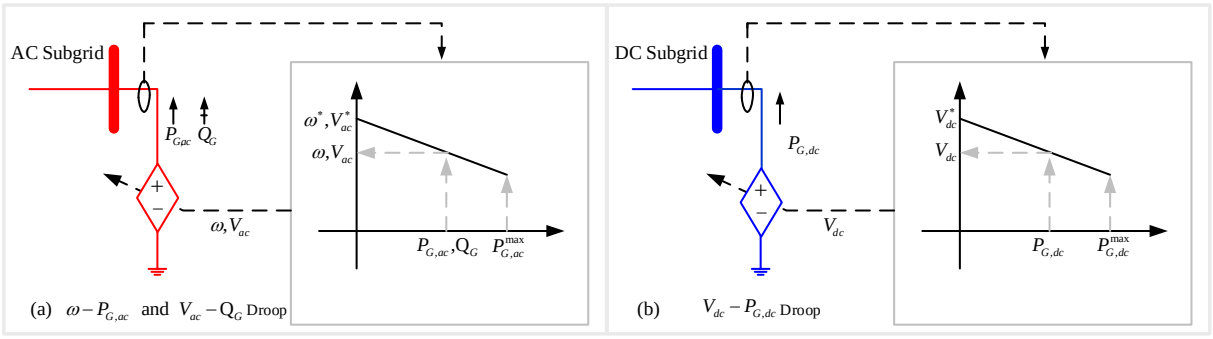

Figure 2.2. The droop characteristics of ac and dc droop-controlled DGs.

1) Developing steady-state and dynamic models of the system components and analysis tools

2) Determining the optimal DER mix, including renewables and storage units

3) Identifying the optimal topology for an ac/dc hybrid system

4) Developing a precise power sharing scheme for the entire hybrid system during islanding

5) Developing an efficient energy management scheme for both modes of operation

2.3 Distributed Energy Resource Droop Control

In autonomous ac microgrids, DERs adopt a droop control strategy in order to share the frequency and voltage control. The active and reactive power droop characteristics of droop-controlled distributed generation (DG) units are depicted in Figure 2.2 (a) and described by (2.1). The active power droop characteristics shown in Figure 2.2 imply a closed loop around the DG active power output so that all DG units settle at the same steady-state frequency and share the active power loading of the system in accordance with their capacities. Likewise, the reactive power droop characteristics imply a feedback loop around the DG reactive power injections so that all DG units share proportionally the reactive power requirements of the system.

$$\omega = \omega^* - m_{p,ac} P_{G,ac}. \tag{2.1}$$

$$V_{ac} = V_{ac}^* - n_q Q_G. \tag{2.2}$$

where
$P_{G,ac}, Q_G$: the active and reactive power outputs of an ac DG unit, respectively;
ω, ω^*: the measured and the no-load/nominal frequencies, respectively;
V_{ac}, V_{ac}^*: the actual and reference ac voltages, respectively;
$m_{p,ac}, n_q$: the active and reactive power droop gains, respectively.

If active power droop parameters $(m_{p_{ac}}, \omega^*)$ in (2.1) are selected based on the DG capacity and the frequency operating range, proportional active power sharing is surely guaranteed. Exact active power sharing in islanded ac microgrids is attributable to the fact that the frequency is a common signal among all DGs. In contrast, the reactive power droop characteristics inherently yield a non-zero steady-state sharing error due to the mismatch in voltage drops across the feeders.

In dc subgrids, the droop characteristics of a droop-based DG unit are as illustrated in Figure 2.2 (b) and described by (2.3). Equation (2.3) implies a closed loop around the output active power or output current so that the dc microgrid loading is shared according to DG capacities.

$$V_{dc} = V_{dc}^* - m_{p,dc} P_{G,dc}. \tag{2.3}$$

where
$P_{G,dc}$: the active power output of a dc DG unit;
V_{dc}, V_{dc}^*: the measured and the no-load/nominal dc terminal voltages, respectively;
$m_{p,dc}$: the active power droop controller gain.

The dc active power droop characteristics expressed in (2.3) are not solely able to establish exact power sharing. This imprecise dc power sharing stems from inconsistent feeder voltage drops.

As well as being controlled with respect to voltage, DERs can also be current controlled. For example, distributed storage (DS) units can be controlled as current sources and charge/discharge based on their droop characteristics. Droop control of DS units can be implemented inversely based on the local measurements of the DS state of charge, the terminal voltage, or the frequency [20, 21]. In the work presented in this thesis, the charging/discharging control strategy adopted for an ac-type DS is based on measurements of the frequency, ω, for active power control, and on those of the ac terminal voltage, V_{ac}, for reactive power control. In contrast, the active power control scheme for a dc-type DS is based on a determination of its dc terminal voltage, V_{dc} [21]. The inverse $(\omega - P)$ droop characteristics for both ac- and dc-type DS units are illustrated in Figures 2.3 (a) and 2.3 (b), respectively.

The $(P - \omega)$ droop of an ac-type DS unit is given by (2.4) [22]. The $(P - V_{dc})$ droop control of a dc-type DS unit can be described mathematically with the help of Figure 2.3

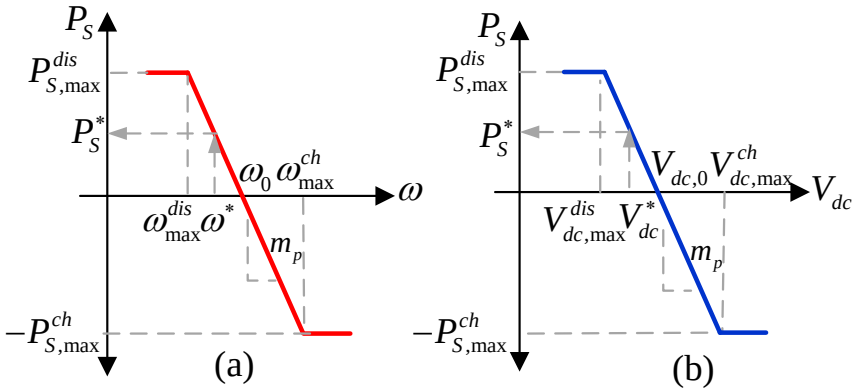

Figure 2.3. DS inverse droop control: (a) ac-type units (b) dc-type units.

(b).

$$P_S = \begin{cases} -P_{S,max}^{ch} & \text{, if } \omega > \omega_{max}^{ch}, \\ \frac{1}{m_{p,ac}}(\omega_0 - \omega) & \text{, if } \omega_{max}^{dis} \leq \omega \leq \omega_{max}^{ch}, \\ P_{S,max}^{dis} & \text{, if } \omega < \omega_{max}^{dis}. \end{cases} \tag{2.4}$$

where
$P_{S,max}^{ch}, P_{S,max}^{dis}$: the DS maximum charging/ discharging active power, respectively;
$\omega_{max}^{ch}, \omega_{max}^{dis}$: the frequencies at which the DS starts to charge/discharge at its maximum charging/discharging rates, respectively;
$m_{p,ac}$: the static active power droop gain of the ac-type DS, which can be designed according to (2.5):

$$m_{p,ac} = \frac{\omega_{max}^{ch} - \omega_{max}^{dis}}{P_{S,max}^{ch} + P_{S,max}^{dis}}. \tag{2.5}$$

The $(Q-V)$ droop control of an ac-type DS is no different from that of an ac-type DG except that it is implemented inversely based on the local measurement of the ac voltage rather than that of the reactive power. It should be mentioned that the droop characteristics of ac/dc DS units can also be implemented in the same manner as for DG units in order to contribute to the local ac/dc voltage control. It should also be noted that conventional droop control can result in the frequency and ac/dc voltages deviating substantially from their reference values. If a communication network is available, this problem can be addressed through the implementation of a secondary controller for frequency and voltage restoration.

2.4 Interlinking Converter Droop Control

The IC that interfaces stand-alone ac and dc microgrids is deemed to be the brain of an islanded HMG. In autonomous operation, ICs implement droop characteristics that determine the amount and direction of power transfer according to the loading levels of both subgrids [15]. Each IC identifies the ac and dc subgrid loading levels independently by measuring the frequency of the ac subgrid and the voltage of the dc subgrid at its terminals. Because it is a common variable in an ac subgrid, frequency is a relatively reliable loading indicator, while dc voltage is only a surrogate indicator of the loading of a dc subgrid, since the unequal voltage drops make it a local variable. For an accurate comparison of the loading of both ac/dc sides, the IC droop controller employs a normalization unit that normalizes the frequency ω and dc voltage V_{dc} within the same range [-1, 1], as expressed in (2.6) and (2.7) [23]. However, other normalization processes such as those in the range of [0, 1] are also possible.

$$\omega_{pu} = \frac{\omega - (\omega_{max} + \omega_{min})/2}{(\omega_{max} - \omega_{min})/2}. \tag{2.6}$$

$$V_{dc,pu} = \frac{V_{dc} - (V_{dc,max} + V_{dc,min})/2}{(V_{dc,max} - V_{dc,min})/2}. \tag{2.7}$$

where $(\bullet)_{min}$ and $(\bullet)_{max}$ indicate the minimum and maximum of quantity $(\bullet)$, respectively.

The difference between the normalized frequency ω_{pu} and the normalized dc voltage $V_{dc,pu}$ is referred to as the error signal and is denoted by $\Delta e_{\omega V}$. The error signal assists the IC in determining the amount and direction of the active power exchange that is required for bringing the error to zero and for attaining equal loading of both subgrids in proportion to their available capacities, as illustrated in Figure 2.4 and expressed by (2.8):

$$P_{ic} = P^*_{ic} - \frac{1}{\gamma_p}(\Delta e_{\omega V} - \Delta e^*_{\omega V}). \tag{2.8}$$

where P^*_{ic} and $\Delta e^*_{\omega V}$ are the active power transfer and error values at the instant of islanding, respectively, and γ_p is the IC active power droop gain.

Equation (2.8) also can be written in terms of the droop gain γ_p, which is the slope of the $(P_{ic} - \Delta e_{\omega V})$ droop curve shown in Figure 2.5, and the point of no power transfer $(P^*_{ic}, e^*_{\omega V}) = (0, 0)$ as

$$P_{ic} = -\frac{1}{\gamma_p}\Delta e_{\omega V}. \tag{2.9}$$

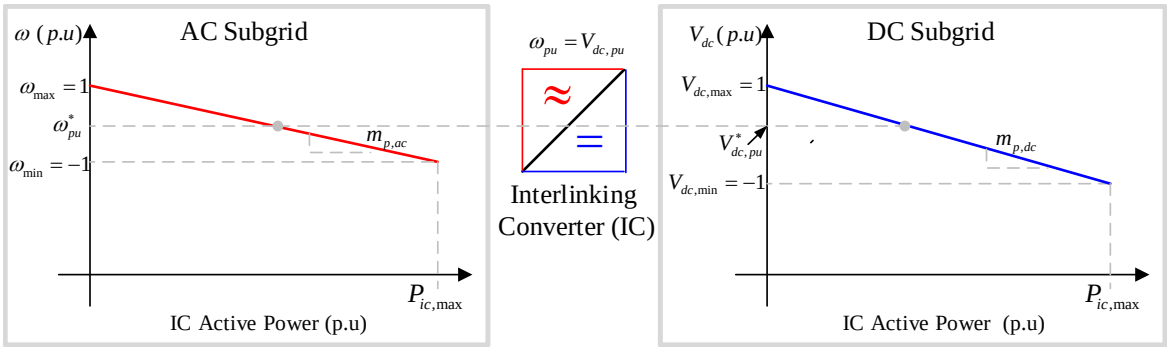

Figure 2.4. Formation of interlinking converter droop characteristics.

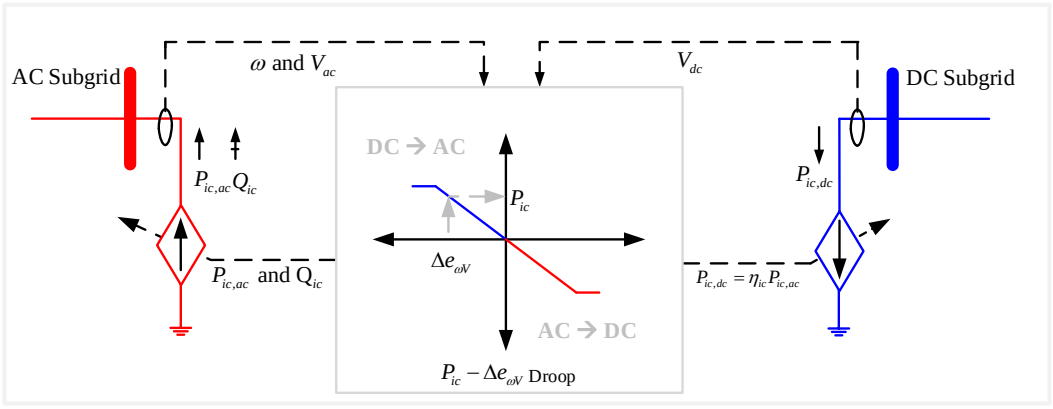

Figure 2.5. Equivalent circuit of the interlinking converter and its active power droop characteristics.

where

$$\Delta e_{\omega V} = \alpha_{\omega}\omega - \alpha_V V_{dc} - \alpha_{\omega V}. \tag{2.10}$$

$$\begin{aligned} \alpha_{\omega} &= \frac{2}{(\omega_{max}-\omega_{min})}, \quad \alpha_V = \frac{2}{\left(V_{dc,max}-V_{dc,min}\right)}, \\ \alpha_{\omega V} &= \frac{(\omega_{max}+\omega_{min})}{(\omega_{max}-\omega_{min})} - \frac{\left(V_{dc,max}+V_{dc,min}\right)}{\left(V_{dc,max}-V_{dc,min}\right)}. \end{aligned} \tag{2.11}$$

A value of $\Delta e_{\omega V} < 0$ indicates that the dc subgrid is relatively loaded in comparison with its ac counterpart, and vice versa. The role of the IC with respect to each subgrid changes as the generation and loading conditions change. Figure 2.5 illustrates how each subgrid identifies the IC and how its active droop characteristics are constructed. Depending on

the power transfer direction, the IC is identified as a current source by the relatively heavily loaded subgrid that is receiving power from the IC but is identified as a load by the relatively lightly loaded subgrid that is supplying power to its neighbouring subgrid. As shown in Figure 2.5, depending on its droop characteristics, the IC remains in "grid following" mode and transmits power to the more heavily loaded subgrid as long as its capacity permits. Once its capacity is reached, the IC switches to constant current-control mode and supplies the maximum current. As a consequence, the IC is then no longer governed by its droop characteristics and operates instead in "grid supporting" mode. The IC also employs the droop characteristics given in (2.12) in order to provide reactive power support to the ac subgrid.

$$Q_{ic} = Q^*_{ic} - \frac{1}{\gamma_q}(V_{ic,ac} - V^*_{ic,ac}). \tag{2.12}$$

where Q^*_{ic} and $V^*_{ic,ac}$ are the references at the instant of islanding, respectively, and γ_q is the reactive power droop coefficient.

In addition to current-control mode, the IC can also be treated as a voltage source for controlling the voltage at either the ac or dc side. For example, if the dc side has a higher capacity and is stiff enough compared to the ac side, the IC can then implement conventional $(\omega - P)$ and $(Q - V)$ droop characteristics similar to those of ac DERs in order to control the frequency and magnitude of the ac voltage. When the IC operates in voltage-control mode, it shares responsibility for controlling the frequency and voltage with other DERs in the ac subgrid and is said to operate in "grid forming" mode. If the IC, for any reason, has difficulty controlling the voltage at its ac terminal, it switches to current-control mode and is said to operate in "grid supporting" mode.

2.5 Power Flow Analysis of AC/DC Hybrid Microgrids

The successful integration of dc clusters into ac grids and the implementation of new smart distribution systems comprising several HMGs that have plug-and-play capabilities can be realized only if intensive feasibility studies, including operational and planning studies in steady-state and contingency conditions, are performed by local distribution companies. Planning and operational aspects of islanded ac/dc hybrid systems include DER planning, network reconfiguration, volt/var optimization, voltage and frequency regulation, power sharing, and energy management, to name just a few. Nevertheless, due to the lack of a power flow analysis tool designed specifically for islanded ac/dc hybrid systems, the majority of the studies reported in the literature have been based on the assumption of a

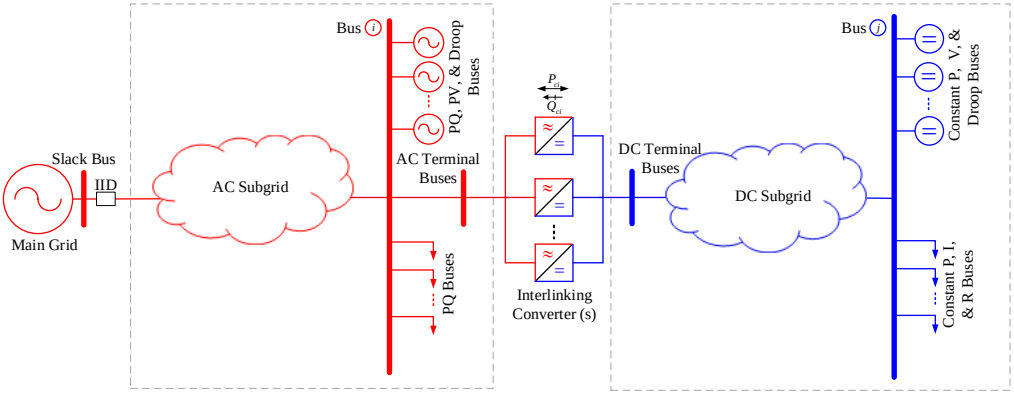

Figure 2.6. A single-line diagram of a generic ac/dc hybrid microgrid.

simple HMG, in which the DERs and loads in each subgrid are represented by one or two parallel DERs that supply a common load at the point of common coupling (PCC).

The new HMG paradigm, with its unique characteristics, introduces new definitions and modelling concepts to the power flow problem. For example, some DERs might be set to deliver constant power and are thus modelled as constant current sources, while other DERs can be voltage-controlled and participate in voltage and frequency control according to their droop characteristics. Further, in an ac microgrid, static loads exhibit frequency and voltage dependency characteristics.

For islanded HMGs, power flow, also known as "load flow," is a computational algorithm that calculates the frequency; the ac/dc bus voltages; the outputs of droop-controlled DERs; and the ac/dc line power flows and by-product, the total power losses. Figure 2.6 shows a one-line diagram for a generic HMG in which some DERs are droop-controlled in order to establish the frequency and voltage control, while other DERs might be controlled to supply constant power regardless of the voltage at their terminals. In the power flow problem, buses with droop-controlled DERs are modelled as droop-controlled buses while those with current-controlled DERs are approximately modelled as constant PQ buses. The set of ICs shown in Figure 2.6 control the power exchange between the ac and dc sides based on their droop characteristics and the relative loading of ac and dc sides.

For ac/dc hybrid networks, the power flow problem can be solved using either a sequential [24] or a unified approach [25]. The authors in [26] developed a sequential Newton-Raphson-based power flow algorithm for islanded HMGs. With a sequential approach, the ac and dc power flow subproblems are solved iteratively and sequentially until the sequential power flow algorithm converges. The advantage of this approach is that it utilizes the

existing ac and dc power flow programs, but a sequential formulation may also be subject to convergence issues [27]. In a unified ac/dc hybrid power flow program, the ac and dc power flow subproblems are solved simultaneously. However, ac/dc power flow programs have been developed only for ac/dc hybrid systems at high voltage levels, i.e., high-voltage dc (HVDC) and multi-terminal HVDC systems [24, 25, 27]. At low- to medium-voltage levels and in islanded operation, the ac/dc hybrid power flow problem requires special attention for the following reasons [28], [29]: 1) Low- to medium-voltage systems tend to have low X/R ratios, 2) Isolated systems preclude the luxury of connection to the utility grid or any other dominating source that functions as an infinite bus supplying a theoretically infinite amount of slack power. 3) AC and DC subgrids can have comparable sizes and limited physical inertia, and thus, no single subgrid can dominate and fill the role of the slack bus for a neighbouring subgrid. 4) Some DER units might operate based on their droop characteristics in order to share the responsibility of controlling the frequency and voltage. 5) Separation from the main grid means that the ac subgrid frequency is no longer constant but rather a floating power flow state variable. 6) The active and reactive loads are quite sensitive to any changes in the voltage and frequency. 7) The primary control objective of the IC is not only to manage the power exchange between adjacent ac and dc subgrids but also to share the entire load in proportion to the capacities of both subgrids.

2.6 Power Sharing Control in Microgrids

In islanded/isolated droop-based ac and dc microgrids, precise power sharing is both technically and economically preferable. From a technical perspective, exact power sharing can eliminate circulating currents among the converters and relieve converter overloading conditions. Another benefit of proportional power sharing is the preservation of the preallocated reserve and loadability margin that provides secure operation during islanding and contingency conditions. Economically, in the case of differently owned local DER units, accurate power sharing can guarantee equal revenue management that corresponds to DER capacities.

Based on communication requirements, power sharing control schemes can be categorized as either communication-based or communication-less [30].

2.6.1 Communication-Based Power Sharing Schemes

Communication-based power sharing schemes can be implemented in a centralized or a distributed manner [31]. Centralized power sharing schemes such as master/slave control

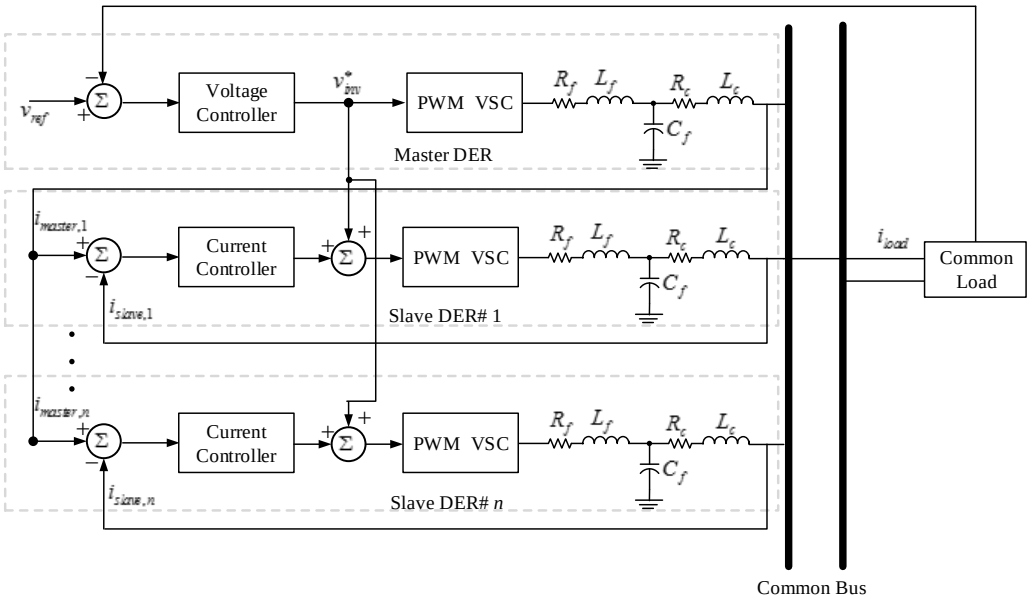

Figure 2.7. Control architecture of master-slave control.

schemes are dependent entirely on the availability of two-way communication between the centralized supervisory controller and the local DER controllers. The control structure of master/slave DERs is depicted in Figure 2.7. As the figure indicates, the master DER controls the output voltage and sends the current set points, i_{master}, to the slave DERs that then track the reference current by measuring their output currents, i_{slave}, in order to share the loading current, i_{load}, proportionally. The most noticeable drawback of such a centralized power sharing control scheme is the single point of failure.

2.6.2 Distributed Power Sharing Schemes

Distributed power sharing schemes [32], such as multi-agent schemes [33], apply the concept of distributed control. Distributed schemes require a lower bandwidth communication link than their centralized counterparts, since each participating DER exchanges its local information only with its DER neighbour. The power sharing decision is thus made collectively. Figure 2.8 shows a schematic diagram of a distributed control architecture. As can be observed in the Figure, each distributed controller involves an additional control loop that controls the output current, i_o, in order to follow the same average current signal, i_{avg}. The error between the measured output current, i_o, and the average current, i_{avg},

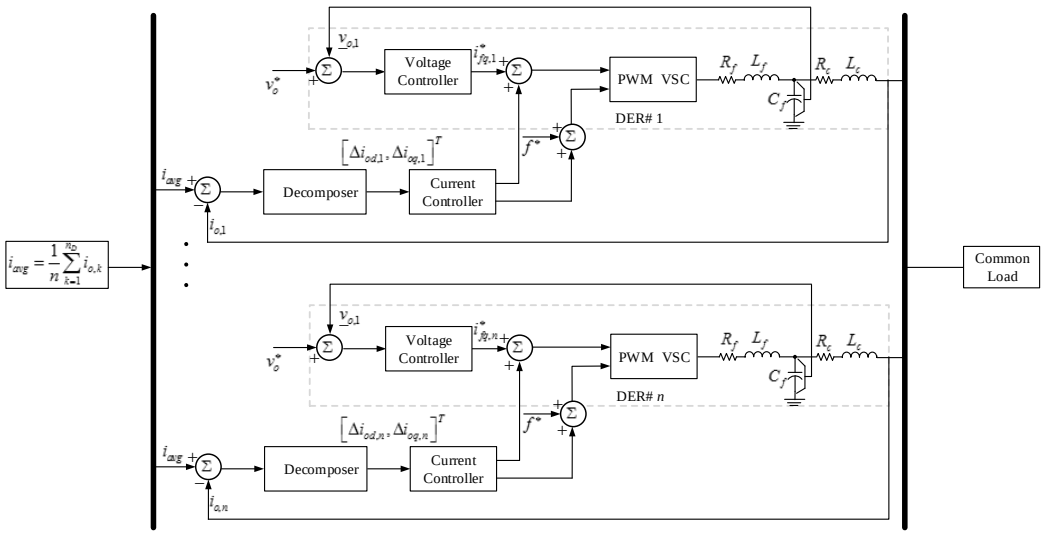

Figure 2.8. Control architecture of distributed control.

is decomposed into two components in the dq frame: $\Delta i_{o,d}$ and $\Delta i_{o,q}$. The d component is used for controlling the frequency while the q component is employed for controlling the output voltage magnitude, v_o. The advantage of distributed power sharing schemes is that they comply with the plug-and-play feature of DERs. An additional benefit is that, unlike centralized schemes, no point of failure is encountered. However, distributed sharing schemes can nevertheless be associated with data synchronization and convergence issues.

2.6.3 Communication-less Decentralized Power Sharing Schemes

Communication-less, or decentralized, power sharing schemes adopt droop characteristics that merely utilize local measurements, and hence require no communication link [34]. The principle behind decentralized droop controllers is that droop-controlled DERs mimic the behaviour of synchronous generators whereby the frequency droops as the DER injects more active power and the voltage droops as the DER delivers more reactive power. DER droop characteristics were discussed in section 2.3. The block diagram of an ac droop-controlled VSC-based DER with its LCL filter is depicted in Figure 2.9. As the figure specifies, the decentralized controller of a droop-based DER comprises three nested control loops: the power loop, which is the outermost loop; the voltage loop, which is the main or outer loop; and the current loop, which is the inner loop. The power loop provides the

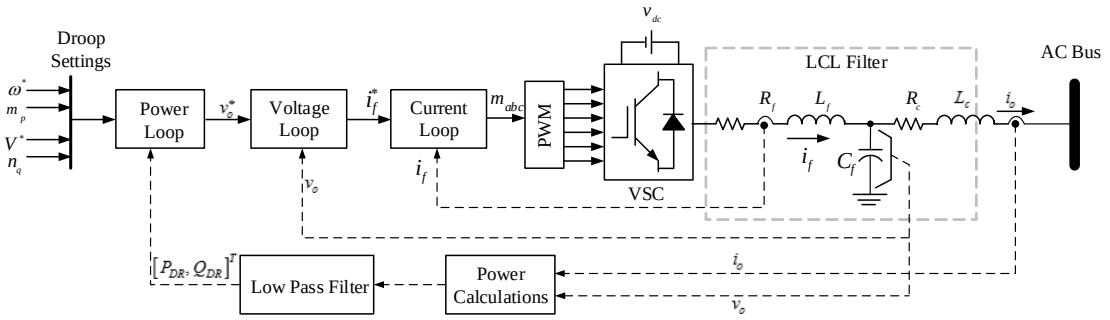

Figure 2.9. Block diagram of a droop-controlled VSC-based DER.

reference output voltage, v_o^*, to the voltage loop. The voltage controller, in turn, tracks the reference output voltage through continuous measurement of the output voltage, v_o. The current loop generates command signals to the pulse width modulator (PWM) of the VSC. The utilization of droop characteristics allows DERs to share the load proportionally with a steady-state error in the reactive power sharing.

In addition to inaccurate reactive power sharing, droop control in ac microgrids has several drawbacks among which:

1) The frequency and voltage can deviate substantially from the nominal in order to provide better load sharing [35],

2) Microgrid stability could be jeopardized by efforts to distribute the load proportionally among droop-controlled DERs [35],

3) Significant currents circulating between parallel converter-based DERs are created due to the unequal feeder impedances [36],

4) A harmonic circulating current is possible when nonlinear loads are present in the microgrid [36],

5) Poor power transient response and slow dynamics result from to the calculations and the filtering of the active and reactive power.

With respect to inaccurate power sharing, droop control in dc microgrids is no better than in ac microgrids. To address the limitations associated with inaccurate power sharing, several attempts have been made to improve droop control and to correct for inexact reactive power sharing in islanded ac microgrids [30, 37–39] and for imperfect active

power sharing in islanded dc microgrids [40–42]. For example, droop control with virtual output impedance based on the addition of a control loop in order to shape the inverter output impedance was proposed in [37]. In [38], another variant of a droop controller was introduced: a derivative term of the DG active power was incorporated in order to stabilize power sharing in ac microgrids. For dc microgrids, the authors of [40] employed a low-bandwidth link that permits communication among local droop controllers in order to achieve simultaneous proportional power sharing and voltage regulation. Another proposal involved the utilization of a virtual resistance: an adaptive droop controller for equalizing the load current sharing and minimizing the circulating current [42]. Given the inherent limitations of conventional droop control methods, operational control issues related to islanded droop-controlled ac and dc microgrids will definitely migrate to HMGs. These operational challenges include, but are not limited to, problems associated with the following:

1) IC power flow control and management [43]
2) AC/DC voltage and frequency regulation [44]
3) The poor transient response of droop-controlled DG units [45]
4) The necessity for a seamless transition between different operating modes [46],
5) Harmonic current sharing and control in the presence of nonlinear loads [47]
6) Optimal power sharing management

When this literature review was conducted, the difficulties related to optimal power sharing in droop-controlled HMGs had yet to be addressed.

Investigations of the problem of power sharing and management in islanded HMGs have been reported in a handful of published studies, which can be divided into three categories: centralized [48]; distributed [49, 50]; and decentralized [51–54]. In [48], a University of Alberta research group designed a centralized controller for controlling the power exchange between autonomous ac and dc microgrids. The centralized controller requests the output power and maximum available power of all DERs and ICs and then sends active power set points to the IC controllers accordingly. It was unclear how frequently the information about both subgrids is updated or which data refreshment rate and bandwidth for the communication link are required for practical implementation.

To minimize communication requirements, the authors of [49] developed a decentralized control architecture with three droop-based power sharing schemes for a HMG topology.

The proposed topology is a three-port ac/dc/DS HMG. The ac and dc sides are interlinked via dual ICs that consist of a bidirectional buck-boost dc converter and a VSC. The dc/dc IC regulates the dc link voltage, while the VSC-based IC is responsible for proportional active power sharing between the ac/dc microgrids. The dc link between the two ICs enables interfaces with multiple DS units. The proposed decentralized control scheme introduced in [49] comprises a multi-level power sharing scheme: a local power sharing scheme in each subgrid, a global power sharing scheme in the entire HMG, and a storage-based scheme for sharing power among DS units. The local sharing scheme seeks precise power sharing among the local DGs in each subgrid. Global power sharing is aimed at equalizing the loading of both subgrids according to their available capacities. The storage-based sharing scheme releases the overloading conditions of both subgrids. The application of multiple DS units was not clearly justified. Multiple DS units can be made to be identical and to have similar droop characteristics, thus eliminating the need for the storage-based power sharing scheme. A further factor is that the IC supplies no reactive power to the ac side, which can be crucial during limited reactive power support.

An HMG could be as simple as a single ac subgrid interfaced with one dc subgrid and as complex as multiple ac subgrids that have different frequencies and are interlinked with multiple dc subgrids having different dc voltage levels. Based on this perspective, in the work reported in [54] the researchers extended the HMG topology introduced in [49] to include multiple ac and dc subgrids. Their multi-HMG structure involves DS units connected to a common dc bus to which the ac subgrids are connected via bidirectional VSCs, and the dc subgrids are joined together through bidirectional dc/dc converters. The ac subgrids have the same frequency while the dc subgrids have the same dc voltage level. The ac/dc ICs and dc/dc ICs operate in voltage-control mode to provide voltage support to the ac and dc subgrids, respectively. For such a topology, the authors of [54] proposed an autonomous coordinated control scheme. Their control strategy is based on local measurements of the common dc bus voltage and the ac/dc terminal voltages. They introduced $P_{dc} - V_{dc}^2$ droop characteristics for the DS units in order to control the dc link voltage and to achieve proportional sharing. A limitation of their proposed management scheme is the assumption that all of the subgrids are connected to the same common dc bus, which can be impossible in practice.

Recent applications of event-based and consensus-based distributed control strategies motivated the authors of [52] to develop a distributed power sharing scheme for multiple ICs. The use of an event-based control method eliminates the requirement for high-bandwidth communication among ICs. Each agent (IC) relies on its local measurements and on the information sent by the neighbouring IC. ICs are also utilized for providing reactive power support. Exact active power sharing among multiple ICs was achieved

through the design of a distributed supervisory controller. The drawback of the distributed control strategy is that the local DGs in each subgrid are represented by an aggregated droop-controlled DG unit whose combined droop characteristics are equivalent for all DGs. Aggregating all droop-based dc-type DGs into one large DG does not accurately represent the dc loading and voltage drop. Even in ac subgrids, although their droop characteristics are counted in obtaining the combined droop characteristics, the availability of local DGs can frequently shift due to an unexpected outage. The sharing error thus becomes significant, especially when the dc subgrids are highly resistive and when the number of DG units in service changes. Another research group from the University of Waterloo proposed a multiagent supervisory controller for power management in islanded dc microgrids [55]. The distributed supervisory controller can achieve two objectives: optimal power sharing and optimal power dispatch. The distributed power management problem was formulated as a convex distributed optimization problem which might not be applicable to the power management of HMGs due to the nonconvexity and nonlinearity of the ac/dc power flow equations.

A hierarchical control architecture has also been proposed as a solution to the problem of unequal power sharing among multiple ICs. The study reported in [50] involved the proposal of a two-layer hierarchical controller: a primary and a secondary controller. The primary layer comprises a data-driven and an adaptive model-free controller so that the ICs can achieve proportional sharing in the entire HMG. The data-driven controller tracks the dc voltage reference, while the dual droop controller targets simultaneous equal sharing and voltage/frequency regulation. Another control layer, a secondary controller, is added to the IC control system in order to restore the frequency and dc voltage following a disturbance. Using the IC as a voltage source for controlling the voltage at either side necessitates the domination of one side by the other. The authors developed a uniform multimode control scheme for ICs in hierarchical-controlled HMGs. With this control strategy, based on the loading conditions in each subgrid, each IC operates in either current-control mode or voltage control mode, without the need for switching between control modes. The proposed multimode controller also encompasses a PI controller for tracking the active power set point sent by the centralized controller.

For autonomous active power sharing among multiple ICs, a novel idea based on a superimposed frequency for mitigating unequal dc voltages at IC terminals was introduced in [51]. Each IC superimposes a small ac voltage signal on its dc terminal voltage, whose frequency is drooped with the output active power. The proposed ac/dc droop controller achieved precise proportional sharing among ICs but at the expense of the introduction of some ripples, thus negatively affecting the quality of the dc voltage.

In their design of an effective power sharing scheme for interfaced ac/dc microgrids

during abnormal conditions, the authors of [56] included consideration of the ac unbalance fault conditions when developing an autonomous control strategy for parallel ICs. Their control methodology was aimed at enhancing the active power transfer capability and filtering out oscillations in the active power transfer as well as ripples in the dc link voltage during ac unbalanced fault conditions. The proposed control scheme is reliant on a redundant IC whose ratings are higher than those of the other ICs. A two-level IC current regulation scheme was introduced as a means of preventing ICs from exceeding their current limits under different unbalance conditions. However, dedicating one large IC to the mitigation of unbalance fault conditions might not provide an economical solution.

2.7 Voltage Instability/Collapse in Microgrids

The term voltage collapse is defined as "the process by which the sequence of events accompanying voltage instability leads to a blackout or abnormally low voltages in a significant part of the power system" [57]. Voltage collapse is a long-term steady-state phenomenon that can develop due to saddle node bifurcation (SNB) or limit-induced bifurcation (LIB) [58] and [59]. The SNB point is the loading point at which the voltage collapses: numerically, the Jacobian matrix of the system becomes singular so that no power flow solution can be achieved. The LIB point is the loading level at which the system can no longer provide the necessary voltage support: some voltage-controlled generators reach their reactive power limits, and voltage control is lost. In voltage stability studies, the SNB is normally studied based on the assumptions that the installed capacity of the generation system is unlimited and that the maximum transferrable power of the transmission system is infinite. In contrast, the LIB point is obtained by varying the system loading while imposing reactive power limits on synchronous-based DERs. Tracking SNB and LIB points requires steady-state modelling of the system components and an analysis tool. It is interesting to note that some load bus voltages can collapse as a result of SNB while others can collapse because of LIB. An additional factor is that limited voltage support, overloading conditions, and severe contingencies can cause either type of bifurcation to develop at loadability levels lower than the installed capacity of the system.

Figure 2.10 presents a PV curve, also known as "the nose curve," which graphically tracks the steady-state behaviour of a load voltage (V) as a function of the maximum power (P) that can be transferred to that load. The figure shows the LIB and SNB points as well as the current loading level, λ_{ac}, at an ac load bus. Two critical loadability levels are defined in the figure: $\lambda_{ac,LIB}$ because of the LIB and $\lambda_{ac,SNB}$ because of the SNB. It is crucially important for a microgrid operator to assess and maximize the loadability margin

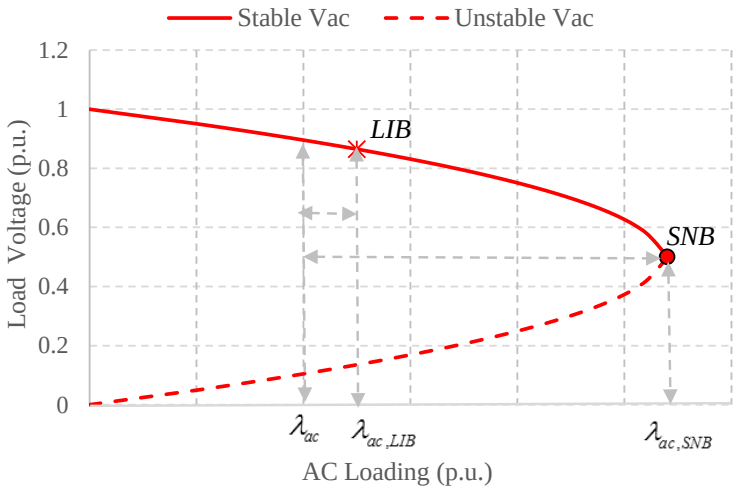

Figure 2.10. PV curve at an ac load bus.

between the current loading level λ_{ac} and the critical loading level during islanding in order to take into account any credible contingencies.

Loadability assessment and maximization are essential considerations in the planning and operation of active distribution networks that include DERs and microgrids. In [60] and [61], the improvement of system loadability was set as a target for DER planning, and it was concluded that appropriate DER size and location can enhance the voltage stability margin. The planning approaches presented in [60] and [61] were based on the availability of a substation for the provision of voltage support. All DERs were thus assumed to be operating in current-control mode, which is not the case in microgrids. Unlike grid-connected distribution systems, microgrids require that some DERs operate as "voltage forming" units. The benefits of converter-based dc segments with respect to the loadability of purely radial systems have been discussed in recent published studies [62] and [63]. It has been demonstrated that system loadability can be increased by the addition of dc links among radial feeders. However, ac/dc loops change the network topology from radial to mesh, which is difficult to operate and control.

With respect to microgrids, a few researchers have focussed their attention on the loadability of droop-controlled ac microgrids [64–67]. The authors of [64] were the first to investigate the loadability of islanded ac microgrids. They extended the conventional Newton-based continuation power flow (CPF) to include the assessment of microgrid loadability during separations from the main grid and the capture of PV and QV curves. PV

and QV curves are used for tracking the steady-state behaviour of load voltages as a function of the active and reactive power loading. The CPF described in [64] was designed for balanced microgrids, based on an assumed insignificant voltage unbalance. Another research group [65] conducted further investigations into the maximum loadability of islanded ac microgrids and developed three formulations based on optimal power flow (OPF): OPF for maximum loadability assessment, OPF for loadability maximization, and OPF for joint cost and loadability optimization. The authors of [64] and [65] concluded that optimizing the droop parameters can maximize the loadability margin. The authors of [65] also proposed a probabilistic approach for the selection of droop parameters that maximize the voltage stability margin and obtained a set of droop parameters for possible islanding conditions [66]. However, because islanded microgrids are typically not associated with loadability issues during normal operation, the droop parameters would be more effective if designed for the presence of contingency events. The same authors also studied the reconfiguration of islanded microgrids in conjunction with the optimal droop parameter settings for maximum loadability [67]. They showed that simultaneously changing the system topology and adjusting the droop parameters during islanding can widen the loadability margin. All of the above studies included consideration of loadability only during normal operating conditions. The concept of DG is expected to eliminate the possibility of voltage collapse in microgrids under normal conditions even during islanding. The analysis presented in this thesis shows that voltage collapse is possible in ac/dc microgrids during serious contingency events such as multiple line circuit outages. This thesis therefore also explores the voltage instability/collapse problem in islanded HMGs under contingencies.

2.8 Energy Management in Microgrids

Energy management in microgrids with hierarchical control structures can be divided into three control layers: primary, secondary, and tertiary [68], [69], as illustrated in Figure 2.11 [70]. In the primary control layer, also called the local control layer, power sharing and local voltage control are achieved by the local controllers (LCs) of the droop-controlled DERs. In converter-based DER units, which are inertia-less, power sharing is achieved with the help of droop characteristics, whereby converter-based DER units mimic the behaviour of synchronous-based DERs. In the secondary control layer, also termed the supervisory controller or the energy management system (EMS), frequency and voltage restoration are achieved by re-dispatching the generation, adjusting ESS charging/discharging, curtailing surplus renewable power, or shifting/shedding controllable loads. The tertiary control layer is the highest layer in the control hierarchy. This control layer involves the optimization

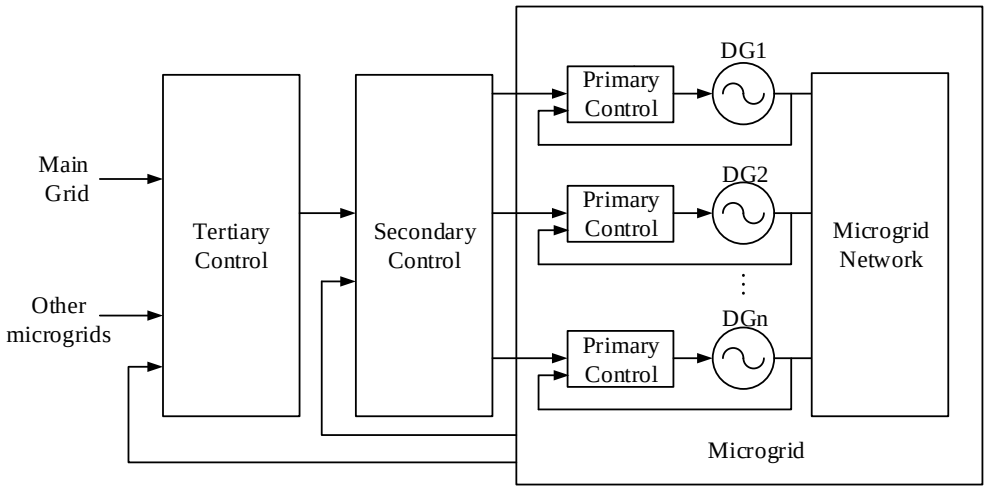

Figure 2.11. The hierarchical control structure of a multi-DG microgrid [70].

of the power import/export transactions between the microgrid and the utility grid and between the microgrid and other adjacent microgrids. The tertiary controller can be merged with the EMS so that the resultant control architecture comprises only two layers.

Since this research is focussed on the secondary control layer, the following information sheds light on the structure, objectives, and challenges related to EMSs in microgrids.

An EMS, also referred to as supervisory control and data acquisition (SCADA), is a collection of control schemes and optimization routines that are used for monitoring, controlling, and operating the power grid as well as for retrieving system information [71].

The general structure of a centralized EMS is illustrated in Figure 2.12, which shows that the EMS collects forecasts for the electricity price, power demand, and renewable power supply. The availability of controllable devices, i.e., DERs and loads, is also communicated to the EMS. In microgrids, the function of the EMS is to perform system-level operations, including the following [72]:

1) Day-ahead supply and demand management: The EMS determines the day-ahead schedule of the dispatchable DG units, including the reserve required and the energy consumption schedule for the next 24 h according to the hourly energy prices, which are announced in advance.

2) Real-time power generation and consumption dispatch: The EMS adjusts the day-ahead generation schedule in order to balance the power mismatch between the supply and demand. Equally importantly, the EMS also sends curtailment and/or deferral decisions to price-responsive loads in order to reduce the peak load.

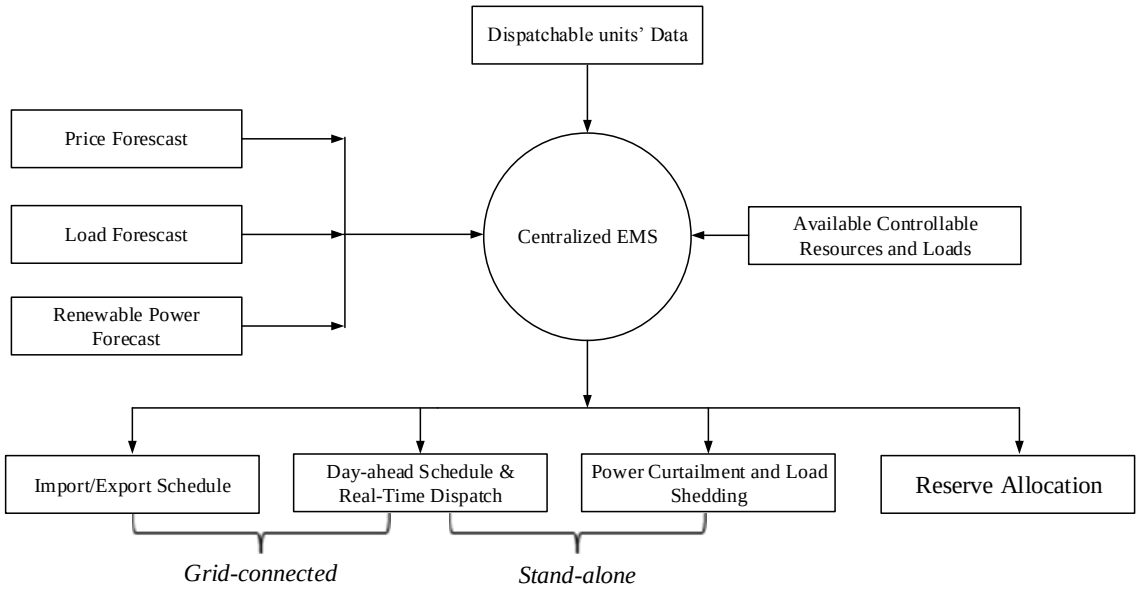

Figure 2.12. A schematic diagram of a centralized energy management system.

Despite the control and operational benefits of clustering distribution systems into microgrids with islanding capability, microgrids create operational challenges that can be summarized as follows [73], [74]:

1) Due to their small size, converter-based DG units tend to have low physical inertia, which in turn, could cause frequency instability during islanding and contingencies.

2) Unlike the case in large-scale power systems in which the frequency can be well regulated, frequency regulation in isolated/islanded microgrids is challenging due to the lack of stiffness and slackness during islanding.

3) In islanded microgrids, the available generation can be limited in amount and stochastic in nature.

4) Operating a microgrid as an independent entity increases the complexity of dispatch decisions because they entail not only decisions about the generation schedule but also about the schedules for imports/exports with the hosting grid during grid-connected mode as well as load/generation curtailment decisions during autonomous operation mode.

5) The plug-and-play characteristics of DERs and the mobility of electric vehicles (EVs) complicate the energy management problem in microgrids.

As the concept of microgrids is increasingly accepted worldwide, the need for an efficient and practical EMS is becoming more pronounced. In this regard, due to the growing trend of transforming distribution grids from traditional to smart, the operation of these new types of grids has been a common subject of recently published research. In [75], an investigation of the day-ahead operation of ac smart grids was reported. The objective was to minimize the operating costs as well as the emissions from the electricity and transportation sectors by utilizing EVs and renewable-based DGs. However, the scheduling problem was formulated as a deterministic optimization problem, and network constraints were not considered. Having realized the significance of the random behaviour of renewables and the demand, the authors therefore incorporated these uncertainties into their subsequent work [76]. However, they did not consider modelling of the network constraints, including the operational limits of the bus voltage and the thermal limits of the distribution feeder. In [77], the authors accurately modelled the network in the day-ahead resource scheduling problem, but the random renewable energy supply and the variable EV demand were modelled deterministically.

The day-ahead resource and reserve scheduling problem associated with demand response in uncertain environments was addressed in [78]. Although the researchers can be commended for considering some critical aspects such as network constraints, reserve requirements, cost/emission reductions, and the stochastic nature of wind energy and the demand, they did not include key elements of future smart grids: ESSs and EVs. In their later work [79], the same authors included consideration of coordinated EV charging in day-ahead operational planning so that operating costs and emissions were minimal. However, all energy resources were assumed to be dispatchable. The energy management problem was also solved in [80], [81], but only for islanding conditions, and the only uncertainty taken into account was that associated with renewable energy. Another factor addressed in recent publications is EV battery degradation. Unrestricted vehicle-to-grid (V2G) might degrade the efficiency of an EV battery and shorten its lifespan [82]. EV battery degradation can be addressed by incorporating a cost component and a set of constraints into the dispatch model in order to limit frequent and deep discharging. In [82], the researchers considered EV battery degradation during V2G, but at the household level, thus neglecting a representation of the network. With respect to electricity markets, another study [83] involved tackling the stochastic day-ahead market clearing problem by applying the demand as a means of providing reserves to cover system security and load reduction during outages. In [84], an EV aggregator was introduced as a component of the

day-ahead market design in order to offer reserve services to the system operator through coordinated charging.

In all of these studies, the proposed dispatch and EMS models targeted only ac-type networks. The energy management of HMGs that operate in grid-connected and islanded modes of operation was not addressed.

2.9 Discussion

This chapter has provided a discussion of an ac/dc structure that can host both ac and dc technologies. Also presented are the main components of future ac/dc grids as well as their control strategies and steady-state models. The state of the art of steady-state analysis, power sharing, voltage stability, and energy management in HMGs have also been reviewed. Existing gaps observed in the literature were highlighted and can be summarized as follows:

1) No mention could be found in the literature of a generalized power flow analysis tool designed for islanded HMGs with droop-controlled DERs and ICs.

2) The problems of imprecise reactive power sharing in ac microgrids and inexact active power sharing in dc microgrids carry over to and are associated with droop-based HMGs. In addition to droop-controlled DERs, the ICs that interface ac and dc subgrids at different interfacing points are also subject to the same problem of inaccurate power sharing.

3) The possibility of voltage instability/collapse in autonomous HMGs during contingencies was not addressed.

4) All of the energy management and optimization models described in the literature targeted only ac-type networks.

The research conducted for this thesis has contributed to the existing body of knowledge about HMGs by filling the highlighted gaps and resulting in the development of 1) a generic ac/dc power flow algorithm for islanded droop-controlled HMGs, 2) a precise power sharing scheme that optimizes the droop characteristics of droop-based DERs and ICs, 3) a voltage-stability analysis of HMGs during islanding and contingencies, and 4) a stochastic centralized EMS model for smart distribution grids that have an ac/dc structure.

Chapter 3

A Unified Approach to the Power Flow Analysis of AC/DC Hybrid Microgrids

3.1 Introduction

A promising configuration for future smart grids is an ac/dc hybrid topology that enables the integration of ac/dc energy resources and modern loads, thus permitting the consequent formation of ac/dc hybrid microgrids (HMGs). An understanding of HMGs and their operational premise during islanding will certainly pave the way toward the realization of a future smart grid that includes a plug-and-play feature. However, the planning and operation of such isolated and hybrid systems are reliant on a powerful and efficient power flow tool. To this end, this chapter introduces a unified, generic, and flexible power flow algorithm for islanded HMGs. The power flow subproblems related to ac and dc subgrids are described mathematically by a set of nonlinear equations and are solved simultaneously using a Newton trust-region method. The developed algorithm is generic in the sense that it includes consideration of the unique characteristics of islanded HMGs: a variety of possible topologies, droop controllability of the distributed energy resources (DERs), and bidirectionality of the power flow in the interlinking converters (ICs). The new power flow formulation is flexible and permits the easy incorporation of any changes in DER operating modes and IC control strategies. The developed algorithm was tested and applied for analyzing selected operational and control aspects of islanded HMGs, including inaccurate power sharing and ICs characterized by differing control strategies. The developed load flow program can form the basis of and provide direction for further studies of islanded HMGs.

The work presented in this chapter has resulted in a full-featured power flow program with the following key characteristics:

- The developed power flow algorithm is a unified approach that simultaneously solves the power flow subproblems associated with ac and dc subgrids. The subproblems are mathematically formulated as a set of nonlinear equations and are solved as a unit using the Newton trust-region (TR) method [85], [86].

- The Newton TR method has a globally convergent property that guarantees the solution whenever it exists regardless of its initial point [85].
- The developed power flow formulation is generic because it models the unique characteristics of isolated HMGs, such as the unavailability of a slack bus and the bidirectionality of the power flow between neighbouring ac and dc subgrids.
- Our unified power flow algorithm (UPF) is flexible and can easily accommodate any changes in the DER operating mode or the IC control strategy.

In this chapter, Section 3.2 highlights the steady-state models of the primary components and introduces the IC control strategies. Section 3.3 explains the newly formulated power flow problem in isolated HMGs. Section 3.4 presents the solution based on the Newton TR method. Section 3.5 provides the main steps in designing ac/dc hybrid test systems. Section 3.6 focuses on the validation of the power flow phasor formulation, algorithm application, robustness, and scalability. Section 3.7 summarizes the main points presented in this chapter.

3.2 System Model and Control

A power flow solution is only as accurate as the steady-state models used for describing each component: line, load, DER, and IC.

3.2.1 Overhead Line and Underground Cable Models

At the ac distribution level, a distinctive property of distribution lines is their low X/R ratios. At the microgrid level, another unique feature is the dependency of the ac line inductance, $X_{ac,Line}(\omega)$, on the system frequency, ω. Distribution lines can be either overhead, as in rural networks, or underground, as in the urban networks found in high-density areas. Two models are normally used for describing overhead lines and underground cables: the PI model and the T model [87]. From a computational perspective, the PI model is preferable to the T model since the system order is increased by the central node of the T model. At the distribution level, the distribution lines are shorter than their transmission counterparts, which enables the line-charging effect represented by the shunt capacitances to be neglected so that the resulting line model becomes merely a series impedance: $Z_{ac,Line}(\omega)$ [88]. DC lines are modelled in steady-state by a series resistance.

3.2.2 Load Model

Depending on the operating voltage, $|V_{ac}|$, ac static loads are often assumed to demand both active and reactive power, $P_{D,ac}, Q_{D,ac}$, regardless of the system frequency. However, at the microgrid level and in islanding mode, load characteristics are dependent not only on the operating voltage but also on the system frequency, $P_{D,ac}(|V_{ac}|, \omega), Q_{D,ac}(|V_{ac}|, \omega)$. The sensitivity of the load to the operating voltage and to the system frequency can be mathematically calculated from (3.1) and (3.2) [58].

$$P_{D,ac} = P_{D,ac0}\left(\frac{|V_{ac}|}{|V_{ac,0}|}\right)^{\alpha}[1 + k_{pf}(\omega - \omega_0)]. \tag{3.1}$$

$$Q_{D,ac} = Q_{D,ac0}\left(\frac{|V_{ac}|}{|V_{ac,0}|}\right)^{\beta}[1 + k_{qf}(\omega - \omega_0)]. \tag{3.2}$$

where
$P_{D,ac,0}, Q_{D,ac,0}$: the nominal active and reactive power demand, respectively;
$|V_{ac,0}|, |V_{ac}|$: the nominal and operating voltages, respectively;
α, β: the exponents of the active and reactive loads, respectively;
ω_0, ω: the nominal and operating frequencies, respectively;
k_{pf}, k_{qf}: the frequency sensitivity parameters.

Typical values for k_{pf} and k_{qf} are in the range of 0 to 3 and -2 to 0, respectively [58]. It is worthy to mention that the load type can also be constant current, I, or constant impedance, Z, depending on the values of the exponents α and β [89].

The dc voltage-dependent loads can be described by (3.1) when k_{pf} is set to zero. Depending on the exponent α , the dc load can be constant power, P; constant current, I; or constant resistance, R.

3.2.3 Distributed Energy Resource Model

In isolated HMGs, the ac-type DER units can operate in three modes PQ, PV, or droop [28]. Likewise, dc-type DER units can also operate in three modes: constant P, constant V, or droop. Figure 3.1 shows these six different DER models. Each ac-type DER unit is associated with four quantities: the magnitude of the ac terminal voltage, $|V_{ac}|$; the phase angle, δ; the active power output, P_{DR}; and the reactive power output, Q_{DR}. In contrast, each dc-type DER unit is related to only two quantities: the dc terminal voltage, V_{dc}, and the active power output, P_{DR}.

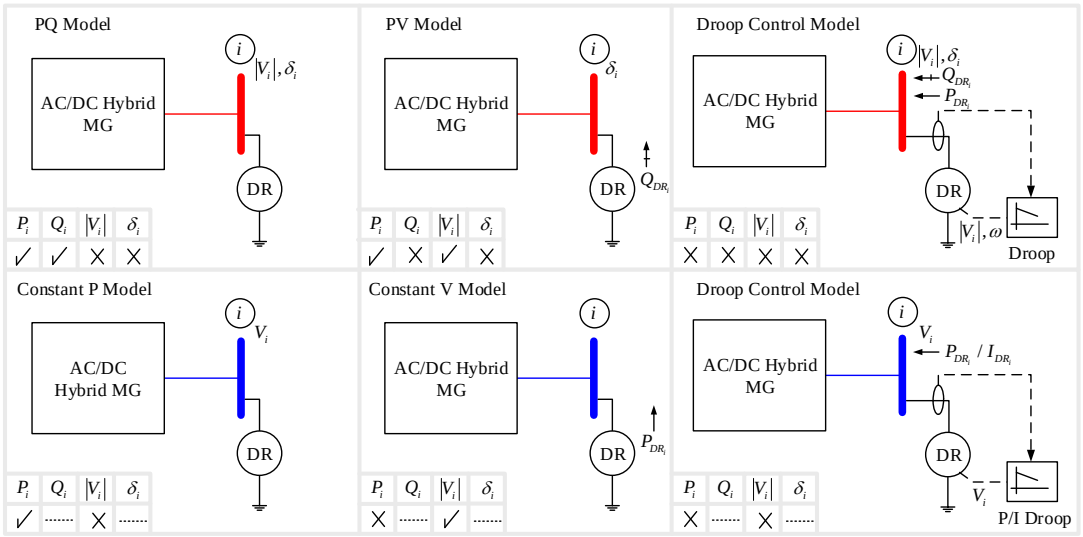

Figure 3.1. Different distributed energy resource models.

The concepts underlying the constant PQ and PV control of ac-type DERs are identical to those that apply to conventional high-voltage power systems. However, in low- and medium-voltage microgrids during islanding conditions, converter-based distributed generation (DG) and distributed storage (DS) units can be controlled autonomously according to droop characteristics [21].

3.2.4 Interlinking Converter Model

In an HMG, the IC functions as an energy buffer for controlling the transfer of active power between neighbouring ac and dc subgrids in order to achieve a specific objective, such as 1) equal sharing of the HMG demand among the DERs according to their ratings or 2) equal loading of the subgrids so that no individual subgrid is overloaded while another is underloaded, while minimizing power transfer based on the loading conditions of both subgrids [15]. An accurate IC model and effective control strategy are therefore critically important when an HMG is islanded. For this reason, three IC control schemes have been incorporated into the UPF algorithm presented in this chapter.

3.2.4.1 Control Strategy I

An ac/dc IC droop control strategy can be achieved based on local measurements of the frequency at the ac terminal and on a determination of the voltage at the dc terminal. This control strategy was discussed in detail in section 2.4. The active power droop characteristics of an IC is illustrated in Figure 3.2. The active power transferred from the dc side to the ac side is based on the droop equation in (2.9) presented in chapter 2. It is

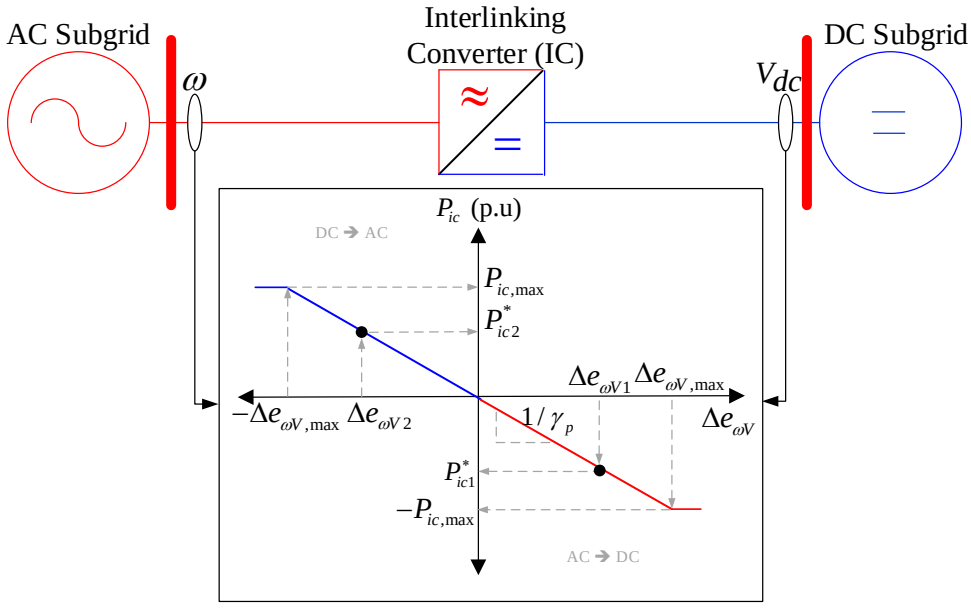

Figure 3.2. AC/DC droop for the interlinking converter.

worth noting that this control scheme is an autonomous control strategy since it requires only local measurements of the frequency and the dc terminal voltage. On the other hand, this strategy does require the continuous operation of the IC, which might be undesirable, owing to associated conversion losses and power oscillations.

3.2.4.2 Control Strategy II

To rectify the shortcomings associated with the previous control strategy and to maintain autonomous operation, we have introduced a dead zone, i.e., a no-power-transfer zone, as shown in Figure 3.3. The dead zone is represented by the portion of the x-axis defined by the interval $[-\Delta e_{\omega V,min}, \Delta e_{\omega V,min}]$. If the error is within the closed interval, then there is

no power transfer permitted: $P_{ic} = 0$. The power transfers corresponding to error values beyond the closed interval does not comply with (2.9). The reason is attributed to the fact that in Figure 3.2 the droop line passes the origin point, while in Figure 3.3 the droop line is shifted from the origin and split into two droop line segments. One droop line, the red line in Figure 3.3, is described by the line $P_{ic} = -\frac{1}{\gamma_p}(\Delta e_{\omega V} + \Delta e_{\omega V,min})$, while the other droop line, the blue line in Figure 3.3, is defined by the line $P_{ic} = -\frac{1}{\gamma_p}(\Delta e_{\omega V} - \Delta e_{\omega V,min})$. Also, the maximum error is shifted by $\Delta e_{\omega V,min}$, i.e., $\Delta \grave{e}_{\omega V,max} = (\Delta e_{\omega V,min} + \Delta e_{\omega V,max})$. Thus, according to Figure 3.3, the control strategy II is described by (3.3) instead of (2.9). Power transfer is permitted only when one subgrid is markedly overloaded while the other is underloaded. This condition can be determined by monitoring the difference between the normalized frequency and the normalized dc terminal voltage, $\Delta e_{\omega V}$, and by allowing power to be transferred between two subgrids only when the difference exceeds a specified threshold: i.e., $|\Delta e_{\omega V}| > \Delta e_{\omega V,min}$. With this procedure, the IC ensures equal loading of the two interconnected ac/dc subgrids and the efficient utilization of the local resources, while at the same time minimizing IC operating time.

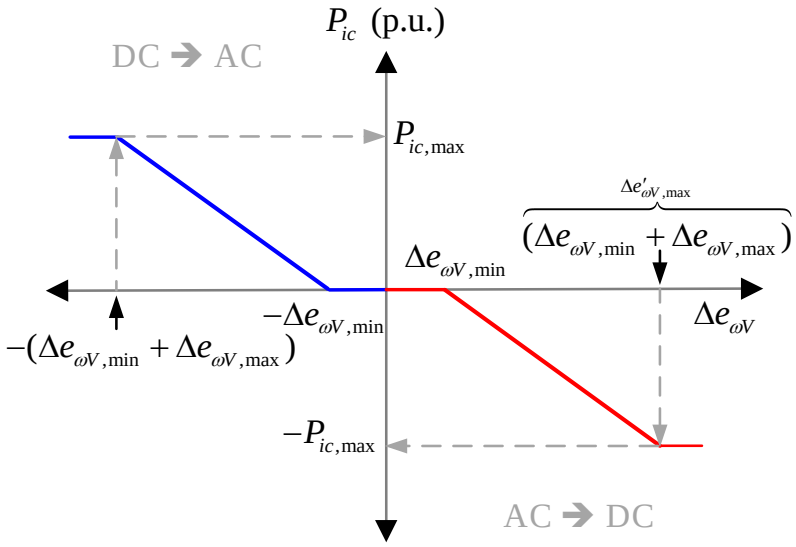

Figure 3.3. Resultant ac/dc droop with a no-power-transfer zone.

$$P_{ic} = \begin{cases} P_{ic,max}, & \text{if} \quad \Delta e_{\omega V} < -\Delta \grave{e}_{\omega V,max}, \\ -\frac{1}{\gamma_P}(\Delta e_{\omega V} + \Delta e_{\omega V,min}), & \text{if} \quad -\Delta \grave{e}_{\omega V,max} \leq \Delta e_{\omega V} < -\Delta e_{\omega V,min}, \\ -\frac{1}{\gamma_P}(\Delta e_{\omega V} - \Delta e_{\omega V,min}), & \text{if} \quad \Delta e_{\omega V,min} < \Delta e_{\omega V} \leq \Delta \grave{e}_{\omega V,max}, \\ -P_{ic,max}, & \text{if} \quad \Delta e_{\omega V} > \Delta \grave{e}_{\omega V,max}, \\ 0 & \text{otherwise.} \end{cases} \tag{3.3}$$

3.2.4.3 Control Strategy III

The ac and dc droop can be utilized as a means of arriving at an aggregated ac/dc droop control scheme [90]. The aggregated ac droop line can be obtained by summing all of the DER ($\omega - P$) droop lines in the ac subgrid, while the equivalent dc droop line is derived from the sum of all of the DER ($V - P$) droop lines in the dc subgrid. The slopes of the aggregated ac and dc droop lines, $m_{p,ac/dc}$, are acquired from (3.4):

$$m_{p,ac/dc} = \frac{\prod_{i=1}^{n_D^{ac/dc}} m_{p,i}}{\sum_{i=1}^{n_D^{ac/dc}} \prod_{\substack{j=1 \\ j \neq i}}^{n_D^{ac/dc}} m_{p,j}}. \tag{3.4}$$

where $n_D^{ac/dc}$: the total number of ac- and dc-type droop-controlled DERs.

The aggregated droop characteristics are obtained based on the assumption that the voltage drops across the dc feeders are very small. Additionally, the resulting ac and dc droop lines can be interpreted as representing all of the droop-controlled DERs in one subgrid based on an equivalent droop-controlled DER. In a practical sense, the capacity of this equivalent DER is the available generation, and its loading can be locally established from measurements of the frequency/dc voltage at the IC terminal. More specifically, if the frequency and/or IC terminal dc voltage are below specified thresholds, $\widehat{\omega}_{min}$ or $\widehat{V}_{dc,min}$, respectively, the corresponding subgrid is detected as overloaded and is hence directed to

request active power from its neighbouring subgrid according to (3.5) or (3.6):

$$\widehat{P}_{ic,ac} = \begin{cases} \widehat{P}_{ac,max} & ,\text{if} \quad \widehat{\omega} < \widehat{\omega}_{min}, \\ \frac{\widehat{\omega}_{min}-\widehat{\omega}}{m_{p,ac}} & ,\text{if} \quad \widehat{\omega}_{min} \leq \widehat{\omega} \leq \widehat{\omega}_{max}, \\ 0 & ,\text{if} \quad \widehat{\omega} > \widehat{\omega}_{max}. \end{cases} \tag{3.5}$$

$$\widehat{P}_{ic,dc} = \begin{cases} \widehat{P}_{dc,max} & ,\text{if} \quad \widehat{V}_{dc} < \widehat{V}_{dc,min}, \\ \frac{\widehat{V}_{dc,min}-\widehat{V}_{dc}}{m_{p,dc}} & ,\text{if} \quad \widehat{V}_{dc,min} \leq \widehat{V}_{dc} \leq \widehat{V}_{dc,max}, \\ 0 & ,\text{if} \quad \widehat{V}_{dc} > \widehat{V}_{dc,max}. \end{cases} \tag{3.6}$$

where
$(\widehat{\bullet})$: the normalized quantity $(\bullet)$ in the range of [0, 1];
$\widehat{P}_{ic}^{ac}, \widehat{P}_{ic}^{dc}$: the power requested from the ac and dc subgrids, respectively, normalized in the range of [0, 1] based on their respective maximum available capacities, $P_{ac,max}, P_{dc,max}$.
Based on the normalized active power requests, the IC determines the actual power transfer, P_{ic}, as expressed by (3.7) and (3.8):

$$\widehat{P}_{ic} = \widehat{P}_{ic,ac} - \widehat{P}_{ic,dc}. \tag{3.7}$$

$$P_{ic} = \begin{cases} \widehat{P}_{ic,ac} \times P_{ac,max} & ,\text{if} \quad \widehat{P}_{ic} > 0, \\ \widehat{P}_{ic,dc} \times P_{dc,max} & ,\text{if} \quad \widehat{P}_{ic} < 0. \end{cases} \tag{3.8}$$

Equations (3.5)-(3.8) permit power transfer when one subgrid is overloaded and the other is underloaded or when both subgrids are not heavily overloaded. The direction of the power transfer is dependent on the $\widehat{P}_{ic}$ sign. If $\widehat{P}_{ic} > 0$, the power is transmitted from the dc side to the ac side, and vice versa if $\widehat{P}_{ic} < 0$. With control strategy III, autonomous IC droop control is guaranteed only if the DERs are assumed to have static droop control and a fit-and-forget design. Thus, for HMGs with adaptive droop control and a plug-and-play feature, this control strategy requires that all droop-controlled ac- and dc-type DERs regularly broadcast their active power droop gains and availability. An additional restriction is that if any or both subgrids are not droop-controlled, this control strategy cannot be implemented. It should be noted, however, that our UPF formulation can easily accommodate any other DER models and IC control strategies.

3.3 Formulation of the Power Flow Problem

The power flow problem for isolated HMGs is defined by a set of nonlinear equations and can be formulated as an unconstrained minimization problem [86], as shown in the vector

notation indicated in (3.9)-(3.10) and the defining equations (3.11)-(3.12):

$$\underset{x\in\mathbb{R}^n}{\text{minimize}} \quad f(x), \quad f:\mathbb{R}^n\to\mathbb{R}^n. \tag{3.9}$$

where

$$f(x)=[f_{ac}(x_{ac}),f_{dc}(x_{dc})]^T, \quad x=[x_{ac},x_{dc}]^T. \tag{3.10}$$

$f(x)$: the vector of the equations describing the power flow problems in the ac and dc subgrids;
x: the vector of the ac/dc control (independent) and state (dependent) variables.

$$f(x^{(k)})=-\mathbf{J}(x^{(k)})\Delta x^{(k)}. \tag{3.11}$$

where $\mathbf{J}(x^{(k)})$ is the Jacobian matrix at iteration k, as defined by: where $\mathbf{J}_{ac}^{(k)}$ and $\mathbf{J}_{dc}^{(k)}$ are the Jacobian matrices for the ac and dc subgrids, respectively, as defined by:

$$\mathbf{J}_{ac}^{(k)}=\left.\frac{\partial f_{ac}}{\partial x_{ac}}\right|_{x_{ac}^{(k)}}, \quad \mathbf{J}_{dc}^{(k)}=\left.\frac{\partial f_{dc}}{\partial x_{dc}}\right|_{x_{dc}^{(k)}}. \tag{3.12}$$

The detailed ac/dc power flow subproblem formulations and variable definitions are provided in the following subsections.

3.3.1 AC Subgrids

The set of ac buses can be classified as PQ buses, $\mathcal{B}_{PQ}=\{1,2,\ldots,n_{PQ}\}$; PV buses, $\mathcal{B}_{PV}=\{1,2,\ldots,n_{PV}\}$; and droop-controlled buses, $\mathcal{B}_D^{ac}=\{1,2,\ldots,n_D^{ac}\}$.

3.3.1.1 PQ Buses

Each PQ bus $i\in\mathcal{B}_{PQ}$ involves two unknown quantities: the bus voltage magnitude $|V_{ac,i}|$ and the phase angle δ_i. The vector of the unknown quantities for each PQ bus can be expressed as (3.13):

$$x_{PQi}=[\delta_i,|V_{ac,i}|]^T. \tag{3.13}$$

Accordingly, the vector of all unknown quantities associated with all PQ buses can be defined by (3.14).

$$x_{PQ}=[x_{PQ1},x_{PQ2},\ldots,x_{PQn_{PQ}}]^T. \tag{3.14}$$

It should be noted that constant I and constant Z buses can be treated in a similar manner.

3.3.1.2 PV Buses

Each PV bus $i \in \mathcal{B}_{PV}$ involves two unknown quantities, δ_i, Q_i and Q_i, and the vector of unknown quantities for each PV bus can be expressed as (3.15):

$$x_{PVi} = [\delta_i, Q_i]^T. \tag{3.15}$$

Accordingly, the vector of all unknown quantities associated with all PV buses can be defined by (3.16).

$$x_{PV} = [x_{PV1}, x_{PV2}, \ldots, x_{PVn_{PV}}]^T. \tag{3.16}$$

It should be mentioned that if the reactive power output of any voltage-regulated DER, $Q_{DR,i}, \forall i \in \mathcal{B}_{PV}$, violates its specified limit, it is then set to the corresponding limit and the PV bus is switched to PQ mode.

3.3.1.3 AC Droop-Controlled Buses

Each ac droop-controlled bus[1], $i \in \mathcal{B}_D^{ac}$, is associated with four unknown quantities: $\delta_i, |V_{ac,i}|, P_i$, and Q_i. The vector describing these quantities can be expressed as (3.17):

$$x_{Di}^{ac} = [\delta_i, |V_{ac,i}|, P_i, Q_i]^T. \tag{3.17}$$

The vector of all unknown quantities associated with all ac droop-controlled buses can then be defined by (3.18):

$$x_D^{ac} = [x_{D1}^{ac}, x_{D2}^{ac}, \ldots, x_{Dn_D^{ac}}^{ac}]^T. \tag{3.18}$$

It is worth pointing out that if either the active or reactive power output of any droop-controlled DER $(P_{DR,i}, Q_{DR,i})$ exceeds its limit, it is then set to the corresponding limit. However, if both the active and the reactive power output exceed specified limits, they are set to their corresponding limits and the DER switches from droop control mode to PQ control mode. Another point worthy of note is that imposing the DER limits would make the power flow problem indirectly constrained.

[1] In isolated microgrids, some DERs may operate in a droop control mode in order to mimic synchronous generators and to provide virtual inertia as a means of stabilizing the system. AC/DC terminal buses can also be droop controlled.

The ac subgrid(s) variables can be written in a compact form as in (3.19):

$$x_{ac} = [\omega, x_{PQ}, x_{PV}, x_D^{ac}]^T. \tag{3.19}$$

It should be noted that since the frequency is a variable, the voltage phase angle of an ac bus, e.g., typically a DER bus, is taken as a reference, $\delta_i = 0, i \in \mathcal{B}_{ac}$, in order to equalize the number of unknowns and the number of equations available.

The ac power flow equations for a general ac bus $i, \forall i \in \mathcal{B}_{ac}$ are defined by equations (3.20) and (3.21).

$$P_i = |V_{ac,i}| \sum_{k=1}^{n_{ac}} |V_{ac,k}||Y_{ik}(\omega)| cos(\delta_i - \delta_k - \theta_{ik}) + \beta_i P_{ic,i}, \quad \forall i \in \mathcal{B}_{ac}. \tag{3.20}$$

$$Q_i = |V_{ac,i}| \sum_{k=1}^{n_{ac}} |V_{ac,k}||Y_{ik}(\omega)| sin(\delta_i - \delta_k - \theta_{ik}) + \beta_i Q_{ic,i}, \quad \forall i \in \mathcal{B}_{ac}. \tag{3.21}$$

where

$$\beta_i = \begin{cases} 1, & \text{if bus } i \text{ is an ac terminal bus,} \\ 0, & \text{otherwise.} \end{cases}$$

$|Y_{ik}(\omega)|, \theta_{ik}$: the magnitude and phase angle of the ik^{th} entry in the bus admittance matrix $[Y_{bus}(\omega)]$, respectively.

The set of equations describing a general ac bus $i \in \mathcal{B}_{ac}$ can generally be defined by (3.22):

$$f_{ac,i} = \begin{cases} P_{DR,i} - P_{D,i} - P_i, & i \in \mathcal{B}_{ac}, \\ Q_{DR,i} - Q_{D,i} - Q_i, & i \in \mathcal{B}_{ac}, \\ P_{DR,i} - \frac{1}{m_{ac,p,i}}(\omega_{i,0} - \omega), & i \in \mathcal{B}_D^{ac}, \\ Q_{DR,i} - \frac{1}{n_{q,i}}(|V_{ac,0,i}| - |V_{ac,i}|), & i \in \mathcal{B}_D^{ac}. \end{cases} \tag{3.22}$$

where
$|V_{ac,0,i}|$: the nominal (no-load) voltage of the DER i;
$m_{ac,p,i}, n_{q,i}$: the active and reactive power droop gains of the DER i, respectively.

3.3.2 DC Subgrids

The set of dc buses can be classified as constant P buses, $\mathcal{B}_P = \{1, 2, \ldots, n_P\}$; constant V buses, $\mathcal{B}_V = \{1, 2, \ldots, n_V\}$; and droop-controlled buses, $\mathcal{B}_D^{dc} = \{1, 2, \ldots, n_D^{dc}\}$.

3.3.2.1 Constant P Buses

Each constant P bus involves one unknown quantity, $V_{dc,i}$, which can be expressed as (3.23):

$$x_{Pi} = V_{dc,i}. \tag{3.23}$$

Accordingly, the vector of all unknown quantities associated with all constant P buses is defined by (3.24):

$$x_P = [x_{P1}, x_{P2}, \ldots, x_{Pn_P}]^T. \tag{3.24}$$

3.3.2.2 Constant V Buses

Each constant V bus $i \in \mathcal{B}_V$ involves one unknown quantity, P_i, which can be expressed as (3.25):

$$x_{Vi} = P_i. \tag{3.25}$$

The vector of all unknown quantities associated with all constant V buses can then be defined by (3.26):

$$x_V = [x_{V1}, x_{V2}, \ldots, x_{Vn_V}]^T. \tag{3.26}$$

It should be mentioned that if the active power output of any voltage-regulated dc-type DER, $P_{DR,i}, \forall i \in \mathcal{B}_V$, violates its specified limit, it is then set to the corresponding limit and the DER is switched from voltage control mode to constant P mode.

3.3.2.3 DC Droop-Controlled Buses

Each dc drooped-control bus, $i \in \mathcal{B}_D^{dc}$, is associated with two unknown quantities, V_i and P_i. The vector describing theses quantities can be defined by (3.27):

$$x_{Di}^{dc} = [V_{dc,i}, P_i]^T. \tag{3.27}$$

The vector of all unknown quantities associated with all dc drooped-controlled buses can then be expressed as (3.28):

$$x_D^{dc} = [x_{D1}^{dc}, x_{D2}^{dc}, \ldots, x_{Dn_D^{dc}}^{dc}]^T. \tag{3.28}$$

It is worth pointing out that some dc-type DERs can be (V-I) droop-controlled rather than (V-P). It should also be noted that if the output power/current of any dc-type droop-controlled DER exceeds its specified limit, it is set to the corresponding limit, and the control strategy becomes constant P or I control.

The dc subgrid(s) variables can be written in compact form as in (3.29):

$$x_{dc} = [x_P, x_V, x_D^{dc}]^T. \tag{3.29}$$

The dc power flow equation for a general dc bus $i, \forall i \in \mathcal{B}_{dc}$, is defined by (3.30):

$$P_i = V_{dc,i} \sum_{k=1}^{n_{dc}} G_{ik} V_{dc,k} - \beta_i P_{ic,i}, \quad \forall i \in \mathcal{B}_{dc}. \tag{3.30}$$

where

$$\beta_i = \begin{cases} 1, & \text{if bus } i \text{ is a dc terminal bus,} \\ 0, & \text{otherwise.} \end{cases}$$

G_{ik}: the ik^{th} entry of the bus conductance matrix $[G_{bus}]$ of the dc subgrid;
$P_{ic,i}$: the actual power transferred through the IC.

The set of equations that describes a general dc bus $i \in \mathcal{B}_{dc}$ is defined by (3.31):

$$f_{dc,i} = \begin{cases} P_{DR,i} - P_{D,i} - P_i, & i \in \mathcal{B}_{dc}, \\ P_{DR,i} - \frac{1}{m_{dc,pi}}(V_{dc,0,i} - V_{dc,i}), & i \in \mathcal{B}_D^{dc}. \end{cases} \tag{3.31}$$

Table 3.1 summarizes the power flow problem for islanded HMGs. The power flow problem is highly nonlinear and is hence solved using a globally convergent iterative method: a Newton TR method [85] and [86].

3.4 Trust-Region Method

In a general TR method, the objective function $f(x)$ is approximated by a model m_k in the neighbourhood of the current iterate x_k, referred to as the trust region, or TR. The TR is defined by an n-dimensional sphere with a radius Δ_k around the current iterate [85]. Once the model m_k and its TR have been defined, the current solution point x_k is updated by taking a step s_k within the TR: i.e., $\|s_k\| \leq \Delta_k$. This step is obtained at each iteration k

Table 3.1
Summary of the HMG Power Flow Problem

Subgrid	Bus Type	Number of Buses	Specified Quantities	Unspecified Quantities	Number of Equations
AC	PQ: $i \in \mathcal{B}_{PQ}$	n_{PQ}	P_i, Q_i	$\delta_i, \lvert V_{ac,i}\rvert$	$2n_{PQ}$
	PV: $i \in \mathcal{B}_{PV}$	n_{PV}	$P_i, \lvert V_{ac,i}\rvert$	δ_i, Q_i	$2n_{PV}$
	(V-P) Droop: $i \in \mathcal{B}_D^{ac}$	n_D^{ac}	—	$\delta_i, \lvert V_{ac,i}\rvert, P_i, Q_i$	$4n_D^{ac}$
DC	Const. P: $i \in \mathcal{B}_P$	n_P	P_i	$V_{dc,i}$	n_P
	Const. V: $i \in \mathcal{B}_V$	n_V	$V_{dc,i}$	P_i	n_V
	(V-P) Droop: $i \in \mathcal{B}_D^{dc}$	n_D^{dc}	—	$V_{dc,i}, P_i$	$2n_D^{dc}$
Total	AC	n_{ac}	$2(n_{ac} - n_D^{ac})$	$2(n_{ac} + n_D^{ac})$	$2(n_{ac} + n_D^{ac})$
	DC	n_{dc}	$(n_{dc} - n_D^{dc})$	$(n_{dc} + n_D^{dc})$	$(n_{dc} + n_D^{dc})$

by solving the subproblem described in (3.32) and (3.33), which minimizes the quadratic model m_k obtained from the second-order Taylor series expansion [86]:

$$\underset{s_k \in \mathbb{R}^n}{\text{minimize}} \quad m_k(s_k) = f(x_k) + s_k^T \nabla f(x_k) + \frac{1}{2} s_k^T B_k s_k. \tag{3.32}$$

$$\text{s.t} \quad \|s_k\| \leq \Delta_k. \tag{3.33}$$

where: B_k: an approximation of the Hessian matrix $\nabla^2 f(x_k)$.

The objective function and its approximate model are evaluated at the updated solution point $x_k + s_k$. The determination of whether the trial step s_k is trusted is based on the ratio of the actual reduction to the predicted reduction, as in (3.34):

$$\rho_k = \frac{f(x_k) - f(x_k + s_k)}{m_k(s_k) - m_k(x_k + s_k)}. \tag{3.34}$$

If the step is successful, it is then accepted (i.e., $x_{k+1} = x_k + s_k$ and the TR is expanded: i.e., $\Delta_{k+1} = \gamma_i \Delta_k$, where $\gamma_i \geq 1$, if $\rho_k \geq \eta_v$, (in the case of a very successful step), or it is kept the same if $\eta_s \leq \rho_k \leq \eta_v$ (in the case of a successful step). If $\rho_k \leq \eta_s$, the step is rejected, and the TR is shrunk: i.e., $\Delta_{k+} = \gamma_d \Delta_k$, where $\gamma_d \leq 1$ (in the case of an unsuccessful step). The process of taking steps and updating the TR is repeated until the convergence criterion, i.e., $\|f(x_k)\|_\infty \leq \epsilon$, is satisfied.

The iterative power flow solution procedure can be best summarized as follows:

Step 1) Start the UPF program for islanded HMGs.

Step 2) Read the line and bus data for ac and dc subgrids.

Step 3) Decide on the models of system components and the control strategy of the IC.

Step 4) Assume a flat start for the ac frequency and ac/dc bus voltages. $\omega^{(0)} = 1.0$ p.u, $|V_{ac}^{(0)}|\angle\delta^{(0)} = 1.0\angle 0^{\circ}$ p.u, $V_{dc}^{(0)} = 1.0$ p.u.

Step 5) Set the iteration counter to zero, $k = 0$.

Step 6) Build the bus admittance matrix of the ac subgrid, $[Y_{bus}(\omega^{(k)}]$, at the frequency $\omega^{(k)}$ and the bus conductance matrix of the dc subgrid, $[G_{bus}]$.

Step 7) Formulate the power flow subproblem for both subgrids., $f(x^{(k)}) = [f(x_{ac}^{(k)}), f(x_{dc}^{(k)})]^T$, where $x^{(k)} = [x_{ac}^{(k)}, x_{dc}^{(k)}]^T$.

Step 8) Build the Jacobian matrices for both subgrids, $\mathbf{J}_{ac}^{(k)}$ and $\mathbf{J}_{dc}^{(k)}$.

Step 9) Call the Newton Trust region solver to solve the power flow subproblems simultaneously.

Step 10) Check for convergence, $\|f(x_{ac}^{(k)}\| \wedge \|f(x_{dc}^{(k)}\| \leq \epsilon$, where ϵ is a prespecified threshold.

Step 11) If the convergence criterion is not met, update the iteration counter $k = k + 1$, then repeat steps (6-10) to update the ac subsystem admittance matrix, the Jacobian matrices, and solve for the power flow variables. Otherwise, go to next step.

Step 12) Calculate the ac/dc line power flows and losses.

Step 13) Print out the ac/dc power flow solution, $\omega^*, |V_{ac}^*|\angle\delta^*, V_{dc}^*, P_{ic}^*, Q_{ic}^*$, etc.

Step 14) End the UPF program.

The flow chart of the UPF algorithm is depicted in Figure 3.4.

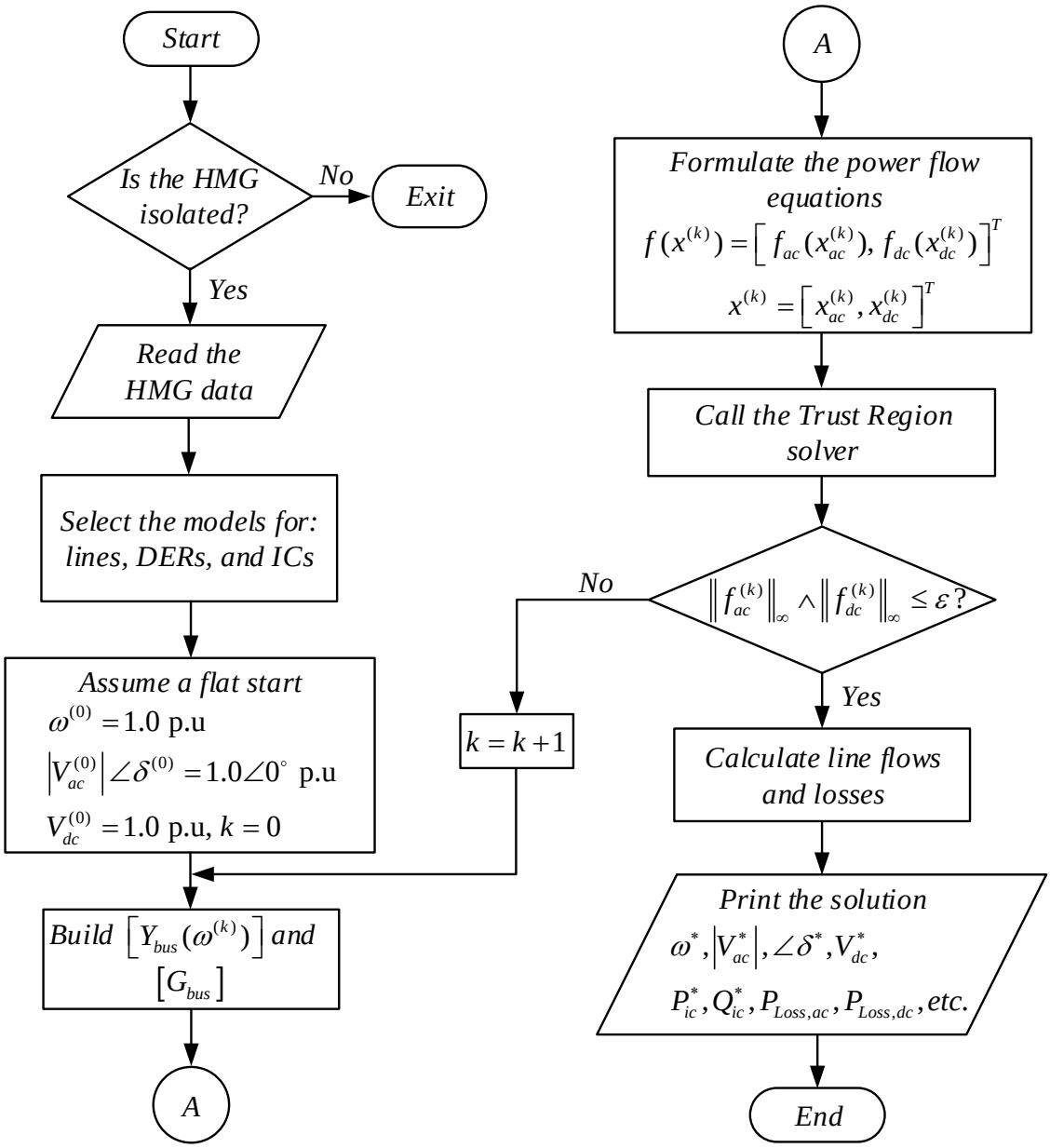

Figure 3.4. Flow chart of the HMG power flow algorithm.

3.5 Design of the AC/DC Hybrid Test Systems

The practical design of a droop-controlled HMG should include but is not limited to the following steps, as demonstrated on a low-voltage 6-bus HMG:

3.5.1 AC and DC Load Data Collection

The load data include the load type, location, nominal power, and distance from the source. The ac load is assumed to be rated at 208 V and 25 kW, operating at a 0.8 lagging power factor (p.f) and located at a distance of 100 m from the ac sources. The dc load is assumed to have a nominal power of 15 kW and is located 100 m and 50 m from the dc sources. Both loads have an efficiency rating of 90%.

3.5.2 AC and DC Voltage Level Selection

Based on the rated ac load voltage and ANSI C84.1 standard [91], the voltage level for a 60 Hz four-wire three-phase ac grid was selected as 208Y/120 V. Once the ac voltage has been selected, the voltage level of a two-wire dc system can be determined based on the criteria described in [92]: $V_{dc} \geq 2\sqrt{2}V_{ac(rms)}$. The resulting dc voltage is 600 V.

3.5.3 AC and DC Subgrid Ratings

3.5.3.1 AC and DC DER Ratings

The ratings of the ac and dc sources are dependent on the ac and dc loads to be supplied according to the design. It is common practice to follow a rule of thumb for sizing generators [93]. However, despite the practical rule of thumb, it should be noted that the design should also include consideration of any data available from the manufacturer. The ac supply is comprised of an inverter-based dispatchable DG, wind-based DG, and a DS. The sum of their ratings is taken as 120% of the ac load to be supplied, i.e., $S_{ac}^{rated} = 37.5$ kVA. The dispatchable DG unit has a rated capacity of 8 kVA at a 0.8 p.f. The wind turbine (WT) generates 14 kW and 10.5 kvar [94], while the DS has a rated capacity of 250 Ah and a nominal dc voltage of 48 V [95]. The corresponding DS rated power is 9.6 kWh (12 kVAh at a 0.8 p.f). The dc supply involves a converter-based dispatchable DG, a

photovoltaic (PV) system, and two DS units. The sum of their ratings is taken as approximately 120% of the dc load, i.e., $P_{dc}^{rated} \approx 18$ kW. The dispatchable DG unit has a rated capacity of 6.72 kW. The PV system is composed of 20 panels of 230 W each (4.6 kW in total). The two DS units are rated 140 Ah at a nominal voltage of 24 V each (3.36 $\times$ 2 kWh).

3.5.3.2 AC and DC DER Droop Gain Settings

The operating modes of all DERs should be identified, and the droop parameters of the droop-controlled DERs should be selected appropriately. The DSs in both subgrids of the 6-bus HMG are droop-controlled, and their static droop gains can be determined as described in section 2.3. In low-voltage networks, it is desirable for the ac frequency and voltage to be within $\pm 1\%$ and $\pm 5\%$, respectively, in order to avoid any dis-synchronization among the DERs during islanded operation [96]. The active droop gains for the ac-type dispatchable DG and DS are therefore 0.09375 and 0.0625 Hz/kW, respectively, whereas, their reactive droop gains are 2.1667 and 1.4444 V/kvar, respectively. Taking the dc voltage range as $\pm 5\%$ of the rated dc voltage, the active power droop gain of the dc-type dispatchable DG and DS can be similarly established: i.e., 4.4643 V/kW each.

3.5.4 AC and DC Cable Selection

Both the physical construction and the electrical specifications of the cables must be designed appropriately:

3.5.4.1 Cable Impedance Calculation

Based on the cable specifications, i.e., size, number of cores, insulation type, shape, and, current-carrying capacity, the resistances and reactances of the ac and dc cable can be selected according to the IEC 60364-5-52 standard [97]. The resistances and reactances of the ac cables are $R_{ac,12} = R_{ac,23} = 0.638$ and $X_{ac,12} = X_{ac,23} = 0.0786$ Ω/km, respectively. The resistance of the dc cables are $R_{dc,12} = R_{dc,23} = 4.7$ Ω/km, respectively.

3.5.4.2 Voltage Drop Calculation

The voltage drops across the ac and dc feeders can be calculated based on the full-load currents I_{ac} and I_{dc}, the load power factor $cos(\phi)$, and the cable lengths $L_{cable,ac}, L_{cable,dc}$ (km), (3.35) and (3.36) [98]:

$$\Delta V_{F,ac} = \sqrt{3} I_{ac}(R_{ac} cos(\phi) + X_{ac} sin(\phi)) \times L_{cable,ac}. \quad (3.35)$$

$$\Delta V_{F,dc} = 2 I_{dc} R_{dc} \times L_{cable,dc}. \quad (3.36)$$

The voltage drops over the ac and dc feeders as percentages of the rated ac/dc voltages are $\Delta V_{F,ac}(\%) = 4.47\%, \Delta V_{F,dc}(\%) = 4.35\%$, respectively, which meet the maximum voltage drop criterion of 5% for a voltage drop across a cable. Once the voltage drops are obtained across each component, i.e., generator, transformer, and feeder, the system voltage drop ΔV_{SYS} from the generator to the load should be within the maximum permissible voltage drop in order to ensure a practical and feasible design.

3.5.5 Interlinking Converter Rating and Control

The IC power rating can be selected based on the minimum of power ratings of both subgrids, i.e., $S_{ic}^{rated} = min\{S_{ac}^{rated}, P_{dc}^{rated}\}$, which means that the IC rated apparent power is $S_{ic}^{rated} = 18$ kW. The IC control strategy can be implemented differently, depending on the control objective and the availability of appropriate communications.

The author wishes to emphasize that these design steps should be used only as a guideline, and caution should be exercised with respect to HMG design, especially for islanded conditions. The one-line diagram of the resulting 6-bus HMG is shown in Figure 3.5. The microgrid data is furnished in appendix A.1.

3.6 Test Results and Discussions

The UPF algorithm that was developed for use with isolated HMGs was implemented in a MATLAB® computing environment and executed on an LG® desktop computer with an Intel (R) Core (TM)® i5-3470 CPU @ 3.20 GHz with 8.0 GB of RAM memory. The phasor UPF formulation has been verified against the time-domain steady state response. Several case studies were carried out with the goal of demonstrating the application and robustness of the developed UPF algorithm.

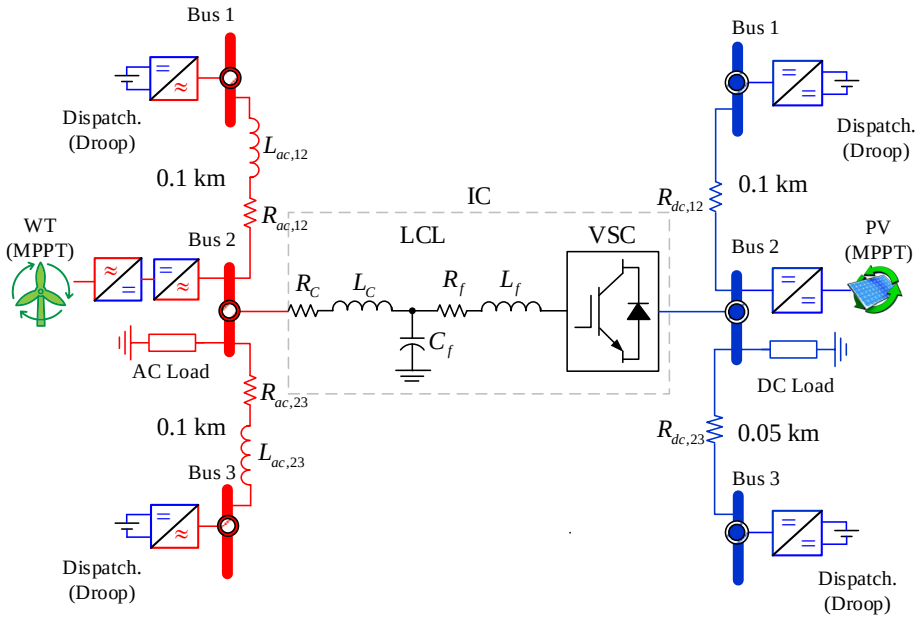

Figure 3.5. 6-bus ac/dc hybrid microgrid.

3.6.1 Algorithm Validation

The islanded 6-bus HMG whose design was explained in Section 3.5 was used for validating the algorithm against the time-domain simulation (TDS). For validation purposes, the two DS units were replaced by two converter-based DG units with the same ratings and droop characteristics as the DS units. The IC is placed between ac bus 2 and dc bus 2, as depicted in Figure 3.5. The rated capacity of the IC, in kW, was taken as the kVA base of the system: $S_{base} = 18$ kVA. The base ac and dc voltages were selected as 208 V and 600 V, respectively. The power flow results produced by the UPF algorithm and those obtained from the TDS were tabulated as shown in Table 3.2. Both our algorithm and the TDS reached steady state at a frequency equal to 0.9926 p.u. As a measure of the level of accuracy, the maximum deviations between the TDS and UPF results were calculated for the bus voltage magnitudes, active power outputs, and reactive power outputs, which were found to be 0.042%, 0.13% and 0.18%, respectively. These results are reliable indicators of the accuracy of the solutions provided by the UPF algorithm for the power flow problem in islanded droop-controlled HMGs.

Table 3.2
Algorithm Validation against Time Domain Simulation

MG	**Bus**	**TDS Results**		**UPF Results**	
	#	$\lvert V_{ac}\rvert$ (p.u.)	V_{dc} (p.u.)	$\lvert V_{ac}\rvert$ (p.u.)	V_{dc} (p.u.)
AC/DC	1	0.9642	0.9659	0.9645	0.9662
	2	0.9627	0.9598	0.9630	0.9601
	3	0.9649	0.9631	0.9653	0.9634
DER	**DER** #	P_{DR} (p.u.)	Q_{DR} (p.u.)	P_{DR} (p.u.)	Q_{DR} (p.u.)
AC	1	0.2625	0.1889	0.2628	0.1893
	2	0.7778	0.5833	0.7778	0.5833
	3	0.3937	0.2775	0.3942	0.2780
DC	1	0.2517	—	0.2522	—
	2	0.2556	—	0.2556	—
	3	0.2727	—	0.2731	—
IC	**IC** #	$\widehat{\omega}$ (p.u.)	$\widehat{V}_{dc}$ (p.u.)	$\Delta e_{\omega V}$ (p.u.)	P_{ic} (p.u.)
	1	−0.0144	−0.0694	0.0550	−0.0550

3.6.2 Algorithm Application

The application of the UPF algorithm for HMG operation was also investigated based on consideration of two test systems. The first is the 6-bus HMG, which was employed as a means of examining the problem of power sharing in droop-controlled HMGs. Two metrics are used to evaluate the power sharing of the droop-controlled DERs and the ICs. These are the active and reactive power sharing indices[2], PSI_p and PSI_q. The second test system is a 12-bus HMG. This test system was used for further testing of the UPF algorithm and the demonstration of the easy incorporation of different DER operating modes and IC control strategies.

[2]The power sharing index (PSI) is the ratio of the droop-controlled DER or the IC active/reactive power output to its corresponding rating.

Table 3.3
The Power Flow Solution for the Islanded 6-Bus AC/DC Hybrid Microgrid: (S_{base} = 18 kVA, $\omega = 0.9923$ p.u.)

MG	Bus #	Bus Type	DER Type	$\|V\|$ (p.u.)	δ (rad.)	P_D (p.u)	Q_D (p.u.)	P_{DR} (p.u.)	Q_{DR} (p.u.)	PSI_p (%)	PSI_q (%)
AC	1	D	DG	0.9645	+0.0000	—	—	0.2752	0.1895	77.40	71.07
	2	PQ	–	0.9631	−0.0001	1.3781	1.0497	0.7778	0.5833	—	—
	3	D	DS	0.9653	+0.0002	—	—	0.4128	0.2779	77.40	69.49
DC	1	D	DS	0.9648	—	—	—	0.2630	—	70.46	—
	2	P	—	0.9505	—	0.8333	—	0.2556	—	—	—
	3	D	DG	0.9681	—	—	—	0.2378	—	63.71	—
						$\sum P_D$	$\sum Q_D$	$\sum P_{DR}$	$\sum Q_{DR}$	P_{Loss}	Q_{Loss}
						2.2114	1.0497	2.2222	1.0507	0.0108	0.0010
IC	IC #	AC Bus	DC Bus	V_{ac} (p.u.)	V_{dc} (p.u.)	$\Delta e_{\omega V}$ (p.u.)		P_{ic} (p.u.)	Q_{ic} (p.u.)	PSI_p (%)	PSI_q (%)
	1	1	1	0.9645	0.9648	0.0462		−0.0462	0.0	4.62	—
	2	3	3	0.9653	0.9681	0.0404		−0.0404	0.0	4.04	—

3.6.2.1 6-Bus AC/DC Hybrid Microgrid

The ac and dc subgrids of the 6-bus hybrid system shown in Figure 3.5 are interconnected through two ICs: IC #1, located at bus 1, and IC #2, located at bus 3. Both ICs have the same ratings as the IC described in Section 3.5, and the control strategy adopted for both was control strategy I. The developed UPF program converged after four iterations at a steady-state frequency equal to 0.9923 p.u. The power flow solution was tabulated as listed in Table 3.3. As the table reveals, proportional active power sharing is guaranteed in the ac subgrid, i.e., the DG and DS are loaded equally, with $\text{PSI}_{ac,p_1} = \text{PSI}_{ac,p_2} = 77.40\%$. However, the reactive power sharing is inexact: $\text{PSI}_{ac,q_1} = 71.07\%$ and $\text{PSI}_{ac,q_2} = 69.49\%$. This inexact sharing could create a current that circulates among the inverter-based DERs, which in turn could cause overloading [99]. The problem of inaccurate reactive power sharing results from unequal line voltage drops; i.e., $|V_1| \neq |V_3|$, even though the line impedances are equal: $Z_{ac_{12}} = Z_{ac_{23}}$. Similarly, active power sharing in the dc subgrid is not guaranteed, with $\text{PSI}_{dc,p_1} = 70.46\%$ and $\text{PSI}_{dc,p_2} = 63.71\%$, despite the two identical droop-controlled dc-type DERs. This effect can be attributed to the fact that the dc line resistances have been created unequal: $R_{dc_{23}} = 0.5R_{dc_{12}}$. In addition to the unequal loading

of the DERs, the ICs are subject to the same problem of inexact power sharing in spite of their equal ratings. As shown in Table 3.3, due to divergent dc terminal voltages, the ICs sense different error signals, i.e., $\Delta e_{\omega V,1} \neq \Delta e_{\omega V,2}$. Nevertheless, both ICs transfer active power to the dc side: $P_{ic} < 0$. A final observation is that although the generation available in each subgrid could supply the local demand, the IC control scheme I requires continuous IC operation in an attempt to bring back to zero the error $\Delta e_{\omega V}$ between the frequency and the dc voltage. Such continuous IC operation can be relieved if control strategy II or III is adopted.

3.6.2.2 12-Bus AC/DC Hybrid Microgrid

The UPF solution technique was also tested on the islanded 12-bus HMG illustrated in Figure 3.6. This system represents a comprehensive test system because it involves radial and meshed topologies, a variety of load models, and different DER operating modes and IC control strategies. For the testing for this study, the ac voltage level was 2.4 kV, while the dc voltage level was 7 kV [100]. The total ac/dc active and reactive demands were 4.7 MW and 1.5 Mvar, respectively. The test system involved two ac/dc links between (ac-dc) buses (2-1) and (5-5). The ratings of both ICs were 3.75 MVA each. The respective bus and line data are shown in Tables A.2 and A.3, included in the appendix. The MVA and ac/dc kV base values were taken as 3.0 MW and 2.4/7 kV, respectively. Two case studies were considered. Case #1 was designed to provide further testing of the UPF algorithm. Case #2 was developed as a means of illustrating the ability of the developed UPF formulation to deal easily with a variety of DER operating modes and IC control strategies. Snapshots of the power flow solutions obtained for both case studies are presented in Table 3.4.

3.6.2.2.1 Case #1: Single Control of DERs and ICs In this case study, all DERs are droop-controlled and the ICs are controlled according to strategy I. For both ICs, the active and reactive power droop coefficients are $\gamma_p = 0.6667$ MW^{-1} and $\gamma_q = 5.33333 \times 10^{-2}$ kV/Mvar, respectively. The renewable-energy-based units are equipped with storage units to support their droop controllability. The tie lines (T.L) in both subgrids are initially open. The UPF algorithm has converged at a steady-state frequency equal to 0.9920 p.u. As indicated in Table 3.4, in the ac subgrid, the DERs share the active power demand proportionally, i.e., $\text{PSI}_p = 80.13\%$. However, the reactive power sharing is inaccurate. In the dc subgrid, the active power sharing is not exact either. The ICs sense that the ac subgrid is dominating the dc subgrid, i.e., $\Delta e_{\omega V,1}, e_{\omega V,2} > 0$, causing both ICs to transfer active power to the dc subgrid. However, the loading of the ICs is unequal due to the discrepancy in the dc voltages of the ICs.

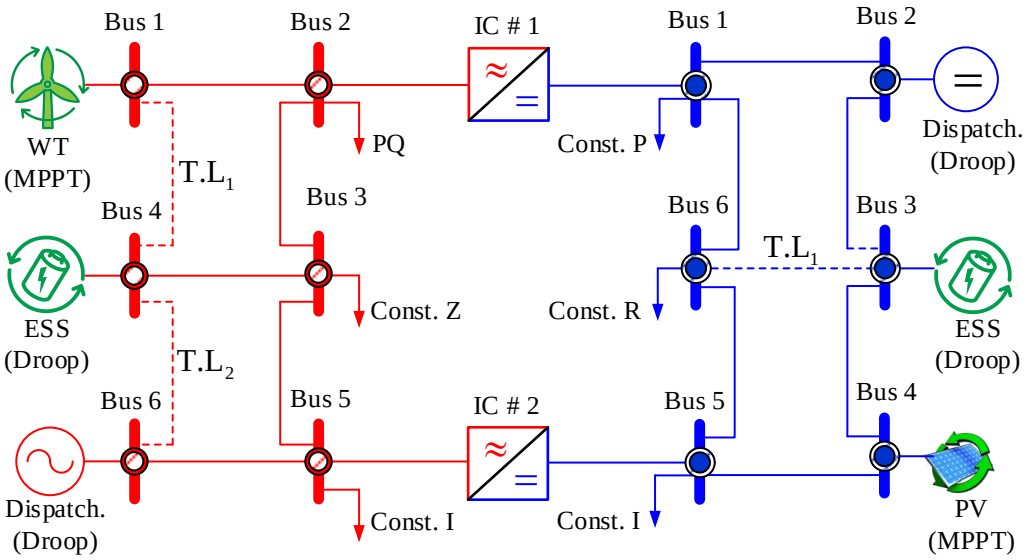

Figure 3.6. 12-bus ac/dc hybrid microgrid.

Table 3.4
The Power Flow Solution for the Islanded 12-Bus AC/DC Hybrid Microgrid (S_{base} = 3 MVA)

MG	Case #1: Single Control of DERs & ICs ($\omega = 0.992$ p.u.)							Case #2: Mixed Control of DERs & ICs ($\omega = 1.008$ p.u.)					
	Bus #	Bus Type	DER Type	P_{DR} (p.u.)	Q_{DR} (p.u.)	PSI_p (%)	PSI_q (%)	Bus Type	DER Type	Control Mode	$\|V\|$ (p.u.)	P_{DR} (p.u.)	Q_{DR} (p.u.)
AC	1	D	DG	0.2137	0.1418	80.13	70.91	PQ	Wind	MPPT	0.9965	0.2667	0.2000
	2	T	—	—	—	—	—	T	—	—	0.9928	—	—
	3	Z	—	—	—	—	—	Z	—	—	0.9911	—	—
	4	D	DG	0.1282	0.0911	80.13	75.89	D	DS	Droop	0.9944	−0.1285	0.0
	5	T	—	—	—	—	—	T	—	—	0.9934	—	—
	6	D	DG	0.4808	0.2509	80.13	55.76	PV	DG	PV	1.0000	0.6000	0.2931
DC	1	T	—	—	—	—	—	T	—	—	0.9904	—	—
	2	D	DG	0.4195	—	65.54	—	V	DG	V	1.0000	0.6115	—
	3	D	DG	0.1078	—	67.39	—	D	DS	Droop	0.9937	0.0201	—
	4	D	DG	0.1527	—	76.33	—	P	Solar	MPPT	0.9922	0.2000	—
	5	T	—	—	—	—	—	T	—	—	0.9853	—	—
	6	R	—	—	—	—	—	R	—	—	0.9882	—	—
	IC #	Control Strategy	V_{ac} (p.u.)	V_{dc} (p.u.)	$\Delta e_{\omega V}$ (p.u.)	P_{ic} (p.u.)	Q_{ic} (p.u.)	Control Strategy	$\Delta e_{\omega V,min}$ (p.u.)	$\Delta e_{\omega V}$ (p.u.)	V_{dc} (p.u.)	P_{ic} (p.u.)	Q_{ic} (p.u.)
IC	1	I	0.9605	0.9575	0.0584	−0.0584	0.0	II	0.05	0.0323	0.9904	0.0	0.0
	2	I	0.9635	0.9529	0.0664	−0.0664	0.0	III	—	0.0	0.9853	0.0	0.0

3.6.2.2.2 Case #2: Mixed Control of DERs and ICs The control strategies followed for ICs #1 and #2 are strategy II and strategy III, respectively. The minimum error specified for IC #1, with control strategy II, is 0.05 p.u. The droop gains for IC #1 are the same as in case #1, whereas the aggregated ac/dc droop gains of IC #2 are determined based on (3.4) in Section 3.2.4.3. The tie line are closed in both subgrids. The UPF algorithm has converged at a steady-state frequency equal to 1.008 p.u. As shown in Table 3.4, each DER injects active and reactive power according to its operating mode. The renewable-energy-based DG units, which operate in maximum power point tracking (MPPT) mode and are located at bus 1 in the ac subgrid and at bus 4 in the dc subgrid, inject their maximum available power. The voltage-regulated DG units, which are located at bus 6 in the ac subgrid and at bus 2 in the dc subgrid, deliver 0.2931 p.u. of reactive power and 0.6115 p.u. of active power, respectively, in order to maintain their terminal voltages at 1.0 p.u. The droop-controlled DS, which is located at bus 4 in the ac subgrid, charges 0.1285 p.u. of active power according to its droop characteristics, as the system frequency is larger than the nominal value: $\omega_0 = 1.0$ p.u. The other droop-controlled DS, which is located at bus 3 in the dc subgrid, discharges 0.0201 p.u. of active power according to its droop characteristics, as its terminal voltage is less than the nominal value: $V_{dc,0} = 1.0$ p.u. A final observation is that although IC #1, which is governed by control strategy II, can determine that the ac subgrid is dominant, i.e., $\Delta e_{\omega V} = 0.0323 > 0$, it does not transfer power to the dc subgrid, owing to the fact that $|\Delta e_{\omega V}| < \Delta e_{\omega V,min}$. In the case of IC #2, which is adhering to control strategy III, neither subgrid requests a power transfer, nor hence, no power exchange takes place: i.e., $P_{ic} = Q_{ic} = 0$. Both control strategy II and control strategy III achieve the same objective: no power transfer will be permitted when both subgrids can supply their own demands. However, control strategy II offers the advantage of being fully decentralized, in contrast to control strategy III, which requires an exchange of information with the local DERs in order to determine their droop controllability and generation availability.

3.6.3 Algorithm Robustness

The robustness of the developed algorithm can be verified using a highly resistive network. For this study, the 12-bus HMG was modified accordingly so that its original R/X ratio was increased to 5:1, 10:1, and 15:1. The high 15:1 R/X ratio represents the steady-state stability limit of stiff distribution systems [101]. For islanded and weak systems, however, the steady-state stability limit might reach neither this level nor even a lower one. Increasing the R/X ratio of the 12-bus test system allows the UPF algorithm to be tested for ill-conditioned HMGs. Table 3.5 shows that the developed UPF algorithm

successfully provided a steady-state solution for the different R/X ratios but at the expense of an increased number of iterations and a correspondingly longer CPU time required for convergence. A closer look at this table reveals that, for both the ac and dc subgrids, the ∞-norms of the voltage profiles ($\|\Delta V_{ac}\|_\infty$ and $\|\Delta V_{dc}\|_\infty$), which represent the respective maximum deviations from the nominal ac and dc voltages, rise as the system becomes increasingly ill-conditioned. Further, the active power losses in the system tend to increase with the R/X ratio. Table 3.5 also reveals that increasing the level of ill-conditioning diminishes the extent of the equal power sharing in both the ac and dc subgrids, as indicated by the maximum error in the reactive power sharing in the ac subgrid, $\|\Delta\text{PSI}_q\|_\infty$, and in the active power sharing in the dc subgrid, $\|\Delta\text{PSI}_{p,dc}\|_\infty$.

Table 3.5
The UPF Algorithm Performance with Respect to R/X Ratio

	Original R/X	5 R/X	10 R/X	15 R/X
No. of Iterations	3	3	4	4
CPU Time (sec)	0.7591	0.7617	0.8104	0.8352
ω (p.u)	0.9920	0.9910	0.9908	0.9766
$\|\Delta V_{ac}\|_\infty$ (p.u)	0.0404	0.0516	0.0771	0.1020
$\|\Delta V_{dc}\|_\infty$ (p.u)	0.0471	0.0819	0.1102	0.1372
$P_{Loss,ac}$ (p.u)	0.0063	0.0179	0.0423	0.0640
$P_{Loss,dc}$ (p.u)	0.0082	0.0281	0.0386	0.0480
$\|\Delta\text{PSI}_q\|_\infty$ (p.u)	0.2013	0.4537	0.6724	0.6878
$\|\Delta\text{PSI}_{p,dc}\|_\infty$ (p.u)	0.1079	0.3457	0.4477	0.4963

3.6.4 Algorithm Scalability

The scalability of the UPF algorithm has been tested on a modified version of a medium-voltage 33-bus test system [102], which is considered a fairly large system for a microgrid. The ac/dc voltage levels of the resulting HMG are 12.66/2.0 kV, while the ac nominal frequency is 60 Hz. The 12.66/2.0 kV HMG was disconnected from the host ac grid by deactivating the island interconnection devices (IIDs) located at ac bus 1 and dc bus 10. This hybrid system, illustrated in Figure 3.7, involves a dc subgrid that is interfaced with

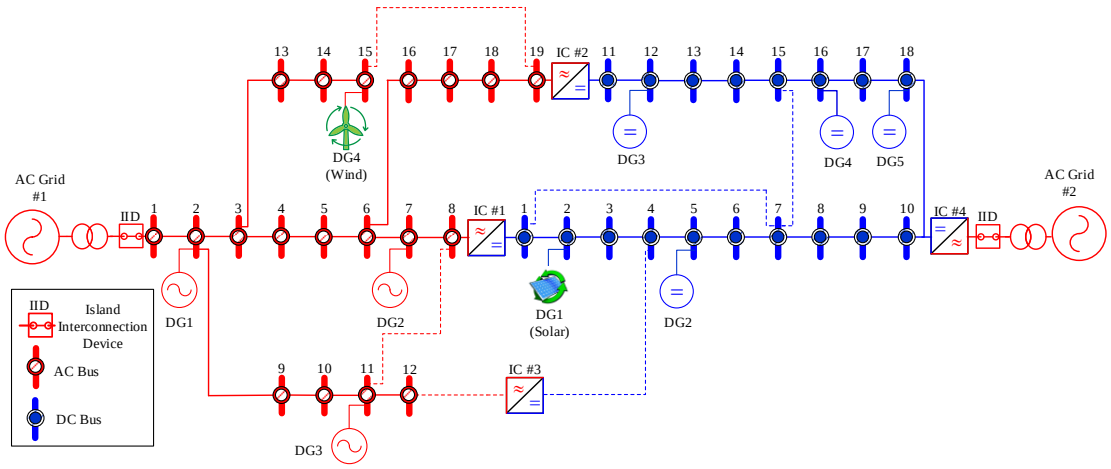

Figure 3.7. 33-bus ac/dc hybrid microgrid.

its adjacent ac subgrid and with the main ac grid #2 through two sets of 12.66/0.96 kV transformers and bidirectional ICs. ICs #1 and #2 are initially connected while IC #3, which is represented by an IC with dashed lines at both sides, is primarily switched off. The ratings and droop characteristics of the three ICs are listed in Table 3.8.

This hybrid system has a total ac active and reactive power demand of 2.42 MW and 1.18 Mvar, respectively, while the dc active power demand is 1.5 MW. The local DERs include seven droop-based DG units, three of which are ac. The ratings and droop parameters of the droop-based DER units are tabulated in Appendix A.3. In addition to droop-based DER units, the ac/dc local supply includes two renewable-based units operating in MPPT mode and located at ac bus 15 and dc bus 2. The locations, ratings, and types of the HMG resources were assumed based on the results from the planning stage. The reactive power demands at the dc buses were set to zero. The original 33-bus system data are available in [103]. Each subgrid has two tie lines, as represented by the dashed lines in Figure 3.7. The ac subgrid has two tie lines: one between buses 8 and 11 and another between buses 15 and 19. The dc subgrid has a tie line located between buses 1 and 7 and another between buses 7 and 15. All of the tie lines are initially open. The MVA and ac/dc base voltage values were selected as 1 MVA and 12.66/2.0 kV, respectively. The permissible operational range for voltage deviations is 2.5% at ac/dc droop-controlled buses and 5% at ac/dc load buses. The frequency of the ac subgrid can deviate from its nominal value by 0.83%. The bus and line data are supplied in Appendix A.3.

For scalability purposes, all of the tie lines and ICs are activated. The power flow solutions for the ac subgrid, the dc subgrid, and the ICs are listed in Tables 3.6, 3.7, and 3.8, respectively. The developed UPF converged after four iterations and in approximately 1.2 s. The computational requirements confirm the scalability and applicability of the UPF algorithm in online applications, especially in the presence of fast-acting smart converters whose dynamics settle in a few seconds.

Table 3.6. Power Flow Results for the 33-Bus AC/DC Hybrid Microgrid: AC Side

Bus Index	Bus Type	DER Type	$\|V_{ac}\|$ (p.u.)	δ (p.u.)	$P_{D,ac}$ (p.u.)	Q_D (p.u.)	P_{DR}^{rated} (p.u.)	Q_{DR}^{rated} (p.u.)	P_{DR} (p.u.)	Q_{DR} (p.u.)	PSI_p (%)	PSI_q (%)
1	PQ	—	0.9918	0	0	0	—	—	—	—	—	—
2	D	DG	0.9918	0	0.0993	0.0604	0.8	0.6	0.6502	0.1974	81.27	32.91
3	PQ	—	0.9893	-0.0008	0.0894	0.0403	—	—	—	—	—	—
4	PQ	—	0.9889	-0.0009	0.1192	0.0805	—	—	—	—	—	—
5	PQ	—	0.9888	-0.0011	0.0596	0.0302	—	—	—	—	—	—
6	PQ	—	0.9894	-0.0015	0.0596	0.0201	—	—	—	—	—	—
7	D	DG	0.9904	-0.0001	0.1987	0.1007	0.8	0.6	0.6502	0.23	81.27	38.33
8	T	—	0.9902	-0.0003	0.1987	0.1007	—	—	—	—	—	—
9	PQ	—	0.992	0.0002	0.0894	0.0403	—	—	—	—	—	—
10	PQ	—	0.995	0.0022	0.0894	0.0403	—	—	—	—	—	—
11	D	DG	0.9962	0.0031	0.0894	0.0403	0.96	0.72	0.7802	0.1106	81.27	15.36
12	T	—	0.9948	0.0012	0.0894	0.0403	—	—	—	—	—	—
13	PQ	—	0.9877	-0.0015	0.0894	0.0503	—	—	—	—	—	—
14	PQ	—	0.9853	-0.0031	0.4172	0.2013	—	—	—	—	—	—
15	PQ	Wind	0.9862	-0.004	0.4172	0.2013	0.4	0.3	0.4	0.3	100	100
16	PQ	—	0.9889	-0.0017	0.0596	0.0252	—	—	—	—	—	—
17	PQ	—	0.9884	-0.0019	0.0596	0.0252	—	—	—	—	—	—
18	PQ	—	0.9871	-0.0033	0.0596	0.0201	—	—	—	—	—	—
19	T	—	0.9865	-0.0042	0.1192	0.0705	—	—	—	—	—	—
		$P_{Loss,ac} =$	0.0072 p.u.	$\sum P_D =$	2.4037	p.u.		$\sum P_G =$	2.4806	p.u.		
		$Q_{Loss,ac} =$	0.0063 p.u.	$\sum Q_D =$	1.1880	p.u.		$\sum Q_G =$	0.8380	p.u.		

Table 3.7. Power Flow Results for the 33-Bus AC/DC Hybrid Microgrid: DC Side

Bus Index	Bus Type	DER Type	V_{dc} (p.u.)	$P_{D,dc}$ (p.u.)	P_{DR}^{rated} (p.u.)	P_{DR} (p.u.)	PSI_p (%)
1	T	—	0.9619	0.09	—	—	—
2	P	Solar	0.9766	0.06	0.18	0.18	100
3	P	—	0.963	0.06	—	—	—
4	T	–	0.9668	0.06	—	—	—
5	D	DG	0.9808	0.12	0.4	0.3067	76.67
6	P	—	0.968	0.06	—	—	—
7	P	—	0.9558	0.06	—	—	—
8	P	—	0.9489	0.045	—	—	—
9	P	—	0.9475	0.06	—	—	—
10	P	—	0.957	0.06	—	—	—
11	T	—	0.9665	0.08	—	—	—
12	D	DG	0.9775	0.05	0.25	0.2249	89.94
13	P	—	0.9698	0.035	—	—	—
14	P	—	0.9655	0.04	—	—	—
15	P	—	0.9622	0.06	—	—	—
16	D	DG	0.9805	0.21	0.5	0.3891	77.81
17	P	—	0.9714	0.15	—	—	—
18	D	DG	0.9828	0.2	0.5	0.3434	68.68

Table 3.8. Power Flow Results for the 33-Bus AC/DC Hybrid Microgrid: ICs

IC Index	AC Bus	DC Bus	V_{ac} (p.u.)	V_{dc} (p.u.)	P_{ic}^{rated} (p.u.)	Q_{ic}^{rated} (p.u.)	P_{ic} (p.u.)	Q_{ic} (p.u.)	γ_p (p.u.)	γ_q (p.u.)	PSI_p (%)	PSI_q (%)
1	8	1	0.9902	0.9619	1	0.75	-0.0875	0	1	0.06667	8.75	0.0
2	19	11	0.9948	0.9665	1	0.75	0.005	0.1825	1	0.06667	0.5	24.33
3	12	4	0.9865	0.9668	0.75	0.5	0.0128	0.1738	0.75	0.1	1.28	23.17

3.7 Discussion

The goal of the work presented in this chapter was to address the unsolved power flow problem for islanded HMGs. The power flow subproblems for ac and dc subgrids have been described mathematically using a set of nonlinear equations and have been solved simultaneously using a globally convergent Newton trust-region method. The unified power flow tool that has been developed incorporates consideration of the special features of islanded HMGs, such as the unavailability of a slack bus, the droop controllability of converter-based DERs, and the bidirectionality of the power flow between neighbouring ac/dc subgrids. The phasor formulation presented offers both fast convergence, as demonstrated by the rapid reduction in the maximum power mismatch, and flexible implementation, as evidenced by the easy accommodation of a variety of DERs and IC control strategies. The simulation results have shown that the problems associated with inaccurate reactive power sharing in ac microgrids and those linked to inexact active power sharing in dc microgrids will both migrate to HMGs. As well, the HMG power flow analysis has revealed that the ICs would be subject to the same difficulty with power sharing as droop-controlled DERs are. For these reasons, proportional power sharing in islanded ac/dc hybrid microgrids was set as a target in the next chapter. In spite of these remaining challenges, however, the power flow tool introduced in this chapter is already powerful enough to help system planners and operators explore the economic and technical challenges related to hybridizing existing ac grids with dc grids at both the medium- and low-voltage levels.

Chapter 4

A Precise and Unified Power Sharing Scheme for Islanded AC/DC Hybrid Microgrids

4.1 Introduction

As previously discussed in chapter 2, an islanded ac/dc hybrid microgrid (HMG) control strategy can be centralized, distributed, or decentralized [46]. A centralized control strategy is characterized by a higher degree of controllability and observability. However, this type of control strategy mandates a high bandwidth communication link between the central and local controllers. Any failure in the central controller could lead to system failure. Examples of centralized controllers are ones involving a single master and multiple slaves, and ones with multiple masters and multiple slaves [104]. Distributed control can be achieved through a multi-agent system. Each agent that represents a local controller would exchange its information with its neighboring agents [32, 33], thus requiring lower bandwidth communication links. Decentralized control can be realized with the use of droop control [68]: an autonomous control strategy that entails only local measurements. It is also worth mentioning that centralized and distributed controllers would resolve to droop-based controllers during communication failures. In HMGs, however, droop control is subject to its own limitations. For example, in an ac subgrid, equal reactive power sharing is inaccurate due to a unique voltage drop across each feeder [105]. In a dc subgrid, active power sharing is also inexact due to unequal feeder resistances [106].

This chapter sheds light on the problem of inexact power sharing in islanded droop-controlled HMGs. The inexact power sharing problem can be defined as the steady-state error in sharing the load among local droop-controlled distributed energy resources (DERs) in proportion to their ratings in an islanded microgrid. To tackle the problem, this chapter introduces a unified power sharing (UPS) scheme that achieves simultaneous exact power sharing in both ac and dc subgrids. The unified and global power sharing scheme coordinates local distributed generation (DG) units and interlinking converters (ICs) so that 1) exact equal power sharing is achieved in each subgrid and 2) all ICs are loaded proportionally. If no access to communication is available, the UPS scheme can be executed in

the design stage and the resulting optimal droop settings can be implemented in the DER droop controllers. If access to communication is limited, the UPS scheme can then be executed in advance, e.g., the day ahead, and the droop controller settings can be scheduled for the next operational day(s). If a communication infrastructure is already in place, it can be used to implement the UPS scheme in the centralized supervisory controller for real-time operations. The microgrid centralized controller (MGCC) is necessary for monitoring and managing the microgrid. The MGCC is also needed to achieve other tasks such as energy management, export/import scheduling with the main grid and adjacent microgrids, and ancillary services [107]. Given that the MGCC already exists, our UPS scheme can be added as another feature of the MGCC to achieve exact power sharing. For multiple HMGs or ac/dc zones, the developed UPS algorithm can also be programmed in the zonal supervisory controller for each zone. Each zonal supervisory controller manages the power sharing within its zone and coordinates power exchanges with the supervisory controller of each neighboring zone. The following are the main contributions of the work presented in this chapter:

1. The developed scheme models the distinctive features of converter-based HMGs, such as the inherent coupling between frequency and dc voltage in ac/dc networks that are interfaced through bidirectional ICs and the droop controllability of converter-based DGs and ICs.

2. The power sharing control problem is approached as an optimization-based control problem, in which the sharing error is minimized while technical and operational constraints are respected.

3. The UPS scheme can be implemented in the supervisory controller of the hybrid microgrid either with a high- or low-bandwidth communication network.

4. Our power sharing strategy is a unified and global scheme that can achieve exact active and reactive power sharing simultaneously in the entire HMG.

The remainder of this chapter is structured as follows. Section 4.2 describes the power sharing problem in ac microgrids, dc microgrids, and HMGs. Section 4.3 presents the mathematical formulation of the power sharing problem in islanded converter-dominated HMGs. Section 4.5 discusses the results of the simulations that were conducted, and the last section, section 4.6, highlights key points.

4.2 Power Sharing Problem in AC/DC Hybrid Microgrids

In smart distribution grids with multiple ac/dc HMGs, the power sharing problem during islanding can be addressed for the entire hybrid system as a single unit or for each ac/dc subgrid separately, depending on whether the hybrid system owner is a single entity or multiple ones and on whether its operational philosophy is to have one integrated system or multiple zones.

A better understanding of the problem can be obtained from consideration of a six-bus ac/dc HMG that consists of a three-bus ac subgrid and another three-bus DC microgrid, as illustrated in Figure 4.1. The two subgrids are interfaced through two identical ICs, and each subgrid has two identical droop-controlled DG units[1]. Each ac/dc line has a specific length unique to that line so that the voltage drop is thus unequal along the feeders.

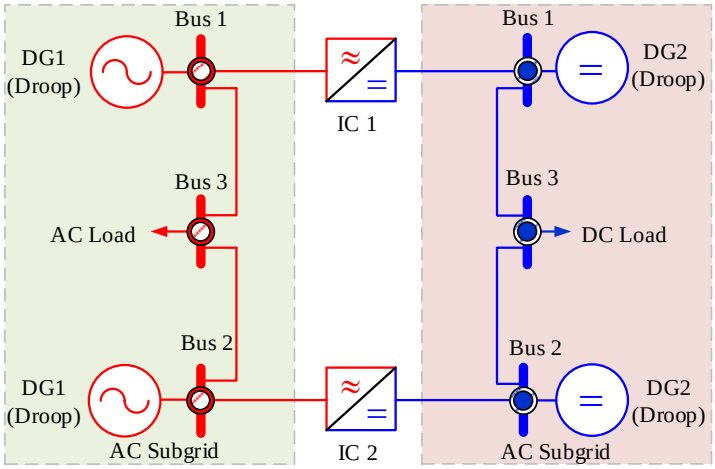

Figure 4.1. Simple six-bus ac/dc hybrid microgrid.

[1]Identical droop-controlled DG units would have the same ratings and similar droop characteristics.

4.2.1 Power Sharing in an AC Subgrid

In droop control, the ac active power, $P_{G,ac}$, is correlated linearly with the frequency ω, as given by the (ω-P) droop equation:

$$\omega = \omega_0 - m_{p,ac} P_{G,ac}. \tag{4.1}$$

where ω_0 is the no-load frequency of the ac DG unit.

The ac active power static droop gain, $m_{p,ac}$, is determined based on the operational range specified for the frequency and can be obtained from (4.2) [108]:

$$m_{p,ac} = \frac{\omega_{max} - \omega_{min}}{P_{G,ac}^{max}} \tag{4.2}$$

It should be noted that the maximum frequency ω_{max} in (4.2) represents the frequency at no load, ω_0.

If a DG unit is dedicated primarily to supplying active power, its nominal apparent power, S_G^{max}, can then be used in (4.2) rather than the maximum active power, $P_{G,ac}^{max}$. Since the two DG units have the same droop characteristics, as indicated in Figure 4.2 (a), and the frequency is a global variable, the active power sharing in the ac subgrid is perfectly exact: $P_{G,ac,1} = P_{G,ac,2}$.

If all participating DGs operate with the same no-load frequency, $\omega_{0,i} = \omega_{0,j}, \forall i \neq j$, equation (4.3) is sufficient for establishing proportional active power sharing among several DGs that have different ratings:

$$m_{p,ac,1} P_{G,ac,1} = m_{p,ac,2} P_{G,ac,2} = \cdots = m_{p,ac,n} P_{G,ac,n}. \tag{4.3}$$

However, if the no-load frequency of each DG, $\omega_{0,i}$, is made an optimization variable, i.e., $\omega_{0,i} \in [\omega_{min}, \omega_{max}]$, then (4.3) no longer holds. It is worthwhile to clarify that in the (ω-P) droop equation (4.1) all droop-based DGs converge to the same steady-state frequency even if their no-load frequencies are set as control variables.

It is worth noting that a small deviation in the frequency, $\Delta\omega$, is sufficient for equal active power sharing. Since the frequency is dictated by the droop characteristics, a flatter droop curve can thus yield exact active power sharing while still preserving system stability. In addition, as an inherent feature of droop characteristics in ac microgrids, exact active power sharing must be maintained when the goal is equal reactive power sharing. One possible way of maintaining exact active power sharing in ac microgrids while optimizing

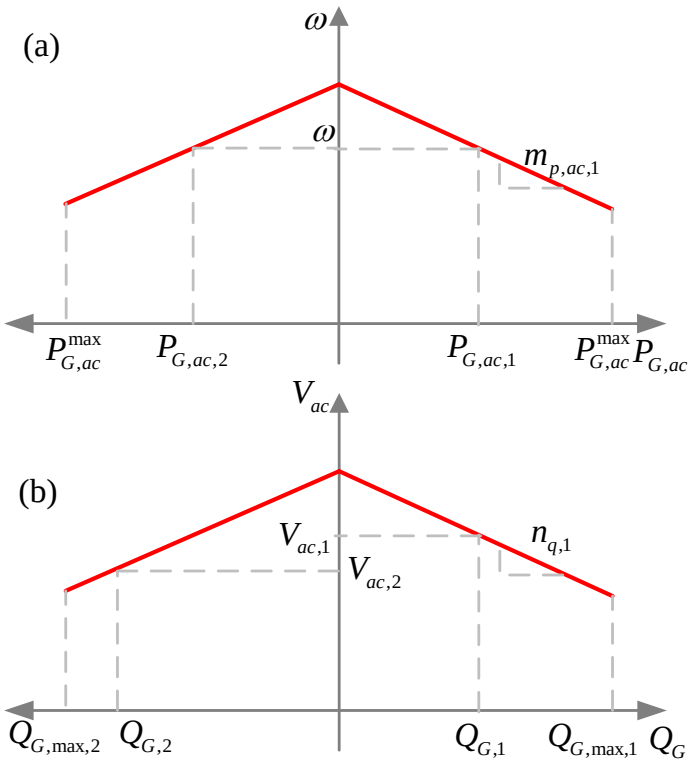

Figure 4.2. Power sharing in an ac subgrid: (a) active power sharing (b) reactive power sharing.

a performance index such as the reactive power sharing error is for all droop-based DGs to have the same no-load frequency, ω_0, and to relate all active power droop gains to the droop gain of one DG unit, e.g., DG 1, as expressed in (4.4):

$$m_{p,ac,k} = \frac{P_{G,ac,1}^{max}}{P_{G,ac,k}^{max}} m_{p,ac,1}. \tag{4.4}$$

Including the active power droop parameters, m_{ac}, ω_0, of each DG unit as optimization variables and incorporating the active power sharing error as part of the total sharing error adds a greater degree of freedom in the search for a set of droop parameters that could possibly move the power sharing error toward zero.

Reactive power is linearly coupled with the ac voltage, as described by the following

(V_{ac}-Q) droop equation:

$$V_{ac} = V_{ac,0} - n_q Q_G. \tag{4.5}$$

where $V_{ac,0}$ is the no-load voltage of the ac DG unit.

The reactive power static droop gain, n_q, is selected based on the operational range specified for the ac voltage, as described by (4.6) [108]:

$$n_q = \frac{V_{ac,max} - V_{ac,min}}{Q_{G,max}}. \tag{4.6}$$

Despite the fact that the two ac DG units are identical, since the dissimilar voltage drops across the lines make their terminal voltages unequal, their reactive power shares do not match exactly; $Q_{G,1} \neq Q_{G,2}$, as illustrated in Figure 4.2 (b).

4.2.2 Power Sharing in a DC Subgrid

In droop control, the dc active power, $P_{G,dc}$, is linearly dependent on the dc voltage, V_{dc}, as given by the (V_{dc}-P) droop equation:

$$V_{dc} = V_{dc,0} - m_{p,dc} P_{G,dc}. \tag{4.7}$$

where $V_{dc,0}$ is the no-load voltage of the dc DG unit.

The dc active power static droop gain, $m_{p,dc}$, is obtained based on the operational range specified for the dc voltage, as described by (4.8) [108]:

$$m_{p,dc} = \frac{V_{dc,max} - V_{dc,min}}{P_{G,dc}^{max}} \tag{4.8}$$

Unlike the frequency in ac subgrids, the dc voltage is a local variable of each bus and varies from one dc bus to another due to unequal line resistances. As depicted in Figure 4.3, the discrepancy in dc voltages leads to inaccurate active power sharing: $P_{G,dc,1} \neq P_{G,dc,2}$, despite the matching DG droop characteristics.

When the goal is equal sharing for a mix of (V_{dc}-P) and (V_{dc}-I) droop-based DG units, the droop resistance, R_d, in (V_{dc}-I) droop characteristics stated in (4.9) can be expressed in terms of the active power droop gain, $m_{p,dc}$, as in (4.10):

$$V_{dc} = V_{dc,0} - R_d I_{G,dc}. \tag{4.9}$$

$$R_d = \frac{\Delta V_{dc}}{I_{G,dc}^{max}} = \Big(\frac{\Delta V_{dc}}{P_{G,dc}^{max}}\Big) V_{dc,min} = m_{p,dc} V_{dc,min}. \tag{4.10}$$

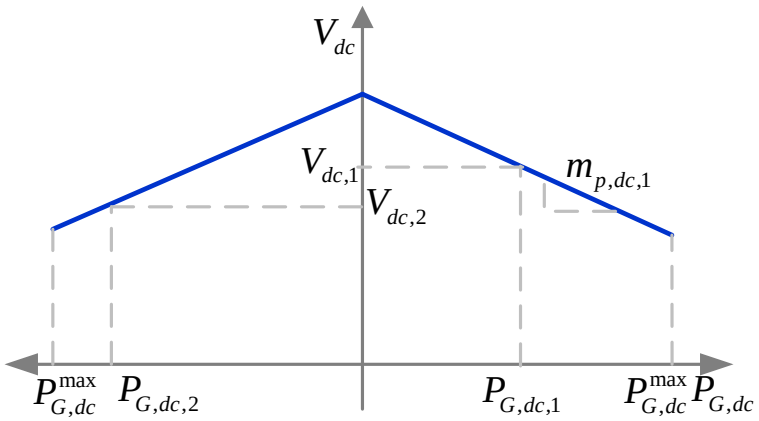

Figure 4.3. Power sharing in a dc subgrid.

where $\Delta V_{dc} = V_{dc,max} - V_{dc,min}$.

As with DG units, precise proportional power sharing among multiple storage units is possible. However, such proportional sharing mandates that, when equal loading is required for either technical or revenue reasons, at any given time interval, participating storage units must operate in the same operating mode, i.e., charging or discharging. Such a requirement might be difficult to achieve in practice since the voltage/frequency and electricity price are time-variant and location-dependent.

4.2.3 Power Sharing Among Multiple Interlinking Converters

In an ac/dc HMG, a bidirectional IC controls the active power transfer between neighboring subgrids in order to achieve a specific objective [15]. An effective control strategy is therefore critically important when the HMG is islanded. During islanding, the IC can adopt a droop-control-based strategy such that the ac and dc sides are comparably loaded. This kind of droop control strategy can be realized based on the equalization of the per-unitized ac frequency and dc voltage at the IC terminals.

With multiple ICs, the ICs share the active power transfer by continuously checking the error with respect to sign and magnitude. Figure 4.4 shows the active power sharing between the ICs in Figure 4.1. Even for identical ICs with the same droop characteristics, as a result of different voltage drops at the IC dc terminals, each IC senses a unique error signal: $\Delta e_{\omega V,1} \neq \Delta e_{\omega V,2}$. The amount of power transferred is hence not distributed proportionally: $P_{ic,1} \neq P_{ic,2}$, as depicted in Figure 4.4.

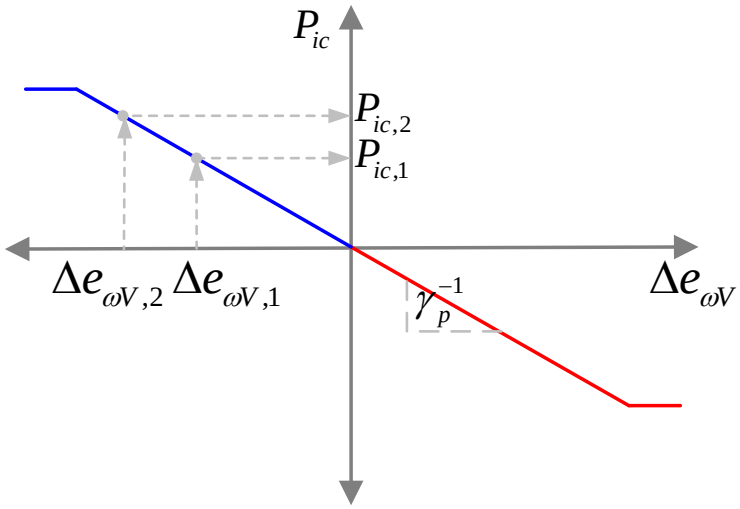

Figure 4.4. Active power sharing between two interlinking converters.

With respect to reactive power support, in contrast to ac DG units, each IC droops its reactive power output with its ac terminal voltage, as expressed in (2.12) in chapter 2. The problem of inaccurate reactive power sharing between two identical ICs at different interlinking points is illustrated in Figure 4.5. As with ac DGs, the uneven voltages at the ac terminals of multiple ICs result in a non-zero error in reactive power sharing: $Q_{ic,1} \neq Q_{ic,2}$, as indicated in Figure 4.5.

Thanks to its droop characteristics, the IC can also be controlled so that it provides reactive power support in ac overloading conditions only if the active power is being transferred to the ac side and its maximum power has not been reached [43], as described in (4.11):

$$Q_{ic} = \left\{ \begin{array}{cc} \min\{-\frac{1}{\gamma_q}\left(V_{ic,ac} - V_{ic,ac,0}\right), Q_{ic,\max}\}, & \text{if} P_{ic} \geq 0 \\ 0, & \text{if} P_{ic} < 0 \end{array} \right\}. \tag{4.11}$$

where $P_{ic} > 0$ indicates the power is being transferred to the ac side.

If equal power sharing among multiple ICs is desired, then the droop controllers of all participating ICs should be implemented so that all ICs either deliver or absorb power. It is also worth noting that proportional sharing of the total power transfer among multiple ICs at different interfacing points during islanding conditions can be challenging: such power sharing equalization requires the same direction of power transfer through the multiple ICs and consequently results in a restriction of the power flow between interfaced ac/dc

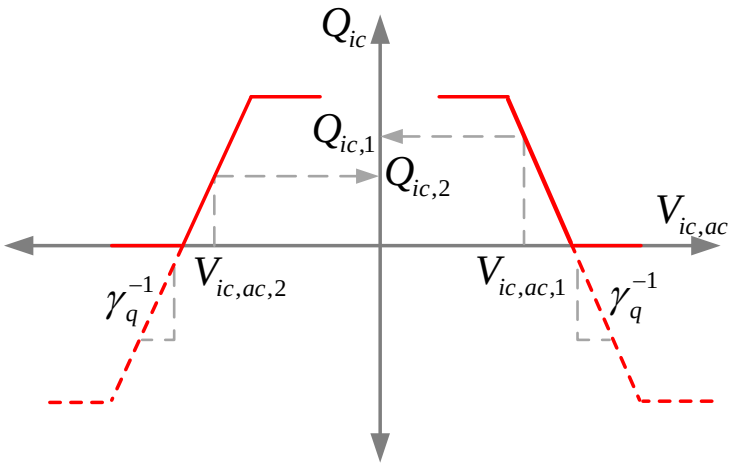

Figure 4.5. Reactive power sharing between two interlinking converters.

subgrids.

4.3 Proposed Unified Power Sharing Scheme

The problem of power sharing is approached as a constrained nonlinear least-squares optimization problem in which the droop settings are optimized within specific lower and upper bounds and the overall power sharing error is minimized. The developed formulation utilizes the coupling between the ac frequency and the dc voltage as a means of transferring the correct amount of active power for facilitating simultaneous power sharing on the ac and dc sides. The unified formulation can also ensure proportional power sharing among ICs with different ratings in the case of multiple interface points between adjacent ac and dc subgrids.

4.3.1 Power Sharing Performance Measure

In islanded microgrids, the power sharing error is one performance measure of how evenly, with respect to their ratings, the DGs take part in supplying the load together. The smaller the sharing error, the better the DG utilization. It would therefore be in the best interests of droop characteristic designers to consider minimizing the overall power sharing error, as

described in (4.12):

$$\underset{u_{lb}\le u\le u_{ub}}{\text{minimize}} \quad \frac{1}{2}\Big\{\big\|\Delta\mathcal{E}_{ac}(u)\big\|_2^2+\big\|\Delta\mathcal{E}_{dc}(u)\big\|_2^2\Big\}. \tag{4.12}$$

where $\Delta\mathcal{E}_{ac}$ and $\Delta\mathcal{E}_{dc}$ are the respective ac and dc sharing errors defined by (4.13) and (4.14):

$$\Delta\mathcal{E}_{ac,i,k}=\big(\frac{1}{\rho_{ac,i}}S_{G,i}-\frac{1}{\rho_{ac,k}}S_{G,k}\big), \quad \forall i,k\in\mathcal{B}_D^{ac}. \tag{4.13}$$

$$\Delta\mathcal{E}_{dc,i,k}=\big(\frac{1}{\rho_{dc,i}}P_{G,dc,i}-\frac{1}{\rho_{dc,k}}P_{G,dc,k}\big), \quad \forall i,k\in\mathcal{B}_D^{dc}. \tag{4.14}$$

where

$\mathcal{B}_D^{ac},\mathcal{B}_D^{dc}$ set of all ac and dc buses that have droop-based units, respectively;

$S_{G,i},P_{G,dc,k}$ actual apparent and active output powers of ac unit i and dc unit k, respectively;

$\rho_{ac,i},\rho_{dc,k}$ desired loading of ac unit i and dc unit k for proportional sharing with other droop-based units of their types, as defined by (4.15).

$$\rho_{ac,i}=\frac{S_{G,i}^{max}}{\sum\limits_{k\in\mathcal{B}_D^{ac}}S_{G,k}^{max}}, \quad \rho_{dc,i}=\frac{P_{G,dc,i}^{max}}{\sum\limits_{k\in\mathcal{B}_D^{dc}}P_{G,dc,k}^{max}} \tag{4.15}$$

In (4.12), u is the control vector of all droop parameters to be optimized. Given the upper limits for DG droop parameters, represented by vector u_{ub}, the droop parameters of each unit i can be replaced by a continuous decision variable z_i which is between zero and one, as expressed in (4.16):

$$u_i=z_iu_{ub,i}, \quad z_i\in\{0,1\}. \tag{4.16}$$

If proportional sharing among multiple ICs is of interest, a sharing error function similar to (4.13) can be written for all ICs and incorporated into (4.12). The objective function (4.12) can also be extended to include the sharing error due to a wider range of system loading conditions by defining a loading multiplier $\lambda\in\{\lambda\in\mathbb{R}^+|0<\lambda\le\lambda_{max}\}$, where λ_{max} is the maximum loadability of the hybrid system, and the resulting system sharing error $\Delta\mathcal{E}(u,\lambda)$ can thus be optimized for the entire range of loading conditions under consideration.

4.3.2 Power Sharing Problem Constraints

The power sharing problem is subject to the following constraints.

4.3.2.1 AC/DC Power Flow Equations

The power flow equations for a general ac/dc bus $b, \forall b \in \mathcal{B}$, where $\mathcal{B}$ is the set of all ac/dc buses, are defined by equations (4.17) and (4.18):

$$\begin{aligned} P_{G,b} - P_{D,b} &= \beta_b V_{ac,b} \sum_{k=1}^{n} V_{ac,k} |Y_{bk}(\omega)| cos(\delta_b - \delta_k - \theta_{bk}(\omega)) + (1-\beta_b) V_{dc,b} \sum_{k=1}^{n} G_{bk} V_{dc,k} \\ &+ (-1)^{(1-\beta_b)} \beta_{ic,b} P_{ic,b}. \end{aligned} \tag{4.17}$$

$$Q_{G,b} - Q_{D,b} = \beta_b V_{ac,b} \sum_{k=1}^{n} V_{ac,k} |Y_{bk}(\omega)| sin(\delta_b - \delta_k - \theta_{bk}(\omega)) + \beta_b \beta_{ic,b} Q_{ic,b}. \tag{4.18}$$

where $P_{D,b}, Q_{D,b}$ represent the active and reactive power demands at bus b, and $\beta_b, \beta_{ic,b}$ are binary variables defined by

$$\beta_b = \begin{cases} 1, & \text{if bus } b \text{ is an ac bus,} \\ 0, & \text{if bus } b \text{ is a dc bus.} \end{cases}$$

$$\beta_{ic,b} = \begin{cases} 1, & \text{if bus } b \text{ is an ac or a dc terminal bus,} \\ 0, & \text{otherwise.} \end{cases}$$

4.3.2.2 Droop-Controlled AC/DC DG Unit Constraints

The active power output of an ac/dc converter-based DG unit located at bus b, $\forall b \in \mathcal{B}_D$, is governed by the maximum active power that can be supplied by the energy source, as shown in (4.19). The DGs in the ac subgrid can inject reactive power up to the remaining capacities of their interfacing converters, as shown in (4.20). The droop parameters of each droop-controlled DG unit are also constrained by lower and upper bounds, as described by (4.21):

$$0 \leq P_{G,b} \leq P_{G,b}^{max}, \quad \forall b \in \mathcal{B}_D. \tag{4.19}$$

$$0 \leq Q_{G,b} \leq \sqrt{(S_{G,b}^{max})^2 - P_{G,b}^2}, \quad \forall b \in \mathcal{B}_D^{ac}. \tag{4.20}$$

$$u_{lb,G,b} \leq u_{G,b} \leq u_{ub,G,b}, \quad \forall b \in \mathcal{B}_D. \tag{4.21}$$

where $u_{lb,G,b}, u_{ub,G,b}$ are the respective lower and upper bounds on the droop parameters of the ac/dc DGs, which are set based on the minimum and maximum allowable deviations in the frequency and ac/dc voltage. One point worthy of note is that high DG droop gains can jeopardize the microgrid stability. Thus, the upper bound $u_{ub,G}$ should be selected based on a stability criteria. $u_{G,b}$ is the vector of the droop parameters of all of the DGs, as defined by

$$u_{G,b} = \begin{cases} [V_{ac,0,b}, \omega_{0,b}, m_{p,ac,b}, n_{q,b}]^T, & \text{if } b \in \mathcal{B}_D^{ac}, \\ [V_{dc,0,b}, m_{p,dc,b}]^T, & \text{if } b \in \mathcal{B}_D^{dc}. \end{cases} \tag{4.22}$$

As the frequency drops, the ac droop-controlled DG units increase their active power output according to their active power droop characteristics, as previously given in (4.1). If it reaches its rating, the DG unit is no longer governed by its droop characteristics and instead switches to constant power mode, with its output power set to the maximum available power. Such a DG unit then loses its frequency support functionality and becomes a "grid-following" unit incapable of forming the system frequency. As well, unlike PV-controlled DG units that control their terminal voltages by varying their reactive power injections, ac droop-based DG units control the ac subgrid voltage by adjusting their reactive power output according to their droop characteristics, as defined in (4.5). Once it reaches its maximum available power, the droop-based ac DG unit loses voltage control and behaves as a constant PQ generator. Such a DG unit could experience large voltage deviations due to changing loading conditions. The behavior of a droop-governed DG unit can be modeled as a nonlinear complementarity problem (NCP) [109], which can be solved using the Fischer-Burmeister method [110] as in [65, 66, 111]. For a general ac DG unit, (4.19) and (4.20) can be written as

$$0 \leq (P_{G,ac}^{max} - P_{G,ac}) \perp \left(\frac{1}{m_{p,ac}}(\omega_0 - \omega) - P_{G,ac}\right) \geq 0. \tag{4.23}$$

$$0 \leq (Q_{G,max} - Q_G) \perp \left(\frac{1}{n_q}(V_{ac,0} - V_{ac}) - Q_G\right) \geq 0. \tag{4.24}$$

where the symbol $\perp$ is the complement operator.
In (4.23) and (4.24) , $0 \leq (P_{G,ac}^{max} - P_{G,ac})$ and $0 \leq (Q_{G,max} - Q_G)$ are active only when the DG unit reaches its maximum available power. Otherwise, the DG unit follows its corresponding droop characteristics.

Similarly, the behavior of a dc DG unit with (V_{dc}-P) or (V_{dc}-I) droop characteristics that reaches its limit can be represented by complementarity constraints, as expressed in

(4.25) and (4.26):

$$0 \leq (P_{G,dc}^{max} - P_{G,dc}) \perp \left(\frac{1}{m_{p,dc}}(V_{dc,0} - V_{dc}) - P_{G,dc}\right) \geq 0. \tag{4.25}$$

$$0 \leq (I_{G,dc}^{max} - I_{G,dc}) \perp \left(\frac{1}{R_d}(V_{dc,0} - V_{dc}) - I_{G,dc}\right) \geq 0. \tag{4.26}$$

4.3.2.3 Interlinking Converter Constraints

Regardless of the auxiliary services that the IC has to offer, such as voltage unbalance compensation and harmonic current sharing, its primary task is to facilitate the active power transfer between neighboring subgrids. The IC rating can thus be dedicated mainly to active power while the IC can still provide reactive power support to the ac side according to its remaining capacity, as indicated in (4.27) and (4.28). In addition to the limit on IC power transfer, the IC droop parameters are also kept within an allowable range with respect to deviations in ac frequency and ac/dc voltages at the IC ac/dc terminals, as expressed in (4.29):

$$P_{ic,c}^2 \leq (S_{ic,c}^{\max})^2. \tag{4.27}$$

$$0 \leq Q_{ic,c} \leq \sqrt{(S_{ic,c}^{\max})^2 - (P_{ic,c})^2}. \tag{4.28}$$

$$u_{lb,ic,c} \leq u_{ic,c} \leq u_{ub,ic,c}. \tag{4.29}$$

where $u_{ic,c}$ is the vector of droop parameters of IC $c \in \mathcal{IC}$ and is defined by

$$u_{ic,c} = [\gamma_{p,c}, \gamma_{q,c}, \alpha_{\omega,c}, \alpha_{V,c}, \alpha_{\omega V,c}]^T. \tag{4.30}$$

A distinctive difference between droop-controlled DGs and ICs which operate in current control mode is that increasing the IC droop gains is in favour of stability. Thus, the IC static droop gains are taken as the lower bounds.

In terms of its bidirectional power transfer capability, the IC operational principle can be modeled based on the complementarity constraints of the squared value of the power transfer [112], as described in (4.31). The constraint defined in (4.32) should also be written in terms of the squared value of the reactive power injection if the IC is permitted to deliver and absorb reactive power:

$$0 \leq \left((S_{ic}^{max})^2 - P_{ic}^2\right) \perp \left((-\frac{1}{\gamma_p}\Delta e_{ic})^2 - P_{ic}^2\right) \geq 0. \tag{4.31}$$

$$0 \leq \left(\sqrt{(S_{ic}^{max})^2 - P_{ic}^2} - Q_{ic}\right) \perp \left(\frac{(V_{ac,0} - V_{ac})}{\gamma_q} - Q_{ic}\right) \geq 0. \tag{4.32}$$

4.3.2.4 Bus Voltage, AC System Frequency, and Branch Current Limits

In the process of optimizing the set points for droop-based DGs and ICs, the supervisory controller of a hybrid system must impose permissible ranges by which the ac frequency and ac/dc voltages at both droop-based and load buses can deviate from their reference values. Current flows must also be within the thermal capabilities of the overhead lines and underground cables, as described by (4.33)-(4.36), respectively.

$$\omega_{min} \leq \omega \leq \omega_{max}. \tag{4.33}$$

$$V_{min,b} \leq V_b \leq V_{max,b}, \forall b \in \mathcal{B}. \tag{4.34}$$

$$\delta_{min} \leq \delta_b \leq \delta_{max}, \forall b \in \mathcal{B}_{ac}. \tag{4.35}$$

$$|I_{bk}| \leq I_{max,bk}, \forall b, k \in \mathcal{B}. \tag{4.36}$$

where $\mathcal{B}_{ac}$ is the set of ac buses.

Figure 4.6 outlines the main steps in the developed UPS algorithm. The algorithm first checks with an islanding detection scheme for possible islanding conditions. Once an island formation is confirmed, from the bank of system component models, the algorithm selects the models that match the operating mode of the available droop-based DG units and ICs. The next step is to identify the range of loading in which the sharing error could be significant. The ac/dc unified power flow algorithm (UPF) developed in chapter 3 is then executed, and the ac DG, dc DG, and IC sharing errors are recorded. The UPS algorithm continues to update the droop parameters while checking the set of constraints described in Section 4.3.2. Once the best power sharing is achieved, the UPS scheme, through the global supervisory controller, sends the droop settings to the local controller of all DGs and ICs equipped with droop characteristics.

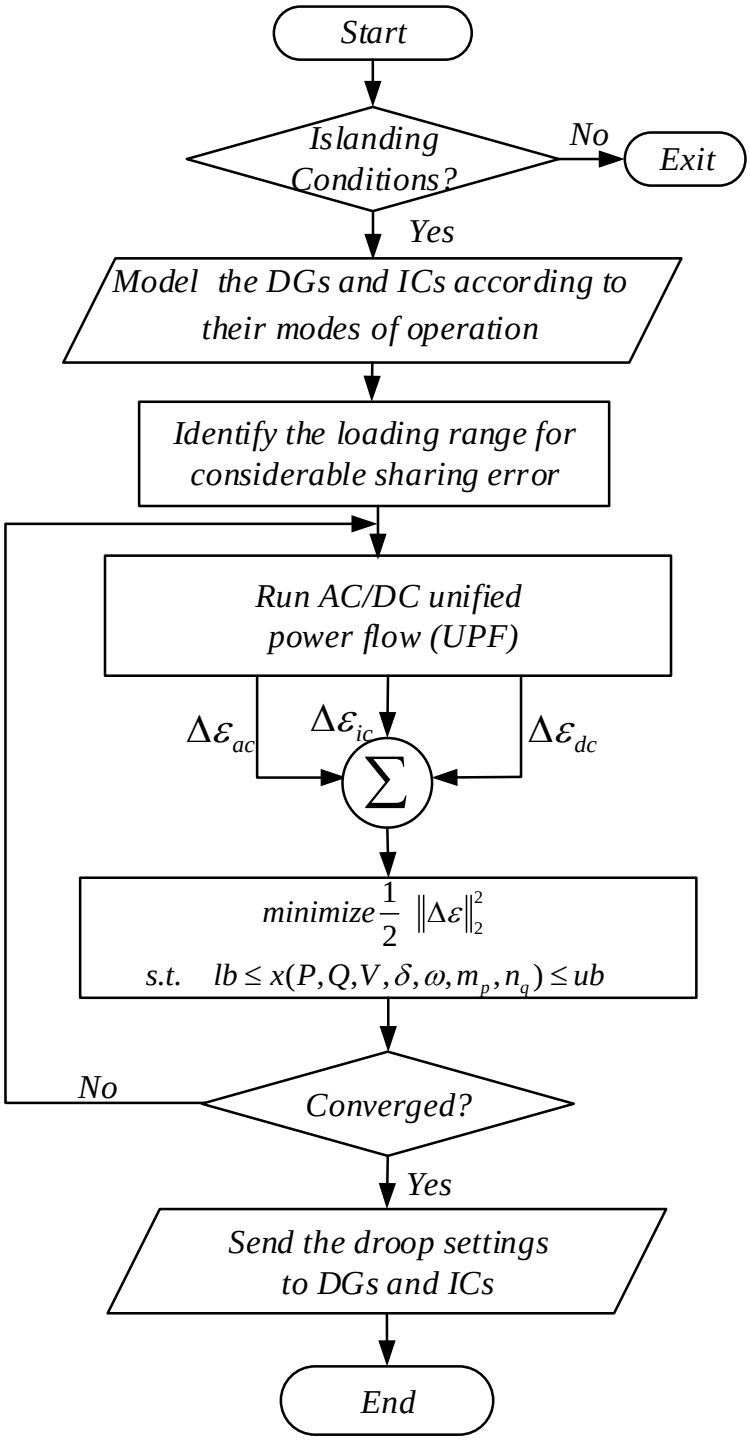

Figure 4.6. Developed UPS scheme for islanded ac/dc hybrid microgrids.

4.4 Implementation Requirements of the Developed UPS Scheme

The supervisory controller in Figure 4.7 collects the loading information of both subgrids and runs the UPS scheme to optimize the droop parameters. Once the computations are completed, the optimal droop decisions are sent back to the local DGs and ICs, as depicted in Figure 4.7. The droop settings can be updated based on event-based control, periodic control, or even continuous control according to the speed of data transmission. The data transmission frequency depends on the communication technology available. The data refreshment rate can vary from hundreds of milliseconds to several minutes [113]. The smallest control interval should be designed such that all time delays (UPS computations and communication delay) as well as the slowest microgrid dynamics (the secondary central controller dynamics) are finished. The developed UPS scheme updates the droop settings every five minutes [81]. This control interval of five minutes is sufficient for 1) the dynamics of the supervisory controller to settle down, 2) the UPS computations to be completed, and 3) the information from and to the supervisory controller to be communicated.

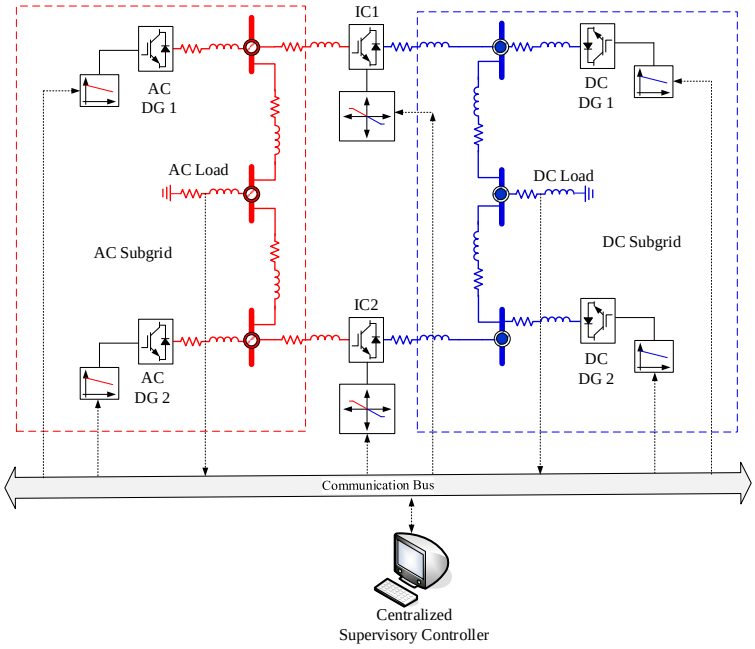

Figure 4.7. Proposed centralized control and communication architecture.

In real time implementation, like any other centralized supervisory controller, our UPS scheme is associated with time delay such as optimization computations and communication delay [114]. However, in our implementation of the UPS scheme, the stability issues assigned with communication delay can be avoided. This is due to the discrete nature of control commands that are adopted in compliance with the system rate of load variations.

4.5 Simulation Results and Discussions

The unified power sharing scheme was implemented in a MATLAB® computing environment and solved using the sequential quadratic programing method (SQP) [115]. In SQP, a sequence of optimization subproblems are iteratively solved. Each subproblem optimizes a quadratic model of the objective function subject to a linearized form of the problem constraints. More details on SQP can be found in [115,116] The test system was the 12-bus islanded droop-controlled ac/dc hybrid microgrid illustrated in Figure 4.8. The ac and dc subgrids have total capacities of 45 kVA and 45 kW, respectively. The ac and dc subgrids each contain three droop-controlled DG units with ac capacities of 20 kVA, 15 kVA, and 10 kVA and dc capacities of 20 kW, 15 kW, and 10 kW.

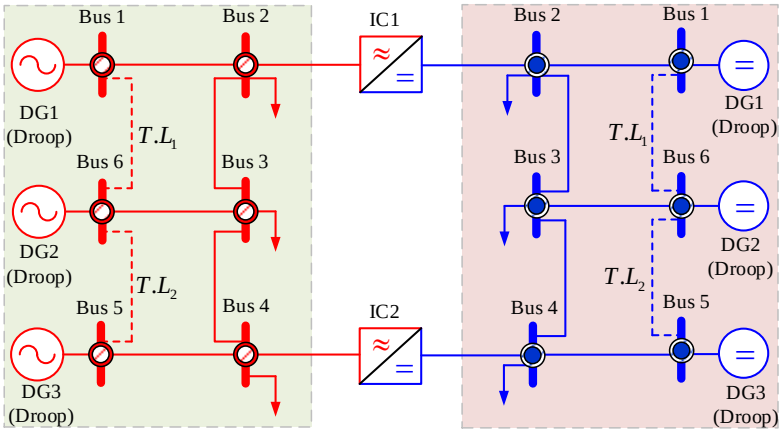

Figure 4.8. 12-bus ac/dc hybrid microgrid.

The subgrids are interfaced through two 10-kVA ICs. The ac loads are modeled as constant resistances and inductances while the dc loads are modeled as constant resistances.

This modeling of the ac/dc loads is based on the fact that, unlike medium-voltage distribution networks, the voltage at the load buses is not well regulated in low-voltage networks. Nevertheless, in case of power electronics-interfaced loads, constant PQ load models can conveniently be included in the UPS scheme. More details about load modeling in low-voltage networks can be found in [117]. In both subgrids, the tie lines are initially open. The base power and ac/dc voltage are 10 kVA and 208/600 V, respectively. The permissible operational ranges of the frequency and ac/dc voltages at the source terminals are taken as ±1% and ±2.5%, respectively.

4.5.1 Power Sharing Versus Loading Level

The loading level can contribute significantly to the power sharing error. For illustration purposes, the loading of each subgrid in the 12-bus test system was increased in steps of 10% up to its peak. As depicted in Figure 4.9, regardless of microgrid type, the sharing error becomes worse as the microgrid loading approaches its peak. It might thus be of considerable interest to a system planner to consider a loading range near maximum loading when optimizing droop characteristics for accurate power sharing during islanding conditions.

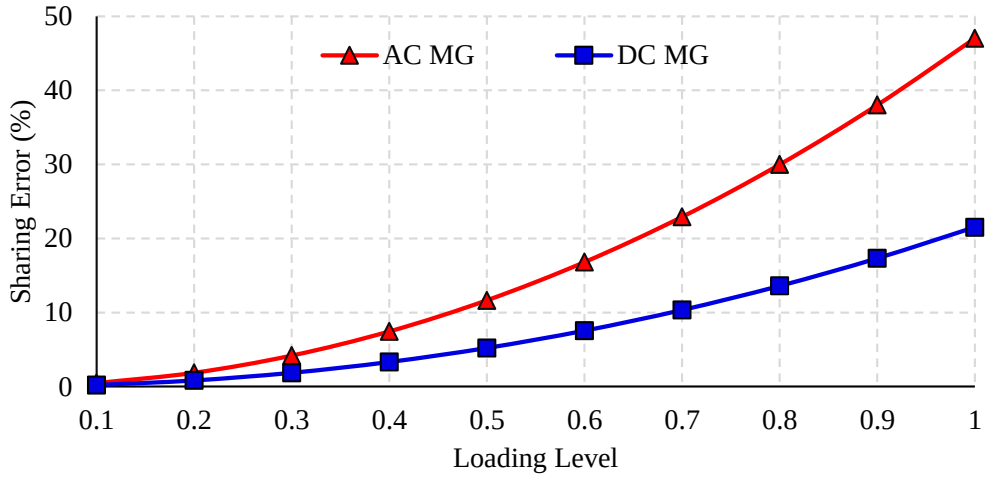

Figure 4.9. Power sharing error versus loading level.

4.5.2 Power Sharing Versus Overloading Conditions

With respect to the operation mode of a hybrid system, two possible scenarios were investigated. In the first scenario, both the ac and dc sides operate in stand-alone mode. In practice, this scenario might arise due to a technical issue such as an internal IC fault. The second scenario provided an opportunity to examine the impact on power sharing when the ac and dc sides are interfaced. The simulation results are tabulated in Tables 4.1 and 4.2. Table 4.1 confirms that inaccurate power sharing might result in some DG units being stressed during overloading conditions, as with ac DG unit 3, which is loaded beyond its rating; i.e., $\mathrm{PSI}_{ac,3} = 103.01\%$. For further load increase, DG 3 overcurrent protection might then be triggered so that DG unit 3 is tripped, which in turn, might activate the load shedding scheme if a power deficit occurs.

The results listed in Table 4.2 support the idea that interfacing ac and dc microgrids can release thermal stress on overloaded DG units, as with DG unit 3, whose loading drops from 103.01 to 97.75% after interlinking the ac and dc microgrids. Another benefit of hybridizing ac with dc is that both sides are loaded comparably with respect to their capacities. As revealed by Table II, ac and dc microgrids have different loading before the interfacing: for the ac microgrid, 92.15% of its total capacity and for the dc counterpart, 87.48% of its total capacity. Interfacing ac and dc subgrids through droop-based bidirectional ICs, which transfer power based on the difference between the normalized ac frequency and the dc voltage, equalizes the loading on both sides: ac and dc microgrids are loaded at 87.82% and 86.04% of their total capacities, respectively. The 1.78% difference between the ac and the dc loading is due to the fact that the dc voltage is only a surrogate measure of the dc subgrid loading. When the difference in loading between the ac and dc subgrid becomes significant, the following error function can be incorporated in the objective function (4.12).

$$\Delta\mathcal{E}_{ac/dc} = \underbrace{\frac{\sum_{k\in\mathcal{B}_D^{ac}} S_{G,k}}{\sum_{k\in\mathcal{B}_D^{ac}} S_{G,k}^{max}}}_{AC\ Subgrid\ Loading} - \underbrace{\frac{\sum_{k\in\mathcal{B}_D^{dc}} P_{G,dc,k}}{\sum_{k\in\mathcal{B}_D^{dc}} P_{G,dc,k}^{max}}}_{DC\ Subgrid\ Loading} \tag{4.37}$$

4.5.3 Static Versus Optimal Droop Parameters

To test the power sharing algorithm, three case studies were considered. Case 1, the base

Table 4.1. Stand-alone AC and DC Microgrids with Static Droop

Quantity	**Stand-alone AC MG**			**Stand-alone DC MG**		
ω (p.u)	0.9917 (59.502 Hz)			—		
V_{min} (p.u)	0.9637 at Bus 3			0.9570 at Bus 4		
P_{Loss} (p.u)	0.08			0.0799		
Load Location	Bus 2	Bus 3	Bus 4	Bus 2	Bus 3	Bus 4
P_D (p.u)	1.4677	1.2842	0.9173	1.8374	0.5542	1.4652
Q_D (p.u)	0.6357	0.6324	0.5034	—	—	—
DG Location	Bus 1	Bus 5	Bus 6	Bus 1	Bus 5	Bus 6
P_G (p.u)	1.6663	1.2497	0.8331	1.7505	1.2903	0.8959
Q_G (p.u)	0.8436	0.3223	0.6058	—	—	—
PSI(%)	93.38	86.04	103.01	87.52	86.02	89.59
$\frac{\sum S_{MG}}{\sum S_{MG,max}}(\%)$	92.15			87.48		

Table 4.2. Interfaced AC/DC Hybrid Microgrid with Static Droop

Quantity	**AC Subgrid**			**DC Subgrid**		
ω (p.u)	0.9920 (59.52 Hz)			—		
V_{min} (p.u)	0.9658 at Bus 3			0.9579 at Bus 4		
P_{Loss} (p.u)	0.0718			0.0771		
Load Location	Bus 2	Bus 3	Bus 4	Bus 2	Bus 3	Bus 4
P_D (p.u)	1.3803	1.1983	0.8667	1.8395	0.5549	1.4681
Q_D (p.u)	0.5975	0.5897	0.4753	—	—	—
DG Location	Bus 1	Bus 5	Bus 6	Bus 1	Bus 5	Bus 6
P_G (p.u)	1.5934	1.1950	0.7967	1.7271	1.2625	0.8821
QG (p.u)	0.7781	0.3181	0.5664	—	—	—
PSI(%)	88.66	82.44	97.75	86.35	84.17	88.21
$\frac{\sum S_{MG}}{\sum S_{MG,max}}(\%)$	87.82			86.04		

Table 4.3. Power Sharing Ratios for the Three Case Studies

	Quantity	Case1			Case2			Case3		
AC	ω	0.9920 (59.52 Hz)			0.9930 (59.58 Hz)			0.9938 (59.63 Hz)		
	$V_{ac,min}$	0.9658 at Bus 3			0.9903 at Bus 3			0.9882 at Bus 3		
	$P_{ac,Loss}$	0.0718			0.0802			0.0773		
		DG1	**DG2**	**DG3**	**DG1**	**DG2**	**DG3**	**DG1**	**DG2**	**DG3**
	V_{ac}	0.9842	0.9914	0.9769	1.0084	1.0180	1.0023	1.0070	1.0147	0.9999
	$PSI(\%)$	88.66	82.44	97.75	95.77	95.77	95.77	93.87	93.87	93.87
DC	$V_{dc,min}$	0.9579 at Bus 4			0.9636 at Bus 4			0.9653 at Bus 4		
	$P_{dc,Loss}$	0.0771			0.0715			0.0746		
		DG1	**DG2**	**DG3**	**DG1**	**DG2**	**DG3**	**DG1**	**DG2**	**DG3**
	V_{dc}	0.9784	0.9790	0.9779	0.9847	0.9844	0.9828	0.9851	0.9865	0.9842
	PSI(%)	86.35	84.17	88.21	83.30	83.30	83.30	85.21	85.21	85.21
IC		**IC1**	**IC2**		**IC1**	**IC2**		**IC1**	**IC2**	
	V_{dc}	0.9590	0.9579		0.9661	0.9636		0.9661	0.9653	
	PSI(%)	2.25	4.55		16.76	6.97		8.04	8.04	

case, is the power flow solution obtained using static droop parameters. In the base case, the hybrid system is operated autonomously based on the primary DG and IC droop controllers. The supervisory controller that sends the set points to the local controllers is deactivated. Cases 2 and 3 are applications of the developed UPS scheme. Case 2 represents optimal power sharing among the droop-based DG units only. Equal power sharing among the ICs is not considered. In Case 3, the goal is power sharing equalization within each subgrid and among the ICs.

The per unit results for the three simulated case studies are tabulated in Table 4.3. As the results indicate, the droop-based DG units adjust their power output to achieve precise power sharing (the fifth row). An additional observation is that, due to variations in line impedances, in case 1, apparent power sharing is inaccurate: $\text{PSI}_{ac,1}$[2] $= 88.66\%$, $\text{PSI}_{ac,2} = 82.44\%$, and $\text{PSI}_{ac,3} = 97.75\%$. In cases 2 and 3, accurate power sharing among droop-based ac DG units was successfully obtained. In the dc subgrid, due to discrepancies in the dc bus voltages, active power sharing is inexact in case 1: $\text{PSI}_{dc,1} = 86.35\%$, $\text{PSI}_{dc,2} = 84.17\%$, and $\text{PSI}_{dc,3} = 88.21\%$. With the UPS scheme, in cases 2 and 3, the active power shares

[2] PSI_{ac}, PSI_{dc}, and PSI_{ic} are power sharing indices for an ac DG unit, a dc DG unit, and an IC, respectively.

for each droop-controlled dc DG unit were exactly equal. With the help of the IC droop characteristics, our UPS scheme can therefore achieve exact simultaneous power sharing in both ac and dc subgrids. It is also clear from the last row of Table 4.3 that the ICs would be subject to the same difficulty of imprecise power sharing as the droop-controlled DG units, as case studies 1 and 2 demonstrate. When the power sharing error among the ICs was incorporated into the objective function (case 3), the UPS scheme was able to equalize the contribution of the active power transfer of each IC: $\text{PSI}_{ic,1} = \text{PSI}_{ic,2} = 8.04\%$. In addition to enabling precise power sharing, the developed UPS scheme can improve the voltage profile of the entire hybrid system. Plots of the ac/dc voltage profile before and after optimization of the droop parameters are provided in Figure 4.10.

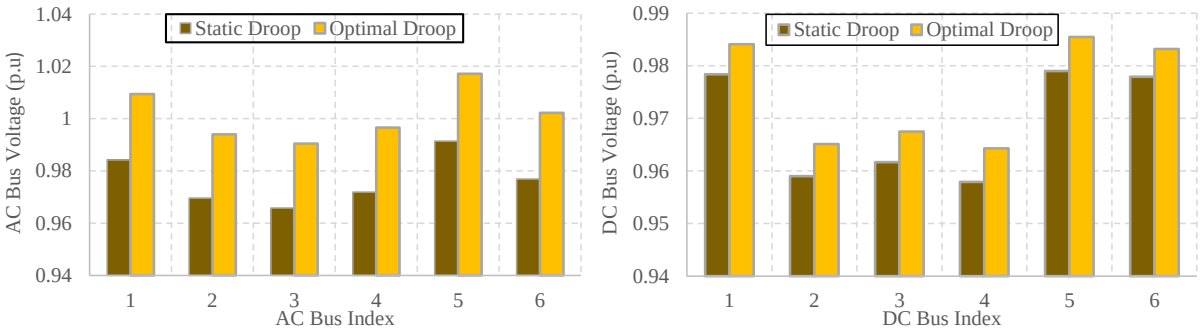

Figure 4.10. AC/DC bus voltages with static and optimal droop.

4.5.4 Power Sharing versus AC/DC Topologies

In networked ac/dc topologies, the power sharing error can be more significant than for radial ac/dc topologies. As a result, exact power sharing can be even more difficult to attain [118]. This case study reveals that system topology can affect the sharing error, as indicated in Figure 4.11, and also demonstrates the capability of the UPS scheme with respect to achieving precise power sharing for different ac/dc topologies: radial/radial, radial/meshed, meshed/radial, and meshed/meshed (Table 4.4). The topology of each subgrid shown in Figure 4.8 was reconfigured with the help of tie lines T.L1 and T.L2. As is evident from the results listed in Table 4.4, the UPS scheme achieved precise power sharing for all possible ac/dc configurations. Table 4.4 also reveals that, with different ac/dc topologies, the UPS scheme alters the DG and IC shares to minimize the power sharing error and to compensate for changes in the system Thevenin impedance identified by each DG. A further look at Table 4.4 shows that operating the ac subgrid in one topology

while the dc subgrid in another topology might provide better DG and IC utilization. This observation suggests that a mix of configurations for the ac and dc sides might be technically preferable.

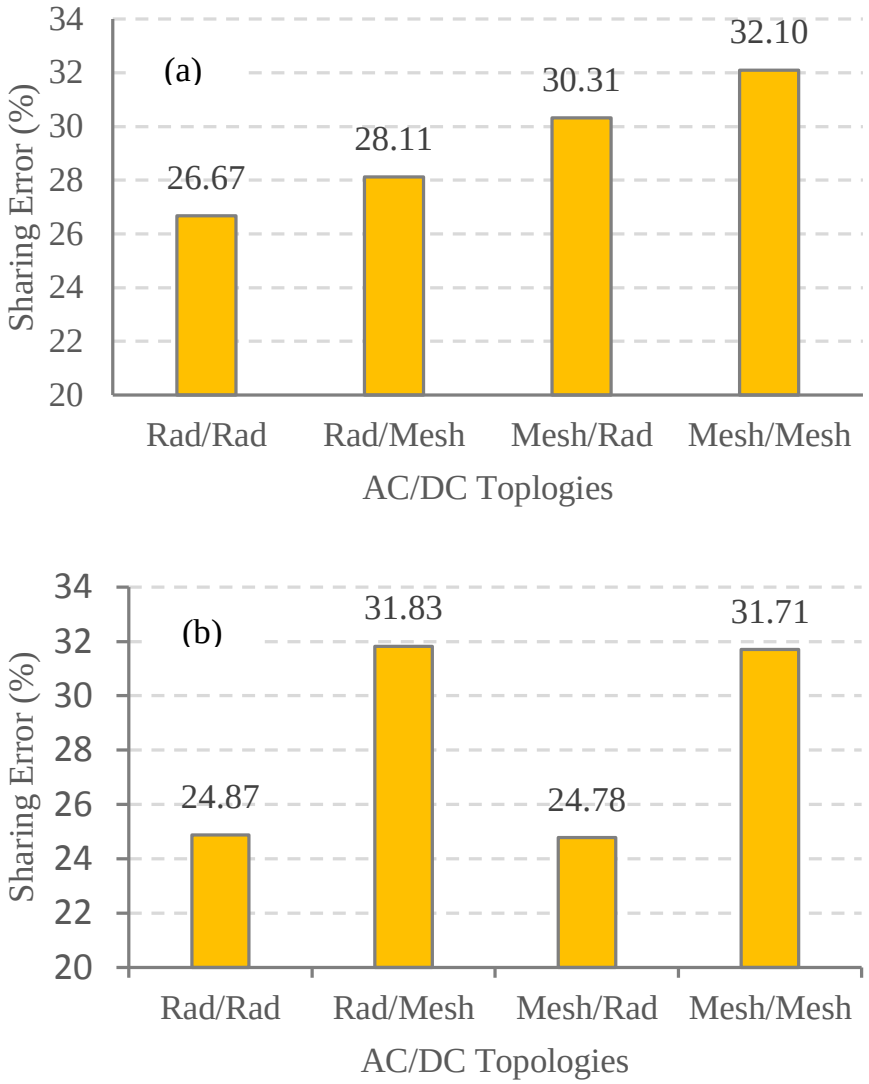

Figure 4.11. Power sharing error versus system topology: (a) power sharing in the ac subgrid (b) power sharing in the dc subgrid.

Table 4.4
Power sharing for different AC/DC topologies

AC/DC Topology	AC Subgrid			DC Subgrid			IC	
	$PSI_{ac}(\%)$			$PSI_{dc}(\%)$			$PSI_{ic}(\%)$	
	DG1	DG2	DG3	DG1	DG2	DG3	IC1	IC2
Radial/Radial	94.50	94.50	94.50	85.29	85.29	85.29	7.45	7.45
Radial/Meshed	100.00	100.00	100.00	85.47	85.47	85.47	19.64	19.64
Meshed/Radial	91.90	91.90	91.90	87.54	87.54	87.54	8.98	8.98
Meshed/Meshed	96.16	96.16	96.16	85.68	85.68	85.68	8.11	8.11

4.6 Discussion

This chapter has a unified power sharing scheme for islanded and droop-controlled ac/dc hybrid microgrids. The scheme can achieve exact simultaneous power sharing not only among droop-based distributed generating units in both subgrids but also among the interlinking converters that connect the subgrids. The developed optimal power sharing scheme treats the problem of imprecise power sharing as an optimization problem, in which the droop parameters are optimized for the minimization of the power sharing error. Simulation results reveal that, along with the droop characteristics, several additional factors, such as system topology and loading level, can also alter the shares of distributed resources and interlinking converters. Imprecise power sharing could reduce the islanded microgrid loadability margin which could possibly lead to voltage instability problems especially during heavy loading and contingency conditions. The following chapter zooms in on the loadability and voltage stability analysis during contingencies.

Chapter 5

On the Loadability and Voltage Stability Analysis in Islanded AC/DC Hybrid Microgrids During Contingencies

5.1 Introduction

The frequency and severity of weather-related outages have increased dramatically in recent years. Over the last 35 years, the United States national grid has been affected by more than 178 natural disasters, with each event causing damage assessed at approximately US$ one billion [119]. Weather-caused grid failures have therefore motivated system planners to enhance grid resiliency by modernizing existing distribution grids through the implementation of smart grid technologies and new operational paradigms such as ac/dc microgrids. In future smart distribution grids, distributed energy resources (DERs) and controllable power-electronics-interfaced loads will provide investors and end-users with the opportunity to interact with system operators and to actively participate in daily system operations [120]. Such DERs can be synchronous-based or converter-based. As well, the interfacing ac/dc and dc/ac converters of future ac/dc architectures will enable the exchange of power with the main grid and the creation of a self-powered island when it is technically not possible to stay connected with the host grid [15]. Such innovative ac/dc structures characterized by a mix of synchronous-based and converter-based ac/dc resources and a high penetration of modern ac/dc loads will be governed by their own operational philosophy [121]. During islanding in particular, dispatchable synchronous-based and converter-based DERs adopt droop characteristics in order to regulate the system frequency and voltage. Plugging DERs in and out for unexpected outages or scheduled maintenance can make microgrid operations more difficult to carry out. An additional factor is that converter-based loads such as variable-speed drives and modern lighting systems exhibit constant power characteristics, which increase the likelihood of voltage [122] and [123] and other types of instability [124–127]. In contrast, motoring loads especially induction motors are voltage-dependent but they still can endanger the short–term voltage stability during starting or fault conditions. End users might also be offered further in-

centives to shift/reduce their energy consumption during unexpected islanding and contingency conditions. However, the reluctance and unwillingness of a considerable proportion of consumers to control their electricity usage voluntarily might drive an islanded system to operate close to its voltage stability limits.

Another microgrid-related consideration is stiffness. Microgrids can be classified as weak grids with low short circuit levels and limited frequency/voltage control capability. The formation of a microgrid can be a result of partitioning a distribution system into clusters, each of which can operate autonomously. In emergencies, for example, a microgrid might disconnect and operate independently of the rest of the distribution system in order to secure continuity of service to the consumers within its boundaries, even though this measure would mean poor voltage quality. In such a microgrid, voltage support might be insufficient to maintain the voltage at all load buses within the desired operational limit, e.g., $\pm 5\%$. As a result, consumers might receive a utilization voltage within a tolerable range B rather than within the acceptable range A defined by the ANSI C84.1-20111 standard [128]. The stiffness of a microgrid can significantly change from one operating condition to another, depending on the available generation and loading level. In this regard, voltage instability, also known as load instability, can occur unexpectedly in islanded microgrids because some load buses might be dragged into a voltage instability problem due to the limited voltage support during contingencies [129]. A contingency can be defined as an event that results in the failure of at least one component and that can possibly occur in the future with some degree of uncertainty associated with how, when, and where it can happen [130]. A power grid with N components is said to be N-K contingency secured if it can remain intact after K components fail to operate within their operational limits and maintain an adequate loadability margin. During a contingency, the loadability of an islanded microgrid can be defined as the maximum deliverable power as a percentage of the base load that the microgrid can deliver during both islanding and the contingency before a voltage collapse phenomenon develops.

The motivation for the work presented here was a desire to extend the concept of maximum loadability to ac/dc hybrid microgrids (HMGs) and to include consideration of their unique features such as the inherent coupling between the frequency and dc voltage. The goal was to unveil useful information about voltage instability/collapse in islanded HMGs during contingency events and to lay the groundwork for the development of reliable voltage stability analysis tools and indices for such systems. Specific objectives were to answer the following questions: Does the problem of voltage instability/collapse exist in islanded but healthy microgrids[1], or can it exist only in microgrids with limited voltage

[1] A healthy microgrid is defined in this thesis as the microgrid that is contingency-free and has sufficient power to supply its load during normal operating conditions.

support and under major contingencies? Is there such a PV curve in dc microgrids? What kind of bifurcations can exist in dc microgrids? Can microgrids have broad loadability boundaries despite islanding conditions and limited voltage support resources? What are the key factors that affect microgrid loadability? How would the loadability of an islanded microgrid be affected when it interfaces with an adjacent microgrid compared to the stand-alone case?

In this chapter, the analysis that addresses these questions is divided into four sections. Section 5.2 describes the problem of voltage collapse in islanded ac/dc microgrids. Section 5.3 presents case studies and a discussion of the results obtained. Section 5.4 provides concluding remarks.

5.2 Problem Description

In autonomous ac microgrid operation, a subset of DG units are assigned to regulate the voltage at their terminals collaboratively, using droop characteristics and employing local measurements. The implementation of (ω-P) and (V-Q) droop characteristics through an external power loop in the DG local controllers provides the reference to the voltage controllers. Accordingly, the voltage at the voltage-controlled buses is controlled within a predefined operating range. In contrast, the voltage at the load buses is always neither controlled nor monitored. In fact, the voltages of such load buses could decline beyond the acceptable minimum voltage due to a slowly accumulating load increase. Additionally, in practice, not all DGs control the voltage but rather might control the current, even though they could be equipped with droop controllers. Further, during overloading and islanding conditions, DGs with voltage support capability may have to operate near their limits. Some of these DGs could reach their limits due to a subsequent contingency and then switch to current-control mode. As a consequence, the entire microgrid could possibly lose voltage control and eventually collapse. It is thus critically important for the microgrid supervisory controller to maintain a secure loadability margin during credible contingencies.

The concept of steady-state voltage stability can be extended to include islanded HMGs with constant power loads and can be described with the help of a simple four-bus ac/dc system whose one-line diagram is depicted in Figure 5.1. The ac side includes one droop-controlled ac DG unit supplying a constant power to an ac load whose characteristics are described by its kVA consumption $S_{D,ac}$ and lagging power factor $p.f$. The dc side consists of one droop-regulated dc DG and one dc load whose steady-state behavior is characterized by constant power consumption $P_{D,dc}$. The ac DG supplies the ac load via two ac line circuits. Both line circuits have equal X/R ratios. The dc DG delivers power

to the dc load through two dc feeders, each of which is represented in steady state by a series resistance R_{dc}.

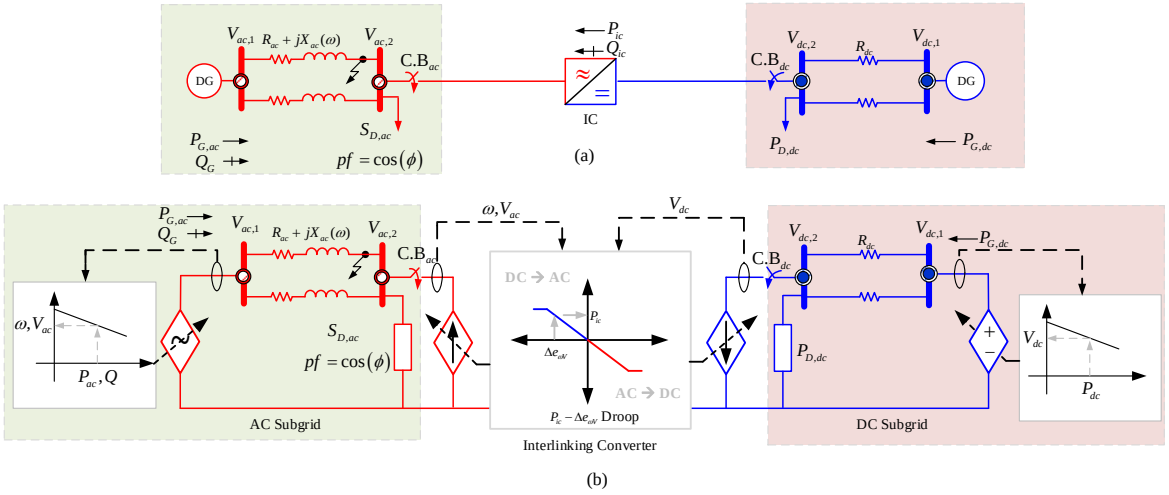

Figure 5.1. A four-bus droop-controlled ac/dc hybrid microgrid: (a) one-line diagram (b) equivalent circuit with the droop characteristics.

The sequence of events is to interrupt one line circuit in each subgrid (N-1 contingency in each subgrid) as follows:

1. **Event 0**: No interfacing and no contingency in either subgrid
2. **Event 1**: Single Contingency in both subgrids before interfacing (Tripping one ac/dc line circuit)
3. **Event 2**: Single Contingency in AC Side with interfacing

The power flow equations at the ac/dc load buses can be written as follows:

$$-P_{D,ac} + f_{p,ac}(V_{ac}, \delta, \omega) + P_{ic} = 0. \tag{5.1}$$
$$-Q_{D,ac} + f_{q,ac}(V_{ac}, \delta, \omega) + Q_{ic} = 0. \tag{5.2}$$
$$-P_{D,dc} + f_{p,dc}(V_{dc}) - P_{ic} = 0. \tag{5.3}$$

where $f_{p,ac}$ and $f_{q,ac}$ are the active and reactive power flow injections at the ac load bus, respectively, and $f_{p,dc}$ represents the active power flow injection at the dc load bus. The ac/dc power flow injections are defined by the following:

$$f_{p,ac}(V_{ac},\delta,\omega) = \frac{V_{ac,1}V_{ac,2}}{\sqrt{R_{ac}^2 + X_{ac}(\omega)^2}}\cos\left(\delta+\theta\right) - \frac{V_{ac,2}^2 R_{ac}}{R_{ac}^2 + X_{ac}(\omega)^2}. \tag{5.4}$$

$$f_{q,ac}(V_{ac},\delta,\omega) = \frac{V_{ac,1}V_{ac,2}}{\sqrt{R_{ac}^2 + X_{ac}(\omega)^2}}\sin\left(\delta+\theta\right) - \frac{V_{ac,2}^2 X_{ac}}{R_{ac}^2 + X_{ac}(\omega)^2}. \tag{5.5}$$

$$f_{p,dc}(V_{dc}) = \frac{V_{dc,1}V_{dc,2} - V_{dc,2}^2}{R_{dc}}. \tag{5.6}$$

P_{ic} and Q_{ic} represent the active and reactive power transfer to the ac side, respectively, and are determined by (2.8) and (2.12) in chapter 2. More details about the power flow analysis of islanded HMGs can be found in chapter 3 or in a previous study published by the author [131].

Prior to the interfacing of both sides, the ac voltage at load bus 2 can be derived from (5.1) and (5.2), and from (5.4) and (5.5), assuming that the interlinking converter (IC) transfers constant active and reactive power to the ac side, as expressed by the following:

$$\begin{aligned} V_{ac,2}^4 + \left[2\big(R_{ac}(P_{D,ac}-P_{ic}) + X_{ac}(Q_{D,ac}-Q_{ic})\big) - V_{ac,1}^2\right]V_{ac,2}^2 \\ +(R_{ac}^2+X_{ac}^2)\big((P_{D,ac}-P_{ic})^2 + (Q_{D,ac}-Q_{ic})^2\big) = 0. \end{aligned} \tag{5.7}$$

The per-unitized ac load voltage can be obtained accordingly from (5.7) after being expressed as per-unit and parametrized with a loading factor λ_{ac}:

$$V_{ac,2,pu} = \sqrt{(\frac{1}{2}+K) \pm \sqrt{K^2 - K - \lambda_{ac}^2 P_{D,ac,pu}^2(1+tan^2(\phi)) + \frac{1}{4}}}. \tag{5.8}$$

where K is defined as

$$K = \Big(R_{ac,pu}(\lambda_{ac}P_{D,ac,pu} - P_{ic,pu}) + X_{ac,pu}(\lambda_{ac}Q_{D,ac,pu} - Q_{ic,pu})\Big). \tag{5.9}$$

$P_{D,ac,pu}$ and $Q_{D,ac,pu}$ are the active and reactive power demands of the ac load in per-unit values, respectively, and are defined by

$$P_{D,ac,pu} = S_{D,ac,pu} \times pf, \quad Q_{D,ac,pu} = S_{D,ac,pu}\sin\left(\cos^{-1}(pf)\right). \tag{5.10}$$

where $p.f. = cos(\phi)$.

As is evident from (5.8)-(5.10), the ac load voltage is affected largely by the ac feeder X/R ratio, the load size, and the load operating power factor. In droop-based ac microgrids,

the reactive power droop characteristics can also alter system loadability. In this simple example, since the ac side has only one droop-based DG that controls the voltage, the frequency and voltage can be assumed to follow their references. Thus, the DG can be represented by a constant (V-f) bus, with the frequency and voltage being replaced by their reference values. The loading factor λ_{ac} is incorporated into (5.8) in order to enable an investigation of the loadability and voltage stability of the microgrid. The loading factor is then increased in incremental steps, and the PV curve that tracks the steady-state behaviour of the ac voltage at load bus 2 is graphed as depicted in Figure 5.2 (a). Figure 5.2 (a) also shows that the load voltage drops quadratically with the loading up to the point at which the voltage breaks down. This point is the saddle-node bifurcation (SNB), as shown on the PV curve in Figure 5.2 (a). Figure 5.2 (a) indicates that the ac side has a broad loadability margin during normal operation, meaning that the critical loadability due to SNB, $\lambda_{ac,SNB,0}$, is at a substantial distance from the installed capacity. The limit-induced bifurcation (LIB) also happens at a loadability level beyond the installed capacity of the microgrid: $\lambda_{ac,LIB,0} > 1$. AC microgrids with no contingencies are thus less likely to be subject to a voltage collapse problem. A single contingency is then introduced by interrupting one of the line circuits between ac buses 1 and 2. The circuit-tripping event is represented by doubling the feeder impedance. As illustrated in Figure 5.2 (a), a single contingency causes the SNB to appear while the microgrid is still able to deliver power: $\lambda_{ac,SNB,1} < 1$. However, due to the distinctive features of ac microgrids, such as the distributed nature and closeness of the DERs to the loads and the low X/R ratios of the distribution feeders, the SNB might be not provoked during an N-1 contingency. In

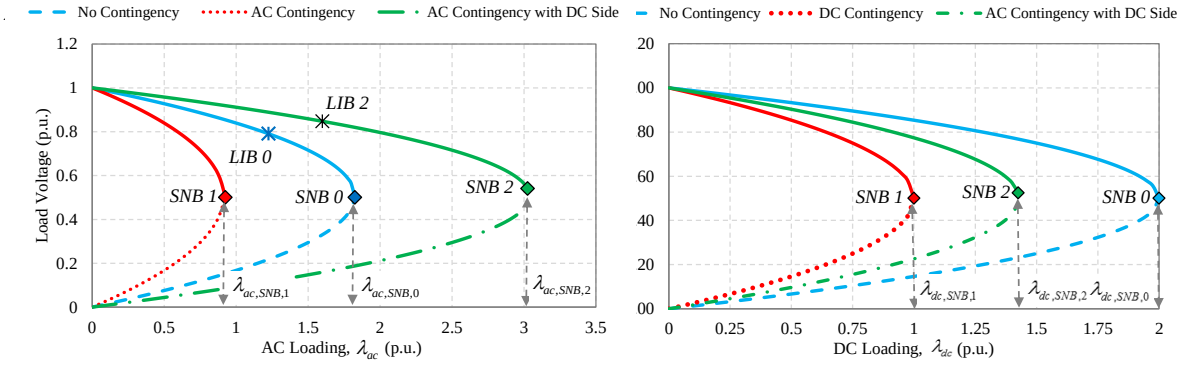

Figure 5.2. PV curves for a stand-alone two-bus ac/dc microgrid: (a) ac subgrid (b) dc subgrid.

the same way, the dc load voltage can be derived when the IC transfers constant active

power to the ac side, as defined by

$$V_{dc,2} = \frac{1}{2}\left(V_{dc,1} \pm \sqrt{V_{dc,1}^2 - 4R_{dc}\left(P_{D,dc} + P_{ic}\right)}\right). \tag{5.11}$$

As can be observed in (5.11), the dc load voltage is in a quadratic relation with the dc feeder resistance and the load size. Further, in islanded dc microgrids, if $V_{dc,1}$ in (5.11) is regulated based on droop characteristics, which is probably the case, the load voltage is also affected by the droop parameter settings. For the sake of analysis, (5.11) can be written in per-unitized form as

$$V_{dc,2,pu} = \frac{1}{2}\left(1 \pm \sqrt{1 - 4\left(\lambda_{dc}P_{D,dc,pu} + P_{ic,pu}\right)}\right). \tag{5.12}$$

From (5.12), the maximum servable dc load in per-unit values can be defined such that $1 - 4(\lambda_{dc}P_{D,dc,pu} + P_{ic,pu}) \geq 0$ which implies that

$$\lambda_{dc} \leq \frac{1}{4(P_{D,dc,pu} + P_{ic,pu})}. \tag{5.13}$$

To investigate the voltage stability and plot the PV curve at the dc load bus, (5.12) is parameterized with the loading factor λ_{dc} as depicted in Figure 5.2 (b): $\lambda_{dc,SNB,0} > 1$. As with its ac counterpart, the dc microgrid without contingencies tends to have wide-ranging loadability, as demonstrated in Figure 5.2 (b): $\lambda_{dc,SNB,0} > 1$. Figure 5.2 (b) shows that, in islanded dc microgrids during a contingency, the SNB could also be stimulated because of the nature of dc systems and dc droop characteristics: the voltage is directly coupled with the active power and can deviate from its nominal value. However, as a meritorious advantage, a LIB related to insufficient reactive power support does not exist in dc systems.

Interlinking ac and dc microgrids can have a substantial influence on the loadability of each microgrid. In an islanded ac/dc HMG, the amount and direction of power transfer as well as the IC droop characteristics can significantly change the loadability of both subgrids. In the example presented here, the IC transfers active and reactive power to the ac side. Figure 5.2 (a) indicates that the loadability of the ac subgrid that is receiving power is enlarged: $\lambda_{ac,SNB,2} > \lambda_{ac,SNB,0}$. In contrast, the loadability of the dc subgrid that is transmitting power to the ac side has shrunk, as shown in Figure 5.2 (b). The figure also reveals that, because of their vulnerability to voltage instability upon transmitting power, special care should be given to the terminal ac/dc buses and their voltage monitor. From an operational security perspective, the power-transferring subgrid can limit the amount of power transfer once its loadability approaches a prespecified loadability margin.

5.3 Case Studies

An analysis of voltage stability during contingencies was carried out for a 12-bus ac/dc HMG whose single-line diagram is depicted in Figure 5.3. The test system comprises one ac subgrid and one dc subgrid. Both subgrids are evenly loaded: 42 kVA for the ac side and 42 kW for the dc side. The locations and ratings of the ac and dc loads are shown in Figure 5.3. Before interfacing, the base load in each side is supplied by two DERs. The DER capacities in the ac and dc subgrids are 45 kVA and 45 kW, respectively. The subgrids are interfaced via two identical droop controlled ICs with a capacity of 10 kVA each. The DER and IC droop characteristics are tabulated in Table 5.1. The base kVA and ac/dc voltages are selected as 10 kVA and 208/600 V. The operating range for the frequency and ac/dc voltage are ±1% and ±5%, respectively. The tie lines and IC circuit breakers are initially open. The test system was designed based on an N-1 contingency in order to demonstrate that an N-1 contingency-based microgrid design might fail to capture the development of a voltage collapse phenomenon during severe events such as extreme weather conditions.

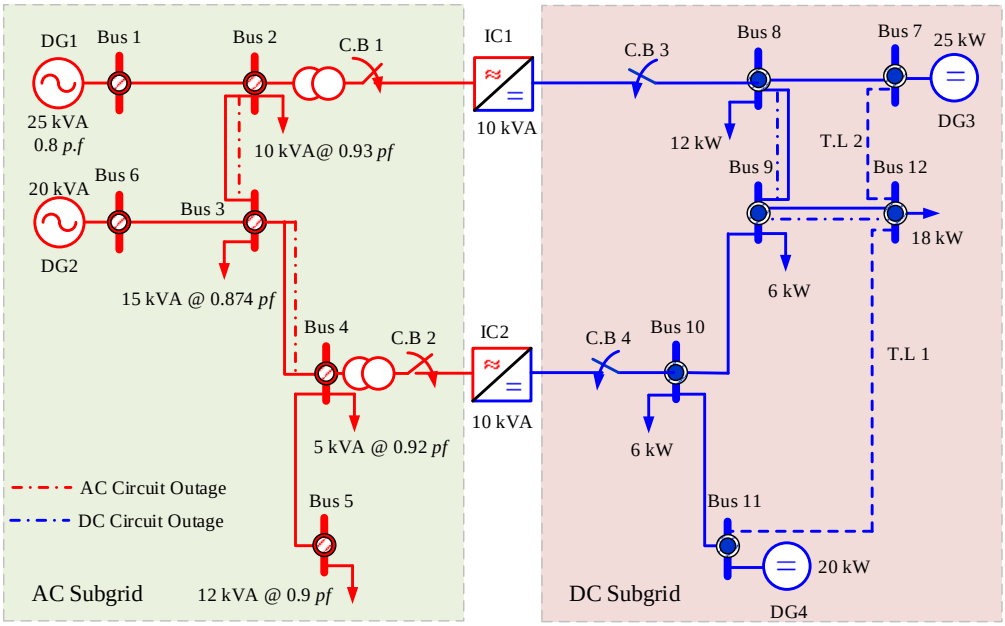

Figure 5.3. 12-bus ac/dc hybrid microgrid.

The sequence of simulated events subsequently interrupts two circuits in each subgrid as follows:

- **Event 0**: No contingency
- **Event 1**: Single Contingency (Tripping one ac circuit of line 2-3)
- **Event 2**: Double Contingency (Tripping one ac circuit of lines 2-3 and 3-4)
- **Event 3**: Single Contingency (Tripping one dc circuit of line 8-9)
- **Event 4**: Double Contingency (Tripping one dc circuit of lines 8-9 and 9-12)

Table 5.1. Droop Parameters of Distributed Energy Resources and Interlinking Converters

AC	**DER#**	$m_{p,ac}$ (Hz/W)	n_q (V/var)	ω^* (p.u.)	V^*_{ac} (p.u.)
	DER1	2.40×10^{-5}	6.93×10^{-4}	1.01	1.05
	DER2	3.00×10^{-5}	8.67×10^{-4}	1.01	1.05
DC	**DER#**	$m_{p,dc}$ (V/W)		V^*_{dc} (p.u.)	
	DER1	1.20×10^{-3}		1.0	
	DER2	1.50×10^{-3}		1.0	
IC	**IC#**	γ_p (1/W)	γ_q (V/var)	$V^*_{ic,ac}$ (p.u.)	
	IC1	2.0×10^{-4}	1.04×10^{-3}	1.0	
	IC2	2.0×10^{-4}	1.04×10^{-3}	1.0	

5.3.1 Impact of a Contingency on the Loadability of the AC Microgrid

Their classification as weak grids means that microgrids are not immune to contingencies, and unexpected contingencies can cause system loadability to deteriorate. Figure 5.4 illustrates the steady-state behaviour of the voltage at load bus 5 before and after the occurrence of contingencies on lines 2-3 and 3-4 (events 1 and 2) during the operation of the ac subgrid in stand-alone mode. A number of observations can be made based on Figure 5.4. First, contingency-free microgrids typically have wide loadability margins and

are less likely to be subject to voltage instability during normal operation. In Figure 5.4, the ac microgrid loadability is $\lambda_{ac,LIB,0} = 1.325$, which permits a load increase of approximately 32.5 % of the base load. Second, a contingency and shortage of reactive power resources can precipitate in LIB development, causing the islanded microgrid to leave the voltage stability region. For the ac subgrid in Figure 5.4, a contingency on line 2-3 (event 1) leads to the appearance of LIB at a loadability of $\lambda_{ac,LIB,1}$ equal to 0.925, resulting in the loss of 7.5 % of the servable base load despite the fact that the installed capacity of the ac microgrid is sufficient to supply the entire base load: $\lambda_{ac,base} = 1$. Third, multiple contingencies, interrupting another circuit (event 2), causes LIB to develop sooner at a loadability of $\lambda_{ac,LIB,2}$ equal to only 82.5 % of the base loadability, shrinking the number of stable equilibrium points on the PV curve and making it practically impossible to operate at a loading level beyond the LIB. These results suggest that the planning and operation criteria for islanded ac microgrids should be designed based on N-2 contingencies in order to ensure the security of an islanded system after credible contingency events.

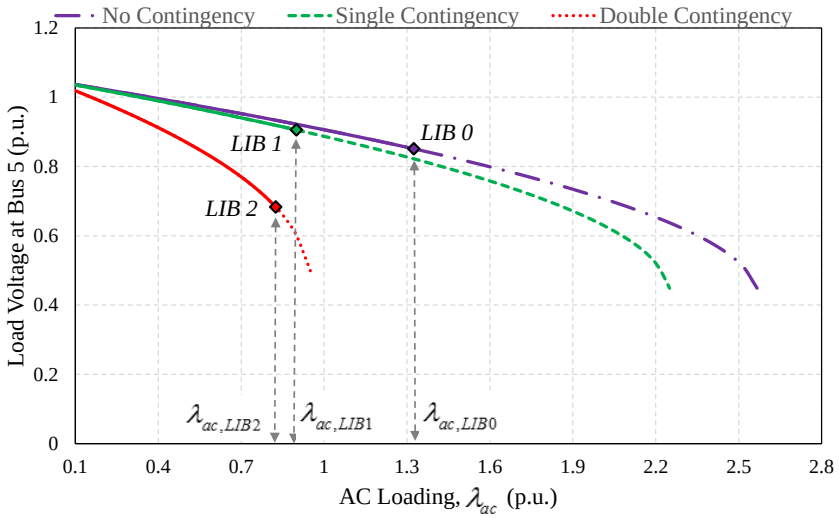

Figure 5.4. AC subgrid loadability before and after contingencies.

5.3.2 Impact of Reactive Power Droop Gains on AC Microgrid Loadability

In droop-controlled ac microgrids, (V-Q) droop characteristics are based on an assumed existence of tight coupling between the DER terminal voltage and the DER reactive power

output. The slope of the (V-Q) droop characteristics shown in Figure 5.1 (b) determines how far the operating voltage can deviate from its reference V_{ac}^{*}. Adjusting the reactive power droop gain, which is the slope of the (V-Q) curve, affects system loadability. Figure 5.5 depicts four scenarios for the droop gain n_q settings. Scenarios 1 and 2 are the pre- and post-contingency events (events 0 and 1) with the static droop gains $n_q = n_{q,0}$ provided in Table 5.1. In scenario 3, the droop gain n_q is set to a lower value than the base value, $n_q = 0.5n_{q,0}$, while in scenario 4, the droop gain n_q is set to a higher value: $n_q = 1.5n_{q,0}$. From Figure 5.5, setting the reactive power droop gain to $n_q = 0.5n_{q,0}$ results in 30% of the base load unable to be supplied: $\lambda_{ac,LIB,2} = 0.7$, while a reactive power droop gain value of $n_q = 1.5n_{q,0}$ gives better loadability: $\lambda_{ac,LIB,3} = 1.05$, allowing the load to increase by 5%. Thus, although flatter reactive power droop characteristics result in better voltage regulation, loadability can be impaired, as is evident with scenario 3. A key conclusion from this case study is therefore that reactive power droop characteristics can broaden or worsen microgrid loadability during extreme events. There is also an optimal set of droop parameters that yield maximum loadability. A droop characteristics designer should thus consider the likelihood of a contingency by combining optimization and contingency analysis.

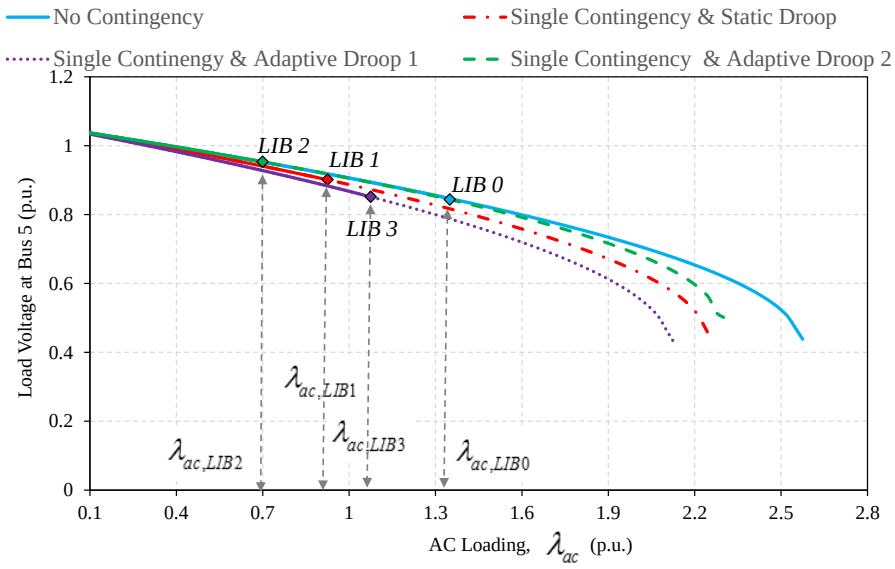

Figure 5.5. AC subgrid loadability versus reactive power droop coefficients.

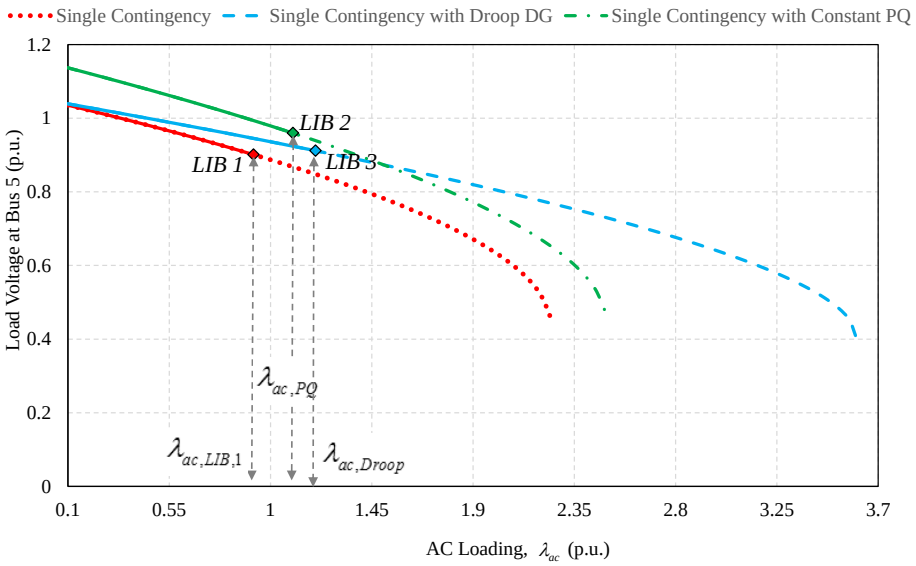

Figure 5.6. AC subgrid loadability versus DER location and control.

5.3.3 Impact of DER Location and Control Mode on AC Microgrid Loadability

The location, size, and control strategy of a DER can significantly influence microgrid loadability. Figure 5.6 shows the ac subgrid loadability during single contingency (event 1), and two other scenarios. The first scenario is the occurrence of event 1, but when DER 2 at bus 6 is replaced with two identical DERs of 10 kVA each at buses 4 and 6, the DER at bus 4 supplies constant power at a lagging power factor of 0.8. This scenario is labelled as (Single Contingency with Constant PQ DG) in Figure 5.6. The second scenario is the post-contingency one, but in this case, the DER 2 is replaced by two identical droop-controlled DERs: one at bus 4 and one at bus 6. This scenario is labelled as (Single Contingency with Droop DG) in Figure 5.6. As can be observed, regardless of the control strategy, the connection of a DER with the proper size and location increases microgrid loadability: $\lambda_{ac,PQ} = 1.125$ and $\lambda_{ac,Droop} = 1.225 > \lambda_{ac,LIB,1} = 0.95$. However, loadability can be further increased if the DER control strategy is selected appropriately. Figure 5.6 demonstrates that a droop-controlled DER yields better loadability than a constant power DER: $\lambda_{ac,Droop} > \lambda_{ac,PQ}$. The superiority of droop control over constant power control is that droop control not only allows a greater load to be served but also provides the

necessary voltage support during islanding and contingencies. These findings justify the application of droop control in islanded microgrids. They should also confirm for system planners the value of selecting microgrid loadability as a key criterion in DER planning.

5.3.4 Impact of Shunt Capacitors on AC Microgrid Loadability

Shunt capacitors are deemed to be effective loadability boosters for ac systems during both normal and abnormal conditions. Figure 5.7 shows that placing a shunt capacitor of 6 kvar at the weakest bus, bus 5, moves the LIB point away to the right: from $\lambda_{ac,LIB,1} = 0.925$ to $\lambda_{ac,LIB,2} = 1.15$. It is thus technically advisable to apply shunt capacitors in islanded ac microgrids in order to account for credible contingencies and to maintain a reactive power reserve, since they remain the least expensive solution. Nevertheless, if not properly sized and sited, shunt capacitors may cause reactive power over compensation at some load buses, as a result of which, voltage collapse could occur within acceptable voltage limits, creating an inability to identify voltage collapse based only on the monitoring of the voltage magnitude. For further investigation, the shunt capacitor size can be varied incrementally, and the loadability that corresponds to the LIB can be shown graphically.

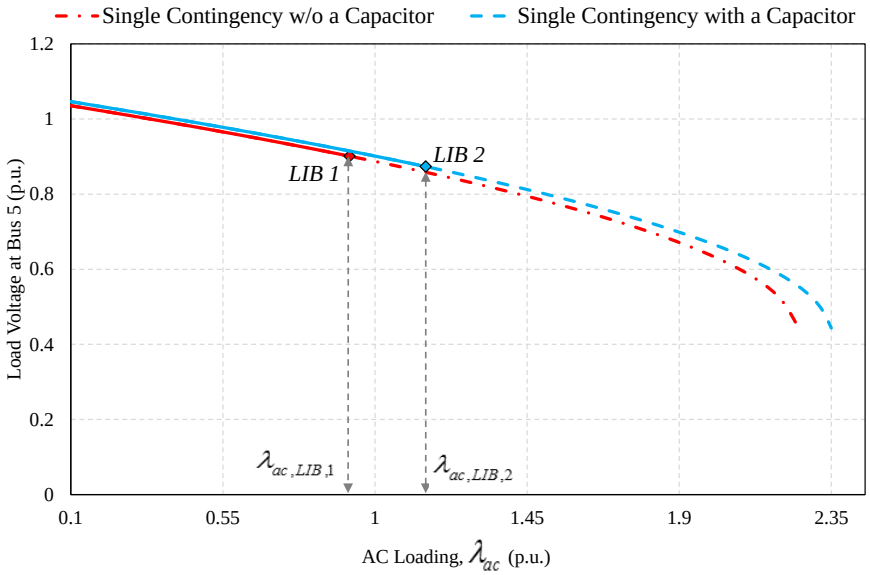

Figure 5.7. AC subgrid loadability versus shunt capacitor placement.

5.3.5 Impact of a Contingency on the Loadability of the DC Microgrid

DC microgrids can be subject to voltage collapse due to SNB. The dc microgrid depicted in Figure 5.8 has a maximum loadability of $\lambda_{dc,SNB,0}$ of 2.35 before a contingency. As indicated in Figure 5.8, a contingency in one of the line 8-9 circuits (event 3) reduces the servable dc load to $\lambda_{dc,SNB,1} = 1.875$. Another contingency (event 4) leads to a working loadability of $\lambda_{dc,SNB,2} = 0.95$, which is below the base loadability, with the servable load reduced by 5%. These results suggest that the maximum loadability of a healthy dc microgrid with $\lambda_{dc,SNB,0} > 1$ can shrink to a value of $\lambda_{dc,SNB} < 1$ due to a cascading contingency. Two types of action can be taken to protect the microgrid from collapse: proactive and corrective. A proactive action would be to maintain an adequate reserve loadability margin, such as 5% of the maximum loadability, in order to save the microgrid from potential collapse. A corrective action would be to curtail the unserved demand before the voltage leaves the stability region. From a planning perspective, the successful islanding of dc microgrids should be checked based on N-2 contingency criteria. From an operational prospective, under voltage dc relays should be put in place in order to avoid any probable voltage collapse events.

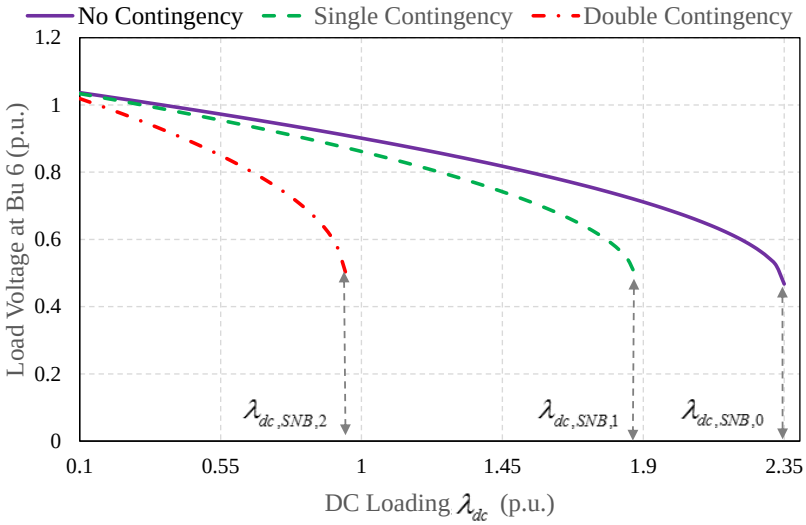

Figure 5.8. DC subgrid loadability before and after contingencies.

5.3.6 Impact of Active Power Droop Gains on DC Microgrid Loadability

As with ac microgrids, the loadability of dc microgrids can shrink or expand by means of adjustments to the droop parameters, $m_{p,dc}, V_{dc}^{*}$, of droop-based DERs. Figure 5.9 provides a comparison of the effect of fixed and adaptive droop gains on dc microgrid loadability during a contingency. Scenarios 1 and 2 represent pre-contingency and double contingency (event 0 and 2) with static droop gains. Two other scenarios were considered: double contingency with dynamic droop gains equal to twice the static droop gain values and double contingency with droop gains equal to one-fifth of the static droop gains: $m_{p,dc} = 0.2m_{p,dc0}$. The third and forth scenarios are labeled as (Double Contingency & Droop 1 and 2). As illustrated in Figure 5.9, adjustment of droop gain values can enhance loadability during a contingency, as in scenario 3: $\lambda_{dc,SNB,2} = 1.8 > \lambda_{dc,SNB,1}$. Further, scenario 4 shows that the loadability of a dc microgrid with a double contingency can be re-established if the droop gains are adjusted appropriately: $\lambda_{dc,SNB,4} = \lambda_{dc,SNB,0} = 2.35$.

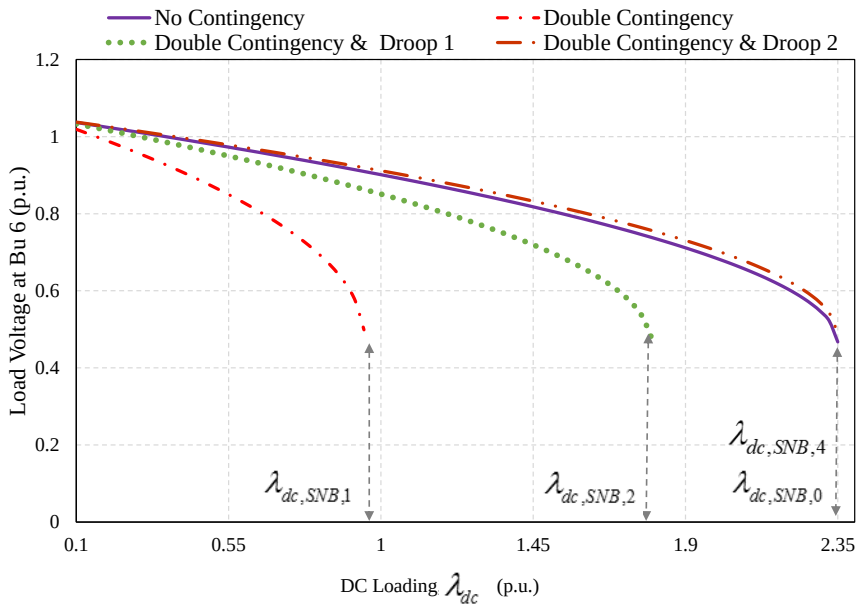

Figure 5.9. DC subgrid loadability versus active power droop coefficients.

The adjustment of the reference voltage command V_{dc}^{*} can also restore part of the initial microgrid loadability prior to the contingency. Once an islanded microgrid is diagnosed with a contingency, the supervisory controller can thus be programmed to optimize and

broadcast the optimal droop parameter settings via a low-bandwidth communication link to the local DER controllers. As a side note with respect to droop parameter adjustment, the droop controllers will lose power-sharing accuracy if the new set of droop parameters are not optimized based on accurate power sharing. Exact power sharing implicitly guarantees maximum loadability since the installed capacity of the system is utilized efficiently.

5.3.7 Impact of Network Reconfiguration on DC Microgrid Loadability

The severity of a contingency event is partially dependent on how the microgrid is configured. Figure 5.10 presents a comparison of the loadability of four scenarios: no contingency (event 0), double contingency with a radial topology (event 2), double contingency with a weakly meshed topology, and double contingency with a strongly meshed topology. As indicated in Figure 5.10, a cascaded contingency in the dc microgrid with a radial topology negatively affects loadability: $\lambda_{dc,SNB,1} = 0.95 < 1$. Reconfiguring the microgrid to be weakly meshed by closing tie line 1-12 increases the loadability of the microgrid under a contingency to $\lambda_{dc,SNB,2} = 3.825$. A further reconfiguring action of closing tie line 11-12 increases the loadability to $\lambda_{dc,SNB,3} = 4.8$.

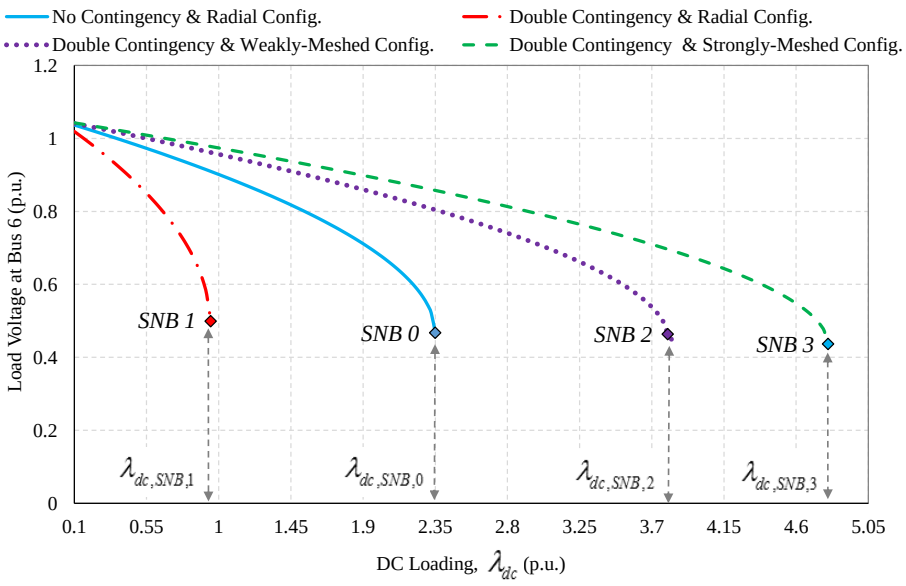

Figure 5.10. DC subgrid loadability versus network topology.

Based on these findings, 1) dc microgrids with a radial topology have the least loadability while meshed-networked microgrids have the highest, and 2) reconfiguration during a contingency can not only restore the previous loadability margin but can also further enhance system loadability. A microgrid operator could thus consider microgrid reconfiguration once a severe contingency has occurred. Figure 5.10 also suggests that system planners should take loadability into account when designing a topological layout for a microgrid.

5.3.8 Impact of AC and DC Microgrid Interfacing on the Loadability of the AC Side under a Contingency

Interfacing ac and dc microgrids can provide operational benefits for a microgrid that is at potential risk of voltage collapse. Figure 5.11 depicts the LIBs resulting from a single contingency (event 1) in an ac subgrid that operates 1) in stand-alone mode and 2) in conjunction with an adjacent dc microgrid. In this case study, the initial power transfer takes place from the dc to the ac side. As can be seen in Figure 5.11, the ac subgrid operating in stand-alone mode is subject to LIB at a loadability level of $\lambda_{ac,LIB} = 0.925$

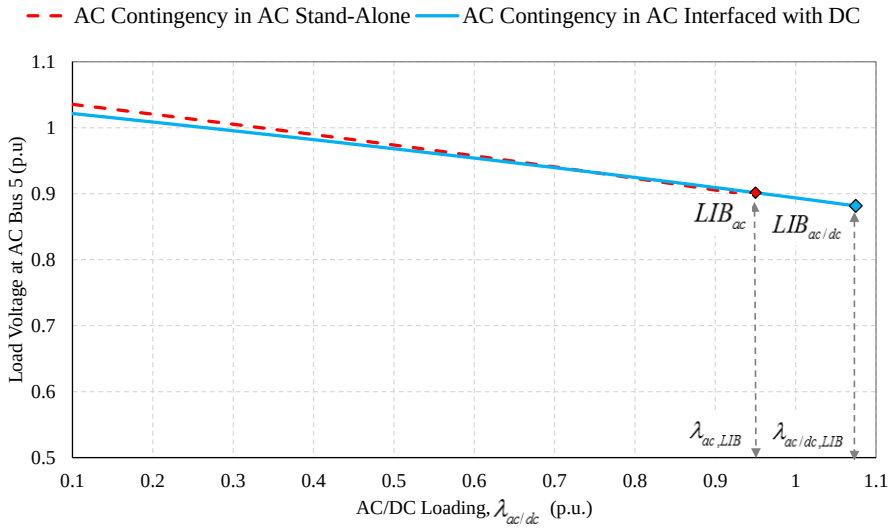

Figure 5.11. AC subgrid loadability during a contingency before and after interfacing with the dc subgrid.

after a single contingency (event 1). However, interlinking the contingency-contaminated ac microgrid with a healthy dc microgrid moves the LIB beyond the base loadability level for the same contingency: $\lambda_{ac/dc,LIB} = 1.075 > \lambda_{ac,LIB}$. These results indicate that the loadability margin of a single microgrid while interfaced with another microgrid is greater than its loadability in the stand-alone case. The superior loadability of a microgrid interlinked with a neighbouring microgrid via a droop-based IC is attributable to the fact that the neighbouring microgrid serves as a droop-controlled current source whose droop characteristics are dictated by the loading of both microgrids.

5.3.9 Impact of AC and DC Microgrid Interfacing on the Loadability of the DC Side under a Contingency

The previous case study demonstrated that hybridizing ac and dc microgrids can have a favourable effect on a subgrid that is affected by a contingency. However, this advantage is not always the case but instead depends on the amount and direction of the power being transferred between the neighbouring microgrids. For the system plotted in Figure 5.3, the active power is initially being transferred from the dc to the ac side because of the relatively high loading of the ac subgrid compared to its dc neighbour. If multiple contingencies are applied to the dc subgrid (event 4) when it is providing power to the ac subgrid, the SNB appears earlier in the dc subgrid ($\lambda_{dc/ac,SNB} = 0.75$) than it does in the stand-alone case ($\lambda_{dc,SNB} = 0.95$), as shown in Figure 5.12.

5.4 Discussion

This chapter has presented an investigation of the possibility of voltage instability/collapse in islanded ac/dc HMGs during contingency conditions. Based on the voltage stability analysis, it can be concluded that, regardless of their type, whether ac, dc, or ac/dc, healthy microgrids are unlikely to be subject to a voltage instability/collapse problem even during islanding. This finding can be attributed to the distinctive features of microgrids: the short feeders, the proximity of DERs to the load, and the constant impedance characteristics of many ac/dc loads. However, voltage instability can be witnessed in islanded microgrids under some circumstances, among which are the occurrence of multiple contingencies, the presence of DERs with limited reactive power capabilities, and the proliferation of modern loads that have constant power characteristics. Therefore, prior to microgrid implementation, planners and operators of microgrids should address "what if" scenarios

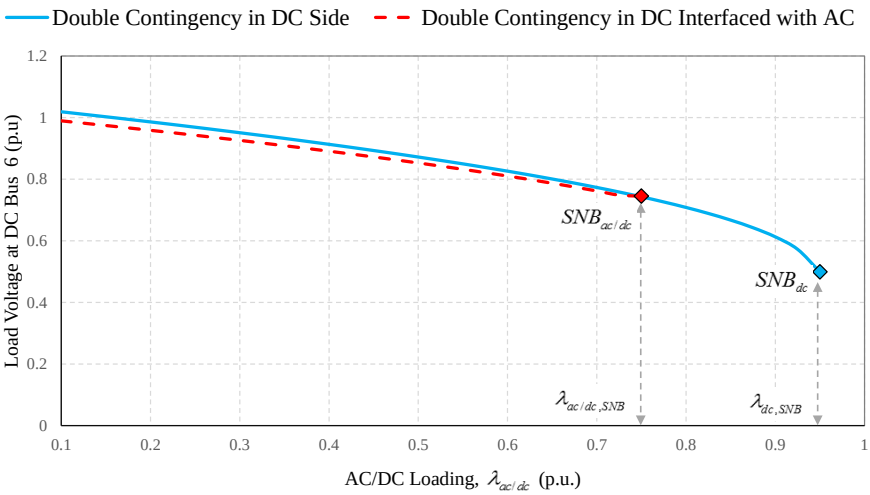

Figure 5.12. DC subgrid loadability during a contingency before and after interfacing with the ac subgrid.

and identify the most severe events that can occur during islanding and contingencies. The analysis presented here has also revealed that, when ac and dc microgrids are hybridized, the loadability margin of a subgrid that is under a contingency is increased, thus alleviating the effects of single-element or multiple-element contingencies. However, if the power-transferring subgrid is subjected to an unexpected contingency, the entire HMG is at risk of collapse. Microgrid planners are therefore advised to design each subgrid of an HMG based on N-2 criteria for three main reasons: 1) The N-1 contingency test might not reveal the possibility of and vulnerability to voltage collapse within the base loadability. 2) Compared to large-scale power systems, the small size of microgrids facilitates online and offline N-2 contingency computations. 3) Each subgrid can be a stand-alone system that operates independently of the other subgrid, which might not be available during contingencies.

Several proactive measures can be taken to boost the immune system of an islanded microgrid against voltage collapse.

1. The voltage instability in islanded microgrids with limited voltage support and constant power loads can be mitigated by using the capability of smart inverters of PV panels and modern converter-based loads such electric vehicles to supply reactive power, and hence; increasing the power transfer capability of the islanded system [124].

2. The load dynamics can be decoupled from the system dynamics by using the concept of power buffering [129] and [132].

3. Another proactive step to further increase the system loadability margin is to equip each applicable DG and controllable load with a power curtailment scheme. Alternatively, under voltage relays can be installed at the premise of distribution transformers to shed in discrete steps a portion of controllable loads in attempt to recover the voltage in case of contingencies.

4. Although small-scaled synchronous-based and converter-based DGs have fast response, reserve is still needed for microgrids in case of islanding and contingency conditions.

5. Due to their fast response, a portion of the inverter-based DG capacities can be assigned for reactive power reserve. The reactive power reserve can be adaptively assigned based on the available generation.

6. Due to their flexibility, distributed storage units can be used to preserve a desired loadability margin.

7. Identifying the set of weak load buses, the load buses that are the most prone to voltage decline. Using a load shedding mechanism, the load at the weak buses can be curtailed to move the system away from the point of voltage collapse.

The previous two chapters have discussed two major operational aspects of HMGs during normal conditions (the power sharing problem) and abnormal conditions (the voltage collapse problem). Nevertheless, in HMGs that include elements that are stochastic in nature such as renewable energy resources (RESs) and electric vehicles (EVs), difficulties in energy management can arise even during interfacing with the main grid. Energy management under uncertainty during grid interfacing is the subject of the next chapter.

Chapter 6

Stochastic Centralized Dispatch Scheme for AC/DC Hybrid Smart Grids

6.1 Introduction

The future ac/dc hybrid smart grid with two-communication capability facilitates the central controller to coordinate among various ac/dc energy resources and loads with a high degree of observability and controllability. Figure 6.1 shows the general structure of an ac/dc hybrid smart grid with a centralized controller. As depicted in this Figure, the centralized controller requests information from the local distributed energy resources (DERs) and controllable loads which in turn periodically send the information back to the central controller. With the full knowledge about the system, the central controller also determines when it is technically and economically feasible to interface both ac and dc sides together and with the utility grid. The use of this type of ac/dc hybrid topology will result in considerable benefits for the distribution system, as already discussed in section 2.2. The achievement of these benefits is predicated on effective key design elements in the ac/dc hybrid architecture: identification of an optimal topology, selection of the dc voltage level and IC ratings, sizing and siting of the DERs, and development of a coordinated dispatch scheme [133], [121].

An optimal ac/dc hybrid topology can be adopted at both the secondary distribution level (low voltage (LV)) and the primary distribution level (medium voltage (MV)). At the secondary level, the dc grid can be designed as an embedded layer in the existing LV ac grid, resulting in a bilayer LV distribution system [134]. The dc layer, which connects dc loads such as electric vehicles (EVs) and residential rooftop photovoltaic (PV) panels, is integrated with its counterpart ac layer at the distribution transformers [134]. At the primary level, the dc grid can be designed as a stand-alone grid tied to its counterpart ac grid via interlinking converters (ICs), creating an ac/dc hybrid MV distribution system. The dc grid connects large dc loads, such as parking lots in commercial areas, and dc DERs, such as energy storage systems (ESSs) that are owned by investors and the utility. With respect to the dispatch scheme, an essential feature is its ability to account for

the uncertainties inherently associated with renewable energy, demand, and energy price. The goal of the research presented in this chapter was therefore to develop a stochastic centralized dispatch scheme for ac/dc hybrid smart grids that includes consideration of these uncertainties.

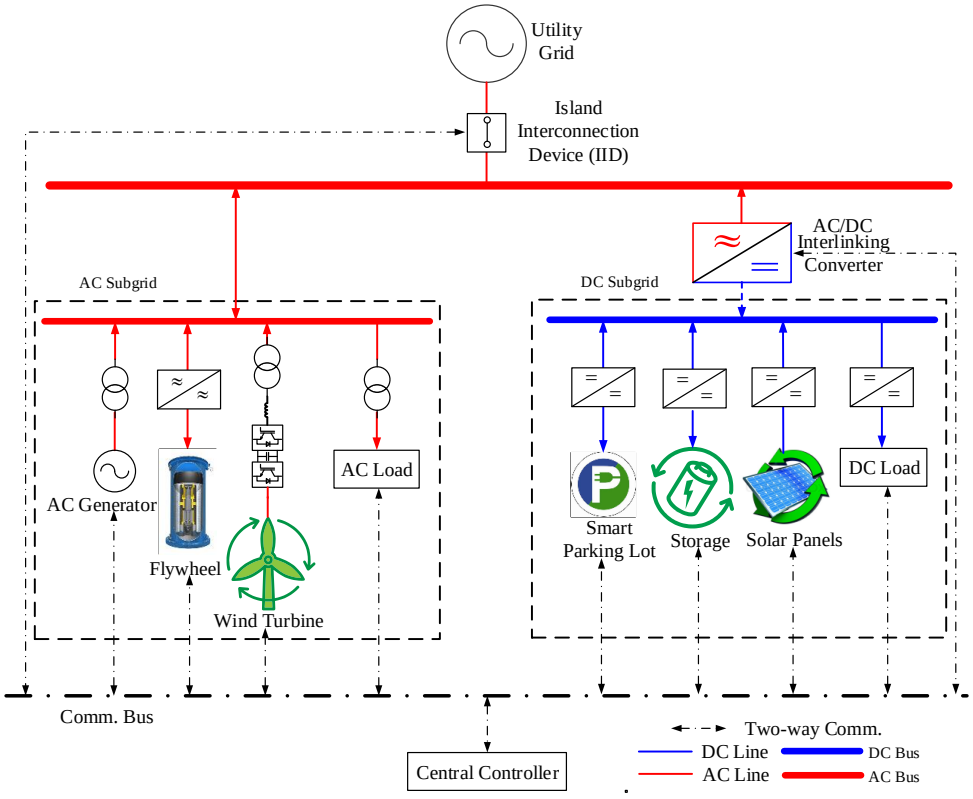

Figure 6.1. AC/DC hybrid smart distribution system.

In the developed dispatch model, the stochastic nature of the renewable power supply, regular demand, EV demand, and real-time price (RTP) are modelled explicitly. The primary objective of the developed scheme is to minimize the expected daily operating cost, which includes the cost of operating dispatchable units, the cost of importing from and exporting to the upstream grid, and the cost of EV discharging and battery degradation due to vehicle to grid (V2G) action. The main contributions of the research in this chapter can be summarized as follows:

- Detailed modelling of the key elements of the envisioned ac/dc hybrid smart grids: distributed generators (DGs), ESSs, EVs, and ICs.

- Economic and technical representation of EV battery degradation in smart grid operations.
- Stochastic representation of intermittent renewable energy, variable regular and EV demand, and fluctuating energy prices.
- Development of a stochastic centralized control scheme for energy coordination in ac/dc hybrid smart distribution systems.

This chapter is structured as follows: Section 6.2 introduces the system model and control. Sections 6.3 and 6.4 briefly discuss the two-stage stochastic optimization and scenario reduction technique used. Section 6.5 describes the developed stochastic centralized dispatch scheme. Section 6.6 explains the requirements for implementing our dispatch scheme. Section 6.7 provides the mathematical formulation of the dispatch problem. Section 6.8 presents the test system along with a discussion of the results obtained, and the last section, section 6.9, offers conclusions.

6.2 System Model and Control

This section presents the modelling of the stochastic elements and the ESSs as well as the control strategy adopted for the ICs.

6.2.1 Electric Vehicle Demand Model

The uncertainty associated with EV demand results from the unknown number of hourly EV arrivals in a parking lot, the parking duration and kWh required by each EV, and the maximum charging rate, which is limited by the battery technology, the battery size, and the capacity of the installed charger. The historical data related to arrival rates and parking duration can be collected from the parking records available for conventional vehicles. However, owing to the limited number of EVs on the roads, statistical information about EV batteries, including the energy stored and the kWh required, is not yet available.

Determining the random number of EV hourly arrivals at a parking lot is a counting process $\{N_{EV}(h) = n, h > 0, n \in \mathbb{N}_+\}$ and can be modelled probabilistically as a non-homogeneous Poisson process $N_{EV}(h) \backsim \text{Poisson}(\lambda_h)$, with an intensity of arrivals occurring at a specific rate $\lambda_h \in \mathbb{R}_+$ [135]. In [136], it was shown that the memoryless non-homogeneous Poisson process provides an appropriate representation of EV arrivals

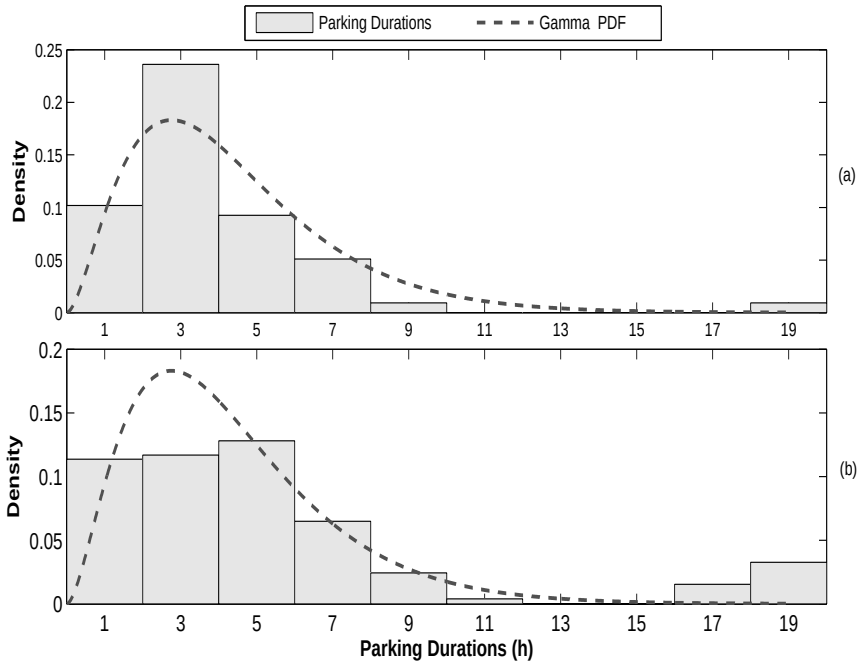

Figure 6.2. Parking durations: a) Lot_1; b) Lot_2.

because the arrival of one EV at a parking lot supplies no information about the arrivals of other EVs. The hourly arrival rate λ_h can be either estimated or predicted based on previous observations of hourly arrivals.

Like EV arrivals, EV parking duration, T_p, is also random and can be seen as the waiting time until a departure takes place. Analysis of previous parking data for conventional vehicles in the Toronto area [137] shows that parking duration follows a gamma distribution $T_p \backsim \text{Gamma}(\alpha, \beta)$, with a shape parameter α and a rate parameter β [138]. The parking durations for two parking lots in the Toronto area are shown in Figure 6.2. It is worth pointing out that, prior to discretization, T_p is a continuous random variable. Another source of uncertainty related to EVs is the amount of energy required. The energy required, E_{EV}^{req}, is upper bounded by the difference between two random variables: the initial energy stored, E_{EV}^{int}, and the capacity of the battery, E_{EV}^{cap}. Due to the lack of historical data, the energy required is assumed to follow a uniform distribution $E_{EV}^{req} \backsim \mathcal{U}(0, E_{EV}^{cap} - E_{EV}^{int})$. It should be noted that E_{EV}^{int} and E_{EV}^{req} are both continuous random variables before discretization, while E_{EV}^{cap} is a discrete random variable.

The last source of uncertainty is the rate at which the EV charges. This charging rate,

P_{EV}^{rate}, is defined by the minimum of the capacity of the charger and the charging rate of the vehicle. Given the existing information available about EV sales and corresponding battery specifications and also about the charging rates of commercially available batteries, the charging rate of each EV and its probability can be obtained. It should be noted that the probability distribution for any of the EV random quantities can change based on the statistical information that is available.

6.2.2 Why this Electric Vehicle Demand Model?

The arrival, in general, to a system in different discipline, job arrivals to a server in computer science, incoming calls to a call center in communications, customer arrivals to a bank tailor in business, and electric vehicles arrivals to parking lots in smart grids, is a memoryless process in which the arrival of one agent, e.g., electric vehicle, does not carry any information about the arrival of other agents, e.g., electric vehicles. Further, the EVs arrive to the parking lot in a stochastic nature. Hence, the EV arrival to a parking lot can be described by the Poisson process, which is a memoryless stochastic process, with some arrival rate $\lambda \in \mathbb{R}$. Since in reality the number of arrivals can be different from one hour to another, we modelled the EV arrivals as a non-homogenous Poisson process with hourly arrival rate $\lambda_h, \forall h \in \mathcal{H}$. The rate at which the EVs arrive to the parking lot does not depend on the rate of arrivals at other hours. Thus, the number of EV arrivals in each hour is simulated independently on the number of arrivals in previous hours. However, while arriving independently, each EV simulated has four possibilities. The first possibility is that upon the EV arriving in a certain hour, there is an empty charger at which the EV can be plugged in and get charged. The second possibility is that there is an empty charger, but it is simultaneously inactive, in stand-by mode, due to reaching the parking lot's capacity by the busy chargers. Thus, the EV still can be admitted and assigned to an empty and inactive charger, but it only starts charging when the charger is back in service. The third possibility is that all the chargers, active and inactive chargers, are occupied, but the late EVs can form a queue and wait for the next available chargers. The last possibility is that when all chargers are busy and there is no queueing, the late arrivals leave the parking lot for another charging facility. From the above discussion, the arrivals and charging of EVs at a parking lot can be summarized in the following:

- The arrivals of EVs to the parking lot is a memoryless process,
- The arrival rate of EVs can vary from one hour to another,

- The arrival rate at which the EVs arrive to the parking lot in a given hour is unrelated to the arrival rates of EVs in other hours,
- The only connection between the EVs arrivals in two different periods is the charging opportunity. If all the EVs arrived in one hour occupy all chargers including the inactive ones, the EV entering the parking lot in the next period will either have to wait for a charger to become available or leave for another parking lot.

6.2.3 Renewable Energy Resource Model

In principle, a renewable DG unit can be modelled as a stochastic negative load. Stochastic DG models are based on daily forecasts of wind power for wind-based DGs and of solar power for solar-based DGs. For an unbiased forecast, common practice is to assume that wind and solar power forecasting errors follow a normal distribution with a zero mean $\backsim \mathcal{N}(0, \sigma_{w/s})$, where σ_w and σ_s are the standard deviations for the wind and solar power forecasting errors, respectively [139]. However, recent findings [140] have shown that the skew-Laplace distribution yields a more precise representation of the wind power forecasting error.

It should be mentioned that the stochastic renewable power supply and the uncertain EV power demand are assumed to be independent random variables [141] because no strong correlation or even dependency has yet been proven between the two.

6.2.4 Energy Storage System Model

The ESS is characterized by the maximum and minimum stored energy (E_{ESS}^{min}, E_{ESS}^{max}), the charging rate (P_{ESS}^{rate}), and the charging and discharging efficiencies (η_{ESS}^{ch}, η_{ESS}^{dis}).

It can be modelled as two fictitious generators (G_1, G_2) with the ability to inject negative and positive power, respectively. G_1 injects the charging power, $P_{ESS}^{ch} \in \mathbb{R}_-$, while G_2 delivers the discharging power $P_{ESS}^{dis} \in \mathbb{R}_+$, as shown in Figure 6.3 [142].

6.2.5 Interlinking Converter Control

In an ac/dc hybrid system, the ICs are coordinated with the utility grid to ensure an uninterruptible and high-quality power supply under random supply and variable demand [15]. The accuracy of the model and the efficiency of the IC control strategy are thus of

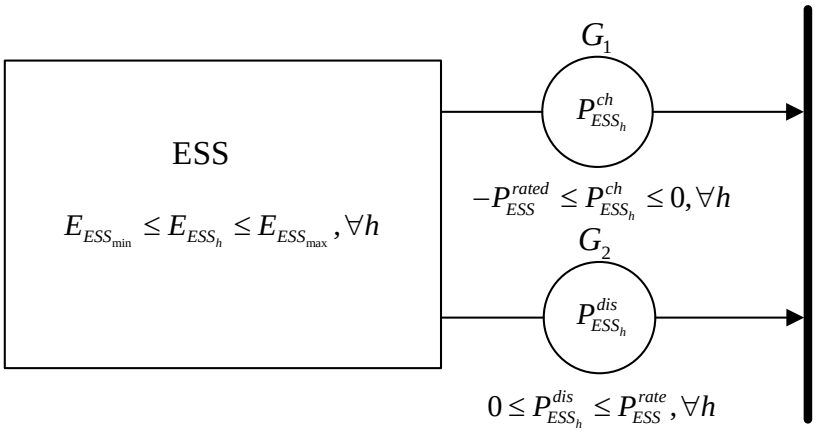

Figure 6.3. Energy storage system model.

great importance. The adopted IC control strategy is based on $(Q - V_{dc})$ control. Under this control scheme, the IC operates at a fixed power factor and shares reactive power requirements with the upstream (main) grid and the local supply sources. The dc terminal voltage of the IC is also regulated because the ac subgrid dominates its counterpart dc subgrid and acts as an infinite bus when the upstream grid is available. The steady-state IC model is described by the set of problem formulation equations (6.12)-(6.16) provided in Section 6.7.

6.3 Two-Stage Stochastic Optimization

In two-stage stochastic programming, a decision is chosen for implementation without complete information about the associated random events [143]. This decision, known as a here-and-now decision, is called the first-stage decision, denoted by vector $x \in \mathbb{R}^{n_1}$. Once the information about the random events, denoted by vector $\xi_s \triangleq \{\xi_1, \xi_2, \ldots, \xi_{n_s}\}$, becomes available, a collection of corrective decisions, known as recourse decisions, are taken. These decisions are called second-stage decisions, denoted by surplus and deficit vectors $y_s^+, y_s^- \in \mathbb{R}^{n_2}$, and $\forall s \in \mathcal{S}$. The two-stage stochastic program with fixed recourse takes the following form:

$$\min_{x, y_s^+, y_s^-} \mathbb{E}\{Z_{SS}\} = \underbrace{f(x)}_{1^{st}\text{- Obj. Fun.}} + \underbrace{\mathbb{E}\{\overbrace{Q^+(y_s^+, \xi_s)}^{Surplus} + \overbrace{Q^-(y_s^-, \xi_s)}^{Deficit}\}}_{2^{nd}\text{- Obj. Fun.}} \tag{6.1}$$

subject to

$$h(x) = b \tag{6.2}$$
$$g_s(x, y_s^+, y_s^-, \xi_s) = b_s, \forall s \in \mathcal{S} \tag{6.3}$$
$$x \geq 0, y_s^+, y_s^- \geq 0, \forall s \in \mathcal{S} \tag{6.4}$$

where $\mathbb{E}\{\bullet\}$ is the expectation operator of a random quantity $\bullet$.

An example of the first-stage decision is the day-ahead schedule of the dispatchable DG units: $x = \{P_{G,1}, P_{G,2}, \dots\}$, and examples of the second-stage decisions are import and export decisions: $\{y_s^-, y_s^+\} = \{P_{imp}, P_{exp}\}$.

6.4 Scenario Reduction Technique

The number of scenarios scales badly with the dimension of the system under study. Nevertheless, scenario reduction can certainly add another feature to our dispatch scheme: reducing the computational requirements. However, a scenario reduction technique should be able to maintain as much statistical information of the sample space as possible. The author applied the fast forward scenario reduction technique [144], and only solved for a subset of the initial scenario set $\mathcal{S}^* \subset \mathcal{S}$. The preserved scenarios are obtained by aggregating similar scenarios, and then assigned new probabilities. The fast forward selection algorithm can be best described by the following steps [144], [145]:

Step 1) Given all possible scenarios $\xi_1, \xi_2, \dots, \xi_{n_s}, \xi_s \in \mathbb{R}^{n_r}$ and their probabilities $p_s, \forall s \in \mathcal{S}, n_s = |\mathcal{S}|$,

Step 2) Decide on the number of preserved (aggregated) scenarios, $n_s^* < n_s$,

Step 3) Set the set of preserved scenarios to empty set, $\mathcal{S}^* \leftarrow \{\}$, and the set of deleted scenarios to the initial set, $\mathcal{S}_d \leftarrow \mathcal{S}$,

Step 4) For each scenario $s \in \mathcal{S}$, compute the distance matrix $D(\xi_s, \xi_{s'})$, where the entry $d_{s,s'} = \|\xi_s - \xi_{s'}\|, \forall s, s' \in \mathcal{S}$

Step 5) Compute $d_s = \sum_{\substack{k=1 \\ k \neq s}}^{n_s} p_k d_{k,s}, \forall s \in \mathcal{S}_d$,

Step 6) Determine the scenario to be preserved $s^* \in \arg\min_{s \in \mathcal{S}_d} d_s$,

Step 7) Update the set of preserved scenarios $\mathcal{S}^* = \mathcal{S}^* \bigcup \{s^*\}$,

Step 8) Remove the scenario s^* form the set of scenarios not selected $\mathcal{S}_d = \mathcal{S}_d \backslash \{s^*\}$,

Step 9) Repeat steps (4-7) until the number of preserved scenarios is obtained, $|\mathcal{S}^*| = n_s^*$,

Step 10) Update the probabilities of selected scenarios $p_s^* = p_s + \sum_{k \in \mathcal{S}_s^*} p_k \forall s^* \in \mathcal{S}^*$, where $\mathcal{S}_s^* = \{s \in \mathcal{S}_d^* : s \in \arg\min_{k \in \mathcal{S}_d^*}(d_{k,1}, d_{k,2}, \ldots, d_{k,n_s^*})\}$.

6.5 Developed Stochastic Centralized Dispatch Scheme

In an ac/dc hybrid smart grid connected to the utility grid through an island interconnection device (IID), a smart grid central controller (SGCC) enables a centralized energy management system (EMS) to be responsible for scheduling the DGs, ESSs, and EV parking lots. This EMS is assumed to receive the preliminary energy price announced for the next 24 h and then to exchange the information with the local controllers (LCs) of the DGs and ESSs, as well as the aggregators (AGs) of the parking lots, as shown in Figure 6.4. Via two-way communication, it then sends out the appropriate decisions for the next 24 h: dispatch decisions to the DG controllers, charging/discharging decisions to the ESS controllers, and charging/discharging decisions to the parking lot AGs. However, the stochastic nature of the renewable energy, the energy required by regular and EV demand, and the energy price make the decision-making process challenging. The present work

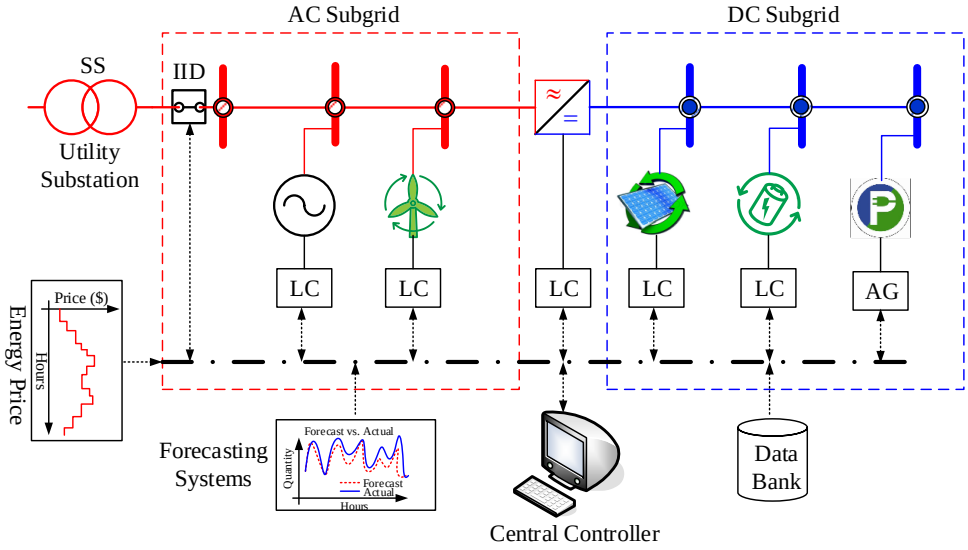

Figure 6.4. Developed architecture for the dispatch scheme.

consequently introduces a stochastic centralized dispatch scheme, whose functional block diagram is depicted in Figure 6.5. The dispatch scheme is based on two-stage stochastic programming [143], with the objective being the minimization of the expected total operating cost. Explicit representations of the intermittent supply; the uncertain demand, which includes EVs; and the variable energy price are achieved through stochastic modelling. As indicated in Figure 6.5, the first-stage decision in the dispatch model determines the day-ahead generation schedule of the dispatchable DG units, while the second-stage decision specifies the corrective decisions that occur after additional information about the stochastic power production and consumption becomes available. These corrective decisions, also known as recourse actions, include day-ahead import/export schedules, day-ahead storage charging/discharging cycles, and day-ahead EV charging/discharging patterns. It is worth pointing out that the generation schedule established as the first-stage decision yields the minimum cost for all scenarios under study and is independent of those scenarios. No matter which scenario might take place on the following day, the operational plan obtained in the first stage is implemented. In contrast, second-stage decisions are scenario-dependent, meaning that there are as many corrective decisions as the number of scenarios. These corrective decisions, e.g., those related to export/import and charge/discharge, are made in the second stage of the optimization process in order to correct for any mismatch between the available supply and demand. Another important feature is that the first-stage and second-stage decisions are based on daily forecast and historical observations, including records of the renewable power supply and previous EV arrivals. The forecast data are updated every 24 h and can be accessed from the forecasting systems, while the historical data can be retrieved from the data bank.

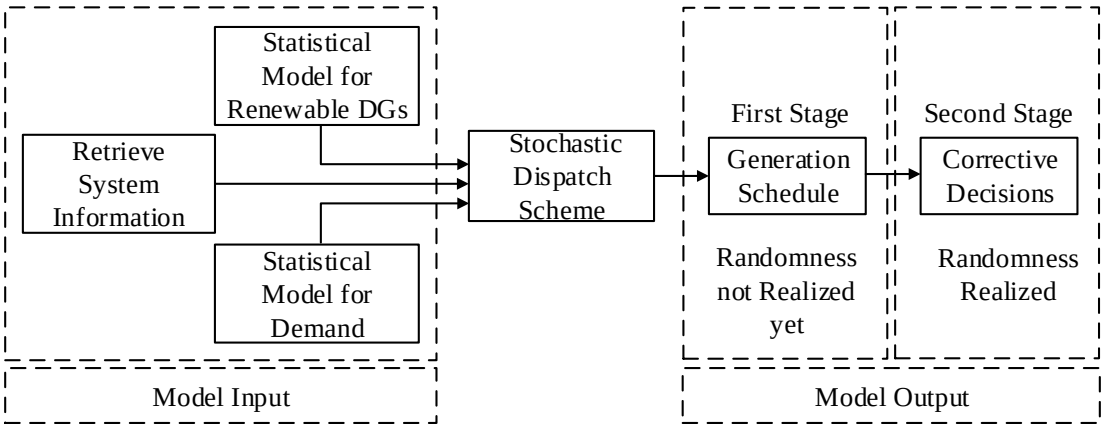

Figure 6.5. Functional block diagram of the two-stage stochastic dispatch scheme.

6.6 Implementation Requirements of the Developed Dispatch Scheme

The developed dispatch scheme is a step forward toward the adaptive and cost-effective energy coordination of future ac/dc hybrid smart grids. The dispatch scheme can be implemented once the pillars of the smart grid, i.e., technology, standards, and policy, have been established. An additional consideration is that the successful implementation of our scheme relies on the adherence of the future smart grid and its infrastructure to the following stipulations:

- The future smart grid must be an independent entity that manages its own assets.
- The future smart grid must have an advanced metering infrastructure (AMI) with automated and two-way communication capabilities.
- The two-way communication protocol must allow the smart grid to communicate with an electricity market that broadcasts preliminary real-time energy prices for the following 24 h.
- The AMI must enable two-way communication between the control center, which is "the brain of the smart grid," and the local DER controllers and parking lot AGs.
- The control center must be equipped with an EMS in which the developed scheme can be implemented.
- The EMS must run a multi-period ac/dc hybrid optimal power flow program and a two-stage stochastic optimization subroutine every 24 h.
- The EMS must include forecasting and scenario-generation tools, which are required for the execution of the stochastic dispatch scheme.

6.7 Problem Formulation

In ac/dc hybrid smart distribution systems, the energy scheduling problem is formulated as a multi-period two-stage stochastic optimization problem with the following objective function and constraints.

6.7.1 Objective Function

The objective is to minimize the expected total operating cost over the scheduling horizon $\mathcal{H}$, i.e., 24 h, as follows:

$$\min_{\substack{x=P_G \\ y_s^+=P_{exp,s},P_{ESS,s}^{ch},P_{Lot,s}^{ch} \\ y_s^-=P_{imp,s},P_{ESS,s}^{dis},P_{Lot,s}^{dis},\forall s\in\mathcal{S}}} \mathbb{E}\{Z_{SS}\} = \underbrace{\sum_{h\in\mathcal{H}}\sum_{b\in\mathcal{B}_G} C_{unit_{b,h}}}_{1^{st}-Stage\ Obj.\ Fun.} + \underbrace{\sum_{s\in S} p_s\Big(\sum_{h\in\mathcal{H}}\big(C_{imp_{h,s}} - C_{exp_{h,s}} + \underbrace{\sum_{b\in\mathcal{B}_{Lot}}\sum_{v\in\mathcal{N}_{EV_b}} C_{V2G_{b,v,h,s}}\big)\Big)}_{2^{nd}-Stage\ Obj.\ Fun.\ con't.}}_{2^{nd}-Stage\ Obj.\ Fun.} \quad (6.5)$$

where
$\mathbb{E}\{Z_{SS}\}$: the expected total operating cost (\$);
$C_{unit_{b,h}}$: the operating cost of the dispatchable unit at bus $b \in \mathcal{B}_G$ in hour $h \in \mathcal{H}$ (\$);
$C_{imp_{h,s}}, C_{exp_{h,s}}$: the costs of import and export in hour h and for scenario $s \in \mathcal{S}$, respectively, (\$);
$C_{V2G_{b,v,h,s}}$: the V2G cost of vehicle $v \in \mathcal{N}_{EV_b}$ at bus $b \in \mathcal{B}_{Lot}$ in hour h and for scenario s, respectively, (\$);
p_s: the probability of scenario s, $\forall s \in \mathcal{S}$.

6.7.2 Constraints

The constraints include the multi-period ac/dc power flow equations, the IC equations, the EV constraints, the ESS constraints, the dispatchable unit constraints, the network constraints, and the main grid constraints.

6.7.2.1 Multi-Period AC Power Flow Equations

In an ac/dc hybrid system, the ac power flow equations are the same as those defined for the ac system. However, to account for the ICs, the power flow equations for the terminal

ac buses[1] include additional terms, as indicated in the following:

$$P_{b,h,s} = |V_{b,h,s}| \sum_{k=1}^{n_{ac}} |V_{k,h,s}||Y_{bk}|cos(\delta_{b,h,s} - \delta_{k,h,s} - \theta_{bk}) + \beta_b \hat{k}_b a_{b,h,s}|V_{b,h,s}|cos\phi_{b,h,s}. \quad (6.6)$$

$$Q_{b,h,s} = |V_{b,h,s}| \sum_{k=1}^{n_{ac}} |V_{k,h,s}||Y_{bk}|sin(\delta_{b,h,s} - \delta_{k,h,s} - \theta_{bk}) + \beta_b \hat{k}_b a_{b,h,s}|V_{b,h,s}|sin\phi_{b,h,s}. \quad (6.7)$$

where
$P_{b,h,s}, Q_{b,h,s}$: the active and reactive power injections at bus b in hour h and for scenario s, respectively;
$|V_{b,h,s}|, \delta_{b,h,s}$: the voltage magnitude and phase angle at bus b in hour h and for scenario s;
$|Y_{bk}|, \theta_{bk}$: the magnitude and phase angle of the bk^{th} entry in the ac bus admittance matrix, respectively;
$\phi_{b,h,s}$: the phase angle between the ac voltage and current of the converter at bus b, at time h, and for scenario s;
$a_{b,h,s}$: the transformer tap ratio of the converter at bus b, at time h, and for scenario s;
$\hat{k}_b$: the parameter of the converter at bus b.

$$\beta_b = \begin{cases} 1 & \text{, if bus } b \text{ is an ac/dc terminal bus, } b \in \mathcal{B}_{ic,ac} \wedge \mathcal{B}_{ic,dc}, \\ 0 & \text{, otherwise.} \end{cases}$$

6.7.2.2 Multi-Period DC Power Flow Equations

The dc power flow equation for each time step $h, \forall h \in \mathcal{H}$, and scenario $s, s \in \mathcal{S}$, is defined by

$$P_{b,h,s} = V_{b,h,s} \sum_{k=1}^{n_{dc}} G_{bk} V_{k,h,s} - \beta_b V_{dc_{b,h,s}} I_{dc_{b,h,s}} \forall b \in \mathcal{B}_{dc} \quad (6.8)$$

where G_{bk} is the bk^{th} element in the dc bus conductance matrix, and $I_{dc_{b,h,s}}$ and $V_{dc_{b,h,s}}$: the dc current and voltage of the converter at bus b, in hour h, and for scenario s, respectively.

The active power injected at general bus $b \in \mathcal{B} = \mathcal{B}_{ac} \cup \mathcal{B}_{dc}$, where $\mathcal{B}, \mathcal{B}_{ac}, \mathcal{B}_{dc}$ are the sets of all buses, ac buses, and dc buses, respectively, must satisfy the active power balance

[1] The terminal ac/dc buses are those ac/dc buses that are directly connected to ICs.

equation $\forall h, s$, as shown in equation (6.9). The reactive power balance equation for each ac bus $b \in \mathcal{B}_{ac}$ can be written in a similar manner.

$$\begin{aligned} P_{b,h,s} = P_{G_{b,h}} \quad + \quad & \underbrace{P_{imp_{b,h,s}} - P_{exp_{b,h,s}}}_{\text{Import/Export Active Power}} + \underbrace{P^{dis}_{ESS_{b,h,s}} - P^{ch}_{ESS_{b,h,s}}}_{\text{ESS Active Power}} \\ + \quad & \underbrace{P^{dis}_{Lot_{b,h,s}} - P^{ch}_{Lot_{b,h,s}}}_{\text{EV Active Power}} + \underbrace{P_{PV_{b,h,s}} + P_{W_{b,h,s}}}_{\text{Renewable Active Power}} \\ - \quad & \underbrace{P_{D_{b,h,s}}}_{\text{Regular Power Demand}} \quad , \forall b \in \mathcal{B} \end{aligned} \tag{6.9}$$

where
$P_{imp_{b,h,s}}, P_{exp_{b,h,s}}$: the active power import and export at bus b in hour h and for scenario s, respectively;
$P^{ch}_{ESS_{b,h,s}}, P^{dis}_{ESS_{b,h,s}}$: the ESS charging and discharging active power at bus b in hour h and for scenario s, respectively;
$P_{PV_{b,h,s}}, P_{W_{b,h,s}}$: the active power outputs of the solar- and wind-based DG units at bus b in hour h and for scenario s, respectively;
$P_{D_{b,h,s}}$: the regular active power demand at bus b in hour h and for scenario s;
$P^{ch}_{Lot_{b,h,s}}, P^{dis}_{Lot_{b,h,s}}$: the aggregated charging and discharging EV active power at bus b in hour h and for scenario s, as defined by:

$$P^{ch}_{Lot_{b,h,s}} = \sum_{v \in \mathcal{N}_{EV_b}} P^{ch}_{EV_{b,v,h,s}}, \quad \forall b \in \mathcal{B}_{Lot} \tag{6.10}$$

$$P^{dis}_{Lot_{b,h,s}} = \sum_{v \in \mathcal{N}_{EV_b}} P^{dis}_{EV_{b,v,h,s}}, \quad \forall b \in \mathcal{B}_{Lot} \tag{6.11}$$

It should be noted that the active and reactive powers of the dispatchable DG units, $P_{G_{b,h}}, Q_{G_{b,h}} \forall b \in \mathcal{B}_{DG}$, are scenario-independent and represent first-stage decisions. In contrast, the ESS charging/discharging active and reactive power, $P_{ESS_{b,h,s}}, Q_{ESS_{b,h,s}} \forall b \in \mathcal{N}_{ESS}$; the active and reactive import power, $P_{imp_{b,h,s}}, Q_{imp_{b,h,s}}$; the active and reactive export power, $P_{exp_{b,h,s}}, Q_{exp_{b,h,s}}$; and the aggregated EV charging/discharging active and reactive power, $P^{ch}_{Lot_{b,h,s}}, P^{dis}_{Lot_{b,h,s}} \forall b \in \mathcal{B}_{Lot}$, are scenario-dependent and represent second-stage decisions.

6.7.2.3 Interlinking Converter Constraints

For each time step $h, \forall h \in \mathcal{H}$, and scenario s, $\forall s \in \mathcal{S}$, the converter located at bus $b, \forall b \in \mathcal{B}_{ac} \wedge \mathcal{B}_{dc}$, is described by (6.12)-(6.16) [146], which are included in the problem formulation as equality constraints for the selection of the converter's optimal settings.

$$V_{dc_{b,h,s}} - \hat{k}_b a_{b,h,s} |V_{b,h,s}| cos\phi_{b,h,s} = 0 \tag{6.12}$$

$$V_{dc_{b,h,s}} - \hat{k}_b a_{b,h,s} |V_{b,h,s}| cos\alpha_{b,h,s} + \frac{3}{\pi} I_{dc_{b,h,s}} X_{ic_b} = 0 \tag{6.13}$$

$$P_{G_{b,h,s}} - P_{D_{b,h,s}} - V_{b,h,s} \sum_{k=1}^{n_{dc}} V_k G_{bk} - V_{dc_{b,h,s}} I_{dc_{b,h,s}} = 0 \tag{6.14}$$

$$V_{dc_{b,h,s}} - V_{dc_b}^{spec} = 0 \tag{6.15}$$

$$cos\phi_{b,h,s} - cos\phi_b^{spec} = 0 \tag{6.16}$$

Where $\alpha_{b,h,s}$ is the firing angle of the converter at bus b in hour h and for scenario ,s, X_{ic_b}: the commutation reactance of the converter at bus b.

The dc voltage V_{dc} and the power factor $cos\phi$ have been selected as control variables and are kept constant for all time steps, $\forall h \in \mathcal{H}$, and scenarios, $\forall s \in \mathcal{S}$, as shown in (6.15) and (6.16).

6.7.2.4 Electric Vehicle Constraints

An EV being charged at a parking lot located at bus $b \in \mathcal{B}_{Lot} \subset \mathcal{B}$, in hour $h \in \mathcal{H}$, and for scenario $s \in \mathcal{S}$, is described by the charging and discharging active power denoted by $P_{EV_{b,v,h,s}}^{ch}$ and $P_{EV_{b,v,h,s}}^{dis} \in \mathbb{R}_+$, respectively, and is defined by (6.17) and (6.18).

$$P_{EV_{b,v,h,s}}^{ch} \leq P_{EV_{b,v,s}}^{rate} U_{EV_{b,v,h,s}}^{ch}, \forall b, v, h, s \tag{6.17}$$

$$P_{EV_{b,v,h,s}}^{dis} \leq P_{EV_{b,v,s}}^{rate} U_{EV_{b,v,h,s}}^{dis}, \forall b, v, h, s \tag{6.18}$$

where
$P_{EV_{b,v,s}}^{rate}$: the uncertain charging level permitted by vehicle v at bus b and for scenario s;
$U_{EV_{b,v,h,s}}^{ch}, U_{EV_{b,v,h,s}}^{dis}$: the charging and discharging decisions for vehicle v being charged at bus b in hour h and for scenario s, $U_{EV_{b,v,h,s}}^{ch/dis} \in \{0, 1\}$.

Charging and discharging are mutually exclusive events, as indicated by

$$U^{ch}_{EV_{b,v,h,s}} + U^{dis}_{EV_{b,v,h,s}} \leq 1, \forall b, v, h, s \tag{6.19}$$

Given the initial energy E^{int}_{EV} at arrival time T_a, the energy stored in vehicle $v, v \triangleq \{1, 2, \ldots, n_{EV_b}\}$, connected at bus $b \in \mathcal{B}_{Lot}$ is updated at the end of the charging interval $h \in \mathcal{H}$, as follows:

$$E_{EV_{b,v,h,s}} = E^{int}_{EV_{b,v,s}} + \sum_{k=T_a}^{h} \Delta E_{EV_{b,v,k,s}}, \forall b, v, h, s \tag{6.20}$$

where

$$\Delta E_{EV_{b,v,k,s}} = (\eta^{ch}_{EV_{b,v}} P^{ch}_{EV_{b,v,k,s}} - \frac{P^{dis}_{EV_{b,v,k,s}}}{\eta^{dis}_{EV_{b,v}}})\Delta h \tag{6.21}$$

where
Δh: the charging time interval in hour h;
$\eta^{ch}_{EV_{b,v,s}}, \eta^{dis}_{EV_{b,v,s}}$: the charging and discharging efficiencies of vehicle v at bus b, respectively.

Throughout the scheduling period, the stored energy $E_{EV_{b,v,h,s}}$ must not exceed the upper and lower limits, $E^{max}_{EV_{b,v}}, E^{min}_{EV_{b,v}}$, as described by

$$E^{min}_{EV_{b,v}} \leq E_{EV_{b,v,h,s}} \leq E^{max}_{EV_{b,v}}, \forall b, v, h, s \tag{6.22}$$

To meet the set of constraints imposed by the vehicle owner, i.e., the parking duration (T_p) and the energy required (E^{req}_{EV}), the energy delivered must match the energy required by the end of the parking duration, which is expressed as

$$\sum_{h=T_a}^{T_a+T_p} \Delta E_{EV_{b,v,h,s}} = E^{req}_{EV_{b,v,s}}, \forall b, v, s \tag{6.23}$$

It is worth noting that the total charging and discharging power during any time interval must not exceed the rating of the parking lot's transformer, $S^{max}_{Lot_b}$, at bus $b \in \mathcal{B}_{Lot}$, as indicated by the following:

$$\sum_{v=1}^{n_{EV_b}} P^{ch}_{EV_{b,v,h,s}} \leq \Psi_{Lot,b} S^{max}_{Lot_b}, \quad \forall b, h, s \tag{6.24}$$

$$\sum_{v=1}^{n_{EV_b}} P^{dis}_{EV_{b,v,h,s}} \leq S^{max}_{Lot_b}, \quad \forall b, h, s \tag{6.25}$$

where $\Psi_{Lot,b} \in [0,1]$ indicates that the system operator can control the total parking lot demand at bus b if the system performance is in danger.

EV battery degradation due to V2G can be modelled by incorporating the cost component in (6.26)-(6.28) [82] into the objective function (6.5) and the set of constraints specified in (6.29) and (6.30).

$$C_{V2G_{b,v,h,s}} = C^{dis}_{EV_{b,v,h,s}} + C^{deg}_{EV_{b,v,h,s}} \tag{6.26}$$

where

$$C^{dis}_{EV_{b,v,h,s}} = (P^{dis}_{EV_{b,v,h,s}} \Delta h) c_{dis_{b,h,s}} \tag{6.27}$$

$$C^{deg}_{EV_{b,v,h,s}} = \left| \frac{k_{Bat}}{100} \right| \left(\frac{P^{dis}_{EV_{b,v,h,s}} \Delta h}{\eta^{dis}_{EV_{b,v}}} \right) C_{Bat} \tag{6.28}$$

where
$C^{dis}_{EV_{b,v,h,s}}, C^{deg}_{EV_{b,v,h,s}}$: the discharging and degradation costs of vehicle v plugged in at bus b during hour h and for scenario s;
$c_{dis_{b,h,s}}$: the cost of the kWh discharged at bus b during hour h and for scenario s;
k_{Bat}: the slope of the linear approximation of the battery life as a function of the charging/discharging cycles [82];
C_{Bat}: the battery cost (\$/kWh).

Equation (6.29) prevents frequent discharging by limiting the number of discharging events to some constant $\beta_v \in \mathbb{N}_+$, whereas (6.30) avoids deep discharging by limiting the amount of energy released during each cycle to some percentage $\gamma_v \in [0,1]$ of the battery capacity.

$$\sum_{h=T_a}^{T_a+T_p} U^{dis}_{EV_{b,v,h,s}} \leq \beta_v, \forall b, v, s, \tag{6.29}$$

$$P^{dis}_{EV_{b,v,h,s}} \Delta h \leq \gamma_v \eta^{dis}_{EV_{b,v}} E^{cap}_{EV_{b,v,s}} \forall b, v, h, s \tag{6.30}$$

6.7.2.5 Energy Storage System Constraints

The power injection of the ESS located at bus $b, \forall b \in \mathcal{B}_{ESS}$, is bounded by the charging/discharging rate, as specified by the following:

$$P^{ch}_{ESS_{b,h,s}} \leq P^{rate}_{ESS_b} U^{ch}_{ESS_{b,h,s}}, \forall b, h, s \tag{6.31}$$

$$P^{dis}_{ESS_{b,h,s}} \leq P^{rate}_{ESS_b} U^{dis}_{ESS_{b,h,s}}, \forall b, h, s \tag{6.32}$$

where
$U^{ch}_{ESS}, U^{dis}_{ESS}$: the charging and discharging decisions, respectively, $U^{ch/dis}_{ESS} \in \{0, 1\}$.

The charging and discharging must not occur simultaneously, as indicated by the following:

$$U^{ch}_{ESS_{b,h,s}} + U^{dis}_{ESS_{b,h,s}} \leq 1, \forall b, h, s \tag{6.33}$$

The energy stored during time interval $h \in \mathcal{H}$ and for scenario $s \in \mathcal{S}$ is updated according to (6.34) and (6.35):

$$E_{ESS_{b,h,s}} = E^{int}_{ESS_b} + \sum_{k=h0}^{h} \Delta E_{ESS_{b,k,s}} \forall b, h, s \tag{6.34}$$

where

$$\Delta E_{ESS_{b,k,s}} = (\eta^{ch}_{ESS_b} P^{ch}_{ESS_{b,k,s}} - \frac{P^{dis}_{ESS_{b,k,s}}}{\eta^{dis}_{ESS_b}}) \times \Delta h \tag{6.35}$$

where
$E^{int}_{ESS_b}$: the initial energy stored in the ESS at bus b;
$E_{ESS_{b,h,s}}$: the energy stored in the ESS at bus b during hour h and for scenario s;
$\eta^{ch}_{ESS}, \eta^{dis}_{ESS}$: the charging and discharging efficiency, respectively.

At any given time, $h \in \mathcal{H}$, the energy stored in the ESS is bounded by the upper and lower bounds , $E^{max}_{ESS_b}$ and $E^{min}_{ESS_b}$, as expressed by the following:

$$E^{min}_{ESS_b} \leq E_{ESS_{b,h,s}} \leq E^{max}_{ESS_b}, \forall b, h, s \tag{6.36}$$

6.7.2.6 Dispatchable Unit and Network Constraints

An additional set of constraints are related to the dispatchable units and the network. These constraints are common in the literature, and thus; the reader can refer to the literature such as [147] for additional details.

6.8 Test System and Simulation Results

6.8.1 System Description

A 12.66 kV 38-bus radial distribution system was modified to form an ac/dc hybrid system. The original system data are available in [103]. At buses with parking lots, the active power demand was replaced by the EV demand. The reactive power demand at the dc buses was set to zero. The resulting hybrid system, shown in Figure 6.6, has a total regular active and reactive power demand of 3.085 MW and 0.89 Mvar, respectively.

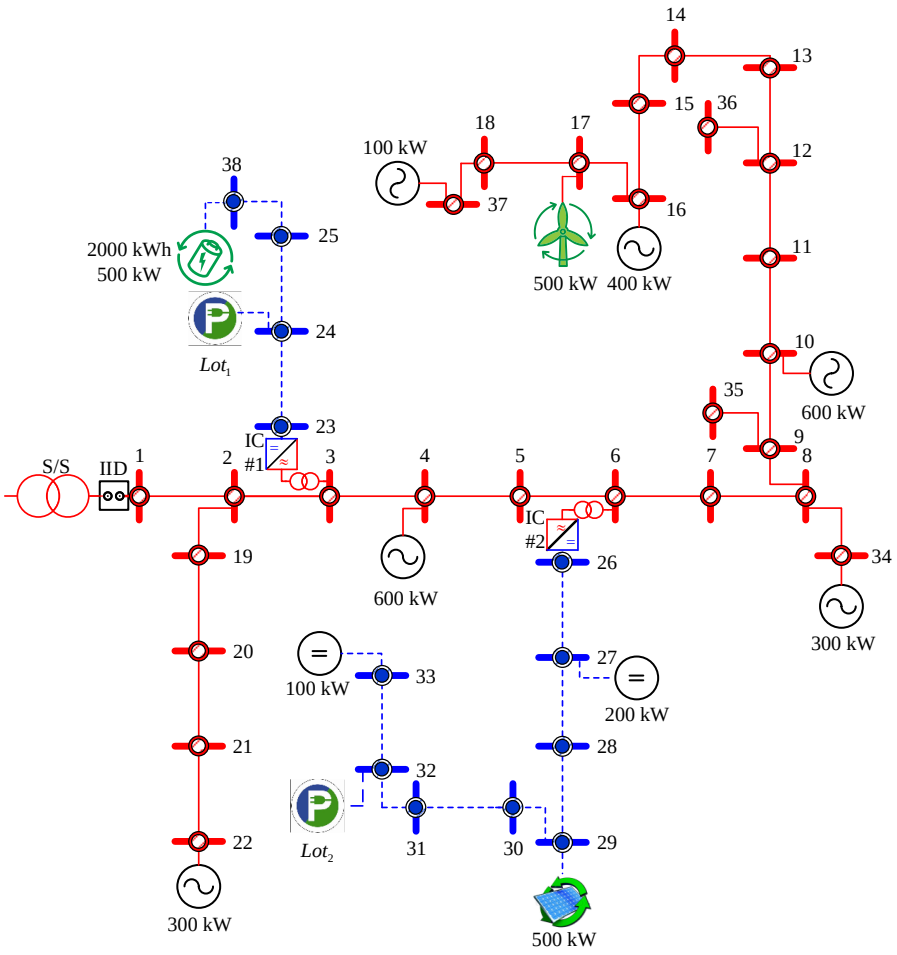

Figure 6.6. 38-bus ac/dc hybrid smart distribution system.

This hybrid system has two dc segments (3-23) and (6-26) connected to the ac side through two 12.66/0.96 kV transformers and bidirectional interlinking converters, IC # 1 and IC # 2. The IC parameter settings are listed in Table 6.1. Based on the criteria specified in [92], the dc voltage was selected to be 2.0 kV. The MVA and ac/dc base voltage values chosen were 1 MVA and 12.66/2.0 kV, respectively. The 12.66/2.0 kV hybrid smart grid is connected to the main ac grid through the substation S/S located at bus 1, which functions as a slack bus for the smart grid. An assumption worth mentioning is that the locations and sizes of the smart grid resources were determined based on the results of the planning stage. The local generation includes eight dispatchable DG units, six of which are ac and are located at buses 4, 10, 16, 22, 34, and 37. These units operate at a 0.95 leading power factor, which is within the range specified by Hydro One, Ontario, Canada [148]. The other two dispatchable units are dc and are placed at buses 27 and 33. The dispatchable units are numbered in ascending order from the least to the most expensive unit. The data for the dispatchable DG units were derived from [149] and [150], and are listed in Table 6.2. In addition to dispatchable units, the local supply includes an ESS plus renewable DG units. The ESS, which has a capacity of 2 MWh and a rating of 0.5 MW, is located at bus 38. The ESS charging and discharging efficiencies are taken as 90 %. The renewable power supply is comprised of one PV system with a capacity of 0.5 MW, located at bus 29, and one wind turbine (WT) with a capacity of 0.5 MW, located at bus 17. The wind and solar power generation represents about 31.14 % of the total system regular load.

Table 6.1. Parameter Settings for the Interlinking Converters

IC #	AC Bus	DC Bus	V_{dc} (p.u.)	$cos\phi$ (p.u.)	X_{ic} (p.u.)	$\hat{k}$ –	S_{ic}^{max} (p.u.)
1	3	23	1.0	0.950	0.0350	1.3505	1.8
2	6	26	1.0	0.975	0.0378	1.3505	2.4

The system also includes two parking lots for EV charging, Lot_1 and Lot_2, which have respective capacities of 0.80 MW and 0.40 MW and are located at buses 24 and 32, respectively, as shown in Figure 6.6. The EV batteries are assumed to be lithium-ion batteries. Lot_1 and Lot_2 contain 100 and 50 two-level chargers, respectively, each of which has a charging rate of 7.2 kW, as recommended by the US standards for EV charging [151]. The EV charging and discharging efficiencies are taken as 95 %. The authors wish to emphasize that any losses incurred as a result of battery efficiency are subject to the contract between the system operator and the AG, and any costs related

Table 6.2. Dispatchable Unit Data

Unit Type	Unit #	Bus #	$S_{G,max}$ kVA	$P_{G,max}$ kW	$P_{G,min}$ kW	a ¢/h	b ¢/kWh	c ¢/kWh^2
AC	1	4	750	600	100	5	4	0.0010
	2	10	750	600	100	5	6	0.0020
	3	16	500	400	100	10	8	0.0025
	4	22	400	300	50	12	10	0.0020
	5	34	400	300	100	10	9	0.0020
	6	37	120	100	50	20	17	0.0012
DC	7	27	—	200	100	22	18	0.0028
	8	33	—	100	50	24	20	0.0032

to charging and discharging losses can thus be passed on to the EV owners or the system operator, depending on the business model in place. The EV penetration level represents about 35 % of the total system demand.

The real-time price (RTP) fluctuates during the day based on conditions in the wholesale market. For this reason, the historical RTP data provided in [152] has been used for modelling the RTP forecasting error: the best distribution is determined and the statistical parameters are estimated using the maximum likelihood method [138]. As shown in Figure 6.7, the RTP forecasting error was found to follow a t location-scale distribution rather than a normal distribution and was simulated by means of a Monte Carlo simulation method.

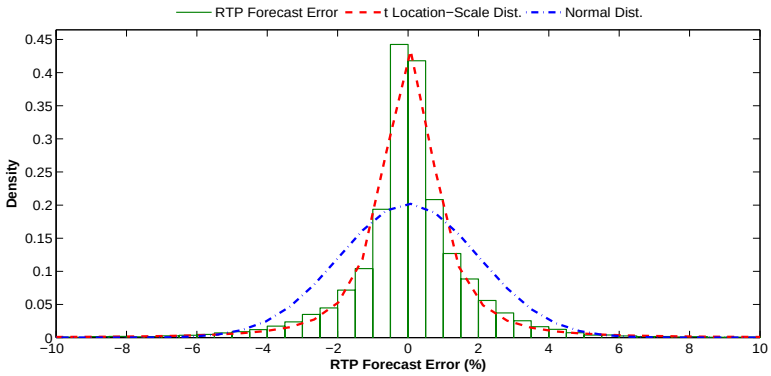

Figure 6.7. Real-time energy price forecasting error.

The hourly RTP profile used in the simulations is shown in Figure 6.8.

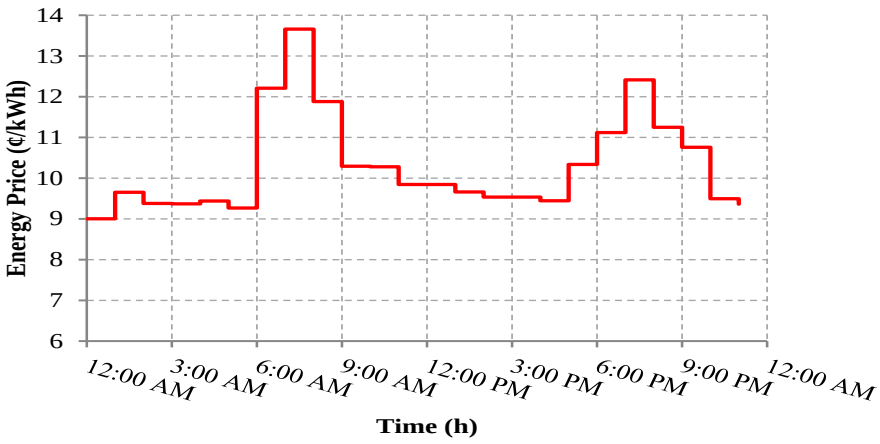

Figure 6.8. Real-time energy price profile.

The forecasting error for the regular demand, which follows a Gaussian distribution [153], was also simulated for the 10 scenarios shown in Figure 6.9 (a). For a 24 h period, Figure 6.9 (b) and 6.9 (c) show 10 scenarios each for solar and wind power generation, respectively. Additional 10 scenarios for the EVs have been generated based on historical data for workday arrival rates and parking durations for conventional vehicles, which were collected from public parking lots in Toronto, Canada [137]. It is worth noting that the total number of scenarios n_s, resulting from all possible combinations of the solar power scenarios n_{pv}, wind power scenarios n_w, regular power demand scenarios n_d, EV scenarios n_v, and energy price scenarios n_p is $n_{pv}n_w n_d n_v n_p$. Each scenario has a probability of $\frac{1}{n_s}$. The use of a fast forward scenario reduction technique [144] enabled the number of scenarios simulated to be reduced from 10^5 to 10^1.

6.8.2 Simulation Results

6.8.2.1 First-Stage Decision

The first stage of the dispatch model is the creation of the day-ahead generation schedule. The results for the dispatchable DG units are shown in Figure 6.10 and Table 6.3. To supply the base load, units 1 and 2, the least expensive units, operate at their maximum capacities (600 kW) most of the time. Unit 3 is turned on from 6:00 A.M. to 10:00 P.M.

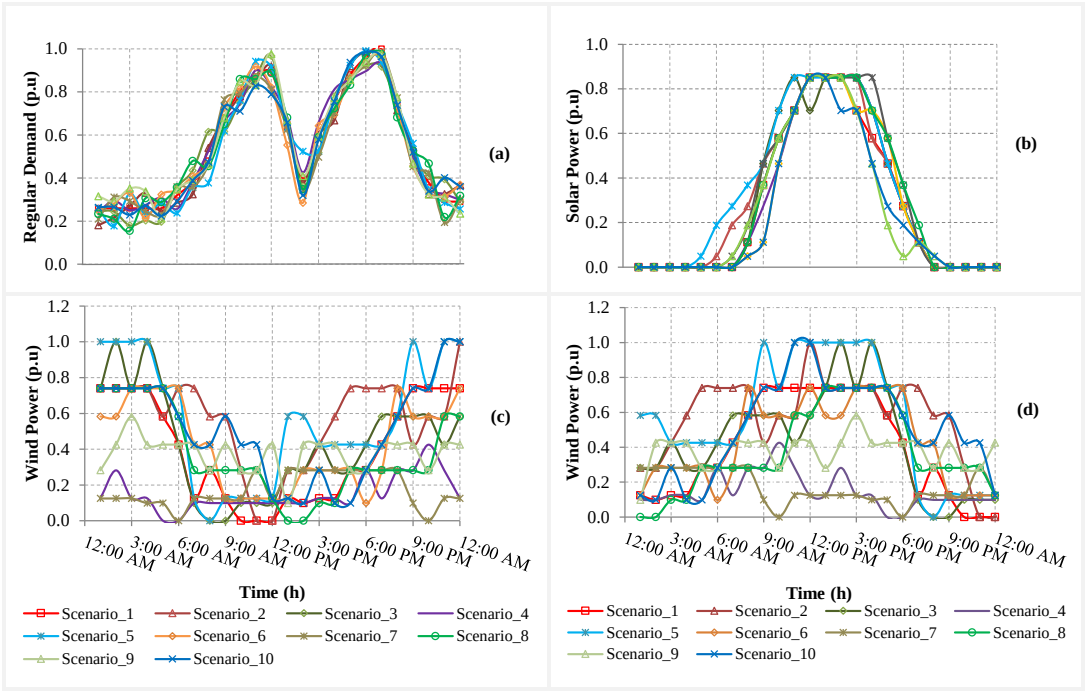

Figure 6.9. 10 scenarios for: (a) regular demand; (b) solar power; (c) (−) correlated wind power; (d) (+) correlated wind power.

and during those hours also operates at its maximum capacity (400 kW) most of the time. However, it is turned down during the off-peak period around 2:00 PM. Unit 4, with a capacity of 300 kW, is brought into service during high demand periods, and its output is reduced between the two peak periods. Unit 5, with a capacity of 300 kW, is also switched on during peak periods and then brought down to its minimum at 2:00 P.M. Unit 6, with a capacity of 100 kW, is turned on for only three hours during the first peak (10:00 A.M. to 1:00 P.M.) and for two hours during the second peak (6:00 P.M. to 8:00 P.M.). Due to the high cost of running them, units 7 and 8, with capacities of 200 kW and 100 kW, respectively, are not turned on for the entire operational day.

6.8.2.2 Second-Stage Decision

In the second stage, when complete information about the random events becomes available, the central controller makes corrective, or recourse, decisions, which include import/export scheduling, ESS charging/discharging, and EV charging/discharging. The

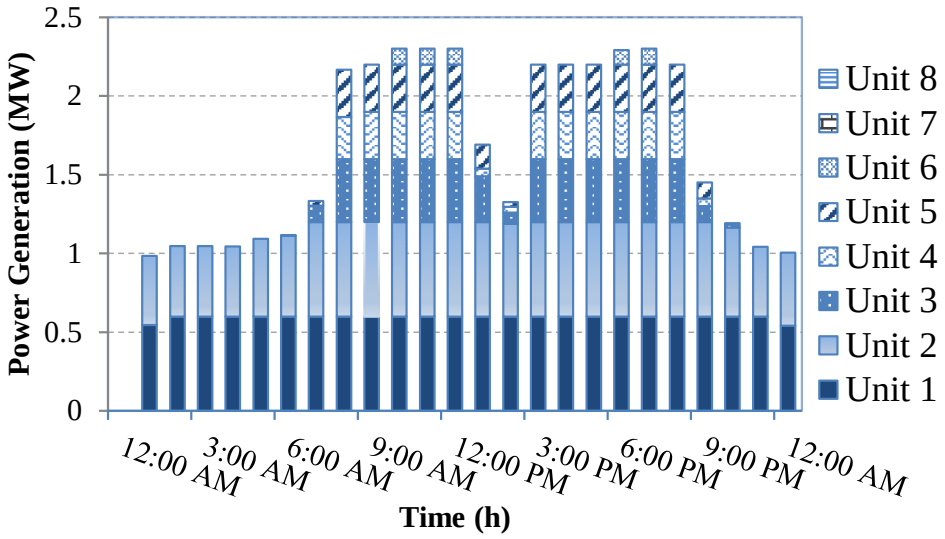

Figure 6.10. Day-ahead generation schedule.

Table 6.3. Generation Schedule for the Dispatchable DG Units, in kW

Unit	Time	A.M.												P.M.											
		1	2	3	4	5	6	7	8	9	10	11	12	1	2	3	4	5	6	7	8	9	10	11	12
1		545.5	600	600	600	600	600	600	600	600	600	600	600	600	600	600	600	600	600	600	600	600	600	600	540
2		439.1	446.2	445.9	444.5	493.5	513.7	600	600	600	600	600	600	600	588.9	600	600	600	600	600	600	600	563.2	442.4	466.4
3							1.89	104.5	400	400	400	400	400	289.9	70.7	400	400	400	400	400	400	100	27.6		
4									266.7	300	300	300	300	50	37.5	300	300	300	300	300	300	50			
5								30	300	300	300	300	300	151.6	30	300	300	300	300	300	300	100			
6											100	100	100						91.9	100					
7																									
8																									

optimal generation and import/export schedules, as well as the ESS charging/discharging cycles and EV charging profiles for one scenario are depicted in Figure 6.11. As indicated in the figure, the power delivered to the system is comprised of the dispatchable DG power generation, the renewable power generation, the ESS discharging power, and the power imported from the main grid. The power consumed, however, includes the regular demand, the EV demand, the ESS charging power, and the power exported to the main grid. Whenever the EV parking durations permit an attempt to avoid an excessive increase in peak demand, the central controller sends charging decisions to the AGs of parking lots Lot_1 and Lot_2 in order to shift the EV charging to off-peak periods. As shown in Figure 6.11, based on the decision received, the AGs of Lot_1 and Lot_2, allow the EVs to charge during off-peak periods. Coordinated charging of the EVs located at Lot_1 and Lot_2 during

periods of lower pricing and off-peak demand ensures better utilization of utility resources and lower charging rates for EV owners. In addition to the EV charging profile, Figure 6.11 also indicates that the ESS starts the daily charging/discharging cycle by charging early in the morning during low pricing periods and then discharging during the peak periods from 10:00 A.M. to 1:00 P.M. and 5:00 P.M. to 9:00 P.M. During the off peak period around 2:00 P.M., when the energy price drops, the ESS charges at maximum capacity and releases the stored energy later on during the second peak period at 5:00 P.M. to 9:00 P.M. A final observation is that, due to system loss considerations, the total power production, as indicated by the entire positive area in Figure 6.11, is slightly larger than the total power consumption, designated by the entire negative area in Figure 6.11.

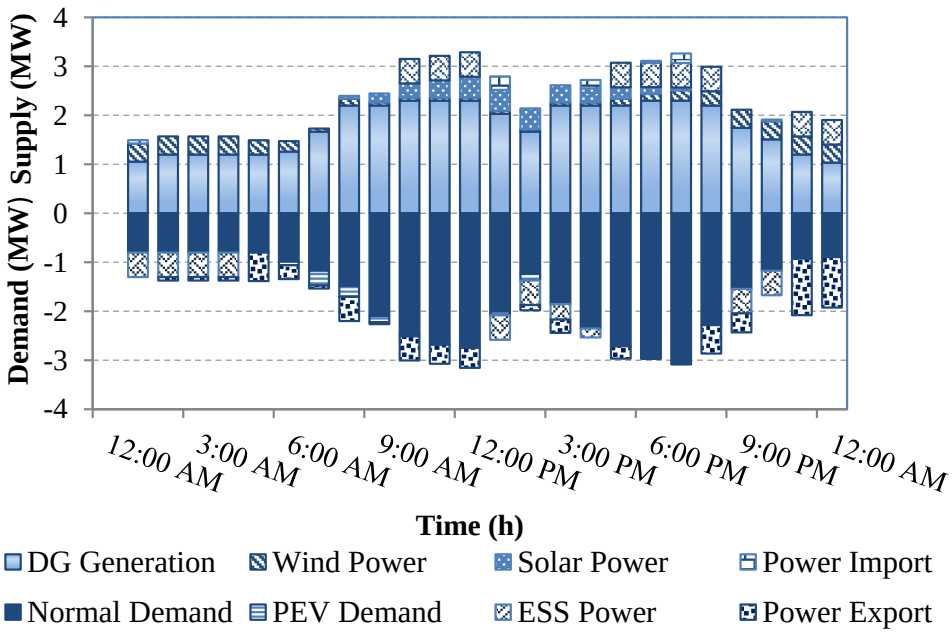

Figure 6.11. Generation and demand profiles for one scenario.

6.8.2.3 Including Representation of EV Battery Degradation

Including V2G EV battery degradation in the dispatch scheme can have an impact on the daily energy cost and on the number of charging/discharging cycles, which was demonstrated through the implementation of the following four case studies:

Case 1 Unrestricted V2G

Case 2 V2G with limiting frequent discharging

Case 3 V2G with limiting frequent and deep discharging

Case 4 V2G with limiting frequent and deep discharging plus the inclusion of costs associated with discharging and battery degradation

In case 1, the V2G is represented neither in the objective function nor in the constraints of the dispatch model; i.e., (6.26)-(6.30) are not included in the problem formulation. In case 2, the V2G is restricted by limiting the number of discharging times; i.e., the constraint expressed in (6.29) is introduced into the dispatch model. In case 3, not only is frequent charging limited but deep discharging is also prevented; i.e., (6.29) and (6.30) are included in the dispatch model. In case 4, in addition to limiting frequent and deep discharging, the battery degradation is also represented by a V2G cost; i.e., (6.26) is incorporated into the objective function. The simulation results for the four cases are tabulated in Table 6.4. As shown in this table, when V2G is unrestricted (case 1), the expected total operating cost is the lowest ($19,818.74), while the number of discharging events occurring at each parking lot (Lot_1 and Lot_2) is the highest (83 and 53 times, respectively). The V2G cost, which is not incorporated into the objective function, is $1,208.49. In case 2, when the number of discharging events per EV battery is restricted in order to preserve its efficiency, the daily energy cost is higher ($19,822.03), while the number of discharging events is reduced in both Lot_1 and Lot_2 to 72 and 44, respectively. As a result of less discharging, the cost associated with V2G is lowered ($1,053.60). In case 3, when the restriction on deep discharging is introduced into the dispatch scheme, the expected energy cost goes up to $19,904.68 due to the lower amount of energy injected back into the grid at the parking lots during peak periods. However, the number of discharging events at Lot_1 and Lot_2 has been further reduced to 57 and 35, respectively. Consequently, the cost that the system operator incurs due to EV battery discharging and degradation is reduced to $809.78. In case 4, when V2G cost minimization is part of the system operator's objective, the dispatch scheme excludes the option of purchasing energy from the EV parking lots (column 6 in Table 6.4). This adjustment can be attributed to the fact that V2G is still an expensive option for the system operator due to the high EV battery discharging and degradation costs per kWh. According to the U.S. energy department, for energy storage to be competitive with other energy resources, its cost must not exceed 150$/kWh [154].

Table 6.4. Effects of Including EV Battery Degradation

		Case 1	Case 2	Case 3	Case 4
Costs ($)	$\mathbb{E}\{Z_{SS}\}$	19,818.74	19,822.03	19,904.68	20,087.31
	C_{unit}	25,325.08	25,332.61	25,315.27	25,354.23
	C_{imp}	6,882.13	7,097.80	6,997.57	6,430.81
	C_{exp}	12,388.46	12,608.38	12,408.17	11,697.74
	C_{V2G}	1,208.49	1,053.60	809.78	0.0
# of	Lot_1	83	72	57	0.0
Discharging Times	Lot_2	53	44	35	0.0

6.8.2.4 Renewable Power Correlation vs. Expected Energy Cost

To investigate the correlation between solar and wind power, a comparative analysis of expected operating costs was carried out. It was found that when solar and wind power are positively correlated and when demand peaks during the day (Figure 6.9 (a), (b), and (d)), the expected overall cost is $19,363.52, which is lower than when they are negatively correlated ($20,087.31) (Figure 6.9 (b) and 6.9 (c)). The reason for this effect is that positive correlation allows most of the peak demand to be supplied by renewable power, which is obtained at no cost. It should be emphasized that a positive correlation can have a positive impact on energy cost only if the peak demand occurs around midday. If a high late evening peak demand does exist, then a negative correlation can reduce expected operating costs. In addition, because the correlation between solar and wind power is location-dependent, no statement can be generalized, although it has been proven that the correlation between the two is negative in some countries [155].

6.8.2.5 Importance of the Stochastic Dispatch Model

To demonstrate the necessity for the stochastic model, two measures have been employed: *the expected value of perfect information* (EVPI) and *the value of the stochastic solution* (VSS) [143]. The EVPI reflects the expected amount of money the decision maker would be willing to pay in order to acquire perfect information about the future [143]. The EVPI can be obtained mathematically by finding the difference between the recourse problem solution, referred to as the stochastic solution (SS), and the wait-and-see solution (WSS).

When the stochastic model is used, the SS is defined as the expected cost, denoted by $\mathbb{E}\{Z_{SS}\}$ and obtained as follows:

$$\mathbb{E}\{Z_{SS}\} = Z_1 + \sum_{\forall s} p_s Z_2(s) \tag{6.37}$$

where
Z_1, Z_2 are the first- and the second-stage objective function values, respectively.

As shown in equation (6.37), the SS is obtained by summing the first-stage objective function value and the expected value of the second-stage objective function, which is obtained from the weighted sum of the second-stage objective values.

When the deterministic solution (DS) is obtained, based on complete information about the behaviour of the random variables in the future, the WSS is defined as the expected cost. Simply put, it represents the average cost associated with all possible scenarios. Mathematically, the WSS, denoted by $\mathbb{E}\{Z_{DS|S}\}$, can be evaluated by executing the deterministic model for each scenario and recording the corresponding cost, The WSS is then defined by the average cost, as described in Algorithm 1.

Algorithm 1 Wait-and-See Solution (WSS)

1: **for** each scenario $s \in \{1, 2, \ldots, n_s\}$ **do**
2: /* Solve the deterministic model and record the corresponding cost $Z_{DS|S=s}$
3: **end for**
4: Given the total number of scenarios n_s, calculate $\mathbb{E}\{Z_{DS|S}\} = \frac{1}{n_s} \sum_{s=1}^{n_s} Z_{DS|S=s}$

Once the SS and WSS are obtained, the EVPI can be determined from the following:

$$\text{EVPI} \quad = \quad \mathbb{E}\{Z_{SS}\} - \mathbb{E}\{Z_{DS|S}\} \tag{6.38}$$

where $\mathbb{E}\{Z_{SS}\}$ is the expected cost of the SS, and $\mathbb{E}\{Z_{DS|S}\}$ is the expected cost of the DS, given scenario $s, \forall s \in \mathcal{S}$.

The VSS reflects the expected amount of money that the decision maker can save if the uncertainty is explicitly modelled and the stochastic model is applied. The VSS is defined mathematically as the difference between the expected cost of using the expected value solution (EEV) and the SS. The EEV is defined as the expected cost when the DS is applied without complete information about the future, e.g., supply and demand. Simply

put, it represents the expected cost of applying the deterministic model while a random variable deviates from its mean value. Computationally, the EEV, denoted by $\mathbb{E}\{Z_{SS|DS}\}$, can be evaluated by executing the stochastic model with the first-stage decisions kept fixed. The VSS can then be obtained from the following:

$$\text{VSS} \quad = \quad \mathbb{E}\{Z_{SS|DS}\} - \mathbb{E}\{Z_{SS}\} \tag{6.39}$$

where $\mathbb{E}\{Z_{SS|DS}\}$ is the expected cost of the SS given the DS of the first-stage decision variables.

Table 6.5 shows the EVPI and VSS related to the expected costs associated with the ac/dc hybrid smart grid under study. The table reveals that if it were possible to have complete information about the renewable power supply and demand including EVs 24 h ahead, the expected cost would be reduced from \$20,087.31 to \$19,003.74. The EVPI also indicates that it would cost the decision maker \$1,083.57 to acquire perfect information about the uncertain renewable energy supply and demand. In addition, if the deterministic model were used without accurate information about the stochastic power generation and consumption, the expected energy cost would be as high as \$21,125.71. The VSS reveals that modelling the uncertainty would reduce the smart grid expenses on average by \$1,038.40. Another interpretation of the VSS is that the decision maker would be expected to sacrifice this amount of money (\$1,038.40) if the stochastic model were not favourable. A large VSS means that the stochastic model performs well compared to its deterministic counterpart when day-ahead smart grid operations are conducted in an uncertain environment. Most importantly, since the future supply and demand cannot be predicted accurately and the deterministic model would produce a high energy cost on average (\$21,125.71), the stochastic model is the best option because it yields an expected energy cost of \$20,087.31.

Table 6.5. Expected Costs, VSS, and EVPI

$E\{Z_{SS}\}$	$E\{Z_{DS\|S}\}$	$E\{Z_{SS\|DS}\}$	EVPI	VSS
20,087.31	19,003.74	21,125.71	1,083.57	1,038.40

6.8.3 Computational Aspects

The stochastic dispatch scheme that has been developed is classified as a large-scale mixed integer nonlinear programming problem (MINLP). An optimization problem of this na-

ture, with integer requirements and highly nonlinear power flow equations, is non-convex and difficult to solve. As a result, some commercial solvers rely on the convexifying of the problem and the relaxing of the integer variables in order to solve the MINLP problem. However, the problem at hand was solved by a simple branch and bound solver (SBB) [156], an MINLP solver in GAMS [157]. The SBB solver combines the classical branch and bound method (B&B) known from mixed integer programming (MIP) with the standard nonlinear programming (NLP) solvers already supported in GAMS. The SBB solver supports different types of discrete variables, including binary and integer variables. Our dispatch model includes seven binary variables: the on or off dispatchable unit status, U_G; EV charging and discharging decisions, $U_{EV}^{ch}, U_{EV}^{dis}$; ESS charging and discharging decisions, $U_{ESS}^{ch}, U_{ESS}^{dis}$; and import and export decisions, U_{imp}, U_{exp}.

It is worth mentioning that adding a dispatchable DG unit to the system will increase the number of binary variables by only 1. Placing another ESS will increase the number of binary variables U_{ESS}^{ch} and U_{ESS}^{dis} by $2n_s$, where n_s is the number of scenarios. However, including an extra parking lot with EV charging capability in the system will increase the number of binary variables for each scenario by twice the number of EVs that can be plugged in simultaneously; i.e., each new EV in the system will be associated with two binary variables: $U_{EV_v}^{ch}, U_{EV_v}^{dis}, \forall v$. Thus, the dispatch problem scales poorly with the number of EV parking lots. A convex relaxation approach such as semidefinite programming can be used to reformulate the non-convex dispatch problem and obtain its convexified version.

Network size can also increase the computational burden, but with less computational complexity than that created by additional EV parking lots. The reason for this discrepancy arises from the assumption that all ac buses are constant PQ buses and all dc buses are constant P buses, which means that each ac bus is associated with two unknown state variables, bus voltage magnitude, $|V_{ac}|$, and phase angle, δ, and that each dc bus is associated with one unknown state quantity: bus voltage magnitude, V_{dc}. Adding another ac bus will increase the number of state variables by $2n_s$. Similarly, and analogously to the ac subsystem, adding one dc bus will increase the number of unknown dc voltages by n_s. Nevertheless, the bus voltage magnitude and phase angle are continuous state variables, which means that the integer requirements will not change as the size of the network grows.

The number of scenarios, n_s, is another contributor to computational complexity. A large number of scenarios will capture a wide spectrum of the uncertainty but only at the expense of increased computational time and memory requirements. A scenario reduction technique can aggregate similar scenarios and identify ones that have a high probability of occurring. In addition to scenario reduction, a decomposition method can also be used to split the dispatch problem into subproblems that can be solved separately. With respect to convergence to the global solution, our dispatch problem is non-convex in nature with

multiple peaks and valleys, and the global optimal solution is hence not guaranteed unless we use a global optimization method and allow for a "theoretically infinite" computation time. A global optimization method based on heuristics can be used to find the global optimum, but the drawback of such a method is the lack of mathematical proof for its convergence to the global optimum.

The simulations reported were carried out on an LG desktop computer with an Intel (R) Core (TM) i5-3470 CPU @ 3.20 GHz. The solver settings and the model statistics are listed in Table 6.6.

Table 6.6. Solver Settings and Model Statistics

Solver Settings	- Iteration limit	9.00E+09
	- Time limit (sec)	86400
	- Gap tolerance	1.00E-06
Model Statistics	- No. of equations	496,010
	- No. of variables	385,294
	- No. of binary variables	105,576
	- Execution time (sec)	10,034.62

6.9 Discussion

Future smart grids are envisioned to have an ac/dc hybrid structure that will host a variety of dc technologies, such as renewable DGs, ESSs, and EVs. An efficient dispatch scheme that can ensure optimal utilization of ac/dc smart grid resources is therefore a fundamental requirement. A smart grid dispatch scheme must account for the variability inherent in renewable energy and demand. For these reasons, this chapter has presented a stochastic dispatch scheme for ac/dc hybrid smart grids. The stochastic dispatch model is comprised of two stages. The first establishes the generation schedule for the next 24 h, while the second determines the import/export schedule, the ESS charging/discharging patterns, and the EV charging/discharging profile for each possible scenario. The developed dispatch model was tested on a 38-bus ac/dc hybrid system. The test results reveal that the new dispatch model can efficiently schedule power production and consumption for day-ahead ac/dc smart grid operation under uncertainty.

With respect to the developed two-stage stochastic dispatch scheme, the following comments should be noted:

1) The first-stage objective value Z_{1st}, i.e., the cost of running the dispatchable units, is "optimal or near optimal" over the set of scenarios under study. That is to say, no matter which scenario might occur on the following day, the first-stage decision, i.e., the schedule of dispatchable generation, is the most economical generation schedule.

2) In practice, a two-stage stochastic model is needed because only one decision is required: the most feasible for implementation. Second-stage decisions are corrective decisions resulting from making the first-stage decision. In the present case, the first-stage decision is the operational plan for the following day: the one-day-ahead generation schedule. The second-stage decisions are scenario-based and represent the hourly import/export and charging/discharging decisions for establishing a specific generation level for each hour.

3) The major difference between a multi-stage stochastic model and any other model based on a Monte Carlo simulation is that the former results in one decision, the first-stage decision, that is feasible and implementable. In contrast, the latter produces many decisions, one for each scenario, with each one being feasible only for the corresponding scenario. Furthermore, in practice, none of the individual decisions can be executed due to the lack of information about which scenario is going to occur on the following day.

Chapter 7

Conclusion, Contributions, and Future Work

7.1 Conclusions

The eager and tenacious efforts of power system planners and operators to develop sophisticated computer programs and architectures for the enhancement of system performance will assuredly continue. One dominant trait of system planners' endless attempts is perhaps the hybridizing of existing ac grids with dc and the designing of newly structured ac/dc hybrid systems. Another widely accepted innovative idea is to cluster the power distribution grid into small subsystems designated microgrids. Microgrids can be of ac or dc types, and either stand-alone or intertied with the main grid or with neighbouring microgrids. The research presented in this thesis was oriented toward enabling the new ac/dc hybrid microgrid (HMG) paradigm to accommodate a variety of distributed energy resources (DERs) and controllable loads. The work has resulted in the accurate modelling of the distinctive features of islanded HMGs, such as the inherent coupling between the frequency and dc voltage in order to 1) develop generalized steady-state models for the system components; 2) develop effective steady-state analysis tools; and 3) address selected operational challenges, such as imprecise power sharing and voltage collapse during islanding conditions as well as stochastic energy management during grid interfacing.

Effective management of HMGs necessitates a steady-state modelling and power flow analysis tool that is able to extract system operating conditions, including the operating frequency, ac/dc voltages, ac/dc power flows, and the amounts and directions of power transfers through the interlinking converters (ICs) that interface the ac and dc subgrids. The third chapter described the development of a unified power flow formulation and its validation against a detailed time-domain model. The simulation results revealed that operational challenges would arise in HMGs during grid-connected or islanded operation modes. The developed unified power flow algorithm (UPF) can serve as a valuable tool that can enable system planners and operators to evaluate the possibility of hybridizing existing ac distribution grids to include dc and the feasibility of designing new distribution grids that contain multiple ac/dc microgrids.

Among the operational challenges is exact proportional power sharing for droop-controlled

DERs and ICs during islanding. Inaccurate power sharing could result in the overloading of some converters, with the consequent triggering of overcurrent protection relays and the activation of load shedding schemes. These concerns led to the development of an optimal universal power sharing scheme capable of achieving exact simultaneous power sharing in the entire HMG. The case studies conducted demonstrated that several contributing factors, such as line parameters, system loading, and topology, can alter the active and reactive power shares among the DERs and among the ICs. The developed power sharing scheme can be implemented in the HMG supervisory controller, which in turn, sends out the optimized droop settings to local droop controllers.

The research presented in this Ph.D. dissertation also included an investigation of the problem of steady-state voltage instability/collapse in islanded HMGs. Despite the fact that ac distribution feeders are normally short and have low X/R ratios, medium- and low-voltage distribution systems can still be subject to a voltage instability/collapse problem, especially in the case of islanded microgrids characterized by limited reactive power capability, constant power loads, and vulnerability to contingencies. The problem of voltage instability was also observed in islanded dc microgrids that have constant power loads during contingencies. A number of factors can affect voltage stability in microgrids; some are specific to each microgrid type and others are common, regardless of microgrid type. In ac microgrids, the loadability margin can be significantly affected by 1) the reactive power capability of synchronous-based DERs; 2) the reactive power droop characteristics of droop-controlled distributed generation (DG) units; and 3) ac load characteristics, such as their operating power factors and their behaviour when voltage declines in steady state. In dc microgrids, a voltage instability problem can be triggered by 1) the droop characteristics of droop-based DGs, 2) the resistances of dc feeders, and 3) the power demands of dc loads. In HMGs, in addition to the above factors for ac and dc microgrids, voltage stability in either the ac or dc subgrid is also sensitive to 1) the amount and direction of power transfers, 2) the droop characteristics of the ICs, and 3) the number and locations of the interfacing points between the ac and dc subgrids. By switching from current-control mode to voltage control mode, an IC can provide voltage support and assist an individual subgrid that operates near its voltage stability limits. To increase its voltage support capability, each IC can be paired with a distributed energy storage (DS) unit.

The operational challenges associated with HMGs are not limited to islanded conditions. The operation and control of HMGs with renewables and electric vehicles (EVs) while interfaced with the main grid or other microgrids are also challenging. The stochastic nature of renewable-based DERs and EVs adds to the difficulty of operation and control. The research presented in this thesis included a close look at the problem of energy management when an HMG is hosted by the main grid. The investigation revealed that the daily oper-

ational cost can be reduced by effective energy coordination. In particular, incorporating the charging/discharging flexibility of DSs and plug-in EVs into the daily operation routine offers a system operator the opportunity to maneuver energy production and consumption in order to achieve technical and cost objectives.

7.2 Contributions

The studies undertaken for this doctoral thesis have led to a number of contributions in the area of HMGs. Highlights of the core contributions of the completed work include the following:

1) *The development of a unified approach to the power flow analysis of HMGs*: This research has contributed to the area of HMGs through the development of a generalized and unified power flow algorithm for steady-state analysis during islanding. Different droop characteristics for DERs were incorporated within the developed algorithm such as (ω-P) droop characteristics for voltage-controlled DERs and their inverse (P-ω) droop characteristics for current-controlled DERs. Furthermore, three control strategies for ICs were implemented. A power transfer dead zone was introduced in the IC droop characteristics in order to avoid an unnecessary operation of the ICs when the loading difference between ac and dc subgrids is insignificant, e.g., $< 5\%$. The developed power flow approach is flexible and can easily accommodate any changes in system topology or in the operating modes of the DERs and ICs. Such a full-featured power flow algorithm serves as a steady-state power analysis tool that enables system planners to explore the possibility of hybridizing existing ac grids by incorporating their dc counterparts.

2) *The development of a precise and universal power sharing scheme in droop-controlled HMGs*: The work presented in this thesis has resulted in the development of a universal power sharing scheme for droop-controlled HMGs that is able to achieve proportional power sharing not only among DERs in each subgrid but also among ICs. To consider the inherent coupling between the frequency and dc voltage, ac/dc droop characteristics were adopted for ICs in order to determine the amount and direction of the power transfer that facilitates precise proportional power sharing. The developed power sharing scheme can be readily implemented in the supervisory centralized controller with low-bandwidth communication requirements.

3) *The investigation of the voltage instability/collapse problem in islanded HMGs during contingencies*: The occurrence of voltage collapse in an islanded HMG during contingencies has been investigated. The voltage stability analysis showed the possibility of the occurrence of the voltage collapse phenomenon in microgrids under contingencies during islanding.

4) *The development of a centralized stochastic dispatch scheme for smart ac/dc hybrid distribution systems*: The developed dispatch scheme provides probabilistic modelling of the uncertainties associated with a renewable power supply, conventional power demand, EV power demand, and electricity pricing. A scenario reduction technique was applied in order to aggregate a large number of scenarios while keeping most of the stochastic information. The resultant stochastic scheme is computationally attractable. To ensure the applicability of the developed dispatch scheme, the EV battery degradation was modelled in order to avoid frequent and deep discharging.

7.3 Directions for Future Work

Although the four main components of this thesis introduced in chapters three to six have contributed to current research in the area of HMGs, some limitations remain to be addressed. As a continuation of the work presented, the following research directions are suggested for future studies:

- *Extension of the developed unified power flow for unbalanced three-phase ac/dc microgrids*: Distribution networks and microgrids are three-phase networks and can have some degree of unbalanced phase loading conditions[1]. In some scenarios, the system unbalance can exceed permissible limits, e.g., 4% in low-voltage and 2% in medium-voltage distribution planning [158]. The unified power flow algorithm described in chapter 3 can therefore be extended for islanded HMGs characterized by unbalanced ac loading.

- *Creation of a voltage-stability-based planning approach for islanded HMGs*: An adequate loadability margin for islanded HMGs during contingencies is a prominent factor in successful islanding and secure operation during severe events. The locations and ratings of droop-based DERs can have a significant influence on microgrid

[1]Unbalance conditions are referred to as unequal phase voltages and/or their phase angles due to the presence of signal-phase loads in the system.

loadability. A subject of future research is therefore the utilization of microgrid loadability and contingency analysis for the identification of the optimal mix of DERs.

- *Investigation of an integrated energy management system for ac/dc hybrid distribution networks that have a reconfigurable topology*: The developed stochastic dispatch scheme can be extended to integrate other functions of the energy management system, such as network reconfiguration and volt/var optimization. In addition to the minimization of operational cost, the objective of the integrated energy management system could be decreased switching times and an improved ac/dc voltage profile.

This thesis has unveiled the operational philosophy and challenges associated with the hybridizing of ac and dc in a new paradigm that could prevail in years to come: smart distribution systems with coupled HMGs.

References

[1] P. Wang, L. Goel, X. Liu, and F. H. Choo, "Harmonizing ac and dc: A hybrid ac/dc future grid solution," *Power and Energy Magazine, IEEE*, vol. 11, no. 3, pp. 76–83, 2013.

[2] K. Kurohane, T. Senjyu, A. Yona, N. Urasaki, T. Funabashi, T. Goya, and T. Funabash, "A hybrid smart ac/dc power system," *IEEE Transactions on Smart Grid*, vol. 1, no. 2, pp. 199–204, 2010.

[3] Renewable Energy Policy Network for the 21^{th} Century (REN21). (2014) Renewables 2013 global status report. [Online]. Available: http://www.ren21.net/portals/0/documents/resources/gsr/2013/gsr2013_lowres.pdf

[4] Ontario Ministry of Energy. (2014) Ontario's long-term energy plan. [Online]. Available: http://www.energy.gov.on.ca/en/ltep/#.UzmH4vldVW0

[5] National Energy Board. (2018) Market snapshot: Growing electric vehicle incentives in canada. [Online]. Available: http://www.neb-one.gc.ca/nrg/ntgrtd/mrkt/snpsht/2018/01-03lctrcvhclncntvs-eng.html

[6] R. H. Lasseter, "Microgrids," in *2002 IEEE Power Engineering Society Winter Meeting*, pp. 305–308.

[7] S. M. Amin and B. F. Wollenberg, "Toward a smart grid: power delivery for the 21st century," *IEEE power and energy magazine*, vol. 3, no. 5, pp. 34–41, 2005.

[8] R. H. Lasseter and P. Paigi, "Microgrid: a conceptual solution," in *Proc. 2004 IEEE Power Electronics Specialists Conf.*, pp. 4285–4290.

[9] F. Katiraei, R. Iravani, N. Hatziargyriou, and A. Dimeas, "Microgrids management," *Power and Energy Magazine, IEEE*, vol. 6, no. 3, pp. 54–65, 2008.

[10] R. H. Lasseter, "Smart distribution: Coupled microgrids," *Proceedings of the IEEE*, vol. 99, no. 6, pp. 1074–1082, 2011.

[11] M. E. Baran and N. R. Mahajan, "Dc distribution for industrial systems: opportunities and challenges," *IEEE Transactions on Industry Applications*, vol. 39, no. 6, pp. 1596–1601, 2003.

[12] L. Piegari, E. Tironi, V. Musolino, S. Grillo, and C. Tornelli, "dc islands in ac smart grids," *IEEE Transactions on Power Electronics*, vol. 29, no. 1, pp. 89–98, 2013.

[13] H. Farhangi, "The path of the smart grid," *Power and Energy Magazine, IEEE*, vol. 8, no. 1, pp. 18–28, 2010.

[14] IEEE Standard 15474, "IEEE guide for design, operation, and integration of distributed resource island systems with electric power systems," 2011.

[15] X. Liu, P. Wang, and P. C. Loh, "A hybrid ac/dc microgrid and its coordination control," *IEEE Transactions on Smart Grid*, vol. 2, no. 2, pp. 278–286, 2011.

[16] R. Majumder, "A hybrid microgrid with dc connection at back to back converters," *IEEE Transactions on Smart Grid*, vol. 5, no. 1, pp. 251–259, 2014.

[17] K. Kurohane, T. Senjyu, A. Uehara, A. Yona, T. Funabashi, and C.-H. Kim, "A hybrid smart ac/dc power system," in *Proc. 2010 IEEE Industrial Electronics and Applications Conf.*, pp. 764–769.

[18] E. Unamuno and J. A. Barrena, "Hybrid ac/dc microgrids—part i: Review and classification of topologies," *Renewable and Sustainable Energy Reviews*, vol. 52, pp. 1251–1259, 2015.

[19] A. Bracale, P. Caramiaa, G. Carpinelli, F. Mottola, and D. Proto, "A hybrid ac/dc smart grid to improve power quality and reliability," in *2012 IEEE International Energy Conference and Exhibition (ENERGYCON)*. IEEE, 2012, pp. 507–514.

[20] X. Lu, K. Sun, J. M. Guerrero, J. C. Vasquez, and L. Huang, "State-of-charge balance using adaptive droop control for distributed energy storage systems in dc microgrid applications," *IEEE Transactions on Industrial Electronics,*, vol. 61, no. 6, pp. 2804–2815, 2014.

[21] J. M. Guerrero, M. Chandorkar, T.-L. Lee, and P. C. Loh, "Advanced control architectures for intelligent microgrids, part i: decentralized and hierarchical control," *IEEE Transactions on Industrial Electronics*, vol. 60, no. 4, pp. 1254–1262, 2013.

[22] P. C. Loh and F. Blaabjerg, "Autonomous control of distributed storages in microgrids," in *2011 IEEE 8th Int. Conf. on Power Electronics and ECCE Asia (ICPE & ECCE)*. IEEE, 2011, pp. 536–542.

[23] P. C. Loh, D. Li, Y. K. Chai, and F. Blaabjerg, "Autonomous operation of hybrid microgrid with ac and dc subgrids," *IEEE Transactions on Power Electronics*, vol. 28, no. 5, pp. 2214–2223, 2013.

[24] J. Beerten, S. Cole, and R. Belmans, "Generalized steady-state vsc mtdc model for sequential ac/dc power flow algorithms," *IEEE Transactions on Power Systems*, vol. 27, no. 2, pp. 821–829, 2012.

[25] M. Baradar and M. Ghandhari, "A multi-option unified power flow approach for hybrid ac/dc grids incorporating multi-terminal vsc-hvdc," *IEEE Transactions on Power Systems*, vol. 28, no. 3, pp. 2376–2383, 2013.

[26] A. A. Hamad, M. A. Azzouz, and E. F. El Saadany, "A sequential power flow algorithm for islanded hybrid ac/dc microgrids," *IEEE Transactions on Power Systems*, vol. 31, no. 5, pp. 3961–3970, 2016.

[27] C. Liu, B. Zhang, Y. Hou, F. F. Wu, and Y. Liu, "An improved approach for ac-dc power flow calculation with multi-infeed dc systems," *IEEE Transactions on Power Systems*, vol. 26, no. 2, pp. 862–869, 2011.

[28] M. M. A. Abdelaziz, H. E. Farag, E. F. El-Saadany, and Y.-R. Mohamed, "A novel and generalized three-phase power flow algorithm for islanded microgrids using a newton trust region method," *IEEE Transactions on Power Systems*, vol. 28, no. 1, pp. 190–201, 2013.

[29] C. Li, S. K. Chaudhary, J. C. Vasquez, and J. M. Guerrero, "Power flow analysis for droop controlled lv hybrid ac-dc microgrids with virtual impedance," in *PES General Meeting Conf. & Exp., 2014 IEEE*. IEEE, 2014, pp. 1–4.

[30] H. Han, X. Hou, J. Yang, J. Wu, M. Su, and J. M. Guerrero, "Review of power sharing control strategies for islanding operation of ac microgrids," *IEEE Transactions on Smart Grid*, vol. 7, no. 1, pp. 200–215, 2016.

[31] T. Vandoorn, J. De Kooning, B. Meersman, and L. Vandevelde, "Review of primary control strategies for islanded microgrids with power-electronic interfaces," *Renewable and Sustainable Energy Reviews*, vol. 19, pp. 613–628, 2013.

[32] M. Yazdanian and A. Mehrizi-Sani, "Distributed control techniques in microgrids," *IEEE Transactions on Smart Grid*, vol. 5, no. 6, pp. 2901–2909, 2014.

[33] Q. Shafiee, J. M. Guerrero, and J. C. Vasquez, "Distributed secondary control for islanded microgrids: A novel approach," *IEEE Transactions on Power Electronics*, vol. 29, no. 2, pp. 1018–1031, 2014.

[34] M. N. Marwali, J.-W. Jung, and A. Keyhani, "Control of distributed generation systems-part ii: Load sharing control," *IEEE Transactions on power electronics*, vol. 19, no. 6, pp. 1551–1561, 2004.

[35] J. He and Y. W. Li, "An enhanced microgrid load demand sharing strategy," *IEEE Transactions on Power Electronics*, vol. 27, no. 9, pp. 3984–3995, 2012.

[36] A. Tuladhar, H. Jin, T. Unger, and K. Mauch, "Control of parallel inverters in distributed ac power systems with consideration of line impedance effect," *IEEE Transactions on Industry Applications*, vol. 36, no. 1, pp. 131–138, 2000.

[37] J. He, Y. W. Li, J. M. Guerrero, F. Blaabjerg, and J. C. Vasquez, "An islanding microgrid power sharing approach using enhanced virtual impedance control scheme," *IEEE Transactions on Power Electronics*, vol. 28, no. 11, pp. 5272–5282, 2013.

[38] Y. A.-R. I. Mohamed and E. F. El-Saadany, "Adaptive decentralized droop controller to preserve power sharing stability of paralleled inverters in distributed generation microgrids," *IEEE Transactions on Power Electronics*, vol. 23, no. 6, pp. 2806–2816, 2008.

[39] H. Mahmood, D. Michaelson, and J. Jiang, "Accurate reactive power sharing in an islanded microgrid using adaptive virtual impedances," *IEEE Transactions on Power Electronics*, vol. 30, no. 3, pp. 1605–1617, 2015.

[40] X. Lu, J. M. Guerrero, K. Sun, and J. C. Vasquez, "An improved droop control method for dc microgrids based on low bandwidth communication with dc bus voltage restoration and enhanced current sharing accuracy," *IEEE Transactions on Power Electronics*, vol. 29, no. 4, pp. 1800–1812, 2014.

[41] V. Nasirian, A. Davoudi, F. L. Lewis, and J. M. Guerrero, "Distributed adaptive droop control for dc distribution systems," *IEEE Transactions on Energy Conversion*, vol. 29, no. 4, pp. 944–956, 2014.

[42] S. Augustine, M. K. Mishra, and N. Lakshminarasamma, "Adaptive droop control strategy for load sharing and circulating current minimization in low-voltage standalone dc microgrid," *IEEE Transactions on Sustainable Energy*, vol. 6, no. 1, pp. 132–141, 2015.

[43] N. Eghtedarpour and E. Farjah, "Power control and management in a hybrid ac/dc microgrid," *IEEE Transactions on Smart Grid*, vol. 5, no. 3, pp. 1494 – 1505, 2014.

[44] S. M. Malik, X. Ai, Y. Sun, C. Zhengqi, and Z. Shupeng, "Voltage and frequency control strategies of hybrid ac/dc microgrid: a review," *IET Generation, Transmission & Distribution*, vol. 11, no. 2, pp. 303–313, 2017.

[45] M. Hamzeh, M. Ghafouri, H. Karimi, K. Sheshyekani, and J. M. Guerrero, "Power oscillations damping in dc microgrids," *IEEE Transactions on Energy Conversion*, vol. 31, no. 3, pp. 970–980, 2016.

[46] E. Unamuno and J. A. Barrena, "Hybrid ac/dc microgrids-part ii: Review and classification of control strategies," *Renewable and Sustainable Energy Reviews*, vol. 52, pp. 1123–1134, 2015.

[47] H. Tian, Y. W. Li, and P. Wang, "Hybrid ac/dc system harmonics control through grid interfacing converters with low switching frequency," *IEEE Transactions on Industrial Electronics*, vol. 65, no. 3, pp. 2256–2267, 2018.

[48] A. A. A. Radwan and Y.-R. Mohamed, "Networked control and power management of ac/dc hybrid microgrids," *IEEE System Journal*, vol. PP, no. 99, pp. 1–12, 2014.

[49] P. Wang, C. Jin, D. Zhu, Y. Tang, P. C. Loh, and F. H. Choo, "Distributed control for autonomous operation of a three-port ac/dc/ds hybrid microgrid," *IEEE Transactions on Industrial Electronics*, vol. 62, no. 2, pp. 1279–1290, 2015.

[50] H. Zhang, J. Zhou, Q. Sun, J. M. Guerrero, and D. Ma, "Data-driven control for interlinked ac/dc microgrids via model-free adaptive control and dual-droop control," *IEEE Transactions on Smart Grid*, vol. 8, no. 2, pp. 557–571, 2017.

[51] S. Peyghami, H. Mokhtari, and F. Blaabjerg, "Autonomous operation of a hybrid ac/dc microgrid with multiple interlinking converters," *IEEE Transactions on Smart Grid*, 2017.

[52] J. Zhou, H. Zhang, Q. Sun, D. Ma, and B. Huang, "Event-based distributed active power sharing control for interconnected ac and dc microgrids," *IEEE Transactions on Smart Grid*, 2017.

[53] J. Wang, C. Jin, and P. Wang, "A uniform control strategy for the interlinking converter in hierarchical controlled hybrid ac/dc microgrids," *IEEE Transactions on Industrial Electronics*, 2017.

[54] Y. Xia, W. Wei, M. Yu, X. Wang, and Y. Peng, "Power management for a hybrid ac/dc microgrid with multiple subgrids," *IEEE Transactions on Power Electronics*, vol. 33, no. 4, pp. 3520–3533, 2018.

[55] A. A. Hamad, M. A. Azzouz, and E. F. El-Saadany, "Multiagent supervisory control for power management in dc microgrids," *IEEE Transactions on Smart Grid*, vol. 7, no. 2, pp. 1057–1068, 2016.

[56] K. Sun, X. Wang, Y. W. Li, F. Nejabatkhah, Y. Mei, and X. Lu, "Parallel operation of bidirectional interfacing converters in a hybrid ac/dc microgrid under unbalanced grid voltage conditions," *IEEE Transactions on Power Electronics*, vol. 32, no. 3, pp. 1872–1884, 2017.

[57] P. Kundur, J. Paserba, V. Ajjarapu, G. Andersson, A. Bose, C. Canizares, N. Hatziargyriou, D. Hill, A. Stankovic, C. Taylor *et al.*, "Definition and classification of power system stability ieee/cigre joint task force on stability terms and definitions," *IEEE Transactions on Power Systems*, vol. 19, no. 3, pp. 1387–1401, 2004.

[58] P. Kundur, N. J. Balu, and M. G. Lauby, *Power system stability and control*. McGraw-hill New York, 1994, vol. 7.

[59] A. Gómez-Expósito, A. J. Conejo, and C. Cañizares, *Electric energy systems: analysis and operation*. CRC Press, 2016.

[60] R. Al Abri, E. F. El-Saadany, and Y. M. Atwa, "Optimal placement and sizing method to improve the voltage stability margin in a distribution system using distributed generation," *IEEE Transactions on Power Systems*, vol. 28, no. 1, pp. 326–334, 2013.

[61] N. C. Hien, N. Mithulananthan, and R. C. Bansal, "Location and sizing of distributed generation units for loadabilty enhancement in primary feeder," *IEEE systems journal*, vol. 7, no. 4, pp. 797–806, 2013.

[62] E. Romero-Ramos, A. Gomez-Exposito, A. Marano-Marcolini, J. Maza-Ortega, and J. Martinez-Ramos, "Assessing the loadability of active distribution networks in the presence of dc controllable links," *IET generation, transmission & distribution*, vol. 5, no. 11, pp. 1105–1113, 2011.

[63] S. K. Chaudhary, J. M. Guerrero, and R. Teodorescu, "Enhancing the capacity of the ac distribution system using dc interlinks-a step toward future dc grid," *IEEE Transactions on Smart Grid*, vol. 6, no. 4, pp. 1722–1729, 2015.

[64] G. Díaz, "Maximum loadability of droop regulated microgrids–formulation and analysis," *IET Generation, Transmission & Distribution*, vol. 7, no. 2, pp. 175–182, 2013.

[65] M. M. Abdelaziz and E. El-Saadany, "Maximum loadability consideration in droop-controlled islanded microgrids optimal power flow," *Electric Power Systems Research*, vol. 106, pp. 168–179, 2014.

[66] M. M. A. Abdelaziz, H. E. Farag, and E. F. El-Saadany, "Optimum droop parameter settings of islanded microgrids with renewable energy resources," *IEEE Transactions on Sustainable Energy*, vol. 5, no. 2, pp. 434–445, 2014.

[67] ——, "Optimum reconfiguration of droop-controlled islanded microgrids," *IEEE Transactions on Power Systems*, vol. 31, no. 3, pp. 2144–2153, 2016.

[68] J. M. Guerrero, J. C. Vasquez, J. Matas, L. G. de Vicuña, and M. Castilla, "Hierarchical control of droop-controlled ac and dc microgrids - a general approach toward standardization," *IEEE Transactions on Industrial Electronics*, vol. 58, no. 1, pp. 158–172, 2011.

[69] A. Bidram and A. Davoudi, "Hierarchical structure of microgrids control system," *IEEE Transactions on Smart Grid*, vol. 3, no. 4, pp. 1963–1976, 2012.

[70] D. Olivares, C. Canizares, and M. Kazerani, "A centralized energy management system for isolated microgrids," *IEEE Transactions on Smart Grids*, vol. PP, no. 99, pp. 1–12, 2014.

[71] EPRI , "Advanced control room energy management system: Requirements and implementation guidance," *EPRI report 1010076*, 2005.

[72] P. Siano, C. Cecati, H. Yu, and J. Kolbusz, "Real time operation of smart grids via fcn networks and optimal power flow," *IEEE Transactions on Industrial informatics*, vol. 8, no. 4, pp. 944–952, 2012.

[73] A. Z. Alabedin, "Generation scheduling in microgrids under uncertainties in power generation," Master's thesis, University of Waterloo, 2012.

[74] C.-X. Dou and B. Liu, "Multi-agent based hierarchical hybrid control for smart microgrid," *Energy Conversion and Management*, vol. 4, no. 2, pp. 771–778, 2013.

[75] A. Y. Saber and G. K. Venayagamoorthy, "Plug-in vehicles and renewable energy sources for cost and emission reductions," *IEEE Transactions on Industrial Electronics*, vol. 58, no. 4, pp. 1229–1238, 2011.

[76] A. Y. Saber and G. K. Venayamoorthy, "Resource scheduling under uncertainty in a smart grid with renewables and plug-in vehicles," *IEEE Systems Journal*, vol. 6, pp. 103–109, March 2012.

[77] J. Soares, H. Morais, T. Sousa, Z. Vale, and P. Faria, "Day-ahead resource scheduling including demand response for electric vehicles," *IEEE Transactions on Smart Grid*, vol. 4, no. 1, pp. 596–605, March 2013.

[78] A. Zakariazadeh, S. Jadid, and P. Siano, "Economic-environmental energy and reserve scheduling of smart distribution systems: A multiobjective mathematical programming approach," *Energy Conversion and Management*, vol. 78, pp. 151–164, 2014.

[79] A. Zakariazadeh, S. Jadid, and P. Siano, "Multi-objective scheduling of electric vehicles in smart distribution system," *Energy Conversion and Management*, vol. 79, pp. 43–53, 2014.

[80] W. Su, J. Wang, and J. Roh, "Stochastic energy scheduling in microgrids with intermittent renewable energy resources," *IEEE Transactions on Smart Grid*, vol. PP, no. 99, pp. 1–9, Nov. 2013.

[81] D. E. Olivares, C. A. Cañizares, and M. Kazerani, "A centralized energy management system for isolated microgrids," *IEEE Transactions on Smart Grid*, vol. 5, no. 4, pp. 1864 – 1875, 2014.

[82] M. A. Ortega-Vazquez, "Optimal scheduling of electric vehicle charging and vehicle-to-grid services at household level including battery degradation and price uncertainty," *IET Generation, Transmission & Distribution*, vol. 8, no. 6, pp. 1007–1016, 2014.

[83] E. Karangelos and F. Bouffard, "Towards full integration of demand-side resources in joint forward energy/reserve electricity markets," *IEEE Transactions on Power Systems*, vol. 27, no. 1, pp. 280–289, 2012.

[84] M. A. Ortega-Vazquez, F. Bouffard, and V. Silva, "Electric vehicle aggregator/system operator coordination for charging scheduling and services procurement," *IEEE Transactions on Power Systems*, vol. 28, no. 2, pp. 1806–1815, 2013.

[85] N. I. M. G. Andrew R. Conn and P. L. Toint, *Trust Region Methods, MOS-SIAM Series on Optimization*. Society for Industrial and Applied Mathematics, 2000.

[86] J. Nocedal and S. Wright, *Numerical optimization 2nd*. Springer Science & Business Media, 2006.

[87] O. I. Elgerd, *Electric energy systems theory: an introduction*. McGraw-Hill Book Company, New York, NY, 1982.

[88] J. J. Grainger and W. D. Stevenson, *Power system analysis*. McGraw-Hill New York, 1994.

[89] W. Price, H.-D. Chiang, H. Clark, C. Concordia, D. Lee, J. Hsu, S. Ihara, C. King, C. Lin, Y. Mansour *et al.*, "Load representation for dynamic performance analysis," *IEEE Transactions on Power Systems*, vol. 8, no. 2, pp. 472–482, 1993.

[90] P. C. Loh, D. Li, Y. K. Chai, and F. Blaabjerg, "Autonomous operation of ac–dc microgrids with minimised interlinking energy flow," *IET Power Electronics*, vol. 6, no. 8, pp. 1650–1657, 2013.

[91] ANSI Standard, "For electric power systems and equipment-voltage ratings (60 hz)," 2006.

[92] A. Yazdani and R. Iravani, *Voltage-sourced converters in power systems: modeling, control, and applications.* John Wiley & Sons, 2010.

[93] IEEE Power Systems Committee, "IEEE orange book–IEEE std 446-1987," 1992.

[94] Evolve Green. (2015) Wind turbine. [Online]. Available: http://www.evolvegreen.ca/windturbines.html

[95] IEEE Standard 1115, "IEEE recommended practice for sizing nickel-cadmium batteries for stationary applications," 2000.

[96] Y. Li and Y. W. Li, "Power management of inverter interfaced autonomous microgrid based on virtual frequency-voltage frame," *IEEE Transactions on Smart Grid*, vol. 2, no. 1, pp. 30–40, 2011.

[97] IEC Standard 60364-5-52, "Low-voltage electrical installations," 2009.

[98] T. Gönen, *Electric power distribution system engineering.* McGraw-Hill New York, 1986.

[99] J. M. Guerrero, L. Hang, and J. Uceda, "Control of distributed uninterruptible power supply systems," *IEEE Transactions on Industrial Electronics*, vol. 55, no. 8, pp. 2845–2859, 2008.

[100] M. E. Baran and N. R. Mahajan, "Overcurrent protection on voltage-source-converter-based multiterminal dc distribution systems," *IEEE Transactions on Power Delivery*, vol. 22, no. 1, pp. 406–412, 2007.

[101] M. AlHajri and M. El-Hawary, "Exploiting the radial distribution structure in developing a fast and flexible radial power flow for unbalanced three-phase networks," *IEEE Transactions on Power Delivery*, vol. 25, no. 1, pp. 378–389, 2010.

[102] M. E. Baran and F. F. Wu, "Optimal capacitor placement on radial distribution systems," *IEEE Transactions on Power Delivery*, vol. 4, no. 1, pp. 725–734, 1989.

[103] D. Singh and R. Misra, "Effect of load models in distributed generation planning," *IEEE Transactions on Power Systems*, vol. 22, no. 4, pp. 2204–2212, 2007.

[104] T. Caldognetto and P. Tenti, "Microgrids operation based on master–slave cooperative control," *Emerging and Selected Topics in Power Electronics, IEEE Journal of*, vol. 2, no. 4, pp. 1081–1088, 2014.

[105] Q.-C. Zhong, "Robust droop controller for accurate proportional load sharing among inverters operated in parallel," *IEEE Transactions on Industrial Electronics*, vol. 60, no. 4, pp. 1281–1290, 2013.

[106] A. Khorsandi, M. Ashourloo, and H. Mokhtari, "A decentralized control method for a low-voltage dc microgrid," *IEEE Transactions on Energy Conversion*, vol. 29, no. 4, pp. 793–801, 2014.

[107] F. Guo, C. Wen, J. Mao, and Y.-D. Song, "Distributed secondary voltage and frequency restoration control of droop-controlled inverter-based microgrids," *IEEE Trans. industrial Electronics*, vol. 62, no. 7, pp. 4355–4364, 2015.

[108] N. Pogaku, M. Prodanovic, and T. C. Green, "Modeling, analysis and testing of autonomous operation of an inverter-based microgrid," *IEEE Transactions on Power Electronics*, vol. 22, no. 2, pp. 613–625, 2007.

[109] W. Rosehart, C. Roman, and A. Schellenberg, "Optimal power flow with complementarity constraints," in *2006 IEEE PES Power Systems Conference and Exposition.* IEEE, 2006, pp. 417–417.

[110] A. Fischer, "A special newton-type optimization method," *Optimization*, vol. 24, no. 3-4, pp. 269–284, 1992.

[111] G. Diaz and C. Gonzalez-Moran, "Fischer-burmeister-based method for calculating equilibrium points of droop-regulated microgrids," *IEEE Transactions on Power Systems*, vol. 27, no. 2, pp. 959–967, 2012.

[112] A. Said, "Toward the integration of dc microgrids into a hybrid ac/dc paradigm," *PhD dessertation, University of Waterloo*, 2016.

[113] A. Baki, "Continuous monitoring of smart grid devices through multi protocol label switching," *IEEE Trans. Smart Grid*, vol. 5, no. 3, pp. 1210–1215, 2014.

[114] S. Liu, X. Wang, and P. X. Liu, "Impact of communication delays on secondary frequency control in an islanded microgrid," *IEEE Trans. Industrial Electronics*, vol. 62, no. 4, pp. 2021–2031, 2015.

[115] J. Nocedal and S. J. Wright, *Sequential quadratic programming*. Springer, 2006.

[116] S. S. Rao and S. S. Rao, *Engineering optimization: theory and practice*. John Wiley & Sons, 2009.

[117] A. J. Collin, G. Tsagarakis, A. E. Kiprakis, and S. McLaughlin, "Development of low-voltage load models for the residential load sector," *IEEE Transactions on Power Systems*, vol. 29, no. 5, pp. 2180–2188, 2014.

[118] Y. Zhu, F. Zhuo, F. Wang, B. Liu, R. Gou, and Y. Zhao, "A virtual impedance optimization method for reactive power sharing in networked microgrid," *IEEE Transactions on Power Electronics*, vol. 31, no. 4, pp. 2890–2904, 2016.

[119] D. T. Ton and W. P. Wang, "A more resilient grid: The US department of energy joins with stakeholders in an r&d plan," *IEEE Power and Energy Magazine*, vol. 13, no. 3, pp. 26–34, 2015.

[120] B. Beihoff, T. Jahns, R. Lasseter, and G. Radloff, "Transforming the grid from the distribution system out," *White Paper, UW-Madison Wisconsin Energy Institute*, 2014.

[121] F. Nejabatkhah and Y. W. Li, "Overview of power management strategies of hybrid ac/dc microgrid," *IEEE Transactions on Power Electronics*, vol. PP, no. 99, 2014.

[122] M. Molinas, D. Moltoni, G. Fascendini, J. A. Suul, and T. Undeland, "Constant power loads in ac distribution systems: An investigation of stability," in *IEEE Int. Symposium on Industrial Electronics*. IEEE, 2008, pp. 1531–1536.

[123] H. Kakigano, Y. Miura, and T. Ise, "Low-voltage bipolar-type dc microgrid for super high quality distribution," *IEEE Transactions on Power Electronics*, vol. 25, no. 12, pp. 3066–3075, 2010.

[124] K. M. Rogers, R. Klump, H. Khurana, A. A. Aquino-Lugo, and T. J. Overbye, "An authenticated control framework for distributed voltage support on the smart grid," *IEEE Transactions on Smart Grid*, vol. 1, no. 1, pp. 40–47, 2010.

[125] S. Anand and B. Fernandes, "Reduced-order model and stability analysis of low-voltage dc microgrid," *IEEE Transactions on Industrial Electronics*, vol. 60, no. 11, pp. 5040–5049, 2013.

[126] P. Liutanakul, A.-B. Awan, S. Pierfederici, B. Nahid-Mobarakeh, and F. Meibody-Tabar, "Linear stabilization of a dc bus supplying a constant power load: A general design approach," *IEEE Transactions on Power Electronics*, vol. 25, no. 2, pp. 475–488, 2010.

[127] J. Wang and D. Howe, "A power shaping stabilizing control strategy for dc power systems with constant power loads," *IEEE Transactions on Power Electronics*, vol. 23, no. 6, pp. 2982–2989, 2008.

[128] A. Standard, "C84. 1-2011, electric power systems and equipment-voltage ratings (60 hertz)."

[129] W. W. Weaver and P. T. Krein, "Mitigation of power system collapse through active dynamic buffers," in *Power Electronics Specialists Conference, 2004. PESC 04. 2004 IEEE 35th Annual*, vol. 2. IEEE, 2004, pp. 1080–1084.

[130] NERC, "NERC reliability concepts," 2007.

[131] A. Eajal, M. A. Abdelwahed, E. El-Saadany, and K. Ponnambalam, "A unified approach to the power flow analysis of ac/dc hybrid microgrids," *IEEE Transactions on Sustainable Energy*, vol. 7, no. 3, pp. 1145–1158, 2016.

[132] X. Wang, D. Vilathgamuwa, and S. Choi, "Decoupling load and power system dynamics to improve system stability," in *Power Electronics and Drives Systems, 2005. PEDS 2005. International Conference on*, vol. 1. IEEE, 2005, pp. 268–273.

[133] M. F. Shaaban, A. A. Eajal, and E. F. El-Saadany, "Coordinated charging of plug-in hybrid electric vehicles in smart hybrid ac/dc distribution systems," *Renewable Energy*, vol. 82, pp. 92–99, 2015.

[134] M. S. ElNozahy and M. M. Salama, "Uncertainty-based design of a bilayer distribution system for improved integration of phevs and pv arrays," *IEEE Transactions on Sustainable Energy*, vol. 6, no. 3, pp. 659 – 674, 2015.

[135] S. Karlin, *A first course in stochastic processes*. Academic press, 2014.

[136] M. Alizadeh, A. Scaglione, J. Davies, and K. S. Kurani, "A scalable stochastic model for the electricity demand of electric and plug-in hybrid vehicles," *IEEE Transactions on Smart Grid*, vol. 5, no. 2, pp. 848–860, 2014.

[137] Toronto Parking Authority. (2014). [Online]. Available: http://parking.greenp.com/

[138] K. Krishnamoorthy, *Handbook of statistical distributions with applications*. CRC Press, 2006.

[139] F. Bouffard and F. D. Galiana, "Stochastic security for operations planning with significant wind power generation," in *Power and Energy Society General Meeting-Conversion and Delivery of Electrical Energy in the 21st Century*. IEEE, 2008, pp. 1–11.

[140] M. S. Nazir and F. Bouffard, "Intra-hour wind power characteristics for flexible operations," in *Power and Energy Society General Meeting*. IEEE, 2012, pp. 1–8.

[141] A. Papavasiliou and S. S. Oren, "Large-scale integration of deferrable demand and renewable energy sources," *IEEE Transactions on Power Systems*, vol. 29, no. 1, pp. 489–499, 2014.

[142] S. Gill, I. Kockar, and G. W. Ault, "Dynamic optimal power flow for active distribution networks," *IEEE Transactions on Power Systems*, vol. 29, no. 1, pp. 121–131, Sep. 2013.

[143] J. R. Birge and F. Louveaux, *Introduction to stochastic programming*. New York: Springer, 2011.

[144] J. Dupačová, N. Gröwe-Kuska, and W. Römisch, "Scenario reduction in stochastic programming," *Mathematical programming*, vol. 95, no. 3, pp. 493–511, 2003.

[145] A. J. Conejo, M. Carrión, and J. M. Morales, *Decision making under uncertainty in electricity markets*. Springer, 2010, vol. 1.

[146] J. Arrillaga and B. Smith, *AC-DC power system analysis*. United Kingdom: IEE, 1998.

[147] M. Carrión and J. M. Arroyo, "A computationally efficient mixed-integer linear formulation for the thermal unit commitment problem," *IEEE Transactions on Power Systems*, vol. 21, no. 3, pp. 1371–1378, 2006.

[148] Hydro One, "Distributed generation technical interconnection requirements," 2013.

[149] T. Logenthiran and D. Srinivasan, "Short term generation scheduling of a microgrid," in *Proc. 2009 IEEE Region 10 Conf.*, pp. 1–6.

[150] S.-J. Ahn, S.-R. Nam, J.-H. Choi, and S.-I. Moon, "Power scheduling of distributed generators for economic and stable operation of a microgrid," *IEEE Transactions on Smart Grid*, vol. 4, no. 1, pp. 398–405, 2013.

[151] K. Morrow, D. Karner, and J. Francfort, "Plug-in hybrid electric vehicle charging infrastructure review," *US Department of Energy-Vehicle Technologies Program*, 2008.

[152] Ameren Illinois Power Co. (2015, May) Real-time pricing for residential customers. [Online]. Available: https://www.ameren.com/illinois/electric-choice/residential-real-time-pricing

[153] R. Jabr, "Adjustable robust opf with renewable energy sources," *IEEE Transactions on Power Systems*, vol. 28, no. 4, pp. 4742–4751, 2013.

[154] U.S Department of Energy (DOE), "Grid energy storage," 2013.

[155] J. Widén, "Correlations between large-scale solar and wind power in a future scenario for sweden," *IEEE Transactions on Sustainable Energy*, vol. 2, no. 2, pp. 177–184, 2011.

[156] R. E. Rosenthal, *SBB Solver Manual - Gams*. GAMS Development Corporation, Washington, DC, USA, 2010.

[157] R. E. Rosenthal, *GAMS-A User's Guide*. GAMS Development Corporation, Washington, DC, USA, 2010.

[158] E. C. (EMC), "Part 3-6: Limits–assessment of emission limits for the connection of distorting installations to mv, hv and ehv power systems," 2008.

APPENDICES

Appendix A

Test Systems Data

A.1 6-Bus AC/DC Hybrid Microgrid Data

Table A.1. Bus Data for the 6-Bus Islanded AC/DC Hybrid Microgrid (S_{base} = 18 kVA, 208/600 V)

MG	Bus No.	Bus Type	V_0 (p.u.)	Load Type	P_D^{rated} (kW)	Q_D^{rated} (kvar)	DG Type	P_G^{rated} (kW)	Q_G^{rated} (kvar)	ω_0 (p.u.)	m_p (p.u.)	n_q (p.u.)
AC	1	D	1.0	—	—	—	D	6.4	4.8	1.0	0.0281	0.1875
	2	T	1.0	PQ	25	18.75	P	14	10.5	—	—	—
	3	D	1.0	—	—	—	D	9.6	7.2	1.0	0.0187	0.1250
DC	1	D	1.0	—	—	—	D	6.72	—	—	0.1339	—
	2	T	1.0	P	15	—	P	4.6	—	—	—	—
	3	D	1.0	—	—	—	D	6.72	—	—	0.1339	—
IC #	AC Bus	DC Bus	P_{ic} (kW)	Q_{ic} (kvar)	ω_0 (p.u.)	ω_{min} (p.u.)	ω_{max} (p.u.)	$V_{dc,0}$ (p.u.)	$V_{dc,min}$ (p.u.)	$V_{dc,max}$ (p.u.)	γ_p (p.u.)	γ_q (p.u.)
1	1	1	18	12	1.0	0.99	1.01	1.0	0.95	1.05	1.0	0.0750
2	2	2	18	12	1.0	0.99	1.01	1.0	0.95	1.05	1.0	0.0750
3	3	3	18	12	1.0	0.99	1.01	1.0	0.95	1.05	1.0	0.0750

A.2 Medium Voltage-12-Bus AC/DC Hybrid Microgrid Data

Table A.2. Bus Data for the 12-Bus Islanded AC/DC Hybrid Microgrid (S_{base} = 3 MVA, 2.4/7 kV)

MG	Bus No.	Bus Type	$\|V_0\|$ (p.u.)	Load Type	P_D^{rated} (MW)	Q_D^{rated} (Mvar)	DR Type	P_{DR}^{rated} (MW)	Q_{DR}^{rated} (Mvar)	ω_0 (p.u.)	m_p (p.u.)	n_q (p.u.)
AC	1	D/PQ	1.0	—	—	—	DG	0.8	0.6	1.0	0.0375	0.25
	2	T	1.0	PQ	0.4	0.3	—	—	—	—	—	—
	3	Z	1.0	Z	1.0	0.6	—	—	—	—	—	—
	4	D	1.0	—	—	—	DS	0.48	0.36	1.0	0.0625	0.4167
	5	T	1.0	I	0.8	0.6	—	—	—	—	—	—
	6	D/PV	1.0	—	—	—-	DG	1.8	1.35	1.0	0.0167	0.1111
DC	1	T	1.0	P	0.6	—	—	—	—	—	—	—
	2	D/V	1.0	—	—	—	DG	1.92	—	—	0.0781	—
	3	D	1.0	—	—	—	DS	0.48	—	—	0.3125	—
	4	D/P	1.0	—	—	—	DG	0.6	—	—	0.25	—
	5	T	1.0	I	1.4	—	—	—	—	—	—	—
	6	R	1.0	R	0.5	—	—	—	—	—	—	—
IC #	AC Bus	DC Bus	P_{ic} (MW)	Q_{ic} (Mvar)	ω_0 (p.u.)	ω_{min} (p.u.)	ω_{max} (p.u.)	$V_{dc,0}$ (p.u.)	$V_{dc,min}$ (p.u.)	$V_{dc,max}$ (p.u.)	γ_p (p.u.)	γ_q (p.u.)
1	2	1	3.0	2.25	1.0	0.99	1.01	1.0	0.95	1.05	1.0	0.0667
2	5	5	3.0	2.25	1.0	0.99	1.01	1.0	0.95	1.05	1.0	0.0667

Table A.3. Line Data for the 12-Bus Islanded AC/DC Hybrid Microgrid

AC Subgrid				DC Subgrid		
From	To	$R_{Line,ac}(\Omega)$	$X_{Line,ac}(\Omega)$	From	To	$R_{Line,dc}(\Omega)$
1	2	0.02646	0.01323	1	2	0.4340
2	3	0.04032	0.02016	2	3	0.4100
3	4	0.02646	0.01323	3	4	0.4100
3	5	0.04032	0.02016	4	5	0.4340
5	6	0.02646	0.01323	5	6	0.2279
6	4	0.04032	0.02016	6	1	0.2279
4	1	0.04032	0.02016	3	6	0.4340

A.3 33-Bus AC/DC Hybrid Microgrid Data

Table A.4. 33-Bus AC/DC Hybrid Distribution System Data: AC Bus Data

Bus Index	Bus Type	DR Type	P_D (kW)	Q_D (kvar)	$P_{max,ac}$ (p.u.)	S_{max} (p.u.)	Q_{max} (p.u.)	$m_{p,ac}$ (p.u.)	n_q (p.u.)	f_0 (p.u.)	$V_{ac,0}$ (p.u.)
1	PQ	—	0	0	—	—	—	—	—	—	—
2	D	DG	100	60	0.8	1	0.6	0.010375	0.041667	1	1
3	PQ	—	90	40	—	—	—	—	—	—	—
4	PQ	—	120	80	—	—	—	—	—	—	—
5	PQ	—	60	30	—	—	—	—	—	—	—
6	PQ	—	60	20	—	—	—	—	—	—	—
7	D	DG	200	100	0.8	1	0.6	0.010375	0.041667	1	1
8	T	—	200	100	—	—	—	—	—	—	—
9	PQ	—	90	40	—	—	—	—	—	—	—
10	PQ	—	90	40	—	—	—	—	—	—	—
11	D	DG	90	40	0.96	1.2	0.72	0.008646	0.034722	1	1
12	T	—	90	40	—	—	—	—	—	—	—
13	PQ	—	90	50	—	—	—	—	—	—	—
14	PQ	—	420	200	—	—	—	—	—	—	—
15	PQ	—	420	200	0.4	0.5	0.3	—	—	—	—
16	PQ	—	60	25	—	—	—	—	—	—	—
17	PQ	—	60	25	—	—	—	—	—	—	—
18	PQ	—	60	20	—	—	—	—	—	—	—
19	T	—	120	70	—	—	—	—	—	—	—

Table A.5. 33-Bus AC/DC Hybrid Distribution System Data: AC Line Data

AC Line	From Bus	To Bus	$R_{Line,ac}$ (Ω)	$X_{Line,ac}$ (Ω)
1	1	2	0.0922	0.047
2	2	3	0.493	0.2511
3	3	4	0.366	0.1864
4	4	5	0.3811	0.1941
5	5	6	0.819	0.707
6	6	7	0.1872	0.6188
7	7	8	0.7114	0.2351
8	2	9	0.164	0.1565
9	9	10	1.5042	1.3554
10	10	11	0.4095	0.4784
11	11	12	0.7089	0.9373
12	3	13	0.4512	0.3083
13	13	14	0.898	0.7091
14	14	15	0.896	0.7011
15	6	16	0.203	0.1034
16	16	17	0.2842	0.1447
17	17	18	1.059	0.9337
18	18	19	0.8042	0.7006
19	8	12	2	2
20	15	19	0.5	0.5

Table A.6. 33-Bus AC/DC Hybrid Distribution System Data: DC Bus Data

Bus Index	Bus Type	DR Type	P_D (kW)	$P_{max,dc}$ (p.u.)	$m_{p,dc}$ (p.u.)	$V_{dc,0}$ (p.u.)
1	T	—	90	—	—	—
2	P	—	60	0.18	—	1.0
3	P	—	60	—	—	1.0
4	T	—	60	—	—	—
5	D	DG	120	0.4	0.0625	1
6	P	—	60	—	—	—
7	P	—	60	—	—	—
8	P	—	45	—	—	—
9	P	—	60	—	—	—
10	P	—	60	—	—	—
11	T	—	80	—	—	—
12	D	DG	50	0.25	0.1	1.0
13	P	—	35	—	—	—
14	P	—	40	—	—	—
15	P	—	60	—	—	—
16	D	DG	210	0.5	0.05	1.0
17	P	—	150	—	—	—
18	D	DG	200	0.5	0.05	1.0

Table A.7. 33-Bus AC/DC Hybrid Distribution System Data: DC Line Data

DC Line	From Bus	To Bus	$R_{Line,dc}$ (Ω)
1	1	2	0.732
2	2	3	1.289
3	3	4	0.7463
4	4	5	0.591
5	5	6	0.5416
6	6	7	1.468
7	7	8	0.3744
8	8	9	0.1966
9	9	10	1.044
10	11	12	0.5
11	12	13	0.341
12	13	14	0.3105
13	14	15	0.9744
14	15	16	0.9744
15	16	17	0.341
16	17	18	0.9744
17	10	18	1.044
18	1	7	0.3105
19	7	15	0.9744

A.4 Low-Voltage 12-Bus AC/DC Hybrid Microgrid Data

Table A.8. Bus Data for the 12-Bus Islanded AC/DC Hybrid Microgrid (S_{base} = 10 kVA, 208/600 V)

MG	Bus No.	Bus Type	$\lvert V_{ac,0}\rvert$ (p.u.)	Load Type	P_D^{rated} (kW)	Q_D^{rated} (kvar)	DR Type	P_{DG}^{rated} (kW)	Q_{DG}^{rated} (kvar)	ω_0 (p.u.)	$m_{p,ac}$ (Hz/W.sec)	n_q (V/var)
AC	1	D	1.0	—	—	—	DG	20	12.3	1.0	3×10^{-5}	4.2276×10^{-4}
	2	T	1.0	Z	14.8	6.3048	—	—	—	—	—	—
	3	PQ	1.0	Z	12.95	6.272	—	—	—	—	—	—
	4	T	1.0	Z	9.25	4.9926	—	—	—	—	—	—
	5	D	1.0	—	—	—	DG	15	9.2	1.0	4×10^{-5}	5.6522×10^{-4}
	6	D	1.0	—	—	—-	DG	10	6.13	1.0	6×10^{-5}	8.4829×10^{-4}
DC	1	D	1.0	—	—	—	DG	20	—	—	7.5×10^{-4}	—
	2	T	1.0	R	20	—	—	—	—	—	—	—
	3	P	1.0	R	6	—	—	—	—	—	—	—
	4	T	1.0	R	16	—	–	—	—	—	—	—
	5	D	1.0	—	—	—	DG	15	—	—	1×10^{-3}	—
	6	D	1.0	—	—	—	DG	10	—	—	1.5×10^{-3}	—
IC #	AC Bus	DC Bus	P_{ic} (kW)	Q_{ic} (kvar)	ω_0 (p.u.)	ω_{min} (p.u.)	ω_{max} (p.u.)	$V_{dc,0}$ (p.u.)	$V_{dc,min}$ (p.u.)	$V_{dc,max}$ (p.u.)	γ_p (p.u.)	γ_q (p.u.)
1	2	2	10	10	1.0	0.99	1.01	1.0	0.95	1.05	1.0	1.04×10^{-4}
2	4	4	10	10	1.0	0.99	1.01	1.0	0.95	1.05	1.0	1.04×10^{-4}

Table A.9. Line Data for the 12-Bus Islanded AC/DC Hybrid Microgrid

AC Subgrid				DC Subgrid		
From	To	$R_{Line,ac}(\Omega)$	$L_{Line,ac}$(mH)	From	To	$R_{Line,dc}(\Omega)$
1	2	0.039	0.068	1	2	0.395
2	3	0.099	0.0902	2	3	0.735
3	4	0.099	0.1122	3	4	0.699
4	5	0.070	0.1565	4	5	0.588
3	6	0.059	0.0673	3	6	0.649
5	6	0.1488	0.1353	5	6	0.588
6	1	0.0927	0.0245	6	1	0.699

A.5 38-Bus AC/DC Hybrid Microgrid Data

Table A.10. 38-Bus AC/DC Hybrid Distribution System Data: AC Bus Data

Bus Index	Bus Type	DR Type	P_D (kW)	Q_D (kvar)	$P_{min,ac}$ (p.u.)	$P_{max,ac}$ (p.u.)	S_{max} (p.u.)	Q_{max} (p.u.)	$m_{p,ac}$ (p.u.)	n_q (p.u.)	f_0 (p.u.)	$V_{ac,0}$ (p.u.)
1	PQ	0	0	0	0	0	0	0	0	0	1	1
2	PQ	0	0.1	0.06	0	0	0	0	0	0	1	1
3	T	0	0.09	0.04	0	0	0	0	0	0	1	1
4	D	DG	0.12	0.08	0	0.08	0.1	0.06	0.25	1.666667	1.01	1.05
5	PQ	0	0.06	0.03	0	0	0	0	0	0	1	1
6	T	0	0.06	0.02	0	0	0	0	0	0	1	1
7	PQ	0	0.2	0.1	0	0	0	0	0	0	1	1
8	PQ	0	0.2	0.1	0	0	0	0	0	0	1	1
9	PQ	0	0.06	0.02	0	0	0	0	0	0	1	1
10	PQ	0	0.06	0.02	0	0	0	0	0	0	1	1
11	PQ	0	0.045	0.03	0	0	0	0	0	0	1	1
12	PQ	0	0.06	0.035	0	0	0	0	0	0	1	1
13	PQ	0	0.06	0.035	0	0	0	0	0	0	1	1
14	PQ	0	0.12	0.08	0	0	0	0	0	0	1	1
15	PQ	0	0.06	0.01	0	0	0	0	0	0	1	1
16	PQ	0	0.06	0.02	0	0	0	0	0	0	1	1
17	PQ	0	0.06	0.02	0	0.4	0.5	0.3	0	0	1	1
18	PQ	0	0.09	0.04	0	0	0	0	0	0	1	1
19	D	DG	0.09	0.04	0	0.6	0.75	0.45	0.033333	0.22222	1.01	1.05
20	PQ	0	0.09	0.04	0	0	0	0	0	0	1	1
21	PQ	0	0.09	0.04	0	0	0	0	0	0	1	1
22	D	DG	0.09	0.04	0	0.24	0.3	0.18	0.083333	0.555553	1.01	1.05
23	D	DS	0	0	-0.24	0.24	0.3	0.18	0.083333	0.555553	1.01	1.05
24	D	DG	0	0	0	0.6	0.75	0.45	0.033333	0.22222	1.01	1.05
25	D	DS	0	0	-0.16	0.16	0.2	0.12	0.125	0.833728	1.01	1.05
26	D	DG	0	0	0	0.08	0.1	0.06	0.25	1.666667	1.01	1.05

Table A.11. 38-Bus AC/DC Hybrid Distribution System Data: AC Line Data

AC Line	From Bus	To Bus	$R_{Line,ac}$ (Ω)	$X_{Line,dc}$ (Ω)
1	1	2	0.000574	0.000293
2	2	3	0.00307	0.001564
3	3	4	0.002279	0.001161
4	4	5	0.002373	0.001209
5	5	6	0.0051	0.004402
6	6	7	0.001166	0.003853
7	7	8	0.00443	0.001464
8	8	9	0.006413	0.004608
9	9	10	0.006501	0.004608
10	10	11	0.001224	0.000405
11	11	12	0.002331	0.000771
12	12	13	0.009141	0.007192
13	13	14	0.003372	0.004439
14	14	15	0.00368	0.003275
15	15	16	0.004647	0.003394
16	16	17	0.008026	0.010716
17	17	18	0.004558	0.003574
18	2	19	0.001021	0.000974
19	19	20	0.009366	0.00844
20	20	21	0.00255	0.002979
21	21	22	0.004414	0.005836
22	8	23	0.012453	0.012453
23	9	24	0.012453	0.012453
24	12	25	0.012453	0.012453
25	18	26	0.003113	0.003113

Table A.12. 38-Bus AC/DC Hybrid Distribution System Data: DC Bus Data

Bus Index	Bus Type	DR Type	P_D (kW)	$P_{min,dc}$ (p.u.)	$P_{max,dc}$ (p.u.)	$m_{p,dc}$ (p.u.)	$V_{dc,0}$ (p.u.)
1	T	DS	0.09	-0.1	0.1	1	1.05
2	PQ	—	0.42	0	0	0	1
3	D	DG	0.42	0	0.45	0.22222	1.05
4	T	—	0.06	0	0	0	1
5	D	DG	0.06	0	0.6	0.16667	1.05
6	PQ	—	0.06	0	0	0	1
7	PQ	—	0.12	0	0.5	0	1
8	PQ	—	0.2	0	0	0	1
9	PQ	—	0.15	0	0	0	1
10	PQ	—	0.21	0	0	0	1
11	D	DG	0.06	0	0.4	0.25	1.05
12	D	DS	0	-0.5	0.5	0.2	1.05

Table A.13. 38-Bus AC/DC Hybrid Distribution System Data: DC Line Data

DC Line	From	To	$R_{Line,dc}$ (Ω)
1	1	2	0.005579
2	2	3	0.005579
3	4	5	0.00177
4	5	6	0.006594
5	6	7	0.005007
6	7	8	0.00316
7	8	9	0.006067
8	9	10	0.001933
9	10	11	0.002123
10	3	12	0.003113

Appendix B

List of Publications

The following is a list of publications by the candidate during his doctoral studies.

B.1 Peer-Reviewed Journal Articles

[J1] **Eajal, A., A.**, Abdelwahed, M. A., El-Saadany, F., E., and Ponnambalam, K., "A unified approach to the power flow analysis of ac/dc hybrid microgrids," *IEEE Transactions on Sustainable Energy*, vol. 7, (3), pp. 1145-1158, 2016.

[J2] **Eajal, A., A.**, Shaaban, M., F., Ponnambalam, K., and El-Saadany, F., E, "Stochastic centralized dispatch scheme for ac/dc hybrid smart distribution systems," *IEEE Transactions on Sustainable Energy*, vol. 7, (3), pp. 1046-1059, 2016.

B.2 Journal Articles under Reveiw

[J1] **Eajal, A., A.**, El-Saadany, F., E., and Ponnambalam, K, "Towards Precise and Unified Power Sharing in Islanded ac/dc Hybrid Microgrids", *IEEE Transactions on Smart Grids*.

[J2] **Eajal, A., A.**, El-Saadany, F., E., and Ponnambalam, K, "On the Loadability and Voltage Stability of Islanded ac/dc Hybrid Microgrids with Contingencies", *IEEE Systems Journal*.

B.3 Articles in Conference Proceedings

[C1] **Eajal, A., A.**, Yazdavar, A. H., El-Saadany, F., E., and Ponnambalam, K.," On the Existence of Voltage Collapse in Islanded Microgrids", Accepted at the 18th annual IEEE Canada Electrical Power and Energy Conference (EPEC), Toronto, ON, 10-11 Oct., 2018.

[C2] **Eajal, A., A.**, Abdelwahed, M. A., El-Saadany, F., E., and Ponnambalam, K.," Power Flow Analysis of ac/dc Hybrid Microgrids", the 2016 IEEE Electrical Power and Energy Conference (EPEC), pp 1-6, London, ON, 12-14 Oct., 2016.

[C3] **Eajal, A., A.**, El-Saadany, E., F., and Ponnambalam, K.,"Equal power sharing in islanded ac/dc hybrid microgrids," the 2016 IEEE Electrical Power and Energy Conference (EPEC), pp. 1-6, London, ON, 12-14 Oct., 2016.

[C4] **Eajal, A., A.**, El-Saadany, F., E., and Ponnambalam, K.," Inexact Power Sharing in ac/dc Hybrid Microgrids", the 2016 IEEE Canadian Conference on Electrical and Computer Engineering (CCECE), Vancouver, BC, 22 Feb., 2016.

[C5] **Eajal, A., A.**, Shaaban, M., F., Ponnambalam, K., and El-Saadany, F., E." Stochastic Energy Coordination in Hybrid ac/dc Smart Grids", the 2015 IEEE Electrical Power and Energy Conference (EPEC), pp 158-163, London, ON, 26-28 Oct., 2015.

[C6] **Eajal, A., A.**, Elrayani, Y., Ponnambalam, K., and El-Saadany, F., E." Two-Stage Stochastic Power Generation Scheduling in Microgrids", the 2014 Canadian Conference on Electrical and Computer Engineering (CCECE), Toronto, ON, 4-7 May, 2014.

B.4 Posters

[P1] "Energy Management in ac/dc Systems, Energy Day, March 30, 2016, Waterloo Institute of Sustainable Energy (WISE).